Ore-Forming Potential of Late-Magmatic Volatiles Forming Under the Roof of the Skaergaard Intrusion, East Greenland

Margrét Traustadóttir

Abstract

Volatiles can have a substantial influence on the constrains and genesis of ore deposit, but are not generally stored in the system afterwards. Small pockets of fluid can however be stored as fluid inclusions. Therefore the study of fluid inclusions has contributed to the extensive understanding of the behaviour of volatiles in different geological settings, and to the conditions during the formation of the mineral that entrapped the fluid inclusion.

The intent of this research is to study the late-magmatic aqueous fluids in the Skaergaard layered gabbro. Both the gabbroic pegmatites and the granophyre masses in the intrusion coexisted with an aqueous solution with the same chemical composition. By using microthermometry it is possible to measure the temperatures at which phase changes happen within a fluid inclusion, which consequently enables the evaluation of the chemical composition and the evolution of the system. Additionally, a geochemical analysis was performed to further assess the magma chamber processes during the crystallization of the intrusion. Samples collected during previous expeditions to Skaergaard were used, and fieldwork was conducted at Vestrahorn to obtain a better understanding of the granophyre and gabbroic pegmatite.

The Skaergaard intrusion drove its own meteoric-hydrothermal circulation system during subsolidus cooling. This resulted in an alteration of the mineral assemblage and possible re-equilibration of the fluid inclusions, without any considerable changes in the chemical composition of the aqueous volatiles stored within the fluid inclusions. The better preserved fluid inclusions correlates with the previous research of the LS, which indicate increased pressure during crystallization as the Skaergaard intrusion was progressively buried by flood basalt. It is suggested that the re-equilibration of fluid inclusion occurred while the system was dominated by hydrostatic pressure, at a sub-solidus conditions.

Acknowledgements

Table of contents

List of figures

List of tables

Abbreviations

CL	Cathodoluminescence
cm	Centimeters
EoS	Equations of state
E	Eutectic point
FI	Fluid Inclusions
Gr	Grams
g/t	Grams per ton
HZ	Hidden Zone
IGB	The Department of Geology and Mineral Resources Engineering
kbar	Kilobar
km	Kilometers
kN	Kilo Newton
LIP	Large Igneous Provinces
LOI	Loss on ignition
LS	Layered Series
LZ	Lower Zone in the LS
LZ'	Lower Zone in the UBS
LZa	Lower zone a in the LS
LZa'	Lower zone a in the UBS
LZb	Lower zone b in the LS
LZb'	Lower zone b in the UBS
LZc	Lower zone c in the LS
LZc'	Lower zone c in the UBS
m	meters
Ma	Million years ago
MBS	Marginal Border Series
MORB	Mid Ocean Ridge Basalt

MZ	Middle Zone in the LS
MZ'	Middle Zone in the UBS
MT	Metric ton
NAIP	North Atlantic Igneous province
NTNU	Norwegian University of Science and Technology (n. Norges teknisk-naturvitenskapelige universitet)
Ol	Olivine
PGE	Platinum Group Elements; platinum, palladium, rhodium, iridium, osmium and ruthenium.
P	Peritectic point
Plag	Plagioclase
Qtz	Quartz
REE	Rare Earth Elements
SEM-CL	Scanning Electron Microscope - Cathodoluminescence
SH	Sandwich Horizon
TEM	Transmission Electron Microscope
$T_{h-Total}$	Homogenisation temperature of the FI
Th phase	The phase that the fluid inclusion became homogeneous in
$Tm_{Hydrate}$	Melting temperature of hydro-halide in the FI
Tm_{ice}	Melting temperature of ice in the FI
$Tm_{initial}$	Initial melting temperature of the FI
UBS	Upper Border Series
UZ	Upper Zone in the LS
UZ'	Upper Zone in the UBS
UZa	Upper Zone a in the LS
UZa'	Upper Zone a in the UBS
UZb	Upper Zone b in the LS
UZb'	Upper Zone b in the UBS
UZc	Upper Zone c in the LS

UZc'	Upper Zone c in the UBS
Vol.%	Volume percent
wt.%:	Weight percen
XRD	X-ray powder diffraction
XRF	X-ray fluorescence
Zr	Zirconium
µl	Microliters
µm	Micrometers

1 Introduction

Late-magmatic aqueous solutions coexisted with the gabbroic pegmatites and granophyre masses during their formation in the Skaergaard layered gabbro, East Greenland. Volatiles can have a substantial influence on the constrains and genesis of the petrogenesis processes, e.g. trace element distribution, the formation of economic ore deposit, or late magmatic metasomatism. The fluids are not generally stored in the system afterwards, however small pockets of fluids can be stored as fluid inclusions (FI). These store samples of the volatile phase that dominated the system, and are therefore the only means by which the volatiles can be characterized. A study of FI makes it possible to analyse these fluids, and to form an extensive understanding of the behaviour of volatiles in different geological settings, and the conditions during the formation of the mineral that entrapped the FI.

FI have been shown to record the pressure under which the Skaergaard intrusion crystallised (Larsen and Tegner, 2006). Therefore the FI in the Layered Series (LS) correlate with progressive burial during flood basalt emplacement, which puts constrains on the duration of the volcanism. This research estimates the pressure conditions of the Upper Border Series (UBS) and the Sandwich Horizon (SH) during crystallization, in order to assess the evolution of system during and after crystallization of the system in the UBS.

1.1 Background

The main purpose of this study is to investigate volatiles in FI in granophyre masses in the UBS of the Skaergaard intrusion, and to compare it to the volatile evolution observed in the LS. Moreover the chemical composition of possible granophyre accumulates from the SH will be examined and compared to samples that are perhaps an iron-rich, intercumulus liquid.

As fieldwork in East Greenland was not feasible due to high costs, it was decided to focus instead on the Vestrahorn layered gabbroic ring-complex in Iceland. Preliminary studies of this location implied that it comprises of granophyres and gabbroic pegmatites which are comparable to the Skaergaard intrusion. Fieldwork at Vestrahorn primarily aimed to provide a deeper understanding of the setting and relationship of volatile-rich granophyre and gabbroic pegmatite during the formation and solidification of gabbroic magma-chambers. It was not the aim to use the results from Vestrahorn to make a systematic comparison with

the Skaergaard Intrusion, but to decide if the field appearance of granophyre and gabbroic pegmatite at Vestrahorn could be analogous to what is known from the Skaergaard Intrusion. The studies consisted of fieldwork, preparation of samples and measurements and interpretation of results. The field work was completed during the summer of 2014, while laboratory work was conducted from spring 2014 to spring of 2015.

1.2 Aim and objective

The principal aim of the study is to gain a more complete understanding of the volatile history of the Skaergaard intrusion, and to determine if late-magmatic aqueous volatiles' pressure conditions in the UBS mimics the previously known evolution of volatile fluids in the LS. Additionally it is attempted to further understand possible silicate liquid immiscibility in the intrusion. Increased insight into these aims might result in advancing knowledge of the magma chamber processes. The most important method used is microthermometric analysis on FI in interstitial granophyric masses situated throughout the entire stratigraphy of UBS.

Therefore the project was separated into the following topics:

- Microthermometric analysis of fluid inclusions to decide whether late-magmatic aqueous volatiles in the UBS mimics the previously known evolution of volatile fluids in the LS and if these fluids were involved in the genesis or modification of the Platinum Group Elements (PGE)-Au deposits found in the Skaergaard intrusion.

- Evaluation of the field appearance of gabbroic pegmatite, granophyric aggregations and other late-magmatic structures at Vestrahorn in light of those found in the Skaergaard intrusion.

- Geochemical analysis of samples from the SH that, being the largest volume of granophyre in the Skaergaard intrusion, may provide additional data on the volatile history and the fluid-melt interaction history. In addition samples that might have formed from an iron-rich, intercumulus liquid were analysed and compared to the SH samples.

2 Regional geology

Mantle plumes originate at the base of the mantle, in the so-called "D" layer (Best, 2013), where they rise to the earth crust and form a mantle "hot-spot" or plume due to the rising of hot lighter melts (Bjarnason, 2008, Morgan, 1972). The mantle plume starts at the mantle-core boundary with a thin tail, which flattens out and expands when it meets the lithosphere, forming the head of the plume. The buoyance force of the mantle plume causes an increased tension in the crust, along with regional uplift and increased regional temperature of about 100-200°C (White and McKenzie, 1989). This can be associated with voluminous basalt eruptions, forming flood basalts and aseismic ridges. Flood basalts eruptions can last for 1-5 Myr and produce enough lava to form Large Igneous Provinces (LIP) (areas larger than 100.000 km^2) (Campbell, 2005).

The Icelandic mantle plume was located under the east coast of Greenland about 55 Ma (Vink, 1984), which resulted in the rifting of the North Atlantic Ocean and the formation of the North Atlantic Igneous province (NAIP). The NAIP consists of about 10 million km^3 of igneous rocks, which erupted over 2-3 Ma (White and McKenzie, 1989). The basalt can be found in West and East Greenland, the northern half of the British Isles and in the Faroe Islands.

About 25-30 Ma the mantle plume began to influence the area where Iceland is located today, leading to the formation of Iceland about 15-20 Ma (Guðmundsson et al., 2003). Today the mantle plume is located underneath central Iceland, causing Iceland to rise 2-4 km above the Mid-Atlantic ridge (Bjarnason, 2008).

2.1 The geological setting of Skaergaard

While underneath Greenland the mantle plume induced uplift and rifting in a triple point where the Kangerdlugssuaq comprises an aulacogen, and the two other arms opened up to form the North Atlantic Ocean. Rifting together with the mantle plume activity resulted in a massive outpouring of several kilometres of regional flood basalts, along with the emplacement of several layered igneous intrusions and alkaline as well as granitic rocks. (Wager and Brown, 1967).

One of the earlier intrusions in the Kangerdlugssuaq area is the Skaergaard intrusion (figure 2-1), which was emplaced 56.02 Ma (Wotzlaw et al., 2012) when it was intruded horizontally between the gneiss basement and the above flood basalt (Wager and Brown, 1967), before being tilted 20° towards south. Its location controlled by faults and bedding planes in the host rock (Nielsen, 2004). It has been modeled as an irregular box, with a volume of approximately 280 ± 23 km^3 (Nielsen, 2004). Due to uplift and erosion about 70 km^2 can be seen in a outcrop with 3 km of vertical profile (Brooks, 2005).
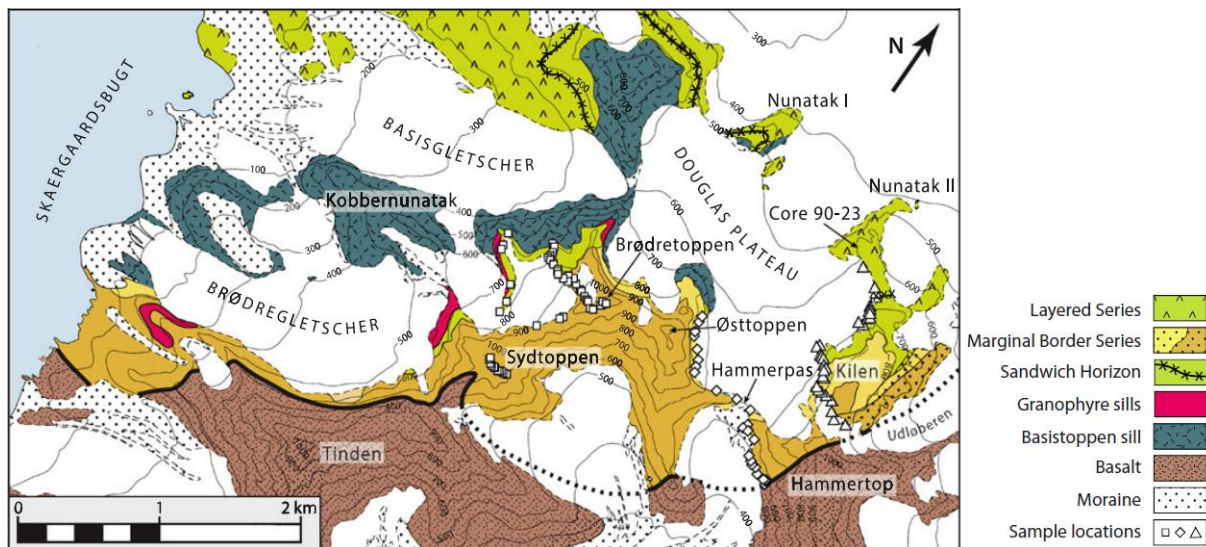
Figure 2-1: Geology map of the Skaergaard intrusion, showing the location of the rock series and the main geography locations.
Source: (Salmonsen and Tegner, 2013).

The intrusion formed from a single pulse of evolved tholeiitic magma, which had a chemical composition similar to the tholeiitic plateau basalts in East Greenland (Nielsen, 2004). The system is considered to have been closed during crystallization (Wager and Mitchell, 1951), as it crystallized slowly from the margins adjacent to the country rock, forming a layered gabbro with cryptic layering and so-called "onion-skin" structure (Nielsen, 2004), which can be seen in figure 2-2. As it crystallized from the margins, inwards towards the center it formed three series; the LS, which crystallized from the floor, the UBS, which crystallized from the roof, and the Marginal Border Series (MBS), which crystallized from the walls. These series met in the center to form a thin discontinuous layer, called the SH, from the last liquid fraction. Additionally the unexposed part at the base of the LS has been classified as the Hidden Zone (HZ), which contains the earliest forming cumulates (Wager and Brown,

1967). The volume of these series has been estimated, and of the 280 ± 23 km^3, the UBS is estimated to be 13.7%, the MBS 16.4%, and the LS, which is the most voluminous due to crystal settling, 69.9% (Nielsen, 2004). Each series shows a distinctive evolution trend towards lower temperature mineralogy inwards, towards the center of the intrusion, as plagioclase, olivine and pyroxene, respectively, becomes more albite-, fayalite-, and hedenbergite-rich (Wager and Brown, 1967).
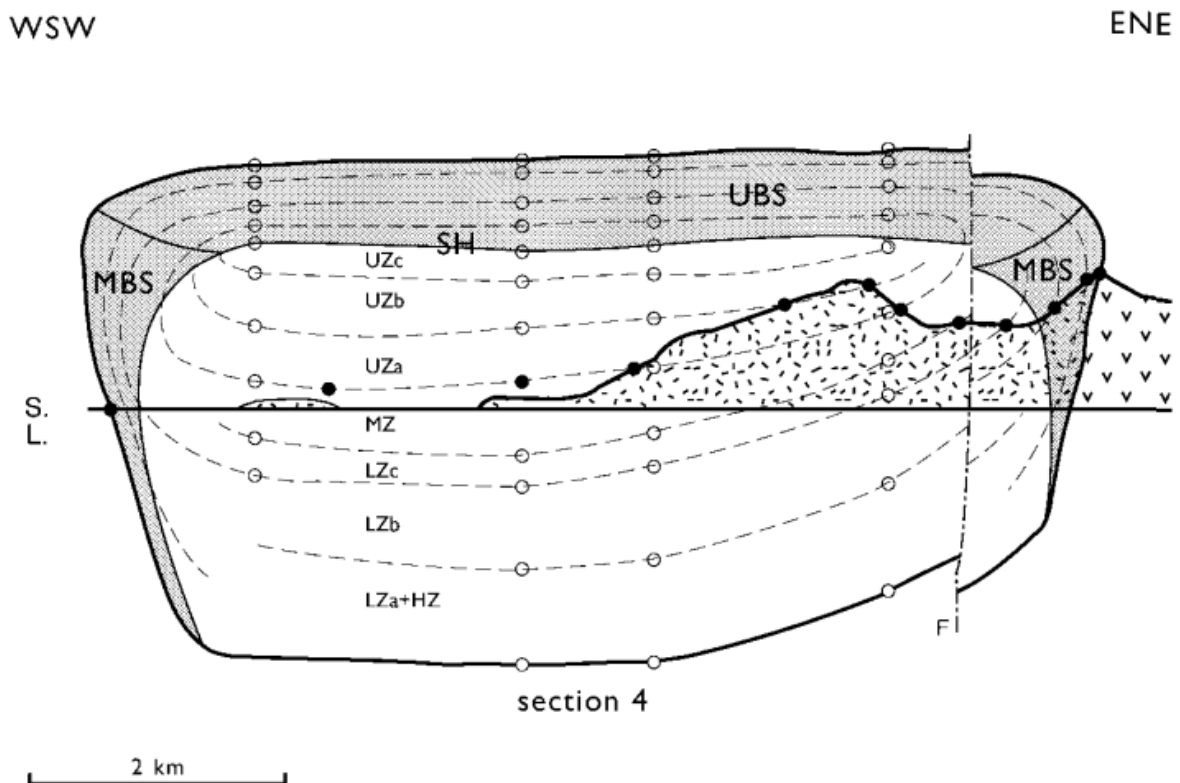
Figure 2-2: The figure shows the onion-skin structure as proposed by Nielsen (2004), which formed due to crystallization from the margins inwards. Additionally the layers in each series are shown.
Source: (Nielsen, 2004)

The cryptic layering forms horizontal layers, which are consistent with crystal fractionation and settling in a cooling magma chamber, as the crystallization front moved inwards towards the center (Winter, 2010). The crystallization sequence is used to divide the intrusion into series and sub-zones. The zones in the LS have been split into the Lower Zone (LZ), which constitutes 66.8% of the LS, a Middle Zone (MZ) constituting 13.5%, and Upper Zone (UZ), which constitutes 19.7% of the intrusion (Nielsen, 2004).

Cumulus olivine and plagioclase mark the LZa, the addition of augite marks the LZb, and the LZc starts where magnetite and ilmenite appear as a cumulus phase. Disappearance of

5

olivine marks the beginning of the MZ. The UZ starts where olivine reappears (UZa), cumulus apatite marks the UZb, and ferrobustamite (which has been inverted to hedenbergite) marks the beginning of the UZc (Wager and Brown, 1967). The same subdivision has been suggested for the UBS, with added apostrophes (Salmonsen and Tegner, 2013), which will be used here. The SH is located in the center of the intrusion, where the LS, UBS and MBS meet.

Although the UBS and the MBS contain the same layers as the LS, there are still considerable variations between the series. Most noticeable is how the UBS contains larger amounts of interstitial granophyric material, in addition to being significantly richer in SiO_2, K_2O, P_2O_5, H_2O and incompatible trace elements, while being poorer in FeO, TiO_2, MgO and CaO. Moreover intrusive dikes make up c. 15% of the outcrop in the UBS, while being rare in the LS (Naslund, 1984).

During the crystallization of the Skaergaard intrusion, two separate phases, one iron-rich and another silica-rich, formed due to immiscibility in the magma. These phases coincide with magma saturation in Fe-Ti oxides, which happened in the LZc. Immiscibility in the intrusion caused the redistribution of both major and trace elements. The iron-rich phase contains 30.9 ± 4.2 wt% FeO and 40.7 ± 3.6 wt% SiO_2 while the silica-rich phase contains 8.6 ± 5.9 wt% and 65.6 ± 7.3 wt%, respectively, resulting in these liquids having different densities. The separation into phases with different densities has been used to explain the formation of silicic layers and pods, melano-granophyres and segregated granophyres, and distribution of elements (Jakobsen et al., 2005).

2.1.1 Rock structures

Located within ferrodiorites are pods, lenses, patches and streaks of melano-granophyre, which are richer in quartz and micropegmatites i.e. granophyre, and poorer in olivine, pyroxene and magnetite than the surrounding host rock. The melano-granophyre are believed to have formed due to liquid-liquid exsolution of the immiscible silica-rich end member (Brown and Peckett, 1977, Holness et al., 2011, Naslund, 1984). The different geometry forms are thought to be the result of a different fluid pressure gradient as the fluid was pressed through porous crystalline matrix, in a high temperature process that followed the initial crystallization of the magma closely (Larsen and Brooks, 1994, Larsen et al., 1992, Larsen and Tegner, 2006, McBirney and Sonnenthal, 1990). They constitute about 15% of the

UZc in the LS and are probably even more common in the UBS. This has been attributed to differential compaction between the LS and the UBS (Jakobsen et al., 2011).

Granophyre pockets are found both in granites and gabbros, bound by primocryst grains, which are in equilibrium with the granophyre. The granophyre are considered to have been the last liquid to crystallize during solidification of the intrusion (Holness et al., 2011, Larsen and Brooks, 1994, Larsen and Tegner, 2006).

Gabbroic pegmatites have been found throughout the LS. Podiform pegmatites dominate the LZ and the lower part of the MZ, while the upper part of the MZ and the UZ are dominated by semi-conformable sheets, parallel to the layering (Larsen and Brooks, 1994). The pegmatites consist of mafic margins with laths of plagioclase that grade into a gabbroic zone, with a granophyre center (Larsen and Brooks, 1994, Larsen et al., 1992). These pegmatites are thought to have formed due to intercumulus liquid migrating upwards before being trapped. They contained high amounts of H_2O and probably also retained P_2O_5, K_2O and rare earth elements (REEs) as they moved higher up in the LS (Larsen and Brooks, 1994). They contain the same $\delta^{18}O$ signature as the surrounding gabbro (Taylor and Forester, 1979) which indicates that they formed by igneous differentiation, at a low temperature (Larsen and Brooks, 1994), but not external derived volatiles as proposed by McBirney and Sonnenthal (1990).

Irregular anorthositic gabbro is found cutting layered rocks in the LZ, which have been altered to more felsic composition (McBirney and Sonnenthal, 1990). These structures formed by aqueous volatiles that escaped from melano-granophyre (Larsen and Brooks, 1994).

Dendritic anorthosites are found in the LS. They consist of white anorthosite in a mafic host rock, which forms a branching tree structure that are only a few centimeters thick, but can reach up to a few meters in length. Pegmatite pipes were found in the same area, and in the LZb gabbroic pegmatites can be found within anorthosite structures (Larsen and Brooks, 1994).

Mafic segregation surrounded by felsic gabbro are found in the MBS. These segregations are elongated, 15 cm – 1 m thick, and oriented parallel to the walls and the layers in the MBS (McBirney and Sonnenthal, 1990). The mineral properties indicate that the segregation

formed due to mobilization of an Fe-rich melt from the gabbro, into pipes associated with high-temperature fluid (Sonnenthal, 1992).

2.1.2   Volatiles and metasomatism in Skaergaard

Generally Skaergaard is considered to have formed from a rather dry magma due to the absence of primary hydrous silicates. However the intrusion does contain primary apatite, along with secondary biotite and amphibole, which are hydrous minerals that contain water, as well as fluorine and chlorine, which contradicts that idea. The primary apatite is fluorine- and hydroxyl-rich right from the beginning, and as the melt evolves it becomes progressively enriched in fluorine (Larsen and Brooks, 1994). The Cl⁻ rich fluid is believed to have exsolved from the evolving magma, while being enriched in trace elements derived from the residual melt. The metasomatising fluid is thought to have caused enrichment of trace elements in the anorthosite rock structures (Sonnenthal, 1992).

The Skaergaard intrusion had an original value of 5.5-5.6 $\delta^{18}O$, a very common value for a primary tholeiitic basalt. The $\delta^{18}O$ values found in plagioclase decrease upwards in the intrusion, from normal values (6.0-6.4) in the LS to -2.4 in the UBS. Because the system was impermeable the depletion must have happened under subsolidus conditions by a hydrothermal circulating system, which the intrusion drove during crystallization and cooling. After crystallization and fracturing the hydrothermal system collapsed inwards, allowing meteoric water to infiltrate the intrusion. This resulted in diverse $\delta^{18}O$ and δD values that did not affect the magma, as it was only after crystallization where the hydrothermal system collapsed inwards to interact with the already crystallized gabbro (Bindeman et al., 2008, Taylor and Forester, 1979, Wotzlaw et al., 2012).

Most of the influx of H_2O into the intrusion happened at high temperatures (>400-500°C) as evident in the low temperature, hydrous alteration minerals. Meteoric water percolated down through the jointed plateau basalt, which had a higher permeability than the basement gneiss, resulting in major $\delta^{18}O$ depletion and a high water/rock ratio. This ratio is only prominent above the gneiss-basalt unconformity, even though the $\delta^{18}O$ exchange happened throughout the intrusion. As the meteoric water percolated downwards through the basalt country rock, the fluids exchanged with the similar mineral assemblage, explaining the limited chemical alteration of the gabbro. The chemical alteration can however been seen on the rims of zircon crystals, which have re-equilibrated with the low $\delta^{18}O$

surroundings, even though they are known to be resistant to a secondary alteration by meteoric-hydrothermal alteration, and that did thoroughly affect the plagioclase (Bindeman et al., 2008, Taylor and Forester, 1979, Wotzlaw et al., 2012).

In addition to the meteoric-hydrothermal cycle, which caused the SH to become even more depleted in $\delta^{18}O$ values compared to the original magma, it has been suggested that the SH partially re-melted by heat from the Basistoppen Sill intrusion. The re-melted melt migrated upwards, resulting in the formation of a horizon rich in incompatible trace elements about 100 m above the SH (Wotzlaw et al., 2012).

2.1.3 Petrography of the UBS

The appearance and disappearance of cumulus minerals is used to subdivide the Skaergaard intrusion into layers, therefore petrography is of great importance. The appearance of cumulus phases is the same in all three series (Salmonsen and Tegner, 2013). The following is a short summary of the main minerals found in the Skaergaard intrusion by previous researchers. An overview of the layers and the appearance of the cumulus minerals in the UBS can be seen in figure 2-3.

Olivine

The disappearance of olivine is used to identify the MZ', and its re-appearance is used to mark the beginning of the UZa'. It is the first mineral to start to crystallize along with plagioclase in the LZa'. It is both the first and last cumulus phase, but it is generally less abundant and highly altered in the UBS compared to the LS and the MBS, which gives olivine a sporadic occurrence in the UBS (Naslund, 1984, Salmonsen and Tegner, 2013).

Plagioclase

Plagioclase occurs as a primocryst throughout the UBS, where it makes up 40-60% of most samples. The plagioclase is a cumulus mineral, where it forms an interlocking framework, which crystallized *in-situ*. The crystals are zoned and show the chemical evolution of the system (Naslund, 1984).

Augite

Augite mainly grew subsequent to olivine and plagioclase, and therefore seems to have formed from an interstitial liquid. The amount of augite oikocrysts increase downwards from

the roof before forming a cumulus phase in the LZb' (Naslund, 1984, Salmonsen and Tegner, 2013).

Magnetite and ilmenite

Oxides are found throughout the UBS, but there is a marked increase in the amount of oxides in the LZc', which marks the onset of cumulus oxides. The oxide grain consist of anhedral aggregates that forms skeletal and dendritic texture (Naslund, 1984, Salmonsen and Tegner, 2013).

Apatite

Apatite is common throughout the UBS, but there is a marked increase in the UZb'. There apatite is found both in the cores and overgrowths rims of plagioclase and pyroxene, which has been interpreted as the beginning of apatite cumulus phase. Throughout the UBS it is found as inclusions in olivine, augite and oxides (Naslund, 1984, Salmonsen and Tegner, 2013).

Ferrobustamite

Aggregates of ferrohedenbergite are found in the UZc' and are considered to have inverted from ferrobustamite (Naslund, 1984). Increase in MnO is taken as an evidence for abundance of ferrobustamite in the UZc', where it forms a cumulus phase (Salmonsen and Tegner, 2013).

Accessory minerals

Sulphur saturation was reached when about 70% of the melt had crystallized (Wager et al., 1957), which happened in the MZ. This resulted in the accumulation of sulphides that did not form a cumulate phase (Naslund, 1984, Salmonsen and Tegner, 2013).

Quarts occur as anhedral grains, granophyre intergrowths or tridymite pseudomorphs. Its abundance increases downward from the roof to the SH. In addition titanite and zircon are found as common postcumulus minerals and biotite as uncommon postcumulus mineral.
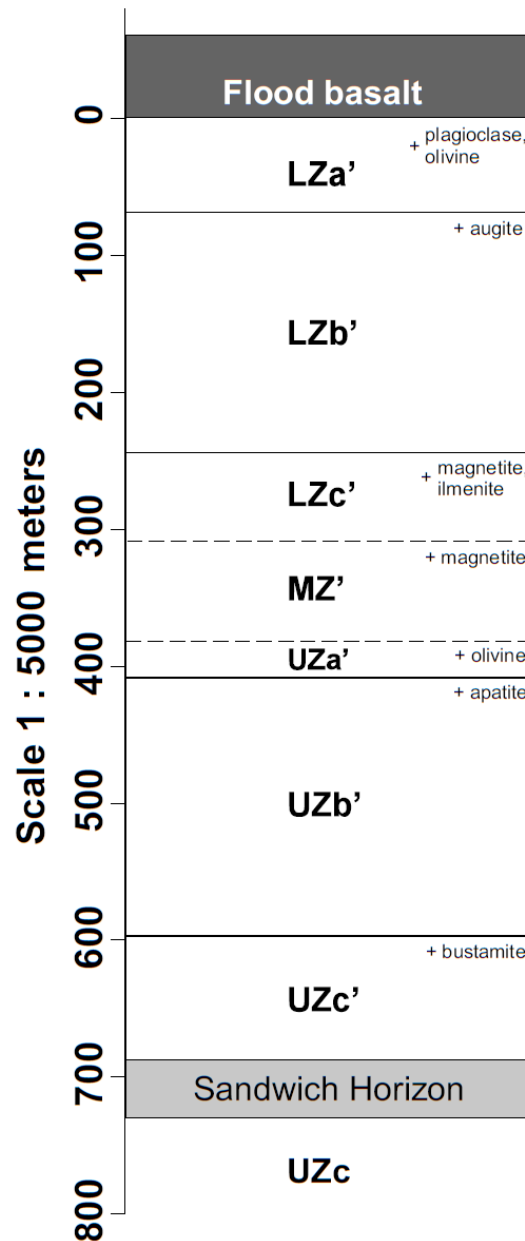
Figure 2-3: Section of the layers in the UBS along with the cumulus minerals which are used to define the beginning of each layer.
Source: (Salmonsen and Tegner, 2013).

2.1.4   The Platinova reef

Near the top of the MZ in the LS is the so-called Triple group, which consists of conformable felsic layers. Associated with them are four leucocratic, macrorhythmic units rich in plagioclase, along with the PGE-Au bearing horizon, which is only 10-50 cm thick and estimated to have formed as a result of orthomagmatic processes. There is no mineralogical or textural difference between the gold-bearing horizon and the layers around it, therefore

the only way to distinguish it is with knowledge of the stratigraphy (Brooks, 2005, Naldrett, 2004). The horizon consists of at least eight layers (about 40 m vertically), where the lowest and the most extensive one of the precious metal layer lies about 21 m below the lowest leucocratic layer, but moving upwards the size of the precious metal layers decreases. The reefs seem to form bowls, which intersect the stratigraphy of the intrusion at a low angle. The gold appears to have concentrated around the rim of those bowls, and where it is richest it can reach concentrations of up to 3.3 g/t (Brooks, 2005).

The economic minerals collected into layers due to fractionation of the magma, causing sulphide immiscibility that formed droplets of sulphides, which scavenged the melt for platinum group (PGE) and Au minerals, and forming the Platinova reef. Due to the magma being stripped of these elements the layers above the reef are totally depleted of economic minerals (Brooks, 2005, Naldrett, 2004, Robb, 2009).

Mineralogy of the Platinova reef

The Platinova reef is a gabbroic rock that has a typical mineral composition. It consists of olivine, plagioclase, pyroxene and iron oxides, along with small amount of sulphides (Brooks, 2005). The copper sulfides formed as immiscible sulphide droplets in the silicate melt during the crystallization of the intrusion at around 0.16-0.3 wt.% sulphur (Robb, 2009), which then fell to the bottom of the intrusion along with oxide minerals and precipitated silicates due to density differences (Wager et al., 1957).

The reef is a low grade deposit, but contains a high volume of material (Brooks, 2005). It has been estimated to be 202.2 MT and contain 0.88 g/t of gold, 1.33 g/t of palladium and 0.11 g/t of platinum (PlatinaResources, 2015).

Prospecting at Skaergaard

In 1986 the company Platinova became interested in prospecting for precious metals in the Kangerdlugssuaq area, due to it being an aulacogen, which was at that time thought to be a likely area for deposits. Skaergaard was not thought to be a likely deposit as it was quite evolved (and iron-rich). Therefore another gabbroic complex was the main focus of their search, and it was only due to coincidence that the Skaergaard intrusion was also sampled.

Therefore it was quite unexpected at that time to find that the Skaergaard intrusion contained the most gold in the area (Brooks, 2005).

Over the following years more excursions were undertaken, which resulted in the knowledge to estimate that there is a gold-rich horizon extending over most of the intrusion. But as the deposit does not contain enough gold or titanium (a possible by-product) it wasn't a certain profit and was therefore not mined. This resulted in Platinova Resources Limited withdrawing from the area in 1992. At the end of the 1990's the increase in palladium prices resulted in other metals being considered as a by-product, making the reef a more feasible mining option. Production was estimated to start in 2009, but so far the reef has not been mined (Brooks, 2005).

2.2 The geological setting of Vestrahorn

Vestrahorn, or Vesturhorn like many people want to call it, has not been studied to the same extend as Skaergaard, so its formation history is not as thoroughly known.

The country rock in southeastern Iceland mostly consists of layers of basalt from the late Tertiary. The basalt was later intruded multiple time; these intrusions crystallized deep under the surface forming gabbro and granophyre (Sigurdsson, 1969) during the differentiation of the rock bodies. Study of zeolites has revealed that the basalt cover above the intrusions was about 1.7 km thick, which had then been removed by glacial erosion exposing the underlying gabbro and granophyric intrusions (Blake, 1966). Furthermore, these intrusions seem to have developed in an immature axial extensional environment (Furman et al., 1992). The acid and intermediate intrusions in SE Iceland are generally related to volcanic centres (Walker, 1964) and range in size from $1 - 19$ km^2, in which Vestrahorn is the largest one (19 km^2) (Klausen, 2006, Thorarinsson and Tegner, 2009) and 900 m thick, consisting of at least 72 separate injections of acid and basic magma (Roobol, 1972). It has a 7° dip to NW, while the surrounding host rock has a 30° dip in the same direction (Roobol, 1974). It is also estimated to have formed at about 6.6 ± 0.3 Ma (Gale et al., 1966, Moorbath et al., 1968, Sigurdsson, 1969), due to increased plume activity 7.5 Ma (Hanan and Schilling, 1997), and consists of evolved transitional tholeiite (Furman et al., 1992).

Vestrahorn is composed of a central core of granite intrusion between two mafic intrusions, where the granite intruded first and was still partly molten when the gabbro intruded. The granite consists of a horizontal sheet structures surrounded by transitional granite that contains agglomerates and net-veined complexes (Guðmundsson, 2009, Roobol, 1974). A geological map of the Vestrahorn area can be found in figure 2-4.
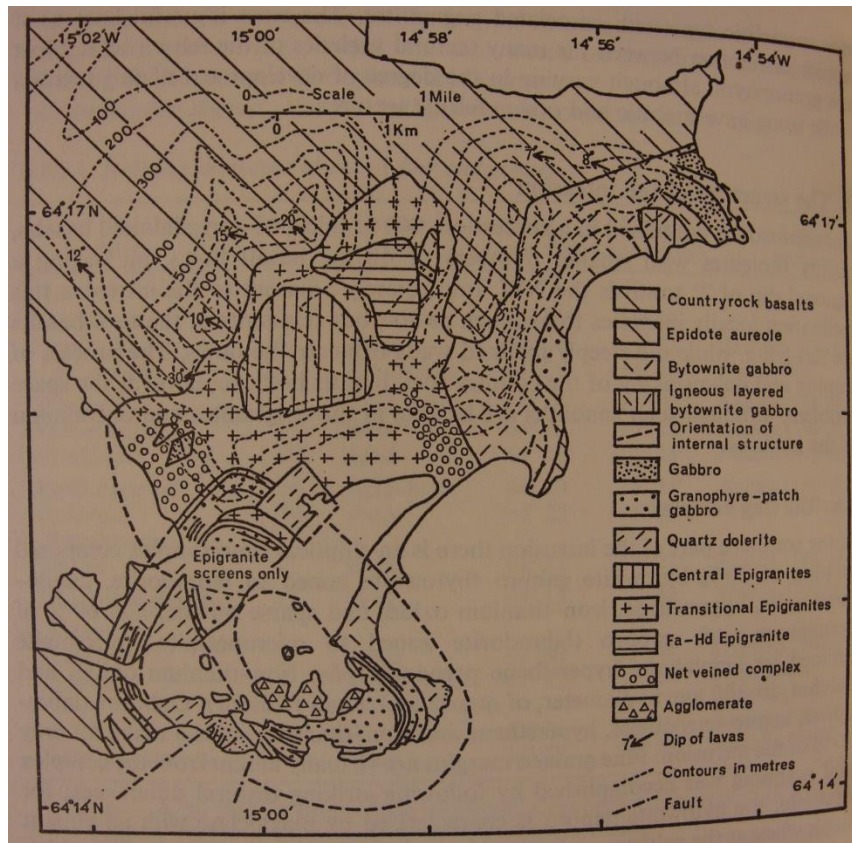
Figure 2-4: Geological map of the Vestrahorn ring complex and the surrounding area.
Source: (Roobol, 1974).

A ring complex is generally comprised of ring dykes and circular intrusions (Best, 2013), which may be all that is left of the underwork of a volcano after erosion (Guðmundsson, 2009). The ring complex is interpreted as being younger than the surrounding country rock, and being superimposed on earlier intrusions and country rock basalts (Roobol, 1974).

The ring complex consists of 60% granophyre-patched gabbro (labradorite zoned to microperthite, ferroaugite rimmed with amphibole, enstatite pseudomorphs, iron-titanium oxides, and patches of quartz and alkali feldspar), 30% bytownite gabbro (bytownite zoned to labradorite, augite-ferroaugite, enstatite, iron-titanium oxides, and scarce olivine) and

10% gabbro (labradorite, augite-ferroaugite, enstatite, and iron-titanium oxides). The complex is composed of a core of metabasalt agglomerate that marginally contains fragments of the surrounding granophyre-patched gabbro (Roobol, 1974).

The granophyres at Vestrahorn are found in the bytownite gabbro, with both granitic and felsic textures, and there is an increase in granophyre content upwards in the intrusion. The granophyres exist as both dykes and small bodies within the host rock. The dykes are found with fine-grained margins, without fine-grained margins, and ragged margins and have granodioritic composition. Each granophyre body has a dioritic composition, with coarse-grained rim (feldspar, pyroxene rimmed with amphibole, and skeletal iron-titanium oxide crystals), which extends into the granophyre centre. These rock structures have been suggested to be the result of an intrusive magma (Roobol, 1974).

Samples from Vestrahorn are actually rhyolitic, although they do not quite follow the tholeiitic magma series when comparing the amounts of TiO_2 and Mg. This is probably the result of differentiation during crystallization. Additionally changes in the concentration of olivine and iron-titanium oxides resulted in chemical composition changes in the remaining melt, thus suggesting that the rocks found in the area formed by fractional crystallization (Guðmundsson, 2009). Guðmundsson (2009) also assumed that the system must have been volatile-rich during the last stages of crystallization, based on the texture of iron-titanium oxides (skeletal texture) and plagioclase and geochemical analysis. This increased volatile content was found as early as 1928, when Cargill et al. (1928) concluded that the failure of graphic structure in the last product of crystallization was the result of increased volatile content and reduced viscosity.

2.3 Previous work at Skaergaard

Between 1898 and 1900 Georg Carl Amdrup undertook the Carlsbergfondet expedition, where the unexplored east coast of Greenland was mapped for the first time. However, the first plutonic intrusions were not located before 1930 (Wager et al., 1937), during the Watkins expedition in 1930-1931. This expedition produced the first preliminary description of the geology in the area in 1932 (Wager, 1932), followed by more expeditions and papers with detailed descriptions from the excursions (e.g. (Deer and Wager, 1938, Wager et al., 1937)).

The first paper to focus on minerals found in the Skaergaard intrusion was written in1938 (Deer and Wager, 1938) and followed by both mineralogical and petrographical articles (e.g. (Nwe, 1976, Wager et al., 1939)), describing the chemistry of the intrusion and distribution of immobile elements (e.g. (Lundegârdh, 1945)). These studies resulted in the identification of zones or layers in the Skaergaard intrusion and possible ways that they might have formed (e.g. (Wager and Brown, 1953, Wager and Mitchell, 1951)). In 1987 the Platinova reef was discovered (Brooks, 2005), resulting in increased interest by deposit geologists and further research (e.g. (Andersen et al., 1998, Brooks, 1989, Nielsen and Schønwandt, 1990)).

Since it was initially discovered, the Skaergaard intrusion has been of a great importance for geologists (i.e. mineralogists, igneous petrologists and deposit geologist) which have led to its continuous research and a large amount of published literature on the area.

2.3.1 Previous fluid inclusions studies

Microthermometry is the most common method to study FI as it can give clues to the thermal history of the rock, pressures during formation or chemical composition of the system during crystallisation. Depending on the focus of each study other methods are also used. These include Transmission Electron Microscopy (TEM) to identify objects that would otherwise be too small for identification (Bakker and Jansen, 1994), Cathodoluminescence (CL) or Scanning Electron Microscope - Cathodoluminescence (SEM-CL) for studying textures (Marshall and Mariano, 1988), or Raman spectrometry to identify the chemical properties of the FI (e.g. (Burke, 2001, Dubessy et al., 1992, Rosasco and Roedder, 1979)).

In order to understand the thermodynamic properties of various fluid-salt systems within FI, a comprehensive model was developed specifically for the interpretations of the H_2O-NaCl system (e.g. (Bodnar and Vityk, 1994)) and various other components. Bakker has compiled FI results from several systems and used programs to easily calculate parameters like salinity, density, and isochores (e.g. (Bakker, 2009, Bakker, 2003, Bakker, 2012)).

The improvement of Equations of State (EoS) is a particularly important element of FI studies, as they are used to analyse phase transitions, and have therefore been the subject of continuous re-evaluation and refinement (e.g. (Bodnar, 1993, Duan et al., 1995)).

FI can leak and decrepitate, or even re-equilibrate, which would affect the result of any measurements that are done. These changes can describe changes in their host rock, and

therefore work has been put into identifying these changes (e.g. (Bakker and Jansen, 1994, Bodnar et al., 1989, Voznyak and Kalyuzhniy, 1976)).

2.3.2 Previous fluid inclusions studies at Skaergaard

Larsen et al. (1992) studied FI in quartz (Qtz), apatite and feldspars in the Skaergaard intrusion. They were found to be liquid-vapour inclusions where solids were normally absent. The salinity is 17.5-22.8 wt.% NaCl with the chemical composition H_2O-NaCl-CH_4 where CH_4 makes up 2-6 mol% of the FI. They are usually homogenised in the liquid phase. From the results it was estimated that they were trapped at 655-770°C and 1.5-2.0 log units below the QFM (quartz-fayalite-magnetite) oxygen buffer, during the emplacement of 5.3-6.3±2.7 km of flood basalt (Larsen and Tegner, 2006).

3   Theory

3.1   Mafic magmatic systems

Mid-ocean ridges associated with the impingement of mantle plumes are the largest producers of basaltic magma in the oceanic lithosphere. Due to mantle plume activity, basaltic magma can also intrude into fractures and cause rifting in the continental lithosphere, and can therefore be found in the crust (Robb, 2009).

Basalts are formed by the partial melting of the mantle which has a mostly peridotitic composition, potentially because of a pressure decrease, an addition of volatiles, or an increase in local heat (Robb, 2009).

During crystallization, elements are selectively removed from the melt as they enter the atomic lattice of minerals. Figure 3-1 shows two different evolutionary trends for basalts that form due to the removal of elements to a various degree. The tholeiite trend, or alternatively the Fenner trend, is the typical evolution trend for basaltic intrusions and islands arcs (the Skaergaard intrusion plots with an even higher Fe content). It is characterised by FeO increases as MgO is removed from the melt in the beginning, and then decreases with respect to MgO and alkalis. The calk-alkaline trend is characteristic of continental margins arc and shows an increased alkalis content with evolution (Best, 2013).
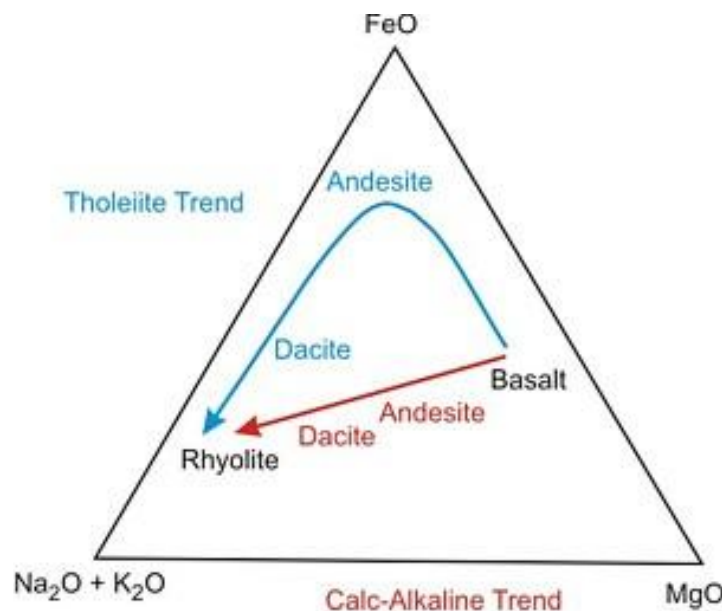
Figure 3-1: An AFM diagram for the evolution of basalt during crystallization showing the tholeiite and calc-alkaline trend.
Source: (Imperial-College, 2007).

Many ore deposits found in igneous settings originate from the concentration of metals by partial melting or fractional crystallization. During crystallization, the elements may partition into either solid phases (compatible elements) or remain in the silicate (incompatible elements) (Robb, 2009).

During crystallization the minerals are denser and consequently sink downwards due to gravitational settling. A temperature gradient and magma density variations may result in a density stratification of the magma chamber (Robb, 2009). Figure 3-2 depicts a cross section through the Skaergaard intrusion that has developed layers during fractional crystallization. The layers of the LS are marked, in addition to the HZ and the MBS. The PGE-Au reef is shown in relation to the layers in the LS.
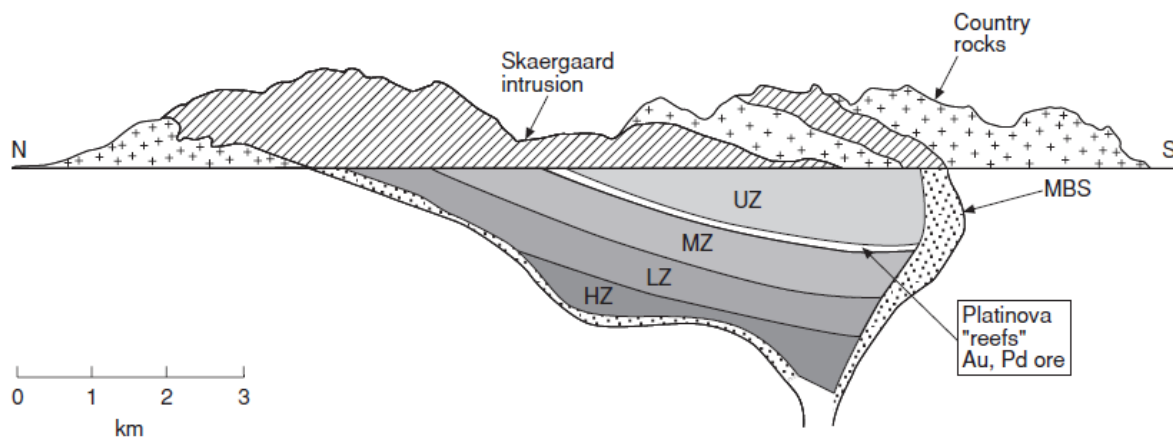
Figure 3-2: A cross section of the Skaergaard intrusion, which developed chemically distinctive layers during crystallization.
Source: (Robb, 2009).

Layered mafic intrusions like the Skaergaard intrusion appears to have formed by a simple gravitational settling process, but it is usually much more complicated. Thermal and chemical diffusion, convection flow of magma and the shape of the magma chamber normally affect the layers. The already crystallized minerals are also sensitive to changes in the magma, for example by the injection of chemically different magma or the magma reacting with the surrounding host rock. All of these processes are important to form the sub-horizontal layers of a mafic intrusion and to possibly form concentrated layers of economic metals (Robb, 2009).

If the crystallized minerals are removed from the melt by gravitational settling, the Rayleigh fractionation model can describe the trace element distribution between the residual liquid

and the crystallized solid. Rayleigh fractionation occurs when crystals are removed from their formation site with a limited equilibrium between the solid and the liquid (figure 3-3). Figure 3-3A depicts where the incompatible trace elements become enriched in the melt during crystallization while the concentration of compatible elements decreases in the melt. When most of the melt has crystallized (~90%) the melt is mostly composed of incompatible elements. In figure 3-3B the first crystals to form and accumulate at the bottom of the magma chamber consist mostly of compatible elements, which gradually contain an increased amount of incompatible elements as more of the melt crystallizes (Robb, 2009).
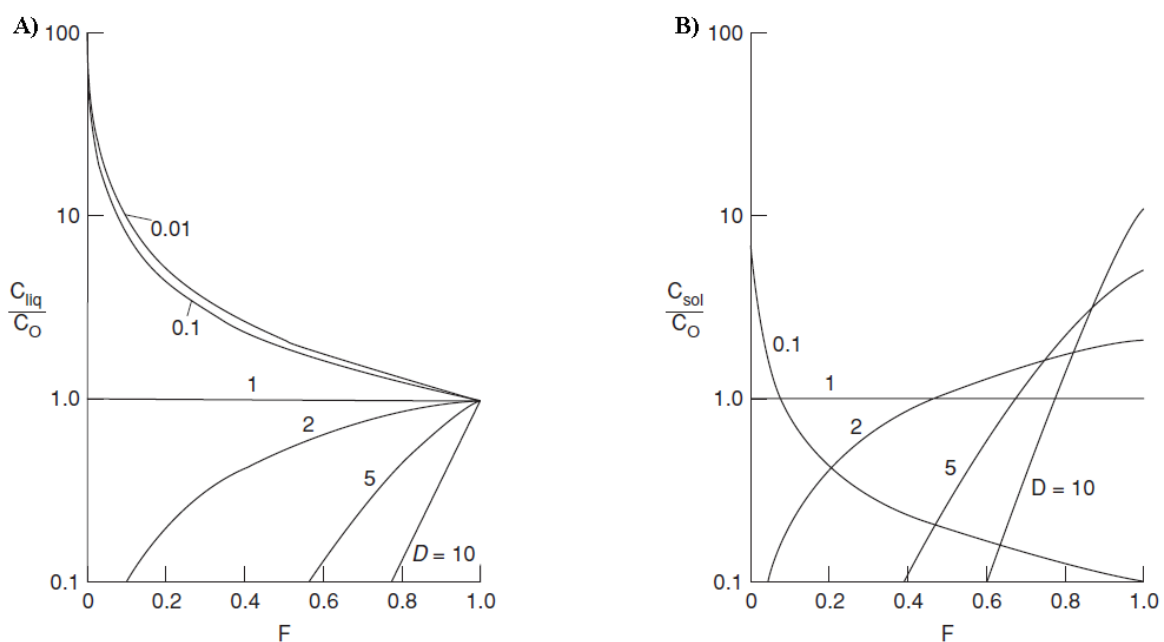
Figure 3-3: Concentration of trace elements in a magma chamber: A shows the concentration of incompatible elements in the residual magma compared to the original melt, and B shows the concentration of incompatible elements in the already crystallized minerals, which accumulate at the bottom of the magma chamber.
Source: (Robb, 2009).

Gravitational settling is not the only process to change the composition of melt. Other processes that may facilitate the formation of layering are for instance filter pressing (magma within accumulated crystals is pressed into areas with lower pressure) and liquid immiscibility (the segregation of two liquids from a previously homogenous magma) (Robb, 2009).

3.2 Formation of an ore deposits – Immiscibility

Most of the earth's ore deposits are the result of fortunate geological events, however these processes are often very similar to the processes that form normal rocks. The formation of a viable ore deposit in intrusions relies on one or more of the following (Robb, 2009):

- Crystal fractionation with gravity induced crystal settling
- Stratification of the magma chamber based on density as the magma undergoes changes in density as a result of fractional crystallization
- Recharge of the magma chamber by injection of magma
- Mixing of new magma with magma already present in the magma chamber
- A transitional phase while only one phase crystallizes
- Formation of sulphide droplets as the magma becomes sulphide saturated
- High partition coefficient for chalcophile elements

Liquid immiscibility is a process that can facilitate the selective concentration of metals. It is the separation of two phases from an originally homogeneous magma; these two liquids can be mineralogically almost identical or very different, e.g. two silicate liquids or silicate and sulphide liquid. Immiscibility is a very important ore forming process in mafic magma bodies, with the most important products forming silicate and oxide liquids or silicate and sulphide liquids. This particular process can lead to the formation of large and economically important deposits (Robb, 2009).

3.2.1 Silica-rich and iron-rich immiscibility

Immiscible liquids are present in so many volcanic rocks that magma unmixing is a common differentiation method during late fractionation. Two separate liquids, formed by liquid immiscibility can be preserved as chemically separate silica-rich and iron-rich phases in tholeiitic basalts or alkaline system, where it is then possible to observe them. The silica-rich phase is typically rich in silica, alumina, and alkalis with approximately 73% composed of silica, while the iron-rich phase is rich in iron and other mafic cations with about 43% silica (Philpotts, 1982).

These two phases are the production of a stable phase separation, which needs to happen at an early stage of the fractionation to enable the separation and segregation of a significant amount of magma. Based on the coexisting minerals' composition of the immiscibility

phases, the immiscibility phases generally form during the later stages of differentiation of tholeiitic magma (Philpotts, 1982). Whether silica-rich and iron-rich immiscibility can form a viable economic deposit is still debated, although their existence has been proven experimentally (Robb, 2009). The first silicate liquid immiscibility in a naturally crystallised pluton was reported from the Skaergaard intrusion. There it is possible to find primary melt inclusions preserved in apatite crystals as iron- or silica-rich inclusions (Jakobsen et al., 2005).

Figure 3-4 shows the immiscibility field for silica-rich and iron-rich liquid in tholeiitic basalt, where the tholeiitic rocks are marked, along with their iron-rich and silica-rich constituents that plot at each end of the immiscibility field. The iron-rich end member is enriched in FeO, MnO, TiO_2, CaO and P_2O_5, while Na_2O, K_2O, Al_2O_3 and MgO preferably enter the silica-rich phase.
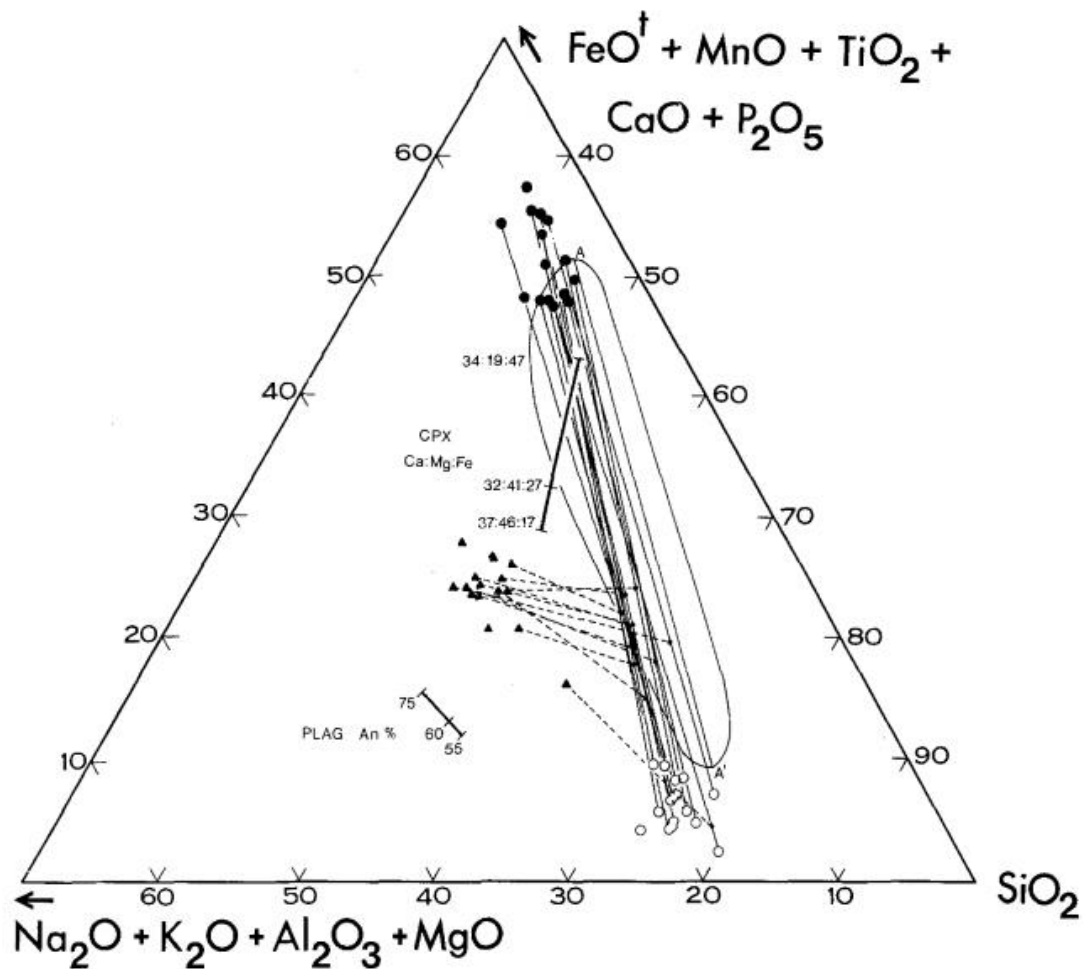
Figure 3-4: The immiscibility field for the silica-rich and iron-rich liquid for tholeiitic rocks. Tholeiitic rocks are plotted as triangles, along with their iron-rich (filled circles) and silica-rich (open circles) components. Source: (Philpotts, 1982).

3.2.2   Silicate – sulphide immiscibility and sulphur solubility

If a homogenous magma contains considerable amounts of sulphur the magma can separate into two liquids, one being silicate-rich while the other consists of sulphides. These two liquids may coexist over a wide chemical range, as seen in figure 3-5, as long as there is enough sulphur in the system. Magma at point A would crystallize fayalite until it intersects the two-liquid field, where sulphide melt would then separate from the melt and coexist with the silicate melt (Robb, 2009).
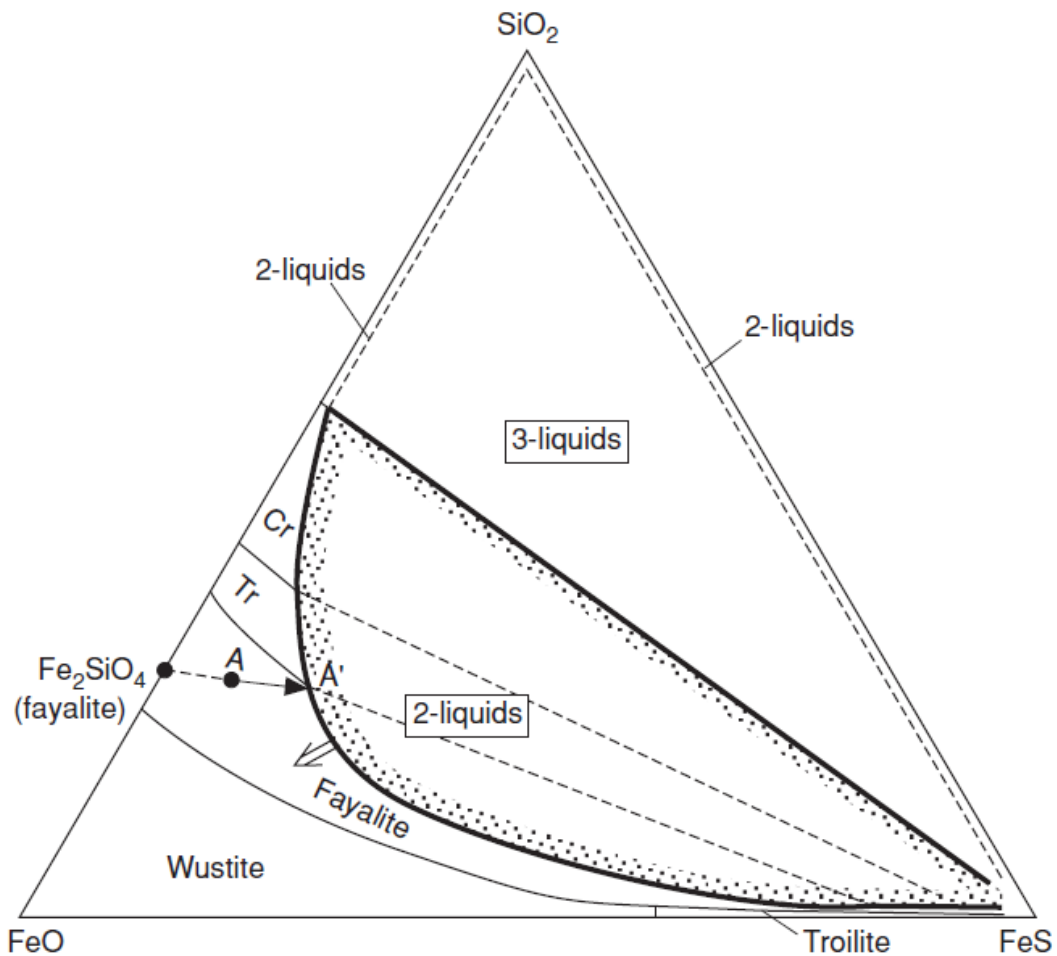
Figure 3-5: The 2-liquids field in the diagram marks immiscibility field for the silicate-sulphides liquid.
Source: (Robb, 2009).

During magma solidification, the amount of sulphides slowly increases in the melt. When sulphide immiscibility is attained, small droplets of sulphides are temporarily suspended in the magma. By forming this new phase, elements with strong affinities for sulphides will partition into the sulphide melts. This has the possibility of forming a concentration of economic minerals and even a deposit if all conditions for its formation are met (Naldrett, 2004, Robb, 2009).

To form a deposit by sulphide immiscibility a sufficient amount of immiscible sulphide melt is required and the sulphide droplets need to be able to react with a large part of the melt while at the same time crystallize to form a single layer (Robb, 2009).

Chalcophile and siderophile elements have a strong affinity for sulphide phases, which results in their dissolution in the sulphide phase. Many of these elements normally stay in the melt during crystallization until sulphide saturation is reached, when they partition

strongly into the sulphide phase and sink to the bottom of the magma chamber. There they may form a thin layer of economically important elements, a so-called "Reef Deposit". These layers can be followed throughout the whole magma system, as they contain concentrated economic elements that are thousand times the amount that was originally distributed in the magma. If, however, a sulphide-rich face does not form these elements end up substituting for other elements in mineral crystal lattices and do not form a concentrated layer (Robb, 2009).

Whether sulphur forms an immiscible phase depends on the amount of sulphur and FeO in the magma, along with temperature and oxygen fugacity, according to the following equation:

$$FeO_{(melt)}+\frac{1}{2}S_2\leftrightarrow FeS_{(melt)}+\frac{1}{2}O_2$$
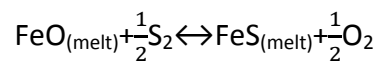
This shows that the sulphide solubility increases with decreasing oxygen content and/or increasing FeO content in the magma. It increases with increasing temperature, but decreases with increasing pressure and SiO_2 content (during evolution of magma) (Li and Ripley, 2005, Naldrett, 2004, Robb, 2009).

This principle was used to constrain the sulphide solubility curve (figure 3-6) for the Bushveld igneous complex. The sulphide solubility decreases during crystallization of olivine and orthopyroxene due to the removal of FeO and decrease in temperature, but when plagioclase begins to crystallize, it levels off again as the FeO starts to increase in the melt. If a melt is undersaturated in sulphides at emplacement, the crystallization of olivine and orthopyroxene results in the melt shifting towards the solubility curve. Thus the sulphide content increases in the magma as the FeO goes into olivine and is removed from the melt, until it reaches the curve and droplets of sulphides start to form in the magma causing its saturation. Although the amount of sulphide droplets would then start to decrease in the melt as the sulphides are removed from the liquid, as the sulphide solubility curve shows. The sulphides could either end up located within cumulus rocks or they might form a separate sulphide layer as they accumulate at the bottom of the magma chamber (Robb, 2009).
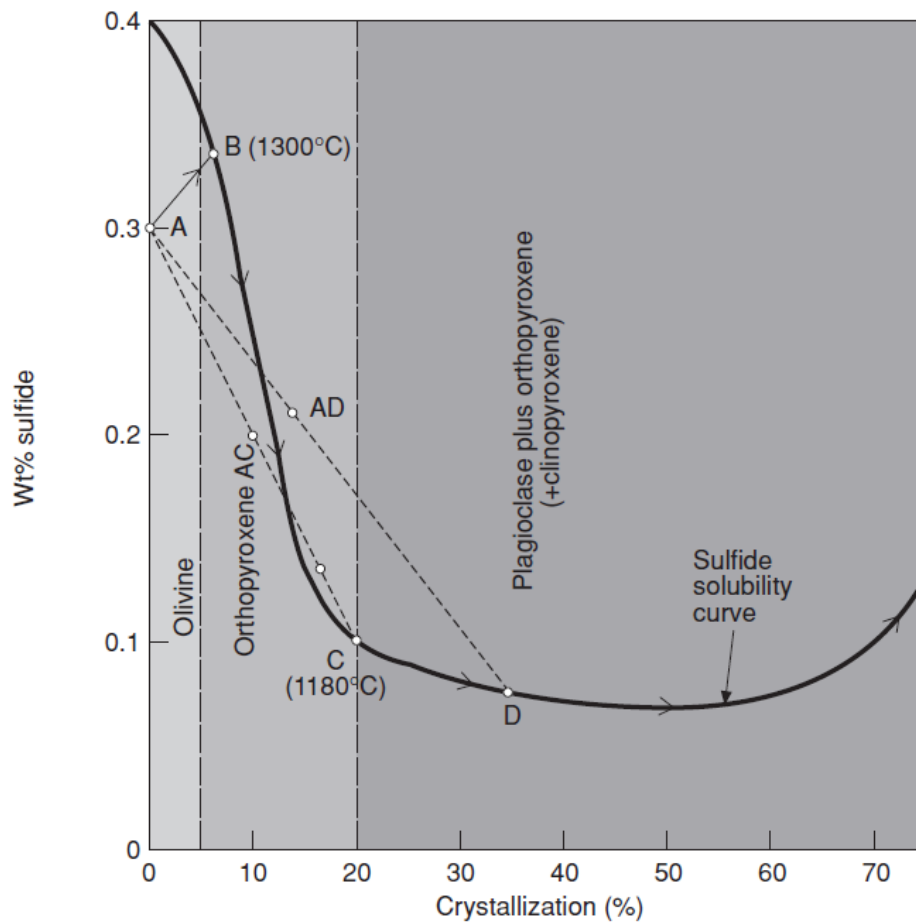
Figure 3-6: An example of a sulphide immiscibility curve from the Bushveld Complex during crystallization.
Source: (Robb, 2009).

Sulphide immiscibility may also be attained with the addition of externally derived sulphur, an injection of new magma which mixes with the pre-existing magma or magma contamination (Robb, 2009).

Oxygen fugacity

In a melt where the silicate melt is in equilibrium with the sulphide-rich liquid, the oxygen fugacity increases as the sulphide solubility decreases. The ability to form an ore deposit with sulphides is strongly dependant on the fO_2, and the less O_2 that is in the melt, the more likely the melt is to form a sulphide deposit (Naldrett, 2004, Robb, 2009). Figure 3-7 demonstrates the decreasing sulphur solubility with increasing oxygen fugacity.

FeO content

Sulphur content is strongly dependant on FeO concentration in the magma, and to a lesser extent on TiO_2 content. The sulphur content in the melt at sulphide saturation increases with

increasing FeO contents because the FeO increases sulphur solubility, as depicted in figures 3-7 and 3-8. Additionally, increased fO_2 results in decreased sulphide solubility in the melt.

During olivine crystallization FeO is removed from the melt, consequently the sulphide solubility decreases (that is also due to lowering of temperature). When plagioclase begins to crystallize the FeO content will increase relative to other elements in the melt, so the sulphide solubility increases. Usually both olivine and plagioclase are removed with the ratio 1:3, which results in the melt going alongside the sulphide saturation curve, without forming a separate phase (Naldrett, 2004).
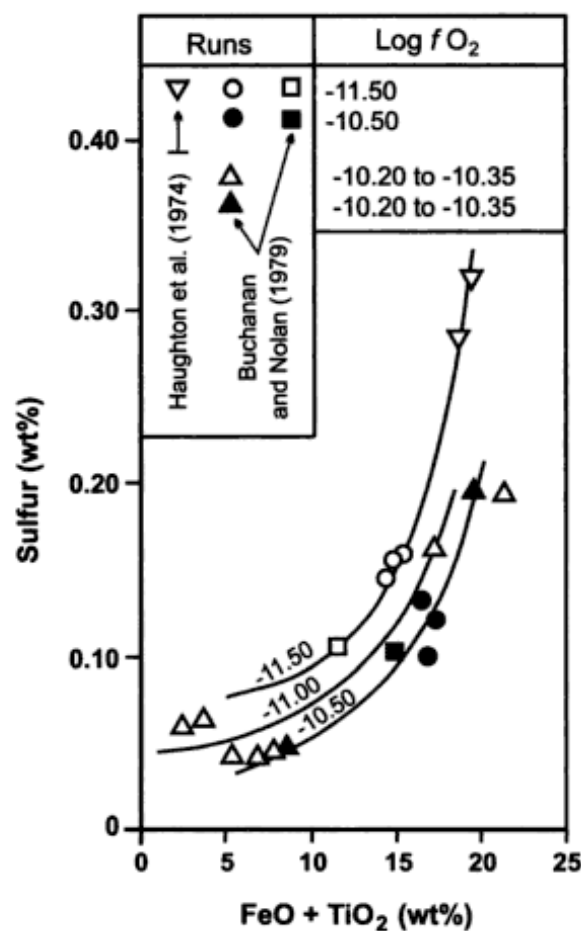
Figure 3-7: Solubility of sulphur as a function of FeO and TiO$_2$, demonstrating the effect of varying oxygen fugacity. Increasing FeO and TiO$_2$ content, and decreasing oxygen fugacity increases the sulphur solubility in the melt.
Source: (Naldrett, 2004).

Temperature

Research on the effects of temperature on sulphide saturation is lacking but sulphide saturation has been show to increase with temperature. At a constant fO_2 and fS_2 the sulphur increases with a factor of 8.5 at 1000°C per 100°C, while at 1400°C the factor increases only by 3 times, but this is also dependant on the melt composition (Naldrett, 2004).

Pressure

Increasing pressure reduces the solubility of sulphur, as shown in figure 3-8. This means that the magma moves steadily away from the sulphur saturation curve as the melt moves upwards in the crust. If a magma forming at a great depth is transferred to the surface, the decrease in pressure results in the melt increasing its ability to dissolve sulphur, so it reduces or loses its ability to form a sulphide ore deposit. (Naldrett, 2004).
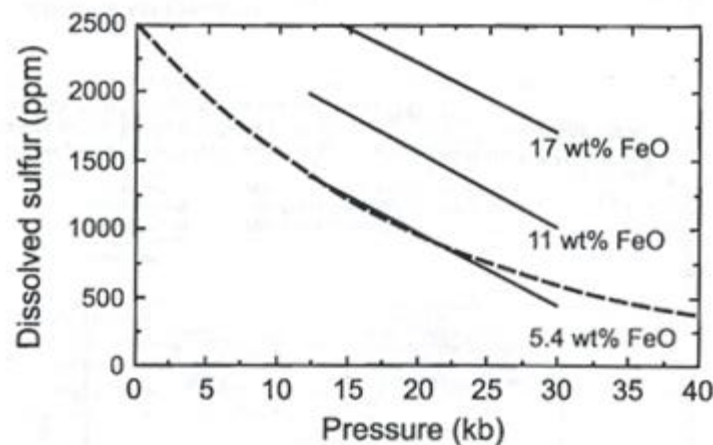
Figure 3-8: Solubility of sulphur in basaltic melt with different FeO content as a function of pressure. An increasing pressure reduces the sulphur solubility in melt, while the increased FeO content decreases the sulphur solubility.
Source: (Naldrett, 2004), which based is it on (Wendlandt, 1982) and (Mavrogenes and O'Neill, 1999).

3.2.3 Partition of chalcophile elements into the melt

Igneous systems contain diverse ore deposits with different metal associations. This can be seen for instance on mixture of chalcophile and siderophile elements normally being associated with mafic system, while lithophile elements are commonly associated with felsic or alkaline systems (Robb, 2009).

Therefore, the melt that forms may be enriched or depleted in certain elements depending on the source rock. Mafic magma is enriched in chalcophile and siderophile elements, meaning that that the source of the magma, the mantle, must also be enriched in the same elements. However the chalcophile and siderophile elements are scarce and cannot form their own mineral phase, so generally they rather substitute for other elements in mineral's crystal lattices, or in crystal lattice defects. These elements are incompatible as they are not the preferred choice for the minerals, therefore they are typically the last elements to leave the melt and go into mineral's crystal lattice during crystallization (Robb, 2009).

The transition metals – Fe, Co, Ni, Pd, Pt, Rh, Ru, Ir, Os, Cu and Au – comprises the metals that partition most strongly into the sulphide liquid (Naldrett, 2004). The ability of an immiscible sulphide liquid in a silicate melt to concentrate trace elements depends on the partition coefficient of the elements and whether they partition into the sulphide or silicate phase (Robb, 2009). The Nernst partition coefficient for a metal with a low concentration in a melt where there is equilibrium between sulphide and silicate melt is:

$$K_D^{i-j} = (wt\% \, i)^{Sul.m} * (wt\% \, j)^{Sil.m} / (wt\% \, j)^{Sul.m} * (wt\% \, i)^{Sil.m}$$

Where i is the metal which becomes concentrated, and j is the metal (e.g. sulphur) that concentrates the metal (Naldrett, 2004).

Chalcophile elements partition strongly into the sulphide phase; these elements are thought to bond with oxygen in the silicate magma, and when a separate sulphide phase forms they rather bond to sulphur ions (Naldrett, 2004). Different chalcophile elements also partition with varying efficiency into the sulphide phase. This is visible in figure 3-9 where the partition coefficient of some chalcophile elements is shown. The more common elements, Ni, Cu, and Co, partition not nearly as strongly into the sulphide phase as the PGE elements, Pt, and Pd due to the difference in partition coefficients (Robb, 2009). Due to the strong partition coefficient, sulphides can be highly enriched in PGE and Au compared to the original concentration in the melt (Naldrett, 2004).

	Ni	Cu	Co	Pt	Pd
Basalt	275	250–2000	80	10^4–10^5	10^4–10^5

Figure 3-9: An example of the partition coefficients of few chalcophile elements in basalt.
Source: Modified from (Robb, 2009).

Accordingly, PGE's partition easily into the sulphide melts. But even if the PGE partition very efficiently into the sulphide melt, finding a viable deposit of these metals is not common. This is because the original melt does not contain many of these elements, or the sulphide droplets are not able to come in contact with large enough sections of the magma in order to concentrate them (Robb, 2009). The enrichment of PGE's in sulphide reefs is due to the delay of separation of the sulphide phase from the melt during crystallization, thereby resulting in the formation of a deposit rich in Cu, Pt, Pd and Au, with low concentrations of Ni, Ru, Ir and Os (Naldrett, 2004).

3.2.4   Ratio of magma to sulphide

A single drop of sulphide magma will probably only come in contact with a small area of the magma, however as the sulphide interacts with more magma the concentration of incompatible elements is likely to increase in the sulphide droplets (Robb, 2009). Therefore the silicate/sulphide ratio, also known as the R-factor, needs to be considered.

The R-factor

Sulphides are dense, which result in them collecting at the bottom of the magma chamber. The R-factor denotes the amount of silicate melt that a single sulphide droplet comes into contact with before it collects at the bottom (Robb, 2009), while it also assumes that the sulphide liquid is in equilibrium with the magma before being removed (Naldrett, 2004).

High R-factors occur when the sulphide droplets comes into contact with a large volume of silicate melts as it travels through the magma chamber. This can be seen in figure 3-10 where the high R-factor is related to an increased concentration of trace metals in the sulphide. Each sulphide droplet needs to come in contact with a lot of magma before it becomes saturated in an element with a high partition coefficient (D). Low R-factor is related

to sulphide droplets either being motionless in the magma, or when it is removed early from the magma, thereby not reacting with the elements even when it has a high partition coefficient. When the partition coefficient is greater than the R factor, the latter controls the enrichment of an element in the sulphide, and vice versa (Robb, 2009).
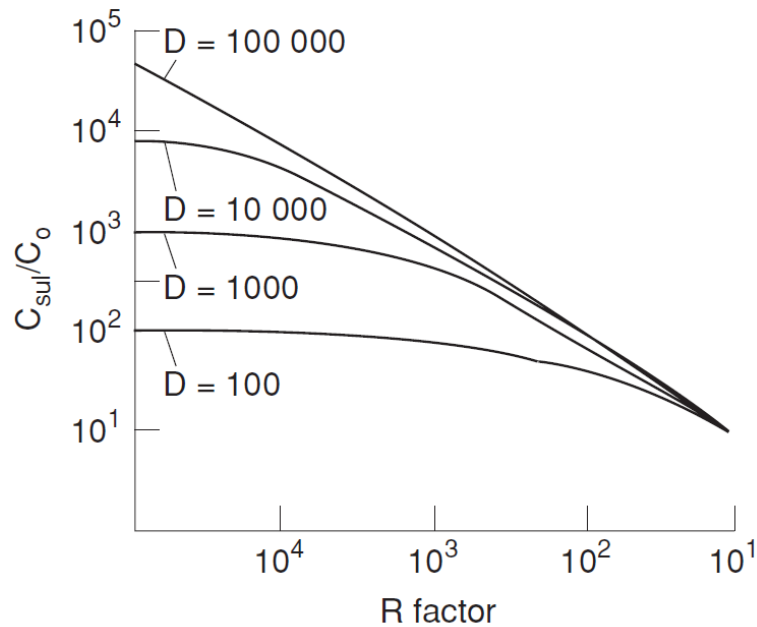
Figure 3-10: The relationship between the trace element distribution in a sulphide melt with the R-factor. Csul is the concentration of trace elements in the sulphide melt, and Co is the trace element concentration in the original magma, D is the sulphide-silicate partition coefficient, and R is the silicate/sulphide melt ratio.
Source: (Robb, 2009).

3.3   Volatiles in mafic systems

A moderate amount of volatiles greatly influences the properties of magma, in which they may be present as dissolved species. H_2O is dissolved as OH^- and is normally the most dominating volatile species, while dissolved carbon dioxide is the second most common, although other volatiles may also be dissolved in the magma (e.g. CH_4, CO, H_2 and H_2S) (Best, 2013). However in a mantle-derived magma, CO_2 may be the dominating fluid, whereas H_2O the second most common (Eggler, 1974, O'Reilly et al., 1990). The genesis of basalts depends on the total pressure, degree of partial melting and the pressures of H_2O and CO_2. For example tholeiitic magma is produced from the mantle, which contains CO_2-H_2O vapour with 40-60 mole% H_2O at 15-20 kbar (Eggler, 1974).

Pressure, temperature and the chemical composition determine the solubility of volatiles in magma. H_2O is strongly dependant on pressure and less so on temperature, as both increase the solubility of water (Mysen, 1977). CO_2 solubility is strongly dependant on pressure but also varies with temperature and the chemical composition of the silicate melt (Eggler, 1974, Mysen, 1977). Because of the difference in solubility between H_2O and CO_2 in silicate melt, partial melting in the mantle results in an H_2O-enriched liquid, while the residual mantle becomes more enriched in CO_2 (Mysen, 1977).

Generally, the fluid pressure in the system is less than the confining pressure, but in a saturated system they are equal, and when the system is oversaturated in volatiles the fluid pressure is greater than the confining pressure. In an over-pressurized volcanic system the pressure of the magma system is less than the fluid pressure in the magma system (Best, 2013).

Often felsic magma is considered to contain more volatiles than mafic magmas, and the volatiles' solubility is generally higher in felsic magma. This appears to be true to the extent that felsic magma bodies are at a lower temperature and can hold slightly more water, but the solubility of water in a felsic melt decreases with increasing temperature, whereas it increases in a mafic magma (Hamilton et al., 1964). H_2O typically dissolves in a silicate melt by reacting with O_2 to form OH^-, but continued experiments show that it is typically more complicated (Best, 2013). Water enhances silicate stability in the melt and depolymerizes the melt, which reduces the melt viscosity, while CO_2 enhances the polymerization in the melt and therefore the viscosity (Best, 2013, Mysen, 1977). Mafic melt are much less viscous than many other melts because of their low SiO_2-content and can consequently easily rid themselves of trapped excess water (Hamilton et al., 1964).

Figure 3-11 shows the increased water solubility in different melts with increased pressure. The water solubility is higher in a silicate melt than in a mafic melt, but the most soluble in pegmatite melt. Melt that contains less water than the solubility curve indicates is undersaturated and vice versa in addition to a separate phase of fluid water.
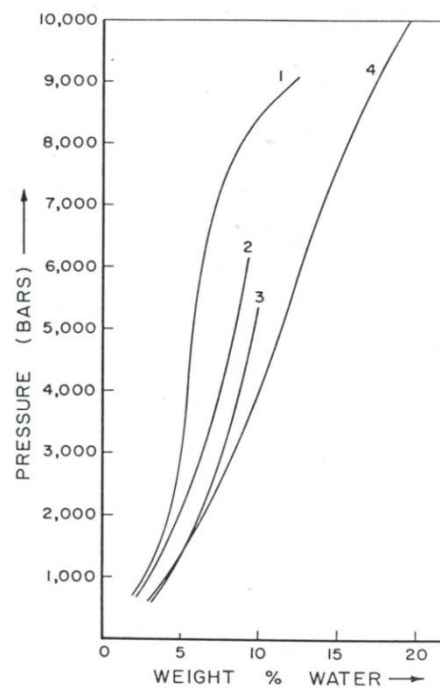
Figure 3-11: The maximum solubility of water in (1) silica, (2) basalt, (3) andesite, and (4) pegmatite melt.
Source: (Hamilton et al., 1964).

Due to the volatiles' low density, silicic magma bodies have higher concentration of volatiles in their upper parts than in the lower. If the magma becomes saturated, the volatiles separate from the melt and form a distinct coexisting fluid phase. This can occur as the magma rises to shallower depths (first boiling) or during cooling and crystallization (second boiling) (Best, 2013).

Oxygen fugacity influences the liquid line of decent, and water acts as a reservoir for oxygen during crystallization and differentiation in a mafic magmatic systems (Hamilton et al., 1964). In addition, volatiles in a magmatic system can lower the liquidus temperature by several hundred degrees (Robb, 2009, Yoder and Tilley, 1956).

Figure 3-12 depicts the melting of a rock with a peridotitic composition with increasing temperatures as well as the difference between anhydrous and hydrated peridotitic mantle (1.9 wt. % H_2O) (Robb, 2009). This figure also shows the melting temperature depression of peridotitic rock with hydration. The volatiles can alter the proportions, temperature range, and the order or crystallization of minerals.
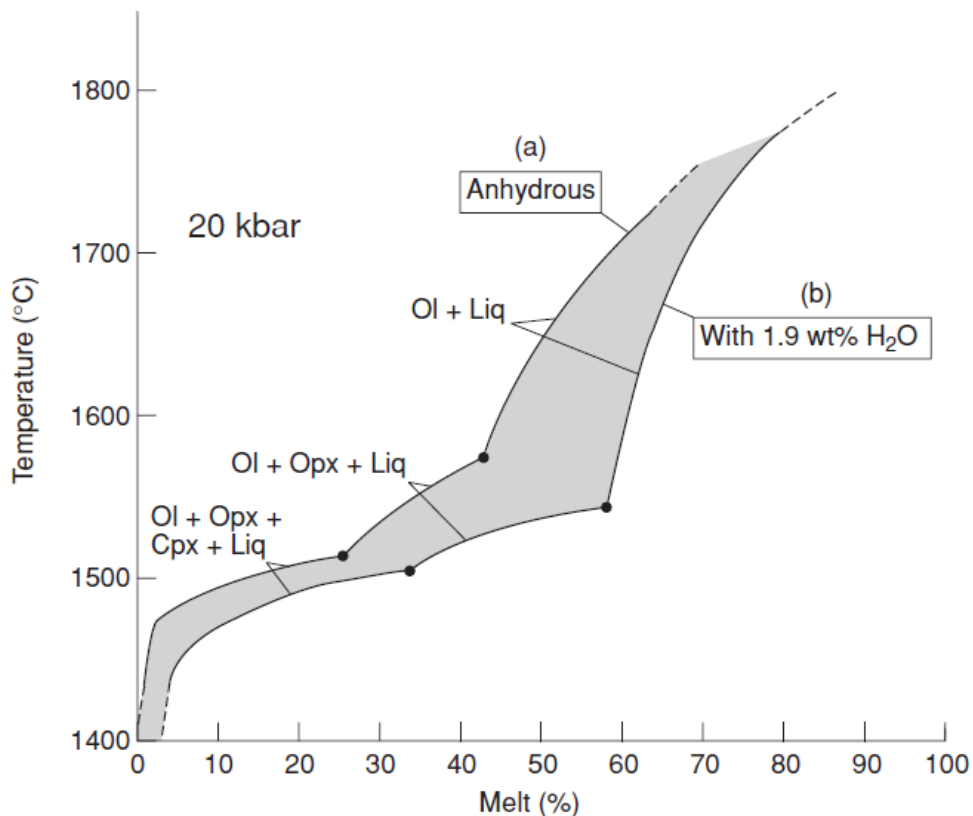
Figure 3-12: The melting of a peridotitic rock, both anhydrous and hydrous. An addition of few weight percent water can depresses the melting curve of the rock considerably.
Source: (Robb, 2009).

3.3.1 Effects of salts

Fluids are important solvents for many elements, but in mafic magmas the ex-solved fluid phase is often overlooked – partially because it rarely is involved in the ore-forming process. Complexing anions, especially Cl⁻, assist in the dissolution of transitional metals and alkali elements. Therefore the fluid phase can be important for the concentration of metals such as Cu, Ni and PGE in mafic-layered intrusions, as these metals are strongly dependant on the concentration of Cl⁻ in volatiles in the system. However a separate fluid phase generally doesn't form until a considerable part of the magma chamber has already crystallized (Robb, 2009).

Both the Bushveld and Stillwater complexes contain a variety of replacement structures, which have an unclear relationship to the layer formation of these complexes. The structures formed at a high temperature, with either a volatile-rich melt or aqueous fluids present (Sonnenthal, 1992). Hydrated minerals in both complexes have illustrated that the magma

contained volatile-rich fluids during crystallization, which is thought to have largely caused the leaching, transportation and precipitation of precious metals (Boudreau et al., 1986, Boudreau, 2002, Mathez, 1995). Additionally the mineral assemblage has an unusually high Cl/F ratio, which is associated with the volatile-rich fluid (Boudreau, 2002). Both complexes have relatively dry parent magma, and the Cl-rich fluid is interpreted to have exsolved from the magma during the solidification of the intrusions and acted as transport agents for the PGE and REE, thus resulting in the formation of a PGE reef where the fluids were trapped by re-dissolution (Boudreau et al., 1986, Boudreau, 2002, Mathez, 1995).

The Skaergaard intrusion is considered to have attained water saturation before the final melt crystallised, as it contains primary hydrated minerals (McBirney and Sonnenthal, 1990). Furthermore primary FI indicate that the granophyre masses formed during volatile saturation (Larsen and Tegner, 2006). Secondary hydrated minerals, in addition to several unusual replacement structures, indicates that a late magmatic hydrothermal solution induced metasomatism of the rock assemblage (McBirney and Sonnenthal, 1990). Both apatite and biotite have unusually high Cl^- content (>2 wt.%), which is associated with metasomatised rock structures (dendritic anorthosites and pegmatites). This metasomatism is considered to have been the result of exsolution of magmatic volatiles that were enriched in trace elements derived from the residual melt. The fluid transported the trace elements, migrated through the crystallized zone and assisted in the development of layers. Moreover it has been suggested that this is a possible reason for the formation of the PGE reef (Sonnenthal, 1992).

Cl^- partitions easily into the aqueous phase of a magma, as seen in figure 3-13, but the partition coefficient is very complex and is, among other factors, pressure dependant. At a lower pressure where H_2O separates into two immiscible fluids (one liquid-rich and the other vapour-rich), the partition of Cl^- into the liquid phase is controlled by the Cl^- saturation in the vapour phase. At higher pressure the H_2O exist as one fluid, where the Cl^- saturation is controlled by the concentration of Cl^- in the melt and increases with greater pressure (Robb, 2009).
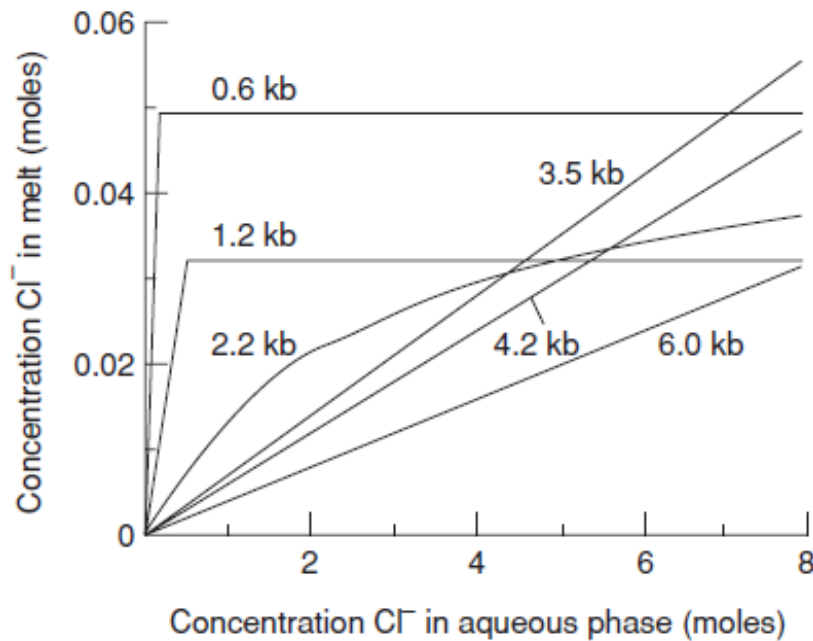
Figure 3-13: The partition coefficient controls the concentration of Cl- in the aqueous phase in granitic melt.
Source: (Robb, 2009).

3.4   Fluid inclusions

A fluid inclusion has been defined as "any quantity of single- or multiphase fluid enclosed (included) within a crystalline or amorphous solid" and can occur in many natural minerals (Samson et al., 2003).

If a fluid phase is present during the formation of crystals, some of the fluid may become trapped within the mineral, forming a fluid inclusion. The fluid can vary in chemical compositions depending on the chemical composition of the original fluid that was present during the crystal's formation (Samson et al., 2003) and can contain fluid with densities typically ranging from 0.1-1.3 g/cm^3 (Roedder, 2002). Most geological fluids consists of water with two components, gases and salts (Bakker and Brown, 2003). The phases found in an inclusion are gas, liquid and solid. The vapour phase forms due to the changes of temperature from trapping to the lower temperature of observation (i.e. room temperature), as the fluid shrinks more than the host crystal. Therefore it is clear that the homogenisation temperature of the liquid and the vapour phase is the lowest possible trapping temperature for the inclusion (Roedder, 2002). FI are the only known source of

information that can be used to find the density of these fluids, and to give an idea of the ore formation history of many metal deposits (Roedder, 2002).

FI can be divided based on the timing of the formation of the fluid inclusion related to the host crystal. Primary fluid inclusions develop at the same time, and as a direct result of the formation of the host mineral, on the continuingly growing crystal surface. Secondary fluid inclusions may form when a crystal fractures, a fluid enters the fracture before it heals and the fluids are then trapped during healing. If fracturing happens during the crystal growth the fluid inclusions that form are called pseudosecondary fluid inclusions, i.e. they are actually primary but look secondary at first glance (Samson et al., 2003). If the volume of the inclusion changes, or if something is added or removed from the system after the FI formed, the inclusion becomes re-equilibrated. That can happen during continuous burial, uplift to the surface, recrystallization, or during the sample preparation or analysis (Samson et al., 2003).

FI that forms from a homogeneous fluid, are trapped at the same pressure and temperature, and pretty much at the same point in rock evolution must contain the same fluid composition and densities, and be identical in appearance unless the volatile system contained two or more immiscible fluid phases. Therefore these FI are ideal to study the systems properties during formation of the FI. Some minerals are well suited for study as they preserve the FI better and have better optical properties (Van den Kerkhof and Hein, 2001). If the FI fulfil Roedder´s Rules it is possible to use them to determine the conditions during its formation from microthermometric data, and to construct isochores for them. These rules are (Samson et al., 2003):

- The inclusion trapped only a single, homogeneous phase (unless immiscibility is present)
- The system must remain at a constant volume
- After trapping nothing has been added or removed from the inclusion

Microthermometry allows for the study of FI, and can indicate diverse geological processes and conditions during the formation and hence the conditions that have affected the rock (Bakker and Brown, 2003). To be able to use microthermometry the FI need to be at least about 4 µm wide, although it also depends on the instruments. This is the most common technique to identify the p-T-V-x properties of FI, but is determined by the phase behaviour

at low temperature (Bakker and Diamond, 2000). The eutectic temperature is characteristic for each chemical system and denotes which components can be found in the FI. The melting of solids can thus be used to identify the concentration of the components (Roedder and Ribbe, 1984).

Fluid inclusions can contain one phase, or combinations of different phases, even though some contain just one observable gas or liquid phase. It is common for FI to contain two fluid phases, that is one dominant liquid phase and one gas phase which is visible as a small vapour bubble, known as aqueous inclusions. Aqueous fluids containing salts are common in many geological environments and are important for the formation of an ore deposit. The most common salts are NaCl, KCl, or $CaCl_2$, but others are also possible (Samson et al., 2003). NaCl is one of the more common ones to be found in FI, forming the H_2O-NaCl system, sometimes also with other components (Bakker, 2012).

3.4.1   The H_2O-NaCl system

The H_2O-NaCl system is one of the most important aqueous systems when it comes to microthermometry measurements as well as one of the most studied (Bodnar and Vityk, 1994). Though in nature it is very unlikely that FI contain pure H_2O-NaCl (Samson et al., 2003). Yet it is commonly used to determine NaCl equivalent salinity, due to lack of information about other salts that causes the freezing point depression in the system (Bodnar, 1993).

During microthermometry the composition is determined from the melting of ice. The eutectic (e) point is located at -21.2°C and 23.2 wt.% NaCl due to the freezing point depression, and the peritectic (p) point at 0.1°C and 26.3 wt.% NaCl. The salinity for these inclusions is determined either by ice melting temperatures, or by hydrohalite or halite melting if the salinities are sufficiently high to stabilize these phases. Both hydrohalite and halite melting can form a metastable state, where the system fails to nucleate a new and stable phase, which results in a slow reaction and the phases existing for some time above their melting point (Samson et al., 2003). The H_2O-NaCl phase diagram (figure 3-14) shows how the different phases in the system are controlled by salinity and temperature. Based on the salinity of the system either halite or hydrohalite might form or exist in the system. The depression of melting temperature results in the first melting in the system to be at the eutectic point at -21.2°C and 23.2 wt. % NaCl.
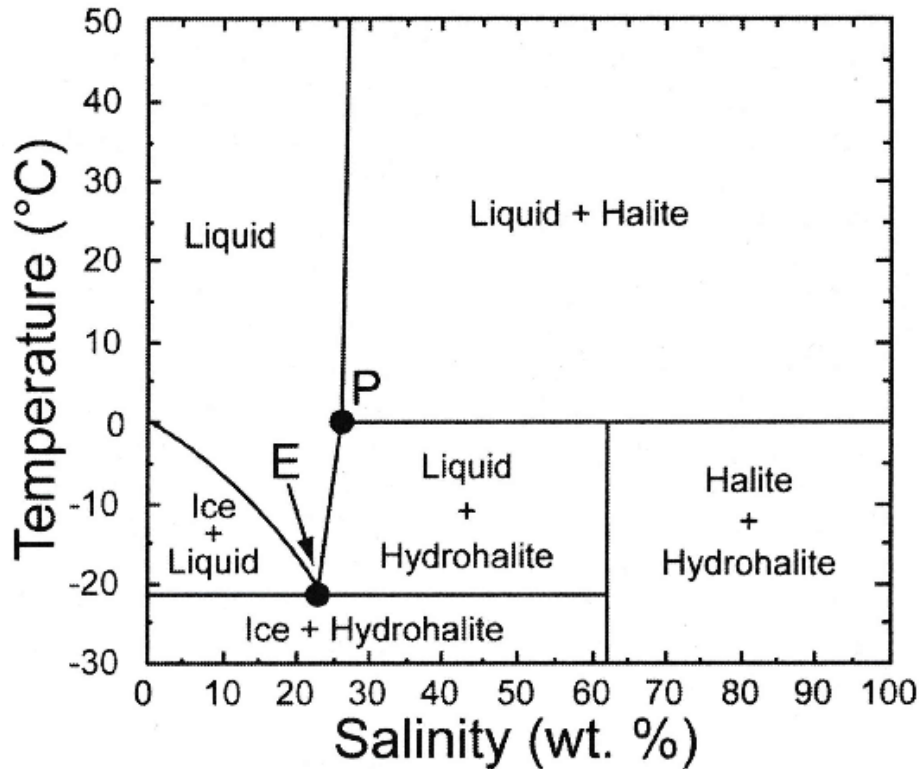
Figure 3-14: Phase diagram for the H2O-NaCl system. The eutectic point (E) is at -21.2°C and 23.2 wt.% NaCl, while the peritectic point is at 0.1°C and 26.3 wt.% NaCl.
Source: (Samson et al., 2003).

3.4.2   Complex salt systems

Systems containing Mg or Fe ions generally complex to form $MgCl_2$ or $FeCl_2$. Both result in the depression of melting temperature of the system they exist in. For example the H_2O-NaCl-$MgCl_2$ system has a eutectic point at -35°C and the H_2O-NaCl-$FeCl_2$ system has a eutectic point at -37°C (Borisenko, 1977). The addition of $FeCl_2$ in a salt system therefore results in an even more depressed melting point than in a system that contains $MgCl_2$, as shown in figure 3-15, where different chemical components depress the melting temperature of various systems to several degrees. The eutectic point exists at a higher temperature if the system does not contain NaCl (Dubois and Marignac, 1997). In both H_2O-NaCl-$MgCl_2$ and H_2O-NaCl-$FeCl_2$ a metastable halite melting has been reported, which happens when a solid does not nucleate (Baldassaro and Bodnar, 2000).

H_2O-NaCl-KCl systems have a eutectic point relatively close to the eutectic point of the H_2O-NaCl system (-22.9°C versus -21.2°C), which makes it almost impossible to distinguish between these systems with only microthermometry. If the system contains salt crystals it is however possible to recognise it, due to it containing both halite and sylvite crystals (Samson

et al., 2003). The addition of KCl in a system typically causes an increased depression of the melting point of the system (Hall et al., 1988, Sterner et al., 1988).
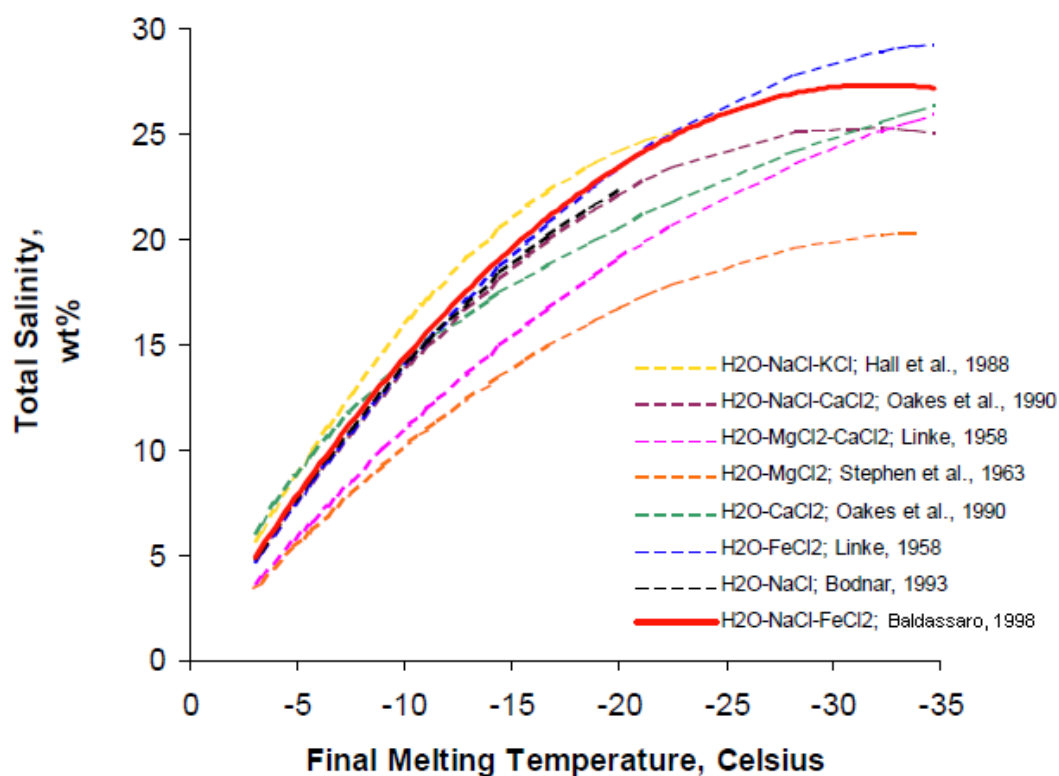
Figure 3-15: Diagram comparing different water-salt systems. Final melting temperature in diverse water-salt systems at different salinities. In all cases increased salinity depresses the melting temperature of the system. The depression of melting temperature varies based on the type of ions in the systems.
Source: (Baldassaro and Bodnar, 2000), which based it off (Bodnar, 1993, Hall et al., 1988, Linke, 1958, Oakes et al., 1990, Stephen and Stephen, 1963).

Salt in a water system results in the H_2O molecules clustering around each salt ion, so there are fewer water molecules available to interact and dissolve non-polar gas. Thus the more salt in the system, the less gas can be dissolved in the fluid. As there is more salt in the system, both the phase relationship and immiscibility field expands with higher pressures and temperatures. Systems that contain NaCl, water and gas have steeper isochores and higher homogenisation temperatures. Gas causes the depression of clathrate and ice stability (Samson et al., 2003).Therefore if the sample contains gas it can result in error, as there would be an apparent increase in salinity, and therefore also an increase in pressure (Roedder and Ribbe, 1984).

3.4.3 Isochores

To analyse fluid inclusions, the temperature of phase transitions is identified and incorporated into EoS. EoS provides a mathematical connection between two or more state variables, such as pressure, temperature, or composition. Each EoS only yields a part of the relationship between these variables, and is in addition restricted to a narrow temperature and pressure range. This is due to the EoS being a best fit to a line, and consisting of the gas constant with some modification factors calculated from experimental data, which only covers specific temperature and pressure range. These equations are constantly developed based on new experimental data, resulting in more accurate results. Due to the complexity of EoS it is desirable to use computer programs (Bakker, 2012). An example of the EoS that was used for calculation of results in this project is in chapter 4.5.2.

These EoSs are of great importance when it comes to construction of isochores (Bakker, 2003, Bakker, 2012). Isochores are lines of equal density and molar volume in a temperature/pressure diagram for a fluid with a given composition (Bodnar, 1993).

Figure 3-16 demonstrates an example of isochores at 20 and 25 wt.% NaCl in the H_2O-NaCl system, which is approximately the salinity at the eutectic point (Bodnar and Vityk, 1994). Increased salinity steepens the isochores that results in greater pressures at the same temperature.
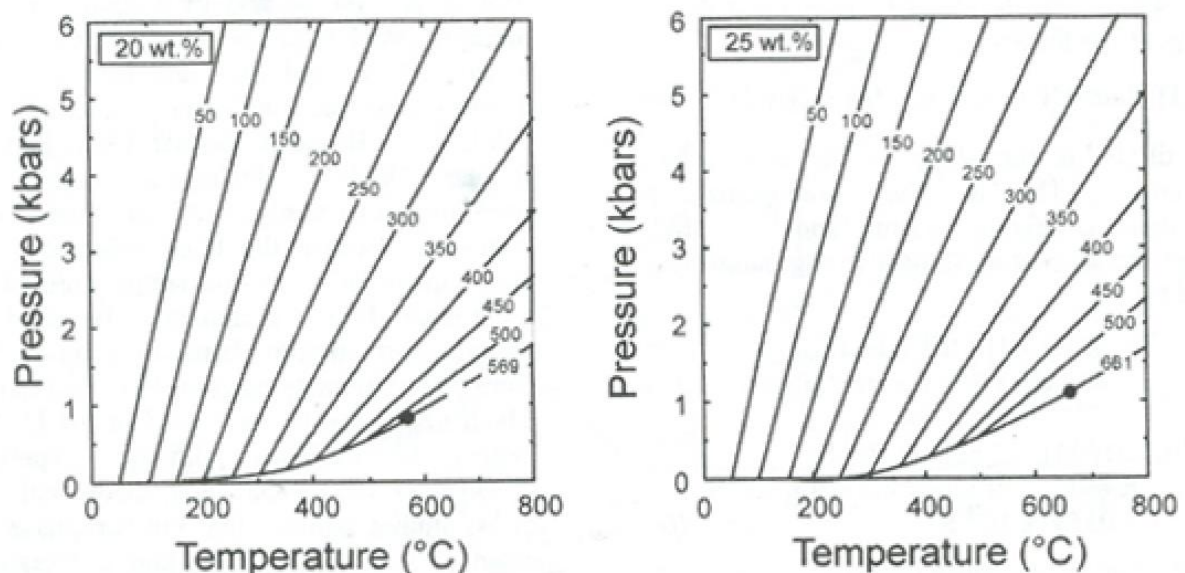
Figure 3-16: Examples of isochores for the H2O-NaCl system at 20 and 25 wt.% NaCl.
Source: (Bodnar and Vityk, 1994).

4 Methods

4.1 Fieldwork

The area that was selected for the fieldwork was chosen based on the formation history and the similar rock structures to the Skaergaard intrusion, which can be seen on the rock face in Vestrahorn, especially pegmatites. Both Vestrahorn and Austurhorn were visited and after careful consideration the best locations were chosen for further observations. After observing Austurhorn, the area was not considered to be of a great importance as it was not found to contain volatile-rich granophyre and gabbroic pegmatite.

The fieldwork was conducted during the summer of 2014 at Vestrahorn in Iceland. In total 5 days were spent in the field. The area that was covered was not very big, but it did cover a large part of the exposed ring complex, where it is possible to see the contact between different rocks and structures that are also visible at Skaergaard.

4.1.1 Field equipment

The fieldwork was conducted with traditional field equipment: hammer, small sledgehammer, safety goggles, tape measurement, notebook, pencils, loupe, camera, Silva Ranger compass (with libella and inclinometer), and GPS (Garmin GPSmap 60CS). The compass was calibrated to account for the difference between magnetic north and true north at Vestrahorn (11°).

4.2 Sample preparation

Samples from the Skaergaard intrusion were collected during two excursions in 1989 and 1990 by Rune Berg-Edland Larsen from the LS, and on three excursions in 2008, 2009 and 2011 from the UBS by Lars Peter Salmonsen for his Ph.D. project under the supervision of Christian Tegner.

The samples from Vestrahorn were selectively collected in the field. The main focus was on the melano-granophyre, gabbro pegmatite and the seemingly coarser-grained gabbro which the pegmatite seemed to be mostly located in. The sample locations were noted and mapped with the GPS device. Each sample was broken off from the rock face. A preference towards samples that were minimally weathered or cracked was made in order to avoid alteration and cracking of the samples during sample preparation. An overview of the

samples collected can be found in appendix A, all the samples were labelled and their rock types classified in the field.

4.2.1 Thick sections

The thick sections were prepared from samples collected from the UBS in the Skaergaard intrusion by Lars Peter Salmonsen and his supervisor Christian Tegner during an excursion in 2008. 18 samples were then prepared into thick sections at the Thin section laboratory (n. Sliplaboratoriet) at the Department of Geology and Mineral Resources Engineering (IGB) at NTNU as a 300 μm samples on glass slides for Rune Berg-Edland Larsen. After viewing them with an optical microscope seven samples were picked, one from each layer except from LZa' since no samples from that layer had been made into a thick section. The samples were chosen based on the amount of fluid inclusions and size, for easier measuring which would lead to optimal results. These were then detached from the glass slide for the microthermometry study. The thick section samples can be seen in table 4.1, along with the layer it originated from and which one was then studied with microthermometry.

Table 4.1: The sample number of the thick section, the layer they were found in and whether the thick section was used for microthermometry study.

Sample number	Layer	Microthermometry
SK08-1	LZb'	No
SK08-2	LZb'	No
SK08-12	LZb'	No
SK08-104	UZc'	No
SK08-105	UZc'	Yes
SK08-106	UZc'	No
SK08-110	SH	Yes
SK08-142	UZa'	No
SK08-150	UZb'	No
SK08-155	UZb'	No
SK08-156	UZb'	Yes
SK08-158	UZa'	Yes
SK08-165	UZb'	No
SK08-162	MZ'	Yes
SK08-197	LZc'	Yes
SK08-198	LZc'	No
SK08-200	LZb'	Yes
SK08-201	LZb'	No

4.2.2 Thin sections

The thin sections were cut and prepared at the Thin section laboratory at the IGB at NTNU. If special features in the rock mass were of interest the area was marked on the rock and the thin section made based on that. All the thin sections were made into polished thin sections as a 30 μm samples on glass slides. Table 4.2 gives an overview of thin sections that were made as a part of this research.

Table 4.2: The thin section samples along with the year they were collected, which series and layer in the intrusion they are located in, and who collected them.

Sample number	Year	Location	Layer	Collected by
SK08-1	2008	UBS	LZb'	Lars Peter Salmonsen
SK08-2	2008	UBS	LZb'	Lars Peter Salmonsen
SK08-12	2008	UBS	LZb'	Lars Peter Salmonsen
SK08-58	2008	UBS	LZb'	Lars Peter Salmonsen
SK08-104	2008	UBS	UZc'	Lars Peter Salmonsen
SK08-105	2008	UBS	UZc'	Lars Peter Salmonsen
SK08-106	2008	UBS	UZc'	Lars Peter Salmonsen
SK08-110	2008	UBS	SH	Lars Peter Salmonsen
SK08-142	2008	UBS	UZa'	Lars Peter Salmonsen
SK08-148	2008	UBS	UZb'	Lars Peter Salmonsen
SK08-150	2008	UBS	UZb'	Lars Peter Salmonsen
SK08-154	2008	UBS	UZb'	Lars Peter Salmonsen
SK08-155	2008	UBS	UZb'	Lars Peter Salmonsen
SK08-156	2008	UBS	UZb'	Lars Peter Salmonsen
SK08-158	2008	UBS	UZa'	Lars Peter Salmonsen
SK08-159	2008	UBS	MZ'	Lars Peter Salmonsen
SK08-162	2008	UBS	MZ'	Lars Peter Salmonsen
SK08-164	2008	UBS	UZb'	Lars Peter Salmonsen
SK08-165	2008	UBS	UZb'	Lars Peter Salmonsen
SK08-197	2008	UBS	LZc'	Lars Peter Salmonsen
SK08-198	2008	UBS	LZc'	Lars Peter Salmonsen
SK08-199	2008	UBS	LZb'	Lars Peter Salmonsen
SK08-200	2008	UBS	LZb'	Lars Peter Salmonsen
SK08-201	2008	UBS	LZb'	Lars Peter Salmonsen
SK11-50	2011	UBS	SH	Lars Peter Salmonsen
SK11-51	2011	UBS	SH	Lars Peter Salmonsen
SK11-52	2011	UBS	SH	Lars Peter Salmonsen
SK11-55	2011	UBS	SH	Lars Peter Salmonsen
458291	2009	UBS	Iron-rich phase	Lars Peter Salmonsen
SK-5A	1989 or 1999	LS	Iron-rich phase	Rune Berg-Edland Larsen
SK-5B	1989 or 1999	LS	Iron-rich phase	Rune Berg-Edland Larsen

4.2.3   Crushing

Preparation of the samples for X-ray fluorescence (XRF) analysis was done under the guidance of Torill Sørløkk at the IGB at NTNU. Table 4.3 lists the samples that were crushed for the analysis.

Table 4.3: The samples that were crushed for geochemical analysis along with the year they were collected, which layer they are located in, and who collected them.

Sample number	Year	Layer	Collected by
SK11-50	2011	SH	Lars Peter Salmonsen
SK11-51	2011	SH	Lars Peter Salmonsen
SK11-52	2011	SH	Lars Peter Salmonsen
SK11-55	2011	SH	Lars Peter Salmonsen
458291	2009	Iron-rich phase	Lars Peter Salmonsen
SK-5A	1989 or 1999	Iron-rich phase	Rune Berg-Edland Larsen
SK-5B	1989 or 1999	Iron-rich phase	Rune Berg-Edland Larsen

First the samples were cut at the Thin section laboratory with a rock saw to obtain the required size. A Fly press rock crusher (figure 4-1A) was used to crush the sample into a fine enough grain size so it would be possible to mill the samples. But before the samples were milled they were split into a suitable sample size (about 20-30 gr) in a sample splitter for aggregates. Then a Disk mill (n. skivesvingmølle) (figure 4-1B) with an agate mill (figure 4-1C) was used to mill the samples into fine powder. Between samples the Fly press rock crusher was cleaned with a vacuum cleaner, compressed air and ethanol, the sample splitter was cleaned with compressed air and ethanol, and the mill was cleaned with warm water, ethanol and quartz sand when needed. These samples were then used for geochemical analysis.

Figure 4-1: A shows the Fly press rock crusher that was used to crush the samples. B shows the Disk mill which the agate mill (shown in C) was inserted into.

4.3 Petrographic study

The petrography study was performed at the Microscopy lab (n. Mikroskopisal) at the IGB at NTNU. The samples that were previously prepared as thin sections were analysed with optical microscope. A Leica DM2500 P optical microscope with both transmitted and cross-polarized light was used with a choice of magnification between 2.5-50x. The microscope was also attached to ProgRes CT3 camera (figure 4-2).

Relief, colour, interference colour and other unique optical properties were identified and used to distinguish the minerals.

Figure 4-2: The Leica DM2500 P optical microscope that was used to identify minerals in thin sections.

4.4 X-ray fluorescence analysis

The XRF analysis, both for the main and trace elements, were performed at the X-ray laboratory (e. Røntgenlaboratoriet) at the IGB at NTNU with the guidance of Torill Sørløkk with S8 TIGER machine from BRUKER. The machine can be seen in figure 4-3.

For the XRF measurements the previously crushed samples were used both for measuring main and trace elements, but from each crushed sample two measurements were made and then A or B was added to the back of the sample number to identify between these two samples.

Figure 4-3: The S8 TIGER machine that was used for the XRF chemical analysis.

4.4.1 XRF preparation for main elements

The samples needed to be made into glass tablets. First about 2.5 gr of each sample was heated at 105°C for about 24 hours to dry the samples. Next the samples were placed in a desiccator with silica gel to stabilise the humidity of the samples. Loss on ignition (LOI) was calculated after weighing the samples before and after heating them at 1000°C for two hours. Finally 0.5 gr of each sample was measured and mixed with 5 gr of lithium tetraborate/metaborate and 60 μl of lithium iodide before being placed in a Claisse Fluxy fusion device where it was melted at around 1050°C and formed into glass tablets which are then measured. The Claisse Fluxy fusion device can be seen in figure 4-4.

Figure 4-4: The Claisse Fluxy fusion device that was used.

To determine the amounts of main elements in the sample tablets a quantitative program, Calibrated program for main elements, was used. This is a program made at the institution, based on 30 geology standards and that measures 10 main elements (Fe_2O_3, TiO_2, CaO, K_2O, P_2O_5, SiO_2, Al_2O_3, MgO, Na_2O, MnO). X-ray analysis depends on the fluorescing abilities of elements to distinguish, identify and quantify them.

When the highest values were over the detective limit of the program a semi-quantitative method, QUANT-EXPRESS, was also used. QUANT-EXPRESS identifies every element that is found in the samples and delivers the results normalised.

4.4.2 XRF preparation for trace elements

For the XRF machine to be able to analyse the samples they need to be prepared into 40 mm powder tablets. To make the tablets 9.6 gr of each sample was mixed with 2.4 gr of wax (Licowax) by using a MU-XRF Mixing set until it was homogenised, which can be seen in figure 4-5A. Figure 4-5B shows a HERZOG laboratory press which was used to press the samples into tablets at 200 kN.

All tools that were used were cleaned with ethanol between preparations of each sample.
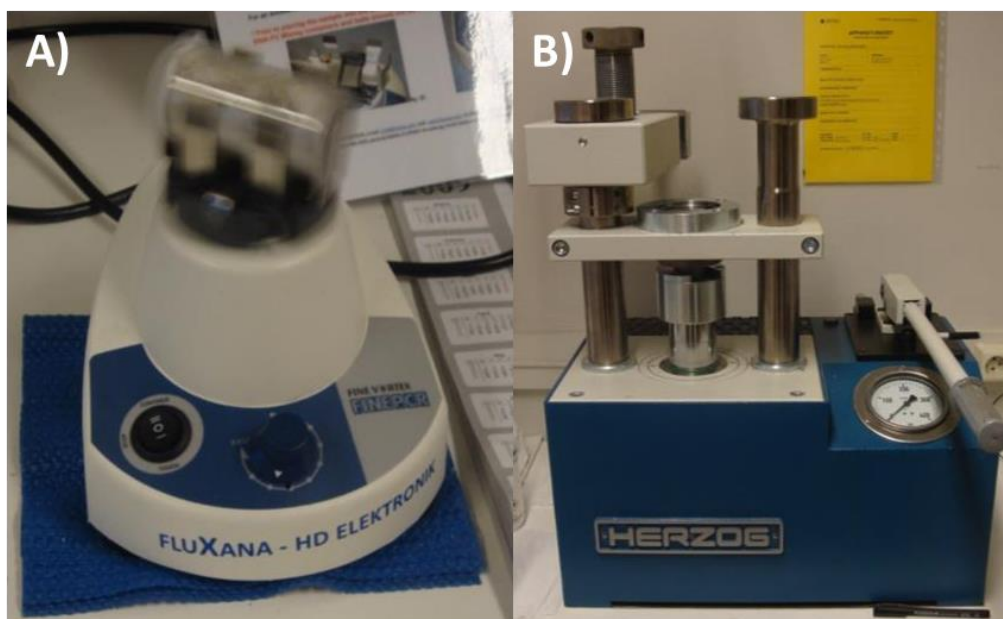
Figure 4-5: A shows the MU-XRF mixer which was used to mix the samples before making the tables. B shows the HERZOG laboratory press which was used to form the samples into tablets.

The semi-quantitative program GEO-QUANT, specially made for geological research, was used to measure the amount of elements in each sample. It measures 27 elements, whereof 24 are trace elements (Sc, V, Cr, Co, Ni, Cu, Zn, Ga, As, Rb, Sr, Y, Zr, Nb, Mo, Sn, Sb, Cs, Ba, La, Ce, Pb, Th, U) (the other 3 are main elements (Fe_2O_3, TiO_2, MnO)). The results are not normalised. With the samples five standards for geology material were also run as a control. When the highest values were over the detection limit of the standards, QUANT-EXPRESS was also used.

4.4.3 X-ray powder diffraction preparation

The X-ray powder diffraction (XRD) preparation and analysis was completed at the X-ray laboratory at the IGB at NTNU with the guidance of Laurentius Tijhus. The XRD analyse was only used for one sample, which was taken from the centre of a pegmatite body in Iceland, to identify the black needles in the matrix. Few needles were carefully picked out to get enough material to measure. Those were milled in a mortel by hand, along with ethanol. The sample was then put on a sample disk and the ethanol was dried.

An D8 ADVANCE XRD machine was used to measure the samples (figure 4-6).
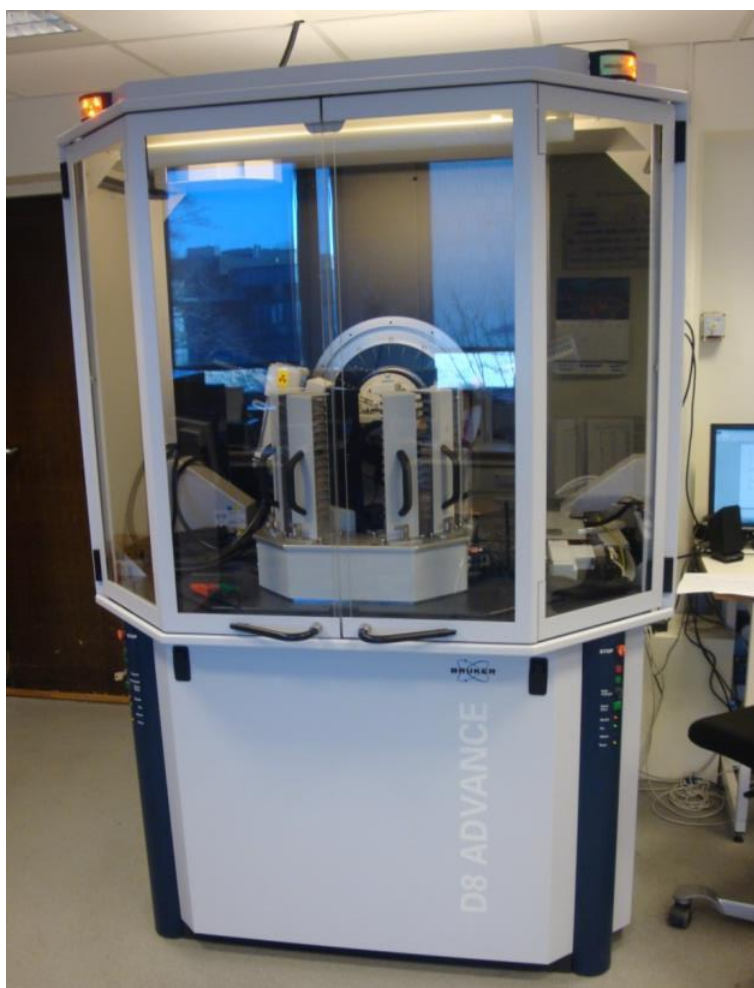
Figure 4-6: The D8 ADVANCE XRD machine that was used for the XRD chemical analysis.

4.5 Microthermometry analyses

The samples were first examined with the Leica DM2500 P microscope to identify the best suited samples based on the amount and quality of primary fluid inclusions. These samples were briefly described and the FI were photographed before starting the non-destructive analyses process.

A Linkam THMSG 600 mounted on a Nikon ECLIPSE E600 optical microscope was used for the microthermometric analysis, along with a Linksys 32 software to control the heating and cooling of the samples. QICAM Fast 1394 digital camera was connected to the microscope to observe the heating and cooling processes in real time on a computer screen with the QCapture software and take photos of the FI and phase changes. The FI were most easily observed at a 50x magnification. Using liquid nitrogen it is possible to cool the samples down to around -196°C. The machines used can be seen in figure 4-7.

The thick sections needed to be removed from the glass slide and broken down into smaller pieces to fit into the chamber of the optical microscope before the analyses.

To find the melting point of the liquid and the hydro-halite melting the samples were cooled down to -196°C before being heated up to -100°C at 50°C/min. Then the heating rate was slowed down to 20°C/min, until the temperature for the anticipated phase change was almost reached and the heating rate was decelerated even more. This way it was estimated to be possible to get precise measurements of phase changes from solid to liquid with error of about 0.1°C. Only a few (1-3) FI were observed at once to make sure not to miss any phase changes. If the precise measurement was missed the sample needed to be refrozen, ideally down to -196°C to avoid undercooling, which might give incorrect results.

All the cooling measurements were finished in each sample before the heating of the samples was conducted to avoid decrepitation of the FI. During this stage as many as possible FI were observed at the same time. The Brownian motion made it quite easy to measure the homogenisation temperature of the FI, but if the phase change was missed the sample was cooled to about 30-50°C and remeasured to be able to observe the loss of one phase (normally the gas phase, but sometimes the liquid phase). No intended decrepitation was performed.
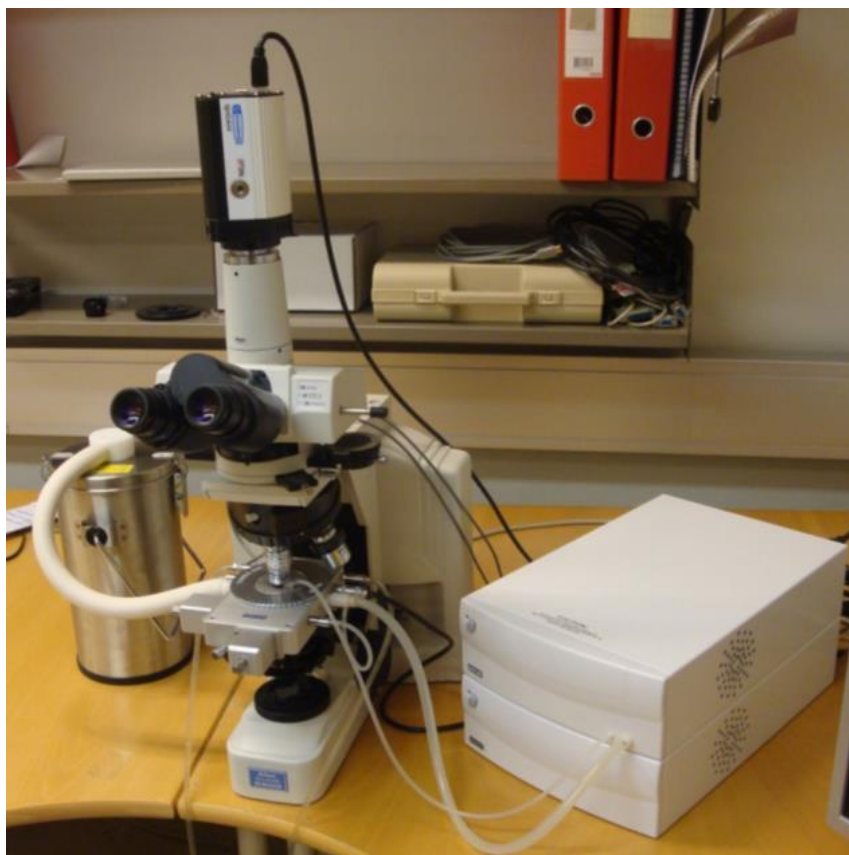
Figure 4-7: The Nikon ECLIPSE E600 microscope used to perform the microthermometry. At the centre of the figure is the optical microscope, on its left side is a tank with liquid nitrogen and on the right side is a nitrogen pump.

4.5.1 Calibration

A synthetic fluid inclusion reference set (from Bubbles Inc., Blacksburg, VA, USA) was used for the stage calibration. The fluid inclusions that were used contained H_2O, NaCl, $CaCl_2$, KCl or CO_2 mixture in different proportions. Two different calibration measurements were done, which can be seen in figure 4-8, and used to construct a calibration curve. The results only differ at the CO_2 melting temperature, so the equation that seemed more plausible compared to the original values was used;

$$y = 0.9373x + 0.099.$$
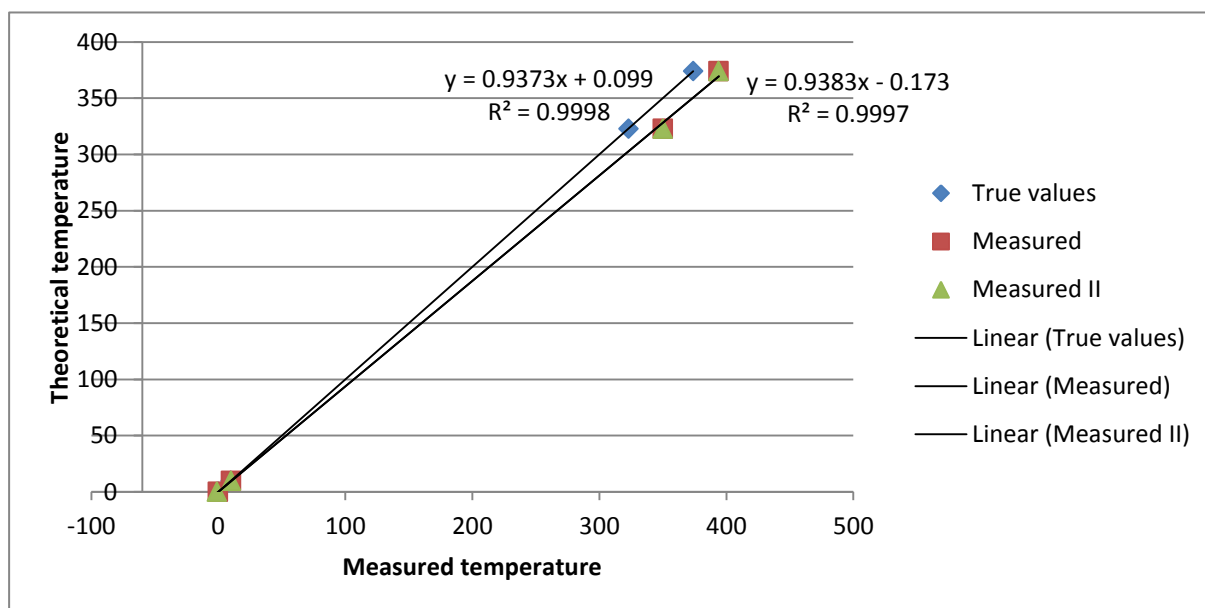
Figure 4-8: The calibration curves which were constructed from the synthetic fluid inclusion measurements. Only one of them was used to calibrate the results.

4.5.2   Calculations of results

The program AqSo1e was used to find the salinity of the fluid in the inclusions (other programs like AqSo Vir or AqSo WHS could also be used). It is based on empirical EoS for H_2O-systems (Bakker, 2003, Bakker, 2012, Bakker and Brown, 2003, Sterner et al., 1988).

Two different methods were used to determine the salinity, both with the AqSole program. The first was done by using the ice melting temperature of the FI. The other method used the median melting temperature of hydro-halites, and the salinity for each layer was then calculated separately. It is expected that all salt in the inclusions is NaCl (Larsen et al., 1992). The H_2O-NaCl system is described by empirical sub-parameters (Bakker, 2012). The computer programs that were used are similar in that their minimal melting temperature is -21.2°C, while the measurement results from this project are lower. The results calculated from Robert J. Bodnar (1993) were used as he uses the most recently revised equation for H_2O-NaCl solution (Bodnar, 1993).

To find the properties of the fluid in the FI, Ronald J. Bakker´s BULK program was used (Bakker, 2003) to calculate the fluid inclusion composition even if not normally utilized for salinities higher than 23.19 mass%. BULK uses the results from microthermometry to calculate the composition and density of the bulk fluid in the inclusion with EoS (Archer, 1992, Bakker, 2003, Bodnar, 1993, Zhang and Frantz, 1987).

The composition and density results from the BULK program were then inserted into the program ISOC by Ronald J. Bakker, which also uses EoS (Bakker, 2003, Bodnar and Vityk, 1994, Knight and Bodnar, 1989) to determine the pressure at the homogenisation temperature for each layer. The program is limited to temperature between 100-800°C and a pressure of 0-6.000 bars. The program can also be used to construct the isochores but instead it was decided to use a different equation to calculate the slope and construct the isochores from the pressure at homogenization.

To calculate the slope of the H_2O-NaCl isochores the following equation was used (Bodnar and Vityk, 1994):

$$dP/dT \ (bar/°C) = a_s + b_s * Th + c_s * Th^2,$$

where the slope of the isochore is dP/dT, Th is the homogenization of the fluid inclusions in °C, while a_s, b_s and c_s are defined by the following:

$$a_s = 18.28 + 1.4413 \ S + 0.0047241 \ S^2 - 0.0024213 \ S^3 + 0.000038064 \ S^4$$

$$b_s = 0.019041 - 1.5268 * 10^{-2} \ S + 5.6012 * 10^{-4} \ S^2 - 4.2329 * 10^{-6} \ S^3 - 3.0354 \\ * 10^{-8} \ S^4$$

$$c_s = -1.5988 * 10^{-4} + 3.6892 * 10^{-5} \ S - 1.9473 * 10^{-6} \ S^2 + 4.1674 * 10^{-8} \ S^3 - \\ 3.3008 * 10^{-10} \ S^4,$$

where the S is the salinity of the fluid inclusions for H_2O-NaCl fluid with salinity of 0-40 wt.% NaCl. These are valid up to the upper limit of the experimental data that was used to formulate this equation, or 6 kbars. At the moment experimental data to extend these isochores beyond 6 kbars does not exist.

The pressure at the homogenization temperature was used as the starting point for the isochores, which was then constructed with the previously calculated slope. The isochores calculated with the program ISOC and the equation by Bodnar and Vityk (1994) was compared and found to be almost identical. As the equation by Bodnar and Vityk (1994) is more recently updated, it was used during calculations of isochores.

4.6 Sources of error

There are many possible sources of error during a project like this, from the choosing of samples all the way to the interpretation of results.

Out in the field it is not possible to observe structures in 3D, and sometimes the structures were not continuous on the surface, which gives room for wrong interpretations. Some structures that might be important as a clue towards the formation of the structures might be overlooked, or not found if they are not exposed.

During petrography study, human error can result in similar minerals being identified as one mineral, minerals being wrongly identified, or not noticing a rarely occurring mineral in the thin sections. The quantity of a mineral can also be estimated inaccurately.

The geochemical analysis consisted of many different steps which increases the possibility of an error. During the crushing and the making of tablets some contamination can happen if the instruments are not cleaned thoroughly. It is also necessary to make sure that the samples were milled fine-grained enough for the XRF machine. The samples and chemicals used to make the tables need to be precisely measured and ensure to tare the scale. The samples and chemicals need to be completely mixed. The quality of the measurements also depends on the length of analysis time in the XRF machine.

While completing microthermometric measurements, it is important to only measure fluid inclusions in the quartz that is a part of the granophyre masses, as that is the last melt to crystallize. It is also necessary to only perform measurements on primary inclusions, as other inclusions might have been altered by later processes. During the measurements it is possible that the temperatures were not recorded correctly during heating or cooling, maybe due to phase changes not correctly observed, or a slow reaction when stopping the temperature controller. Some phase changes might not have been noticed due to poor resolution. These might then lead to difficulties in analysing the results. The volumes of vapour bubbles in the inclusions were only roughly estimated, but due to differences in geometry they might contain more error than the estimated 5% volume error. The programs and equation used to construct the isochores have limited range which has been mentioned previously. The FI measured might also have been trapped under sub-solidus conditions, or they might have leaked after they formed, therefore only inclusions that seemed whole were used. The results are also influenced based on how well the EoS are known.

5 Results

5.1 Field work

Field work was completed at Austurhorn and Vestrahorn in Iceland. The locations are shown on the map in figure 5-1.
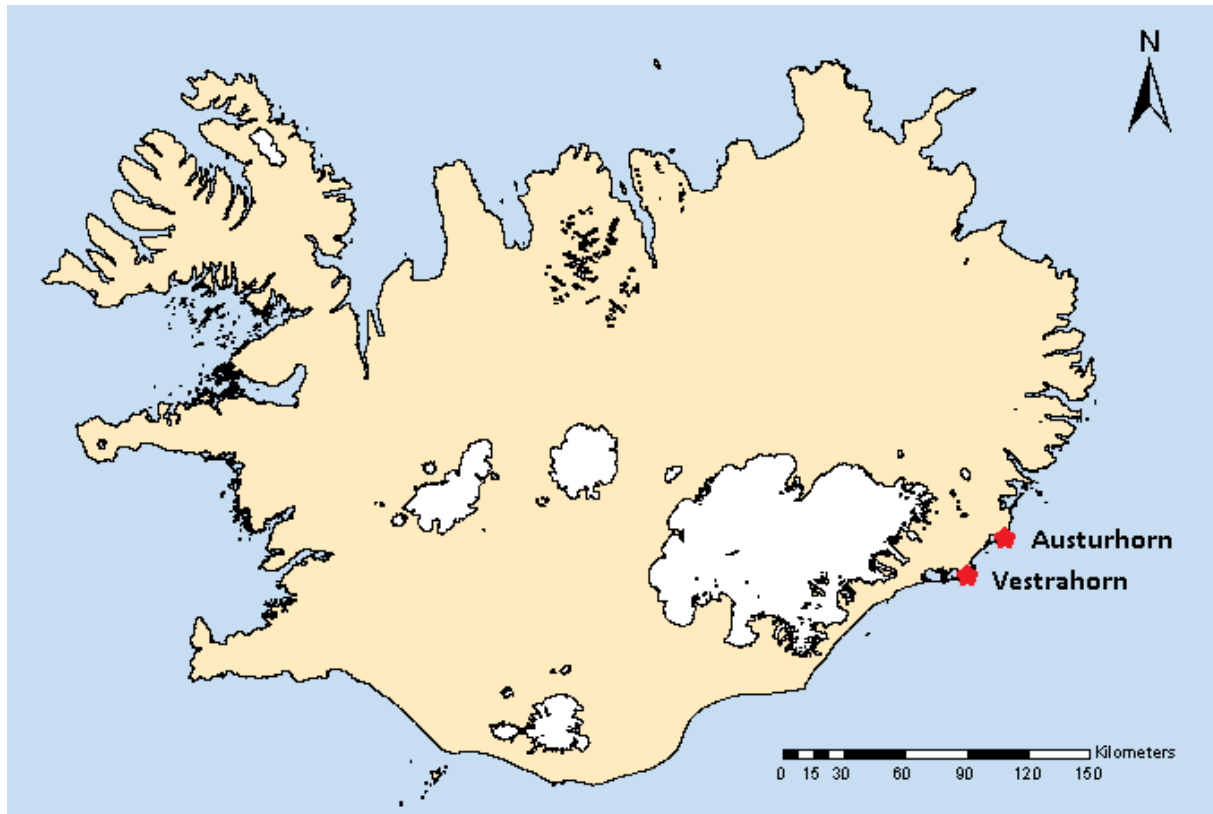
Figure 5-1: Map of Iceland showing the study locations (marked with stars).
Source: IS 50 V Map database, 4th publication, (Einarsson and Saemundsson, 1987).

During fieldwork, Austurhorn was determined to be an excellent example of magma mixing, as previously described by de Jesus Padialla (2011). The enclaves found there were compositionally distinctive from the host rock, as they were more mafic and hotter than the host rock that they intruded into. This was evident on, for instance, the margins of the enclaves, which were very fine-grained, or quenched. The enclaves often had sharp, angular boundaries (figure 5-2A) while others had cuspate or crenulate margins (figure 5-2B). The centres of some of the enclaves contained phenocrysts (figure 5-2A).

Figure 5-2: Examples of the enclaves found at Austurhorn. A shows visible phenocrysts in the enclaves, along with sharp edges, while B shows the cuspate margins.

5.1.1 Vestrahorn

Vestrahorn was the chosen study area as the aim was to decide if the appearance of gabbroic pegmatites and melano-granophyres there could be analogous to the ones in the Skaergaard intrusion. The locations observed during the field work are shown in figure 5-3.

Figure 5-3: The locations observed during the field work at Vestrahorn.
Source: IS 50 V Map database, 4th publication, (Einarsson and Saemundsson, 1987).

Location 1

Location 1 exposed both the contact relationship and internal structure of the pegmatites, which was comprised of both gabbroic and granophyric parts.

The main body covered about 45 m^2 in total. There were dikelets progressing away from the body, as can be seen in figure 5-4. The dikelets extruding to the south and northeast appeared to progress discontinuously to areas that used to contain even larger amounts of pegmatite than the observed body. Either the connection between these pegmatites eroded away, or they were never connected. The dikelets extruding towards the west ended close to the body.

Figure 5-4: The observed pegmatite body with location and directions of veins that lie away from it marked.

Fine-grained felsic material, possibly granophyre, was observed at two places in the body; one was in the eastern wall of the body where it contained coarse-grained amphibole needles in the matrix, and the other was in the vein that leads NE and contained only fine-grained granophyre. The veins and the bodies connected to them appeared to lie from south to north and from a lower elevation upwards, but the pegmatite body in the south was more felsic and fine-grained compared to the body found in the NE vein.

After the field study, one sample of the fine-grained felsic material in the eastern wall was studied in more detail to determine whether it contained ferrobustamite needles, which had been previously reported from melano-granophyre in the Skaergaard intrusion. Therefore a thin section was made, and the black crystals analysed by XRD. The black grain was an amphibole and the sample mainly contained plagioclase (mostly albite and orthoclase) and amphibole, some quartz, in addition to other accessory minerals. The quartz and alkali feldspar did not form a granophyre masses, but the quartz formed masses similar to the underdeveloped granophyre masses in the LZc' of the Skaergaard intrusion.

The contact area between the pegmatite and the host rock was irregular and in places gradually transitioned into gabbro (figure 5-5A). At the pegmatite margin, the average grain size was not as coarse as in the interior of the pegmatite body, though coarser than in the gabbro. The rust weathering surface shown in figure 5-5B made it possible to distinguish the pegmatite body from the host rock (which was redder). In the figure it was also clear that the matrix of the pegmatite body had a finer grain size at the margins than the body itself.
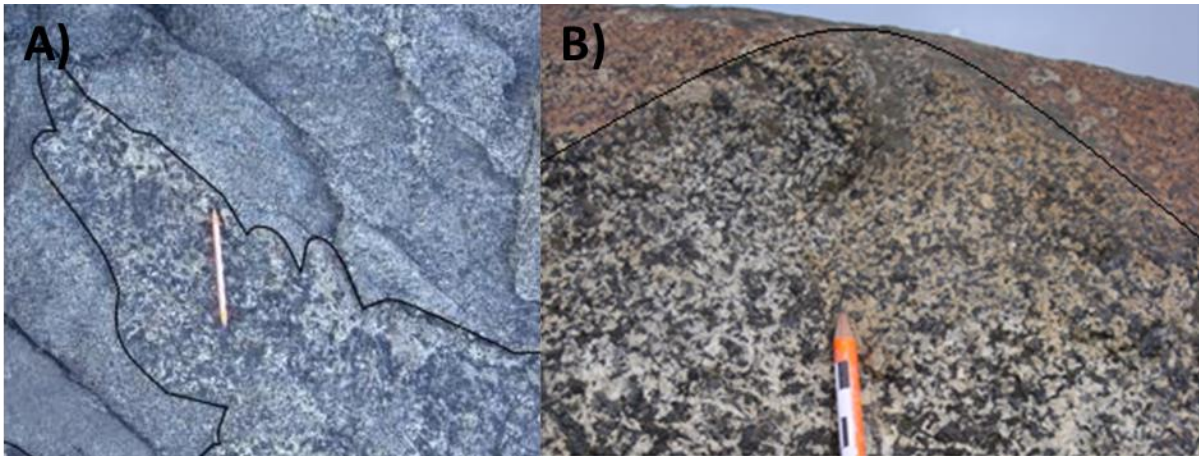
Figure 5-5: A shows the undulating contact between the pegmatite body and the host rock. B shows how the pegmatite body became more fine-grained closer towards the host rock.

The east wall of the pegmatite was logged and is shown in figure 5-6A, along with a photograph of the same area in figure 5-6B. A felsic dyke that intersected the pegmatite was also marked on the figure.
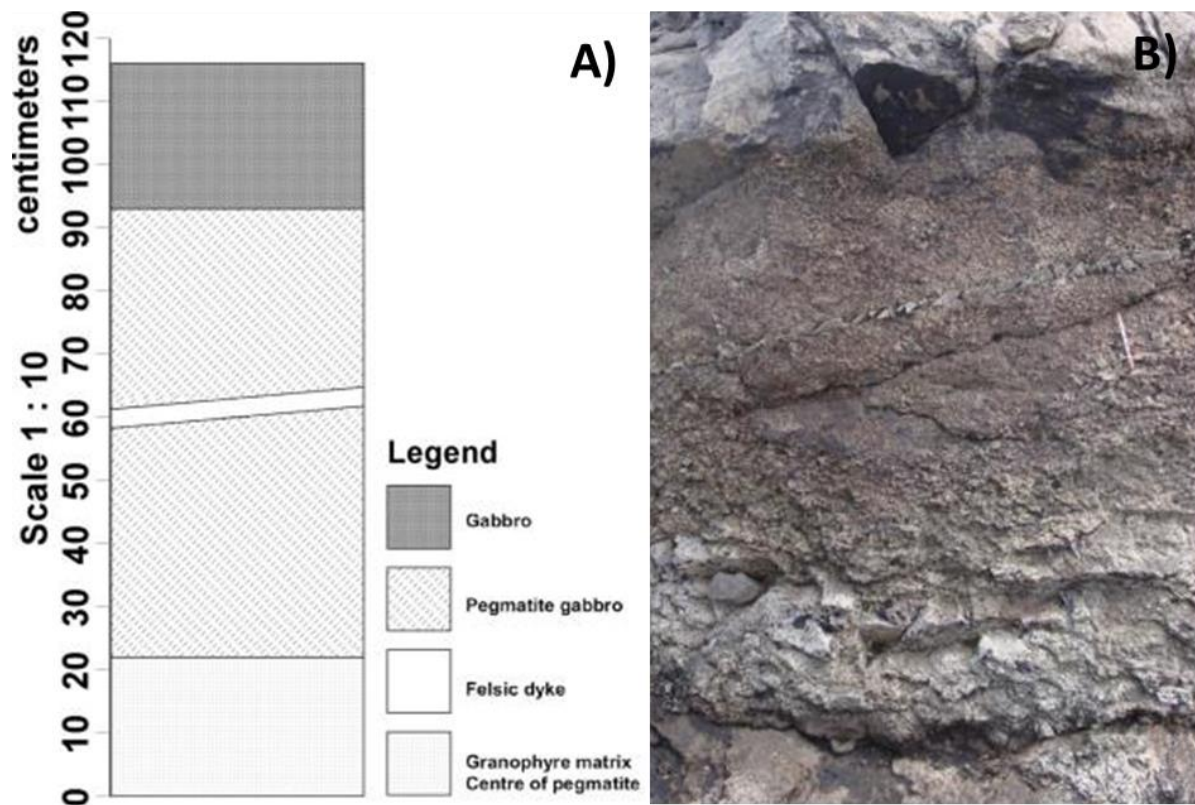
Figure 5-6: A shows the logged profile, while B shows a photo of the same profile.

The pegmatite grain-size varied considerably from very coarse (>1 cm) at the top closest to the contact to fine-grained in the centre of the pegmatite (the grain size of the matrix was <1 mm, but it contained amphibole phenocryst needles which were >1 cm). The decrease in grain size can be observed in figure 5-7.
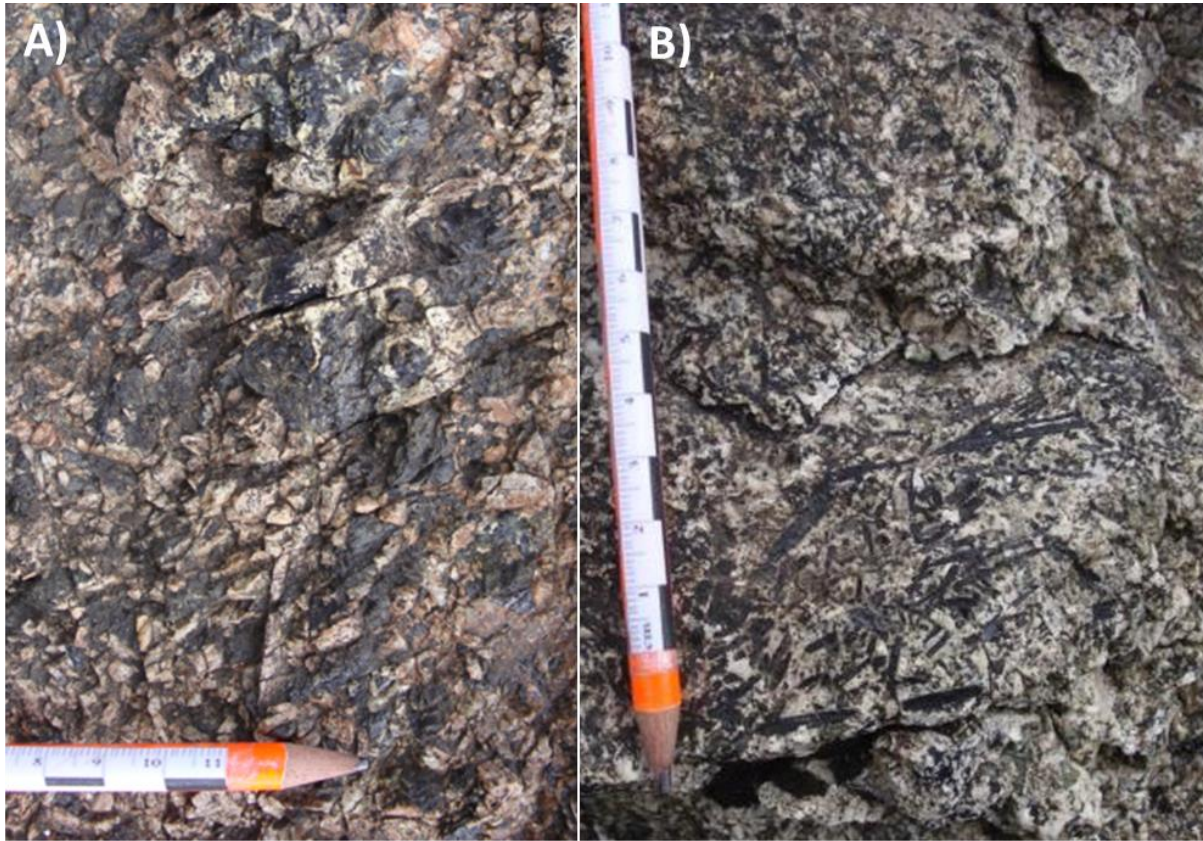
Figure 5-7: A shows the typical matrix of the pegmatite. B shows the centre of the pegmatite with granophyric masses containing amphibole.

Location 2

Location 2 exposed a vertical columnar pegmatite intersecting the gabbro. The gabbro host rock was not as coarse-grained as most of the gabbroic host rock in which the other pegmatite columns were located in.

From the stratigraphic top to bottom, the pegmatite structure developed from a thin felsic dyke (figure 5-8B), which continued upwards into a small pegmatite body and onwards, forming the columnar pegmatite structure. The pegmatite structure in its entirety can be seen in figure 5-8A.

Figure 5-8: A shows the entire pegmatite structure. B shows the stratigraphically lowermost part of the pegmatite structure.

The pegmatite structure was zoned, with coarse-grained margins and a fine-grained centre. The column became thinner and more fine-grained upwards before it divided into several smaller columns.

Location 3

At location 3 the relationship between the two types of gabbro at Vestrahorn was exposed. The two types were distinguished by grain size, as one was coarse-grained while the other was more fine-grained, or closer to the typical gabbro grain size. In figure 5-9 it was observed that the coarse-grained gabbro intruded into the normal gabbro.

Figure 5-9: The figure shows that the coarse-grained gabbro intruded into the normal gabbro.

Location 4

Location 4 exposed a vertical columnar pegmatite and melano-granophyre – granophyric bodies that intersected a coarse-grained gabbro host rock (figure 5-10A). Next to the column there were also some randomly distributed batches of pegmatite. The centres of these batches were fine-grained granophyre whereas the margins were coarse-grained.

Typically, the columnar pegmatites changed from being coarse-grained at the bottom and contacts to fine-grained granophyric centres in the upper sections. The column was about the same thickness at both the top and the bottom, and it was observed to be ellipsoidal in cross section (figure 5-10B).
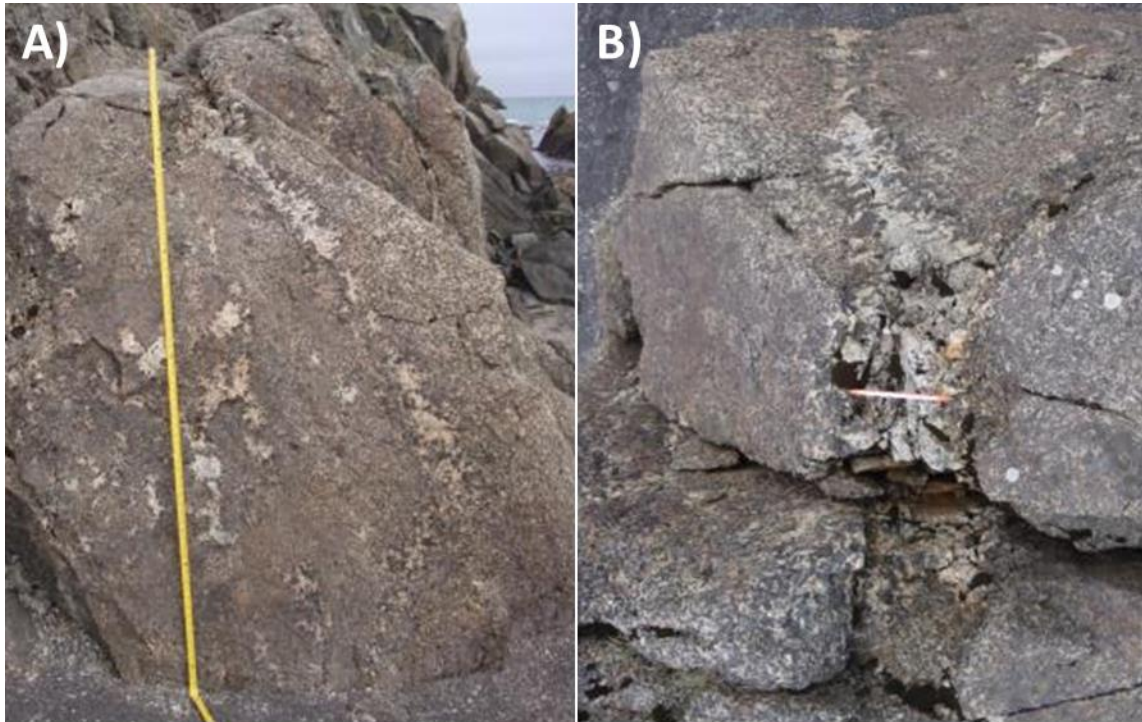
Figure 5-10: A shows the pegmatite column on right on the exposure, and the smaller pegmatite batches that were located to the left of the structure. B shows the ellipsoidal structure of the pegmatite column.

Upon closer inspection it was observed that some of the seemingly discontinuous pegmatite batches were actually connected by dark, coarse-grained pyroxene that resembled the pyroxenes at the margin of the batches (figure 5-11).
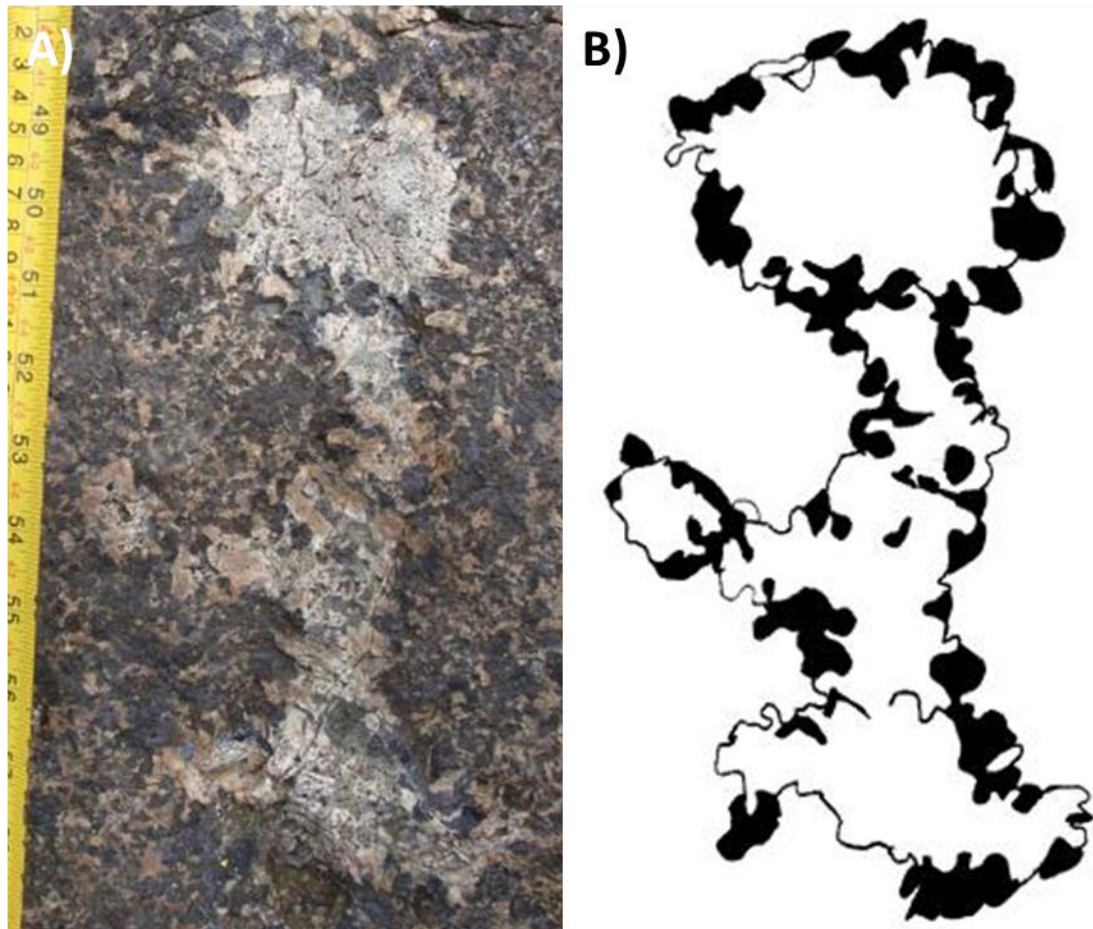
Figure 5-11: A shows a pegmatite batch, where the granophyric parts of the pegmatites were separated by a zone of pyroxene grains. B shows a drawing of the same structure to emphasize the separation of the pegmatite batch, where black marks pyroxene grains.

Location 5

Location 5 was comprised of a skerry exposing an irregular felsic dyke that laid from south to north (figure 5-12). The lowest part of the vein emerged from the coarse-grained gabbro, while the upper part was situated in a fine-grained gabbro. The dyke mostly consisted of granophyric masses, but rather than having coarse margins like the other pegmatite structures found at Vestrahorn, the margins were about as fine-grained as the dyke, although darker (figure 5-13A). Upwards the fine-grained material around the central dyke appeared to be transitioning into more coarser-grained margins.

Figure 5-12: The dyke went from the lower left corner and led upwards towards the top-right corner of the photo. The photo looked towards north.

The dyke laid in curves and formed structures of pinches and swells (figure 5-13B), moreover it had poorly-defined margins towards the gabbro host rock. A number of thinner, perpendicular E-W dykes with the same field appearance merged with the main dyke rather than intersecting it (figure 5-13A). These thinner dykes then tapered away from the main dyke.
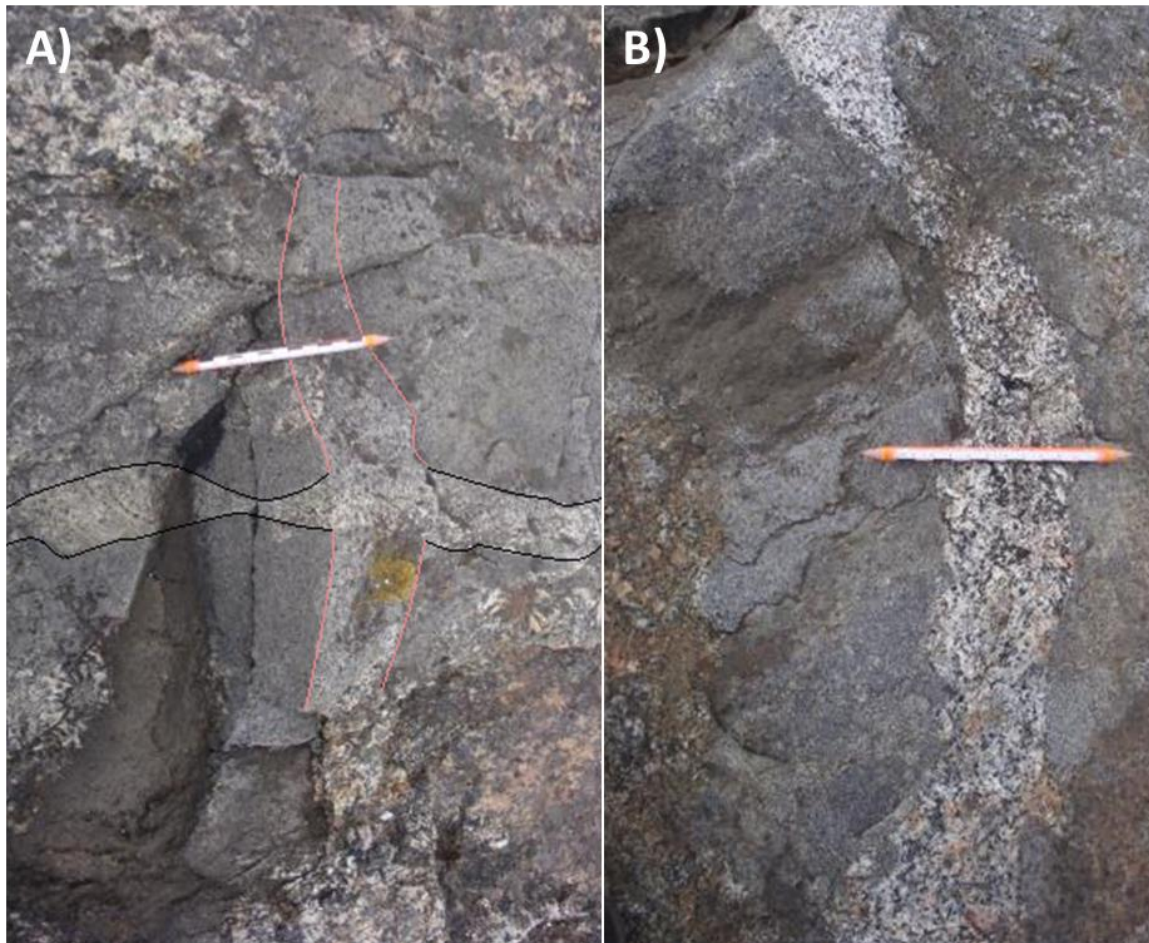
Figure 5-13: A shows the margins around the dyke (~12-15 cm thick), along with the perpendicular dykes (marked with red) that merged with the main dyke (marked with black). The perpendicular dykes were more visible in the margins of the dyke than in the host rock. B shows the pinches and swell structure.

Large amphibole needles (1-2 cm long) were quite common at the centre of the profile, but were almost non-existent at both the top and bottom.

Close to the stratigraphic top, the dyke had split into two thinner dikelets, as seen in figure 5-14, after it had already tapered considerably upwards. At the top, the dikelets were fine-grained and resembled the host rock in grain size, so they were distinguishing on the dikelets being more leucocratic than the host rock.
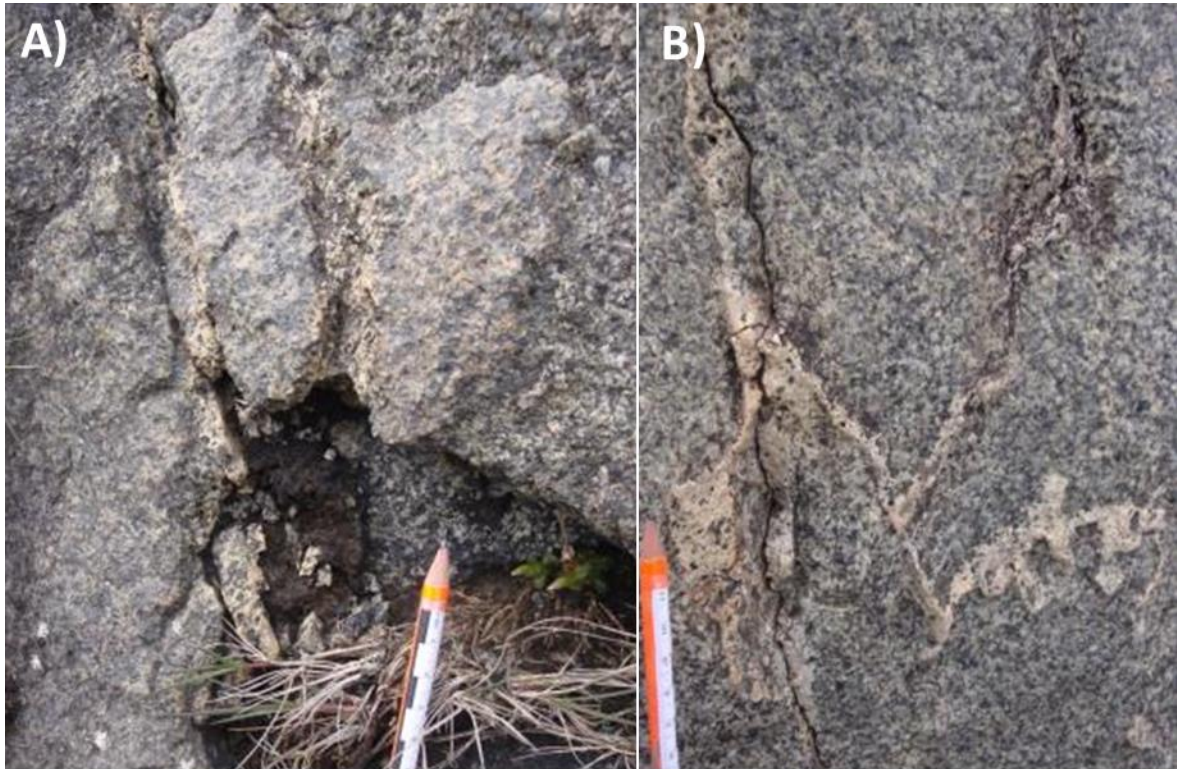
Figure 5-14: A shows the dikelets just after they had split. B shows the top of the dikelets. Both show the fine-grained, felsic composition.

Location 6

Location 6 is in a dimension stone quarry that was exposing an east-facing wall. This was the largest outcrop studied.

The southern part of the mine contained fine-grained gabbro, which slowly graded into a coarser-grained gabbro towards the north. There were no visible boundaries between these two gabbros in the outcrop. The northern section was densely spaced by both felsic and mafic, fine-grained intrusions, while there were no intrusions in the southern part of the mine. These intrusions had well-defined, chilled margins, some of which intersected pegmatite batches (figure 5-15).

Figure 5-15: Felsic intrusion crosscutting a pegmatite batch.

In the northern part of the mine there were three fine-grained, felsic vein structures that differed from the intrusions and pegmatite columns seen earlier, as they had undulating margins and some coarser grains in the matrix. These structures were intermittent, and dipped down towards the north. Additionally, one of them was intersected by a later dyke. Two of them can be seen in figure 5-16A and around them were numerous patches of felsic material as seen in figure 5-16B.

Figure 5-16: A shows two of the felsic veins, while B shows few of the felsic patches that could be found around these same veins.

One of the felsic veins was studied in greater depth. It was discontinuous, but where it was exposed, it formed small, elongated batches of felsic melt. The margins around it were fine-grained like the vein itself, but darker, similar to the margins of the dyke at location 5 (not found around the other two veins). In one place another small felsic veinlet merged with the vein.

At another segment the structure contained a miarolitic cavity with a sulphide crystal (~0,5 cm long) that could be seen in figure 5-17A and figure 5-17B. The exposed margins contained a lot of sulphides where the felsic vein was not visible, as can been seen in figure 5-17C and figure 5-17D. Both the felsic vein and the zone around it contained more sulphides than the host rock.
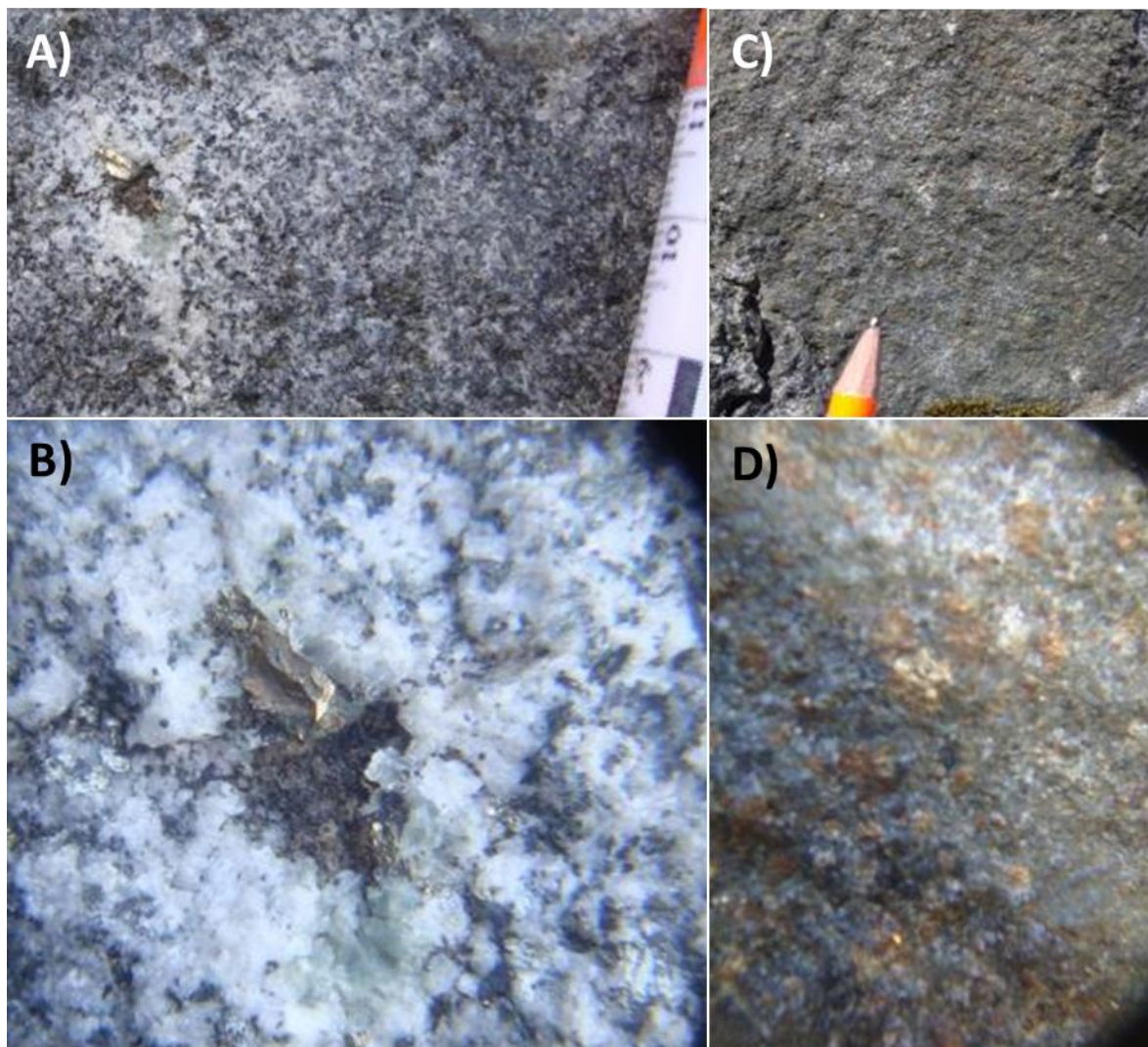
Figure 5-17: A and B show a miarolitic cavity with a sulphide crystal. C and D show the margins that contained sulphide crystals in the matrix.

In the mine only a few pegmatite structures were exposed. One was a pegmatite column, which can be seen in figure 5-18A. It lay upwards for about 3 m before it split into two separate columns and continued upwards (figure 5-18B). The margins were coarse-grained, while the centre contained fine-grained granophyre.
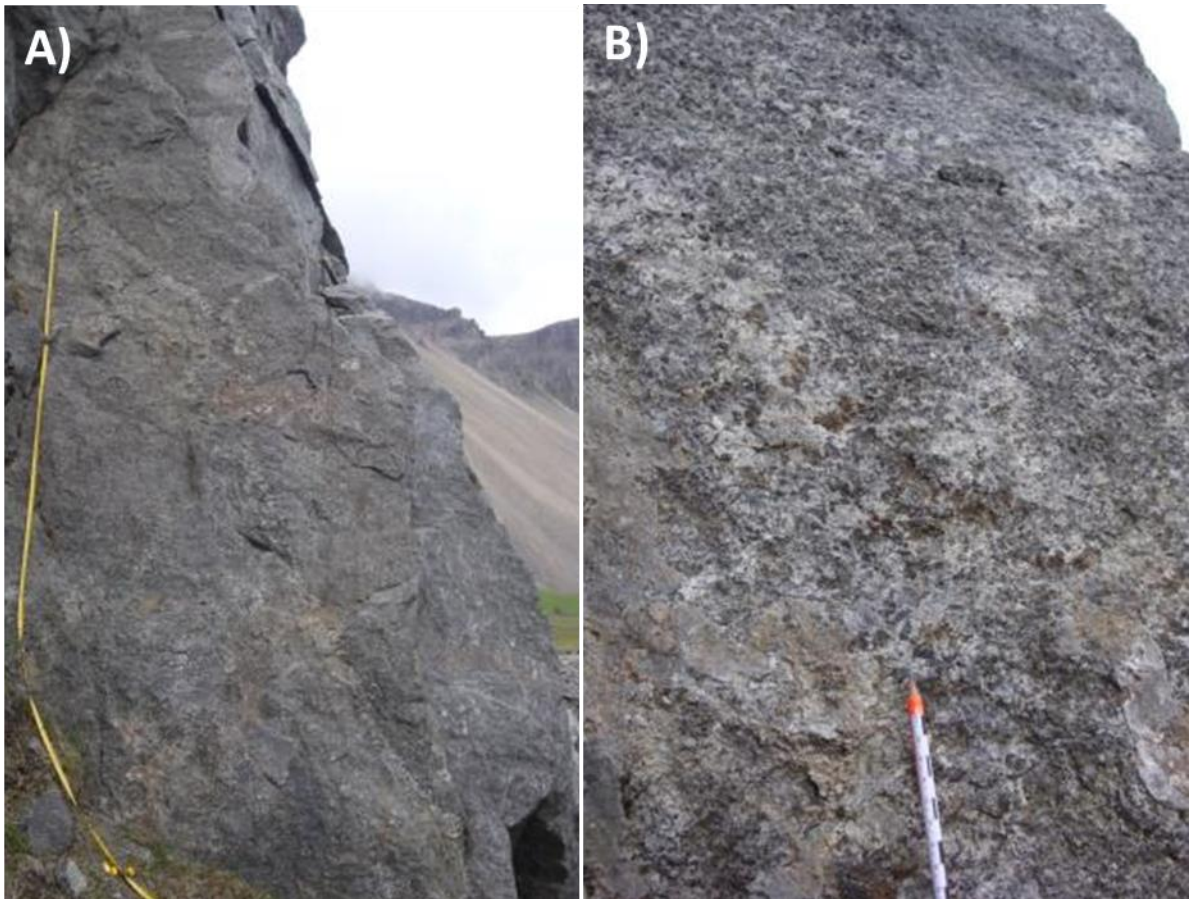
Figure 5-18: A shows the whole pegmatite column and in B it was possible to see how the column split in two just above the pencil.

A shorter pegmatite column ended in a spherical top as can be seen in figure 5-19A, and the sphere itself can be seen in figure 5-19B. The pegmatite column had coarse-grained margins and fine-grained granophyre in the middle, while the whole sphere was coarse-grained.
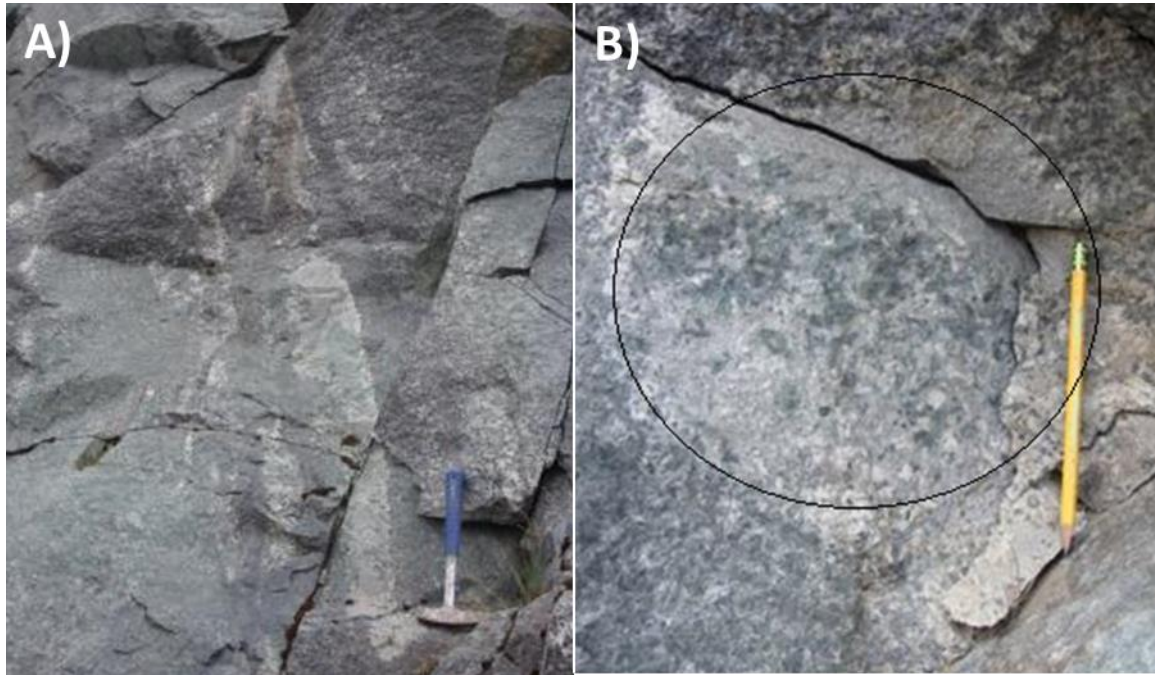
Figure 5-19: A shows the pegmatite column, and B shows the end of it, which formed a sphere.

Additional observations

One area at Vestrahorn contained similar rock formations as the ones seen at Austurhorn (figure 5-20A), but the xenolith did not have quenched margins or pores (figure 5-20B). It was presumed that it was a basalt fragment that was picked up during emplacement of the layered gabbro.
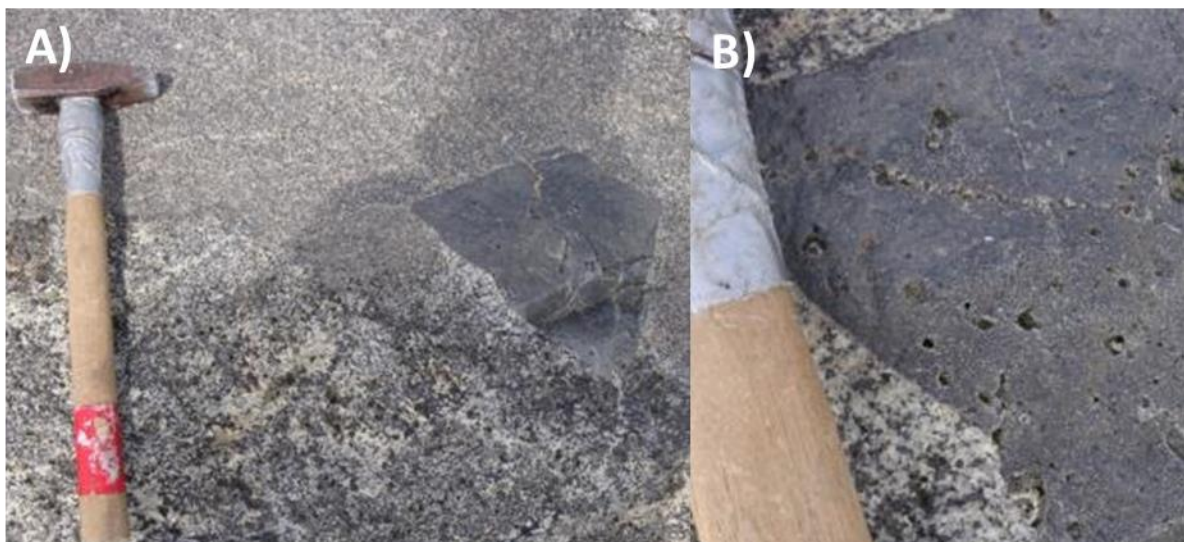
Figure 5-20: A shows the xenolith in the host rock at Vestrahorn, while B is a close up of the margins, which were not quenched.

Many of the felsic batches at Vestrahorn were interconnected, as was best seen exposed in the area shown in figure 5-21. These batches were fine-grained, with no distinguishable margins.

Figure 5-21: A shows a quite extensive, exposed area with interconnected felsic batches. B shows a close up of those batches, which were fine-grained.

5.1.2   Summary of rock structures

Columns with coarse-grained margins and fine-grained centre were the dominant pegmatite formations in the area that was studied. These were found both in medium-grained gabbro and in a coarse-grained gabbro host rock.

In the area, there was a dyke that consisted of fine-grained granophyric matrix, with darker, fine-grained margins. Additionally it had thinner dykes merging with it perpendicularly. The dyke lay in curves with pinch and swells structures.

Both the pegmatite columns and the dyke ended in a fine-grained granophyre without visible margins.

Big pegmatite bodies were found in the area. They were mostly comprised of pegmatite material, but towards the centre evolved into granophyric material. The margins of the bodies varied between straight and undulating. Felsic intrusions in the area postdated these pegmatite bodies.

Batches of variously-sized, felsic, fine-grained granophyre were observed throughout Vestrahorn. Where they were found close to pegmatite columns they had pegmatitic

margins. The batches were interconnected to a great degree over a substantial area and predate the felsic intrusions also found in the region.

The vein structures in the mine consisted of discontinuous, fine-grained granophyre matrix, but additionally it contained some sulphides. The vein was irregular and discontinuous, with fine-grained, dark, and badly-defined margins.

5.2 Petrography study

In total 23 samples were prepared from each layer of the UBS except from the LZa'. In addition, 7 of the samples were also prepared and analysed by XRF - 4 samples from the SH and 3 that presumably formed from a mafic, iron-rich liquid phase. For a short description for each sample, please refer to appendix B.

5.2.1　Minerals

The following describes the major minerals in the samples. Any estimate of the amount of minerals was based on the modal composition.

Plagioclase

Plagioclase was a ubiquitous primocryst in the UBS, especially as the most dominant mineral in the thin sections (about 50-60%) and formed a cumulate texture. The grains were subhedral to euhedral in the LZ', but evolved into anhedral grains in the UZ'. Most of the crystals had twinning (e.g. albite twinning and Carlsbad twinning). There was a decrease in grain size from the UZ' to the SH. An example of the plagioclase in the matrix can be seen in figure 5-22.
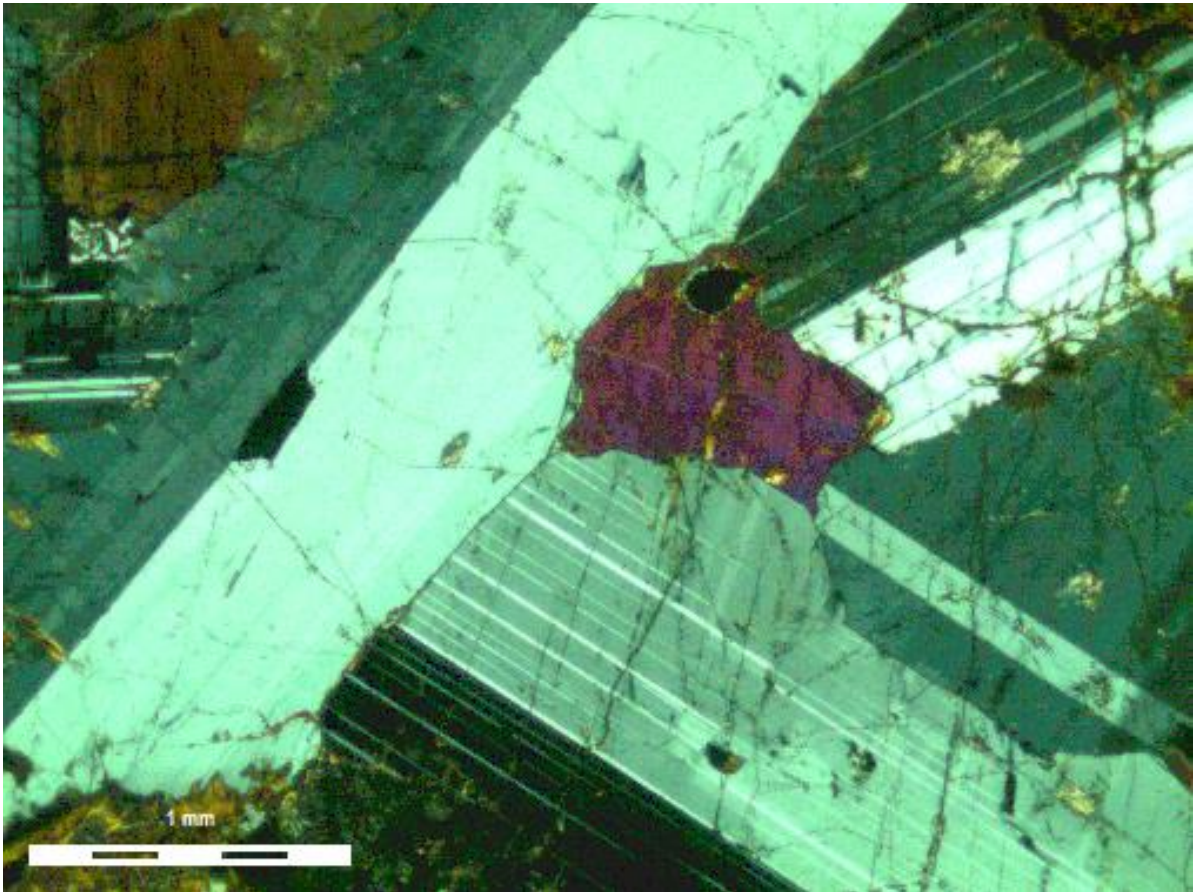
Figure 5-22: Plagioclase crystals from the LZc' (sample SK08-197) with an augite crystal, oxide inclusions and alteration. Cross-polarised light.

Olivine

Olivine was found sporadically throughout the UBS, except in the MZ'. Olivine was more common in the UZ' as larger, anhedral primocryst grains along with plagioclase and augite. It was highly altered in both series and in a few places there were even chlorite pseudomorphs of olivine. An example of olivine can be seen in figure 5-23.
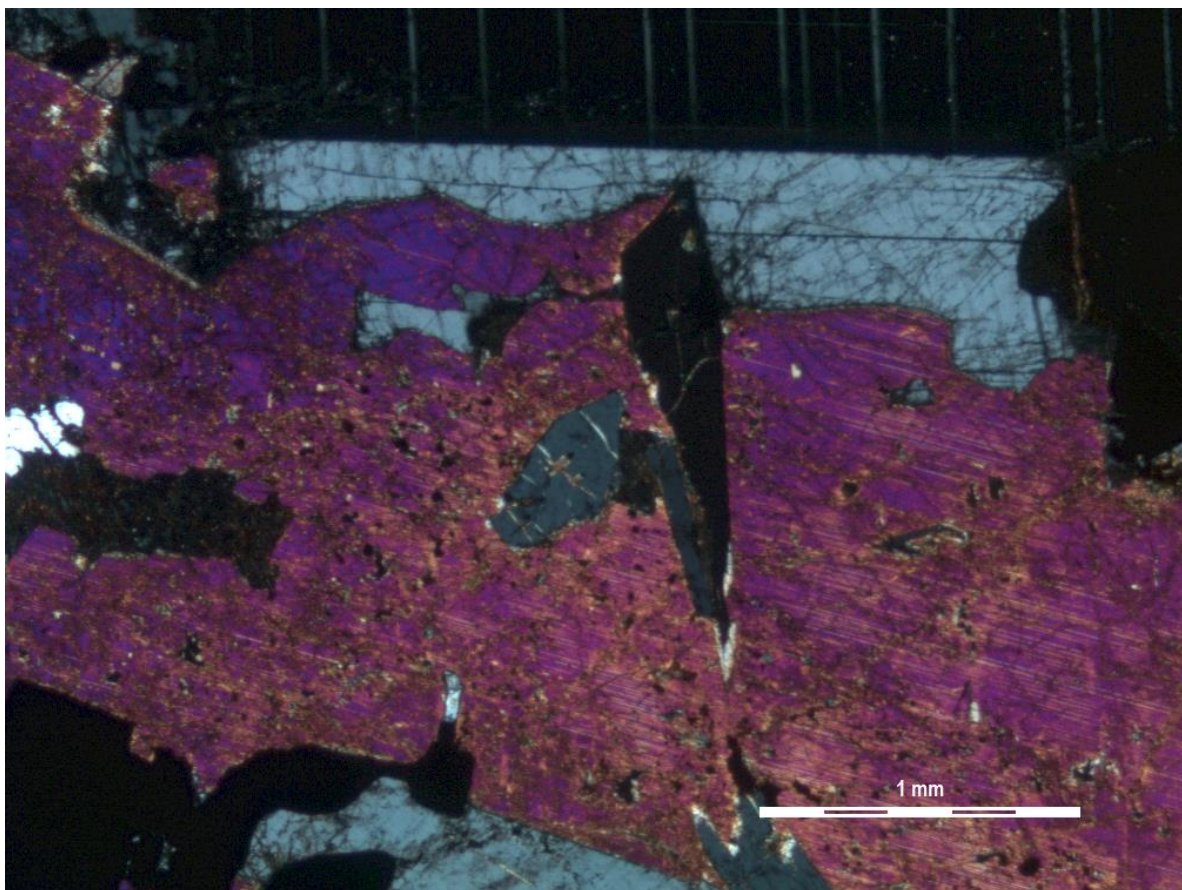
Figure 5-23: Anhedral olivine primocryst, surrounded by plagioclase primocryst and oxides from the UZb'. Additionally it contained apatite inclusions (sample SK08-165). Cross-polarised light.

Pyroxene

Pyroxene appeared to have formed after plagioclase, from interstitial liquid, as the crystal growth was constrained by cumulus plagioclase primocrysts. It was found throughout the UBS and was the second most common mineral (10-30%) in the LZ' and MZ'. Pyroxene crystal abundance increased downwards, but the crystal-size decreased.

In the UZ', the cumulate and intercumulus consisted of lath-shaped plagioclase, along with pyroxene which forms oikocrysts. These pyroxenes also had resorption textures.

Augite was the most common pyroxene (Ca-rich). The crystals contained exsolution lamellae of orthopyroxene (figure 5-24). Ferrohedenbergite was not found, but the UZ' and SH contained needle-shaped pseudomorphs, filled with alteration minerals, which probably were originally ferrohedenbergite.
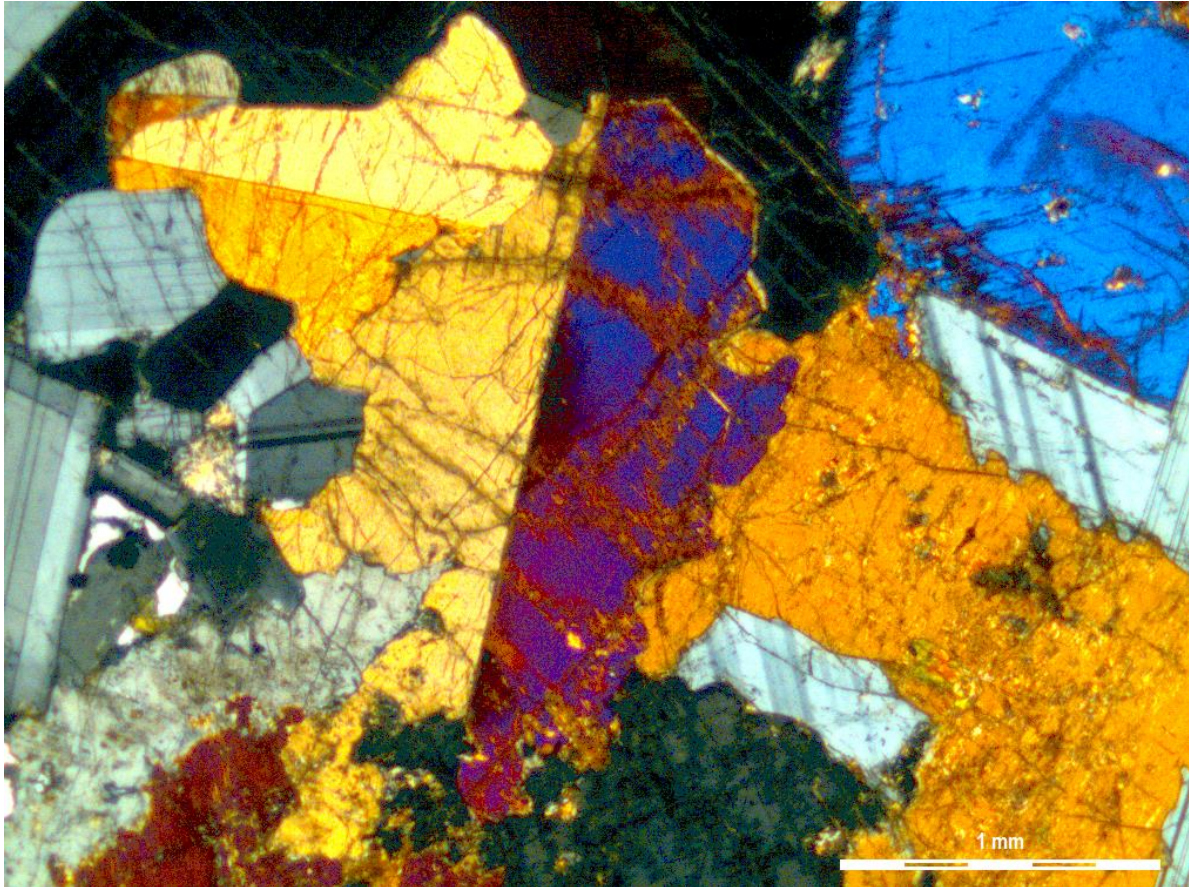
Figure 5-24: Augite crystals surrounded by plagioclase primocrysts from LZc' (sample SK08-198). Cross-polarised light.

Apatite

Apatite was an early phase mineral as it was found as subhedral to euhedral grains and included in different minerals, everything from primocryst to the latest formed granophyre. It was abundant throughout the UBS, but there was an increase in the crystal size and abundance in the UZ'. An example of apatite, located within olivine, can be seen in figure 5-25.
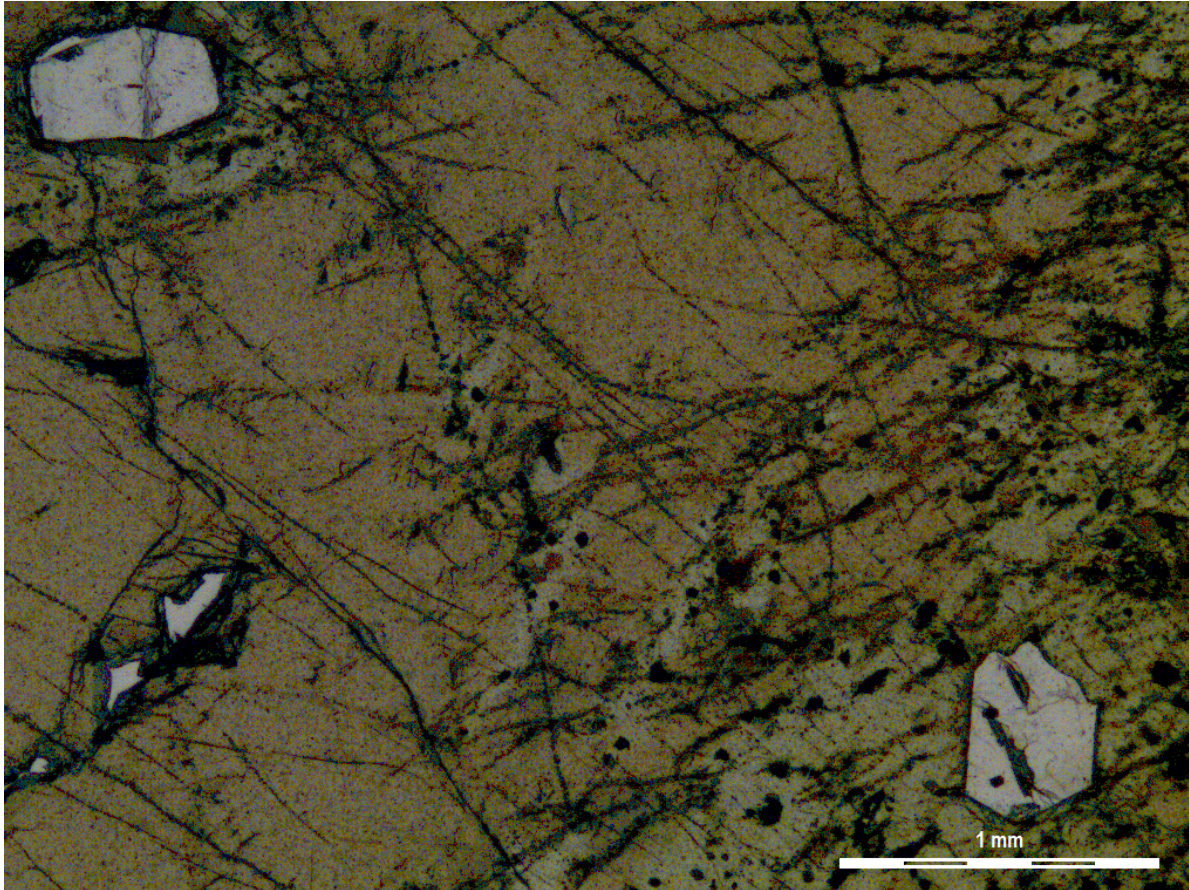
Figure 5-25: Two apatite crystals surrounded by an olivine primocryst (sample SK08-165). Normal light.

Oxides

The oxides were ubiquitous in the UBS. They consisted of magnetite, ilmenite and rutile, the last being alterations of ilmenite. The ilmenite formed anhedral aggregates that occurred as skeletal to dendritic grains throughout the UBS, with a marked increase in the LZc' and MZ', while the magnetite was found as exsolution lamellas within the ilmenite. Many of the oxide crystals contained interstitial pockets with aggregates of small, mixed minerals. Rutile formed small grains, mostly in veins around oxides or olivine, from the MZ' to the SH. An example of a skeletal to dendritic magnetite and ilmenite intergrowth can be seen in figure 5-26.

Samples from the SH contained visible oxide needles in the hand sample (>2 cm long), which were composed of numerous small, anhedral grains.
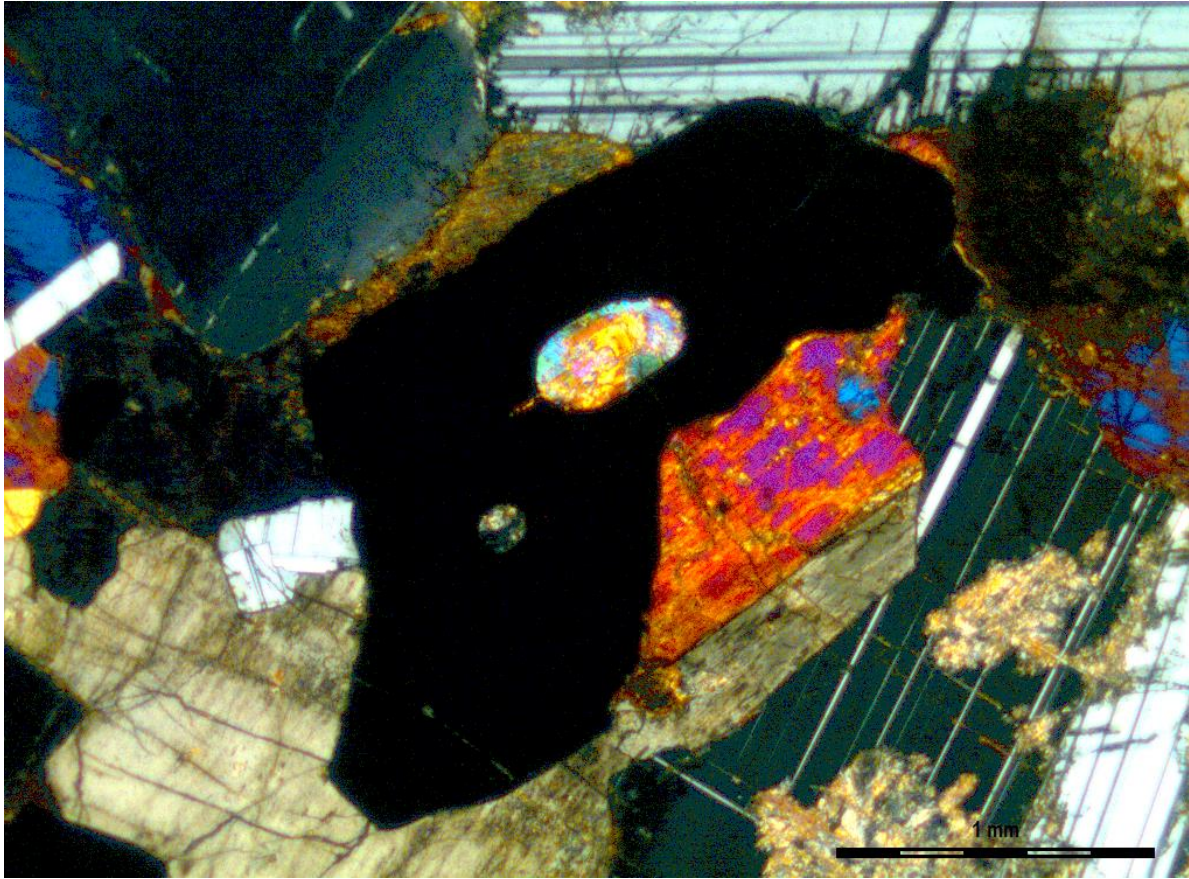
Figure 5-26: Oxide from the LZc' (sample SK08-198), with an inclusion of silicate aggregates. Cross-polarised light.

Accessory minerals

Quartz and alkali feldspar constituted only a small part of the matrix in the thin sections. It was mostly found as anhedral grains, as a part of granophyric intergrowths that formed from the intercumulus liquid (figure 5-27). There was a general trend for a steady increase in granophyric masses, down from the LZ' to the SH. An example of this can be seen in figure 5-32.

Titanite occurred scattered throughout the UBS as subhedral to euhedral grains. Biotite was a rare mineral in the UBS but occasionally formed as an alteration product.
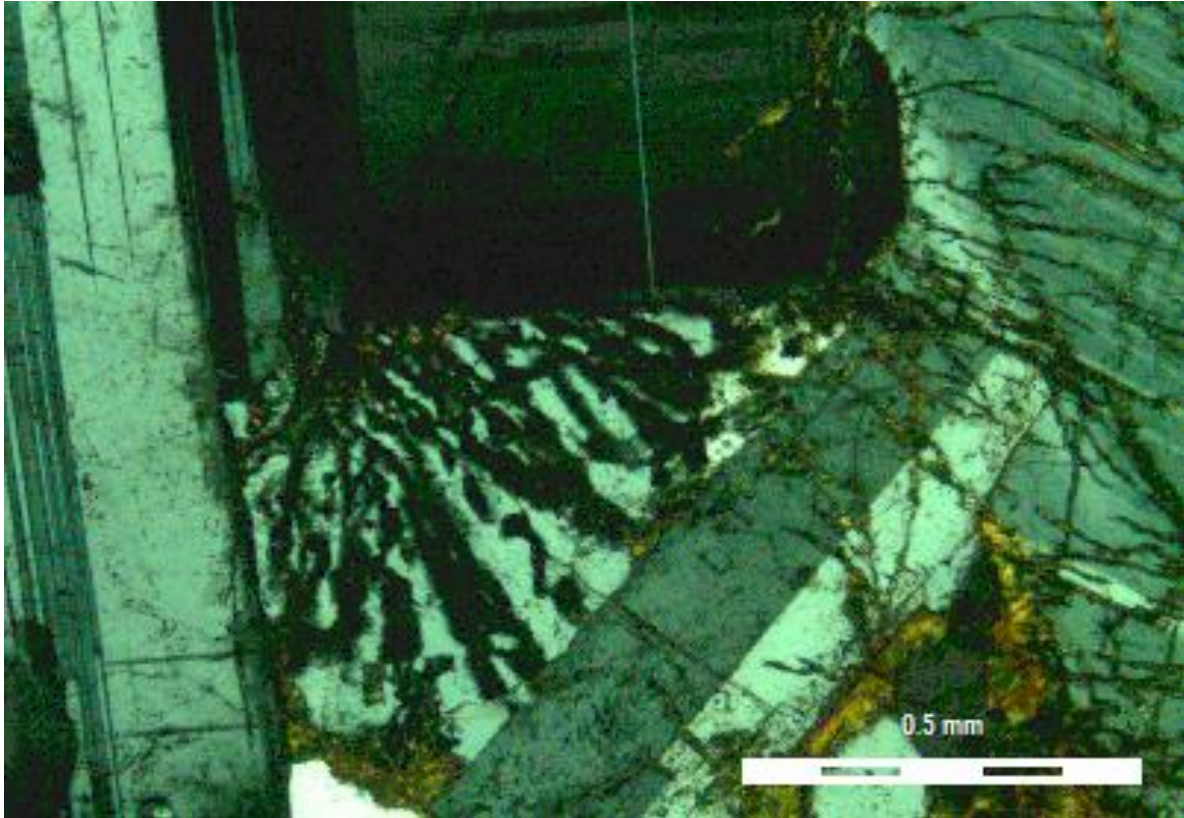
Figure 5-27: Granophyre masse, which is composed of quartz and plagioclase intergrowths. The granophyre formed from intercumulus liquid between plagioclase primocryst (sample SK08-200). Cross polarised light.

In addition sulphides were minor constituents throughout the UBS. Pyrite and chalcopyrite were found throughout the UBS as small anhedral grains.

5.2.2   Alteration

The samples were often highly altered. The most common alteration was sericitisation of plagioclase primocrysts, but other alteration products were serpentine, rutile, amphibole, calcite, chlorite and ilvaite.

The sericitisation occurred in clusters of plagioclase throughout the UBS (figure 5-28). Rutile formed clusters of small grains around oxides or as veins around olivine, serpentinization was found as a complete alteration of crystals or as veins in the matrix, calcite was formed from alterations of single minerals and chlorite found in thin alteration veins or as a complete alteration of crystals.

There was an increase in alteration down from the LZ' to the SH.
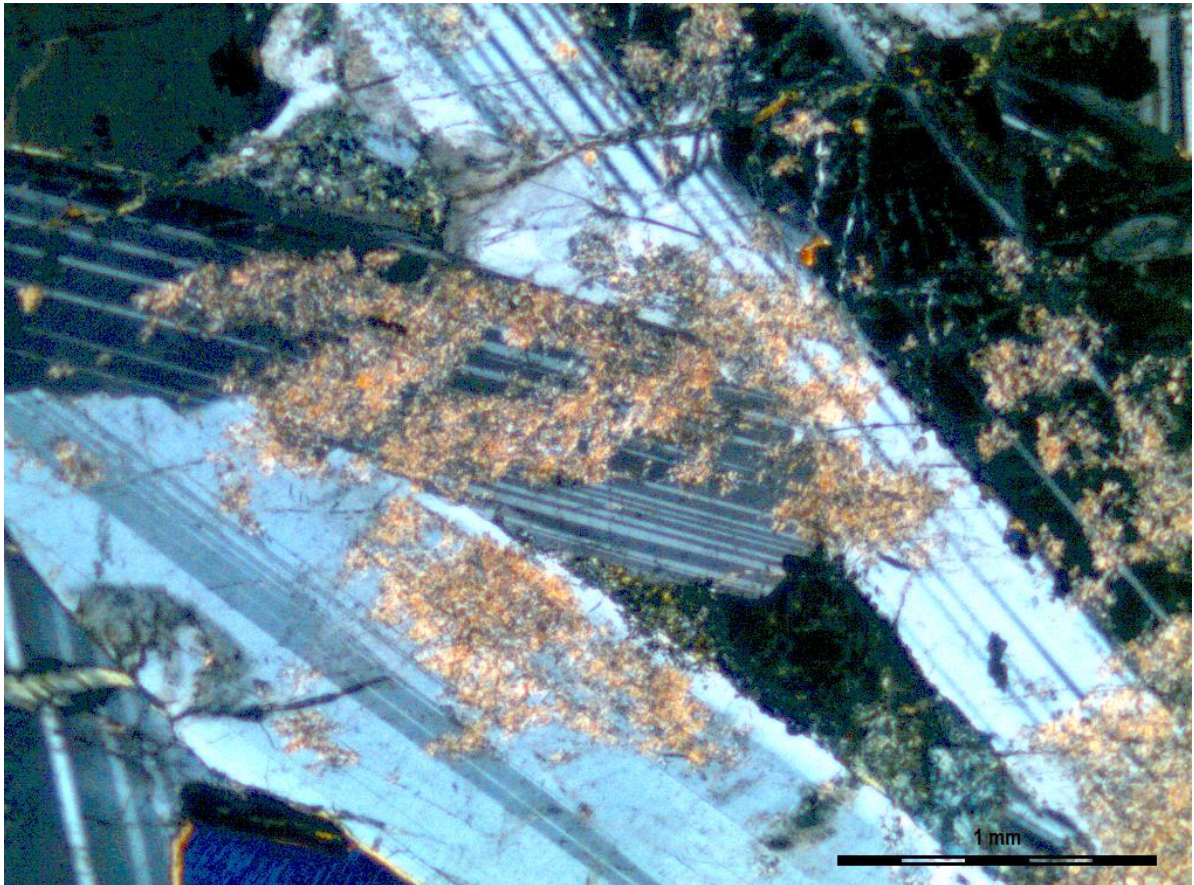
Figure 5-28: Sericitisation in a plagioclase primocryst from LZb' (sample SK08-201). Cross-polarised light.

Ilvaite has previously been observed in the upper part of the Skaergaard intrusion (Naslund et al., 1983), but seems mostly unnoticed in most petrography studies. Ilvaite is an alteration mineral, sometimes associated with hydrothermal fluid. The properties that were used to identify it include its opaque nature, which partially lets light pass through when the light intensity was set to maximum, low reflectance compared to ilmenite, weak pleochroism, and intense anisotropy (Picot and Johan, 1982). It can be seen in figure 5-29.
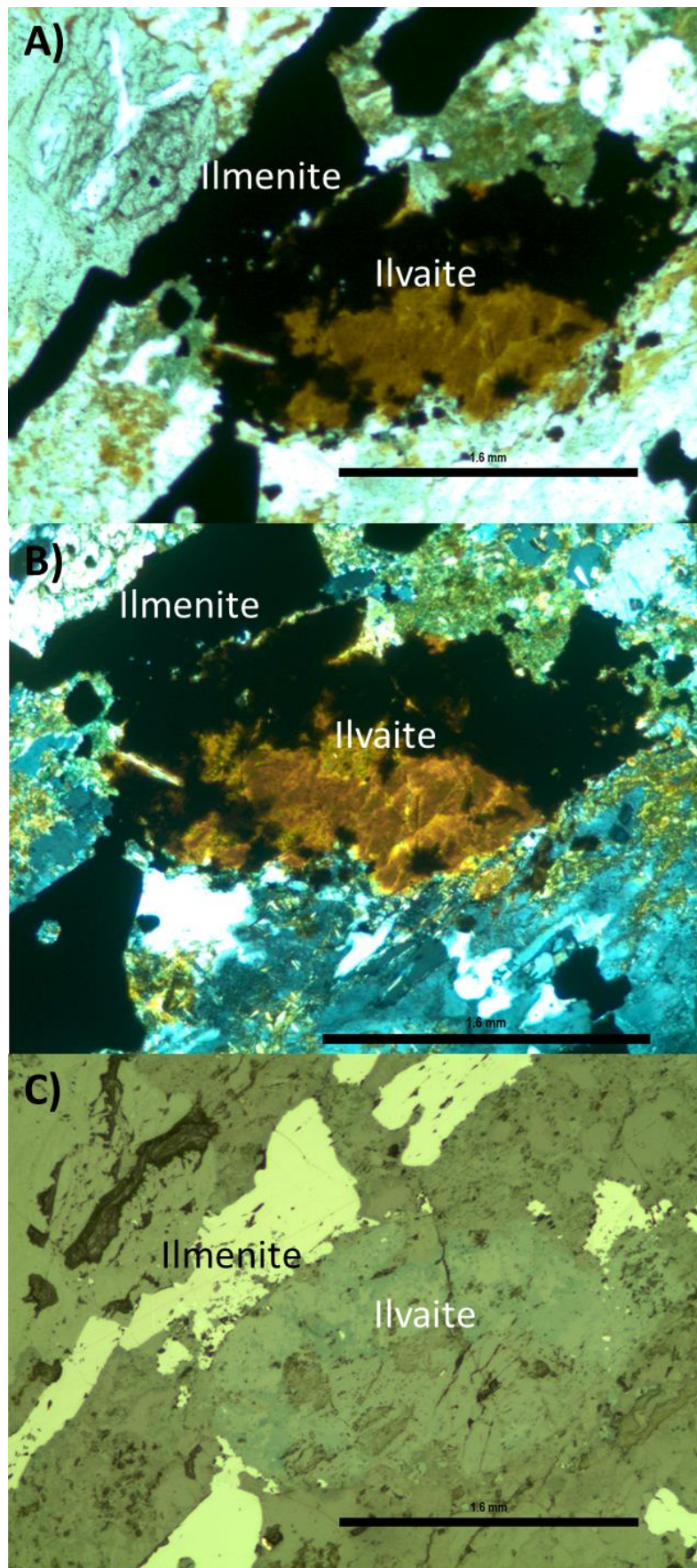
Figure 5-29: Alteration mineral identified as ilvaite (sample SK11-51). A) Normal light, B) cross-polarised light, C) reflected light.

5.2.3 Granophyre textures

Granophyre textures consisted of quartz and feldspar intergrowths, crystallizing simultaneously at the eutectic granitic minimum (figure 5-30). The granophyre masses constituted an increasing amount of the matrix in the samples from the LZ to the SH, as they changed from sporadic interstitial aggregates at the top of the LZ' (c. 2%) to a major rock forming element in the UZ' and the SH (c. 55%). Figure 5-32 shows the increase in granophyre masses.

In the SH and the samples from Brødretoppen the quartz and feldspar intergrowths evolved from granophyric, myrmekite or hieroglyph texture into a more spinifex-like texture (figure 5-31).
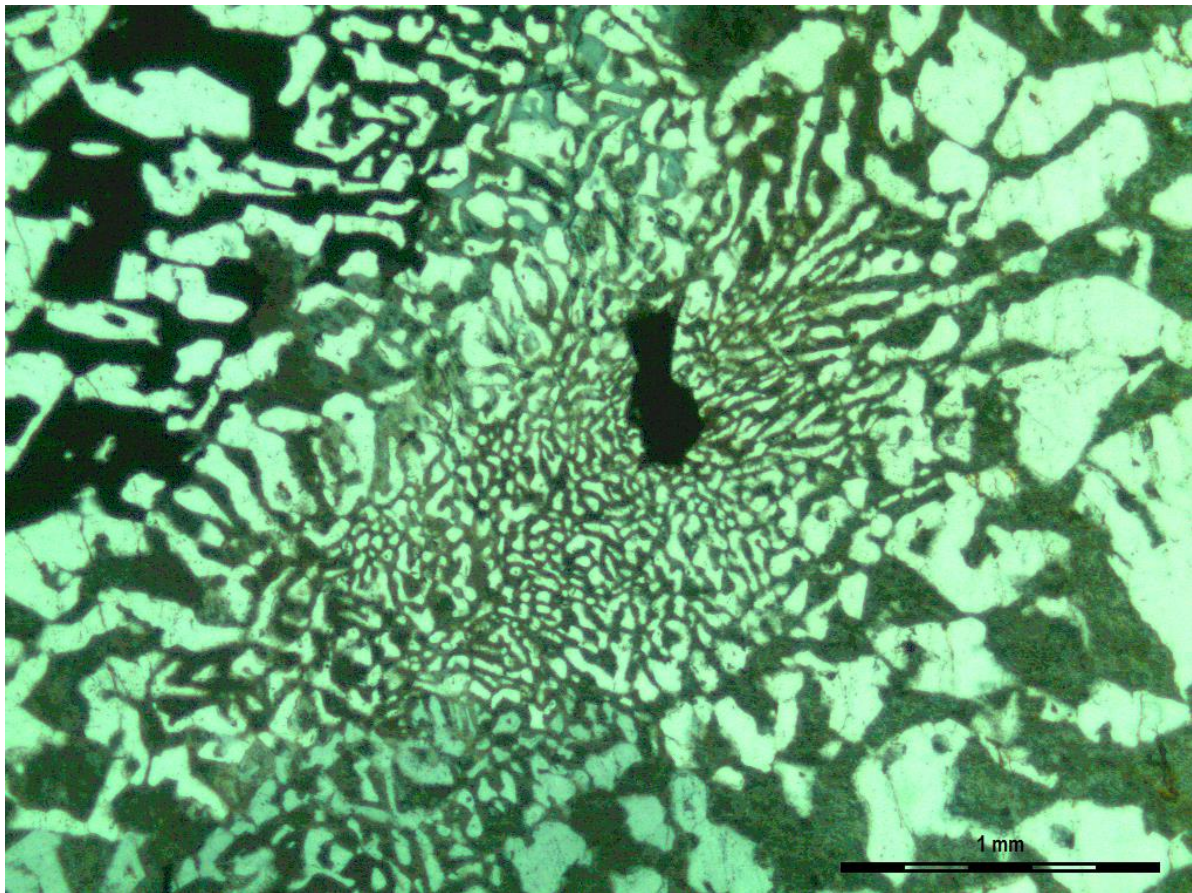
Figure 5-30: Granophyre masse with an oxide in the centre. This sample (SK08-110) was from the SH where there was a high abundance of granophyric masses. Cross-polarised light.
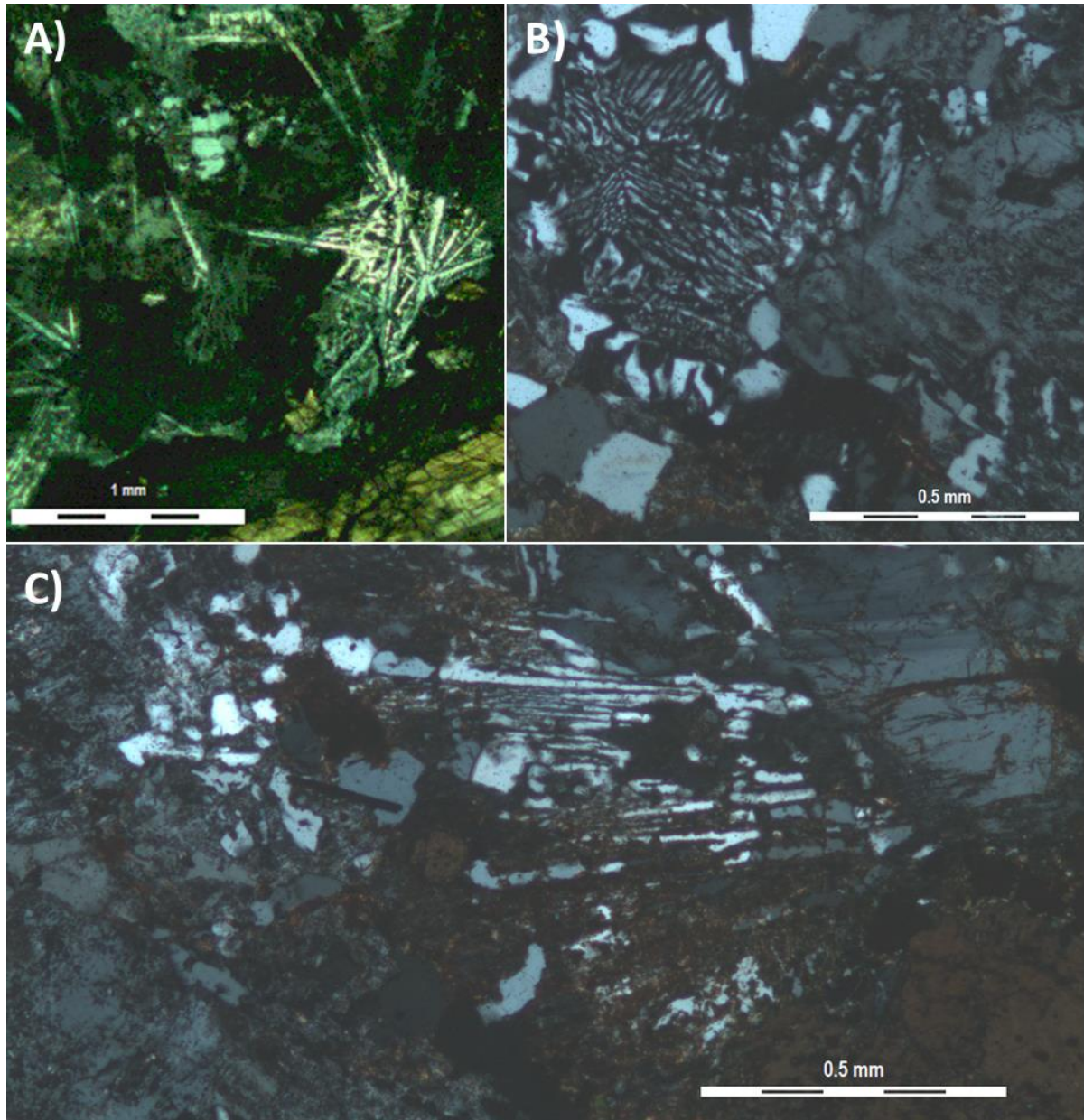
Figure 5-31: A shows a spinifex-like texture that consisted of quartz found in the SH, while B shows how the quartz and feldspar intergrowths form a more hieroglyph-like texture. C shows how the quartz formed elongated neddle-like structures (SK11-51). Cross-polarised light.

5.2.4   Fluid inclusions

The fluid inclusions that were measured were located in the quartz, in granophyre masses, which have been described above. The quartz contained both primary and secondary FI, but only primary inclusions were measured. There was no visible difference in the shape or occurrence between primary and secondary inclusions, except the secondary inclusions formed trails of FI through the crystal.

88

The FI contained two phases, vapour and liquid. Some solid phases were occasionally observed, but they were rare. The FI were subhedral to euhedral, with a few exceptions being anhedral in shape, and an average diameter of about 10 µm. The majority of the FI contained 10-40 vol.% vapour, although some contained up to 80 vol.% vapour. A short summary of FI can be found in figure 5-32.
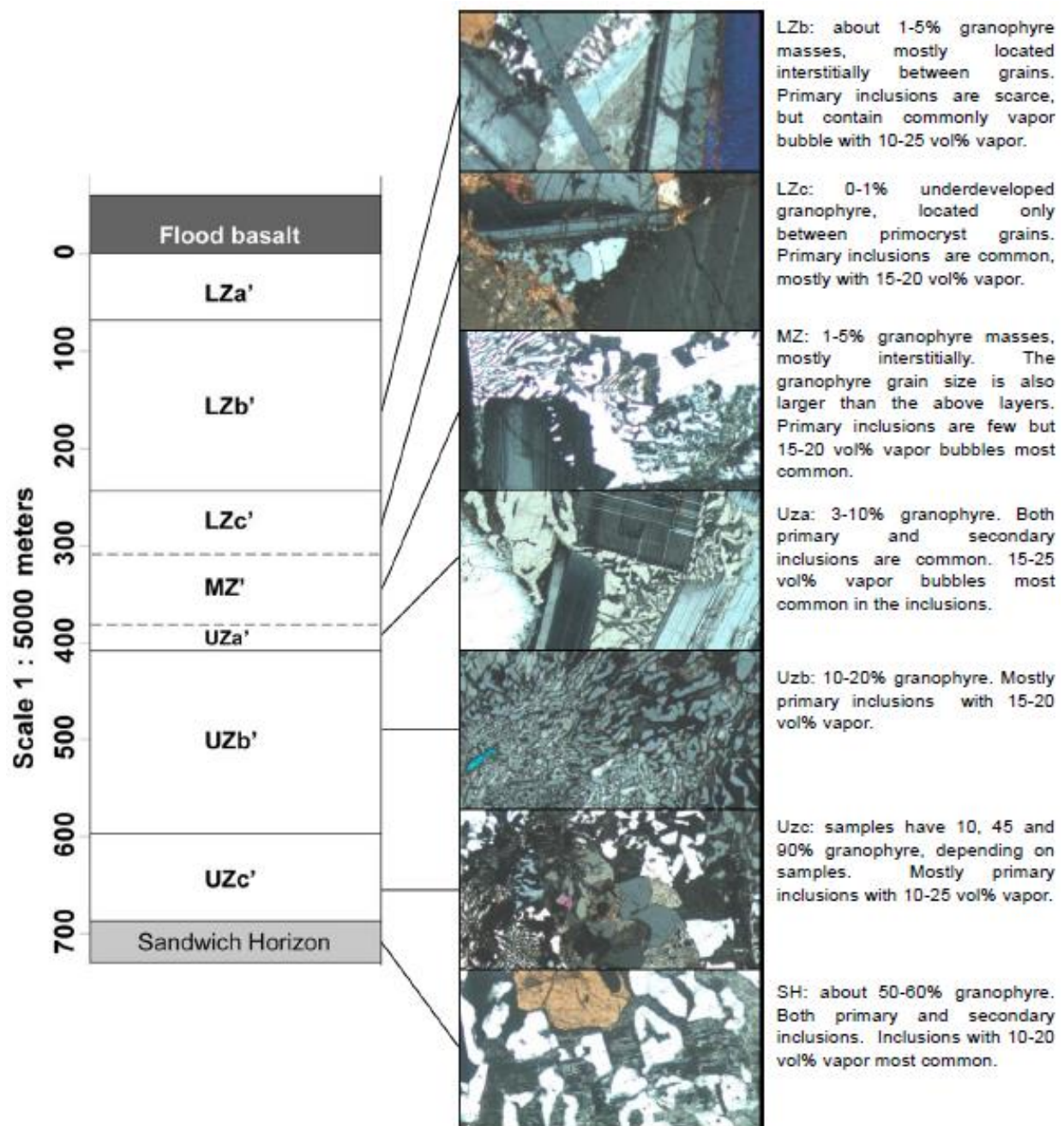
Figure 5-32: There was a general trend of increased amount of granophyre masses in the UBS, from the upper contact towards the centre. Also included is a short summary of FI.
Source: Stratigraphy from Salmonsen and Tegner (2013).

5.3 Geochemical analyses

The results from the XRF analysis are in appendix C. The samples were from the SH and a possible iron-rich intercumulus liquid that was part of a gabbro pegmatite from the UZa'. The latter was thought to have possibly formed as an separate immiscible phase from the granophyre melt. Two XRF samples were prepared and analysed from each of the samples.

Both FeO and Fe_2O_3 were indistinguishable with the XRF analyses and therefore marked as Fe_2O_3 in the results.

There was an obvious chemical difference between samples from the SH and the iron-rich gabbroic pegmatite, which was visible in both main and trace elements. The iron-rich phase samples were rich in Fe_2O_3 (37.47-55.37 wt%), TiO_2 (10.11-17.55 wt%) and MgO (2.69-6.16 wt%), while the SH was rich in SiO_2 (60.55-61.5 wt%), Al_2O_3 (10.34-11.1 wt%) and alkalis (Na_2O and K_2O total 5.68-6.23 wt%). In addition there was also a noticeable difference between the two iron-rich samples, as the sample that was collected in 2009 was richer in iron (51.11-55.37 wt% compared to 37.47-38.63 wt%) and titanium (17.27-17.55 wt% compared to 10.11-11.7 wt%).

The SH samples plot within the tholeiitic, or subalkaline, field in a total alkalis vs. silica plot, and were derived from the evolution of a more primitive magma, while the iron-rich phase did not plot due to lack of silica (figure 5-33). The SH samples were in addition peralkaline, while the iron-rich phase was metaluminous (except for 458291-B which was peralkaline).
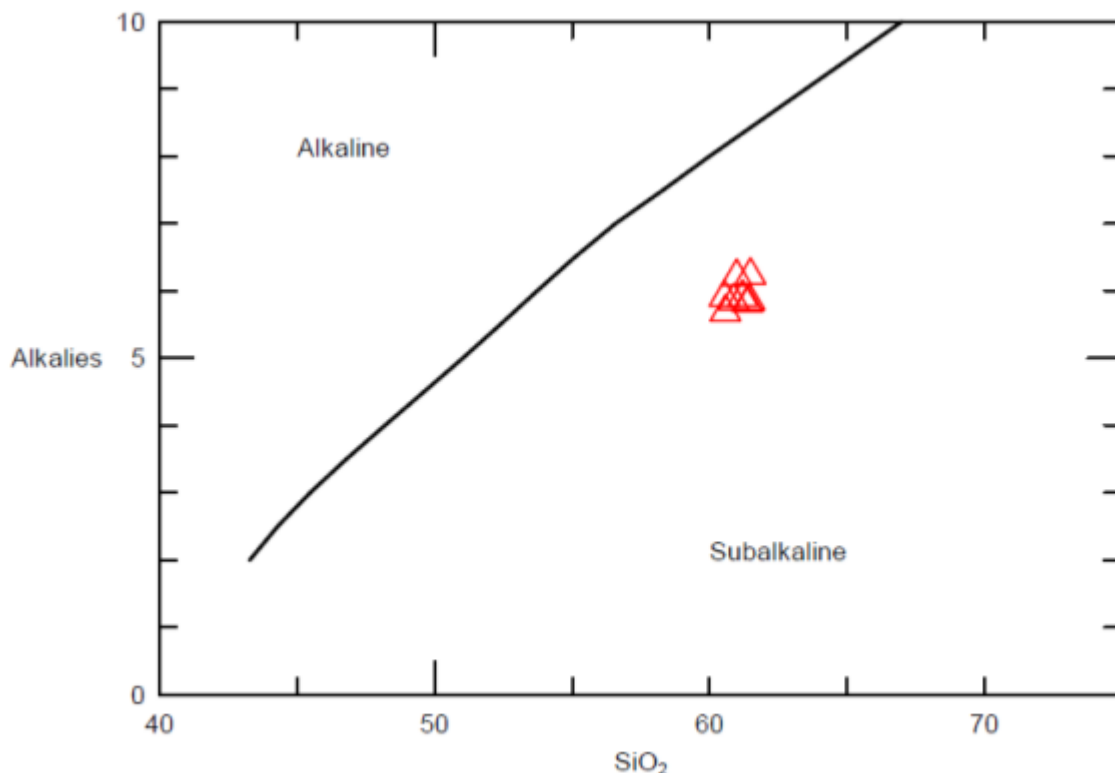
Figure 5-33: Alkalis vs. silica plot which shows how the SH samples plot within the tholeiitic field. The iron-rich phase did not plot on the graph.
Source: (Irvine and Baragar, 1971).

The iron rich phase was obviously relatively primitive compared to the SH when an AFM diagram of the tholeiite evolution trend was plotted (figure 5-34). The iron-rich phase was more iron- and alkali-rich than the typical tholeiitic evolution trend, but the Skaergaard evolution trend generally plot with a higher FeO content than the tholeiitic evolution trend. In addition the SH was not as evolved as the most evolved samples used to plot the Skaergaard evolution trend, but it should be the last melt to crystallize, as it was formed in the centre of the intrusion during its crystallization inwards from the margins.
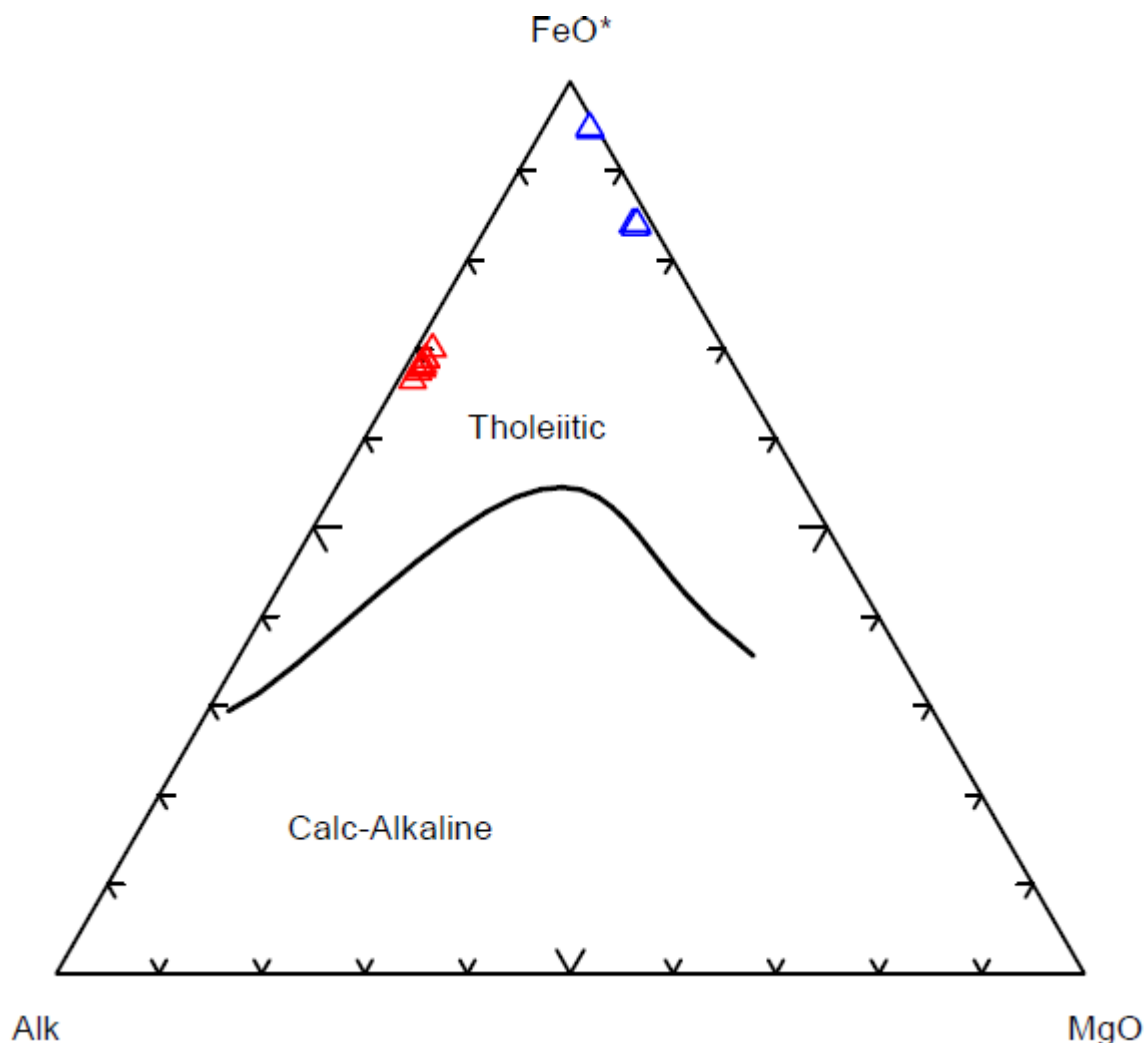
Figure 5-34: An AFM diagram. The red triangles are the SH samples, and the blue triangles from the iron-rich phase samples. The tholeiite evolution trend decreased in alkalis with evolution (moves from right to left). FeO is total iron, and Alk are the alkalis or K_2O+Na_2O.
Source: (Irvine and Baragar, 1971).

The immiscibility field for iron-rich and silica-rich glasses from theoleiitic rocks had been determined but was badly established. Here the samples had been plotted on a ternary diagram, without the immiscibility field which lies at about 20% $Na_2O+K_2O+Al_2O_3+MgO$ and

between 50-90% $Fe_2O_3+MnO+TiO_2+CaO+P_2O_5$, and the result can be seen in figure 5-35. The diagram was split into elements which concentrated in the iron-rich phase ($Fe_2O_3+MnO+TiO_2+CaO+P_2O_5$) and elements that concentrated in the silica-rich phase ($Na_2O+K_2O+Al_2O_3+MgO$).
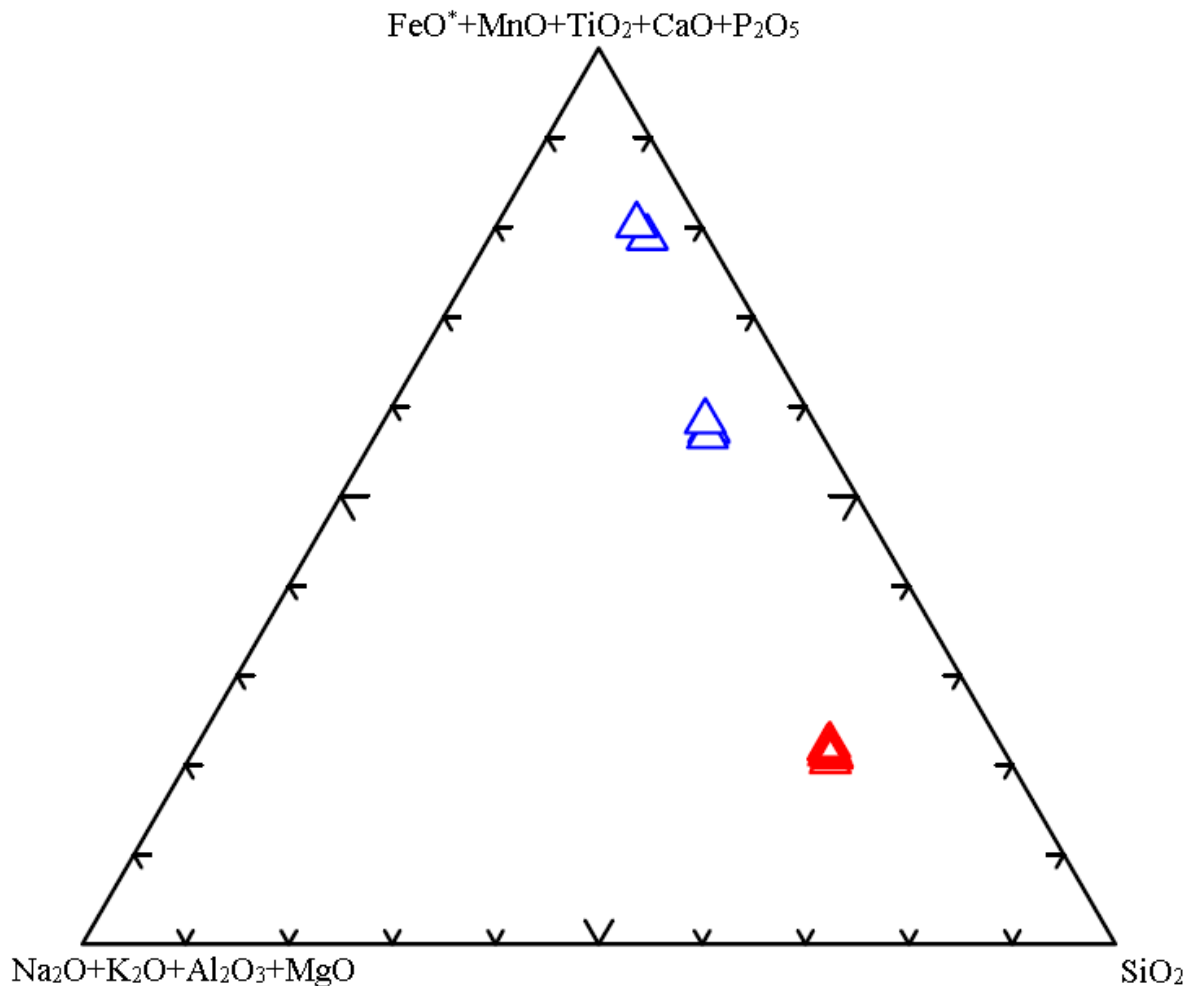
Figure 5-35: Ternary diagram as used by (Philpotts, 1982), which shows some similarities. The red triangles are the SH samples, and the blue triangles are the iron-rich phase samples.

The samples were generally enriched compared to the normal MORB (Mid-Ocean Ridge Basalt) as seen in figure 5-36. There was no trend in enrichment neither in the SH or the iron-rich phase when it comes to the LIL or the HFS elements. The iron-rich phase shows a jagged pattern.

The SH was generally enriched in all elements except Ti, while the iron-rich phase was enriched in everything except Sr, Y and for some samples in P. The iron-rich phase was in

addition generally more depleted than the SH except in Ti, and for some samples in Cs, U and P.

It was evident that the samples from the SH and the iron rich-phase were compositionally non-identical in terms of incompatible trace elements and they had evolved since the magma was emplaced into the crust.
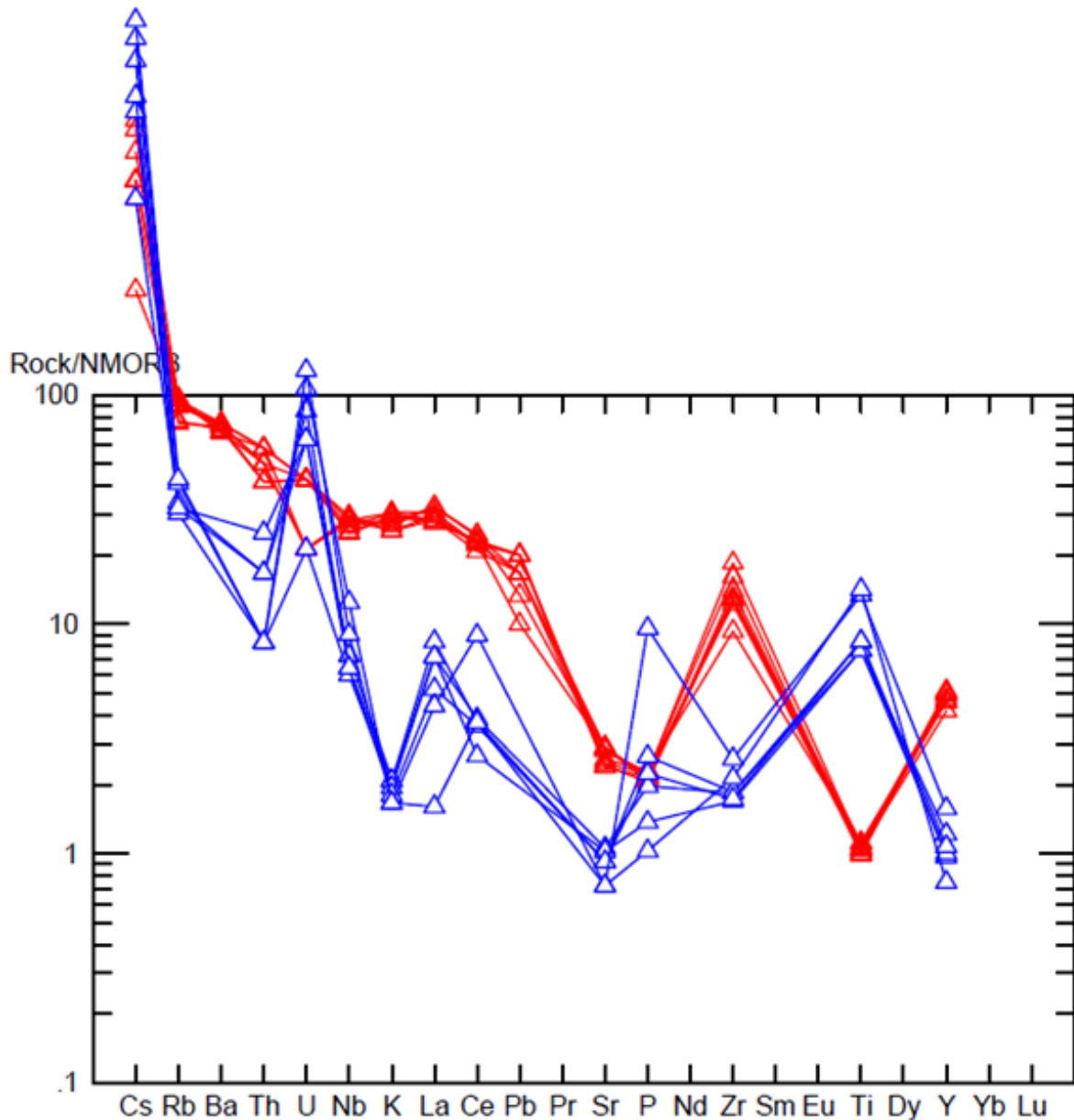
Figure 5-36: A normalized primitive mantle spider diagram for the samples. The samples from the SH are red, and the samples from the iron-rich phase are blue. Both were enriched compared to normal MORB.
Source: (Sun and McDonough, 1989).

The zirconium (Zr) content in the samples was quite high in the samples from the SH, reaching a value of over 1300 ppm in the SH. This was due to Zr being immobile and incompatible element, which ends up in the final most differentiated melt.

Figure 5-37 shows Harker variation diagrams of the samples. Generally Harker diagrams are used to illustrate differentiation trends for a rock series. Not enough samples were analysed to be able to distinguish whether the samples followed a certain differentiation trend. In general the samples contained more iron and less silica than expected. Nevertheless, the SH was the end product of the differentiation of the Skaergaard parental melt and the plots were mostly meant to illustrate the subtle variations in the composition of the SH. Typically Al_2O_3, MgO, Fe_2O_3 and CaO decrease with increasing SiO_2 (with evolution), but from the samples it was evident that the Al_2O_3 and sometimes CaO did not decrease.

The total FeO content in the SH samples correlated with forward modelling which has also been done for the Skaergaard liquid line of descent, using the liquidus melt composition (Thy et al., 2009). However the iron-rich samples were too poor in SiO_2 to plot in the same model.
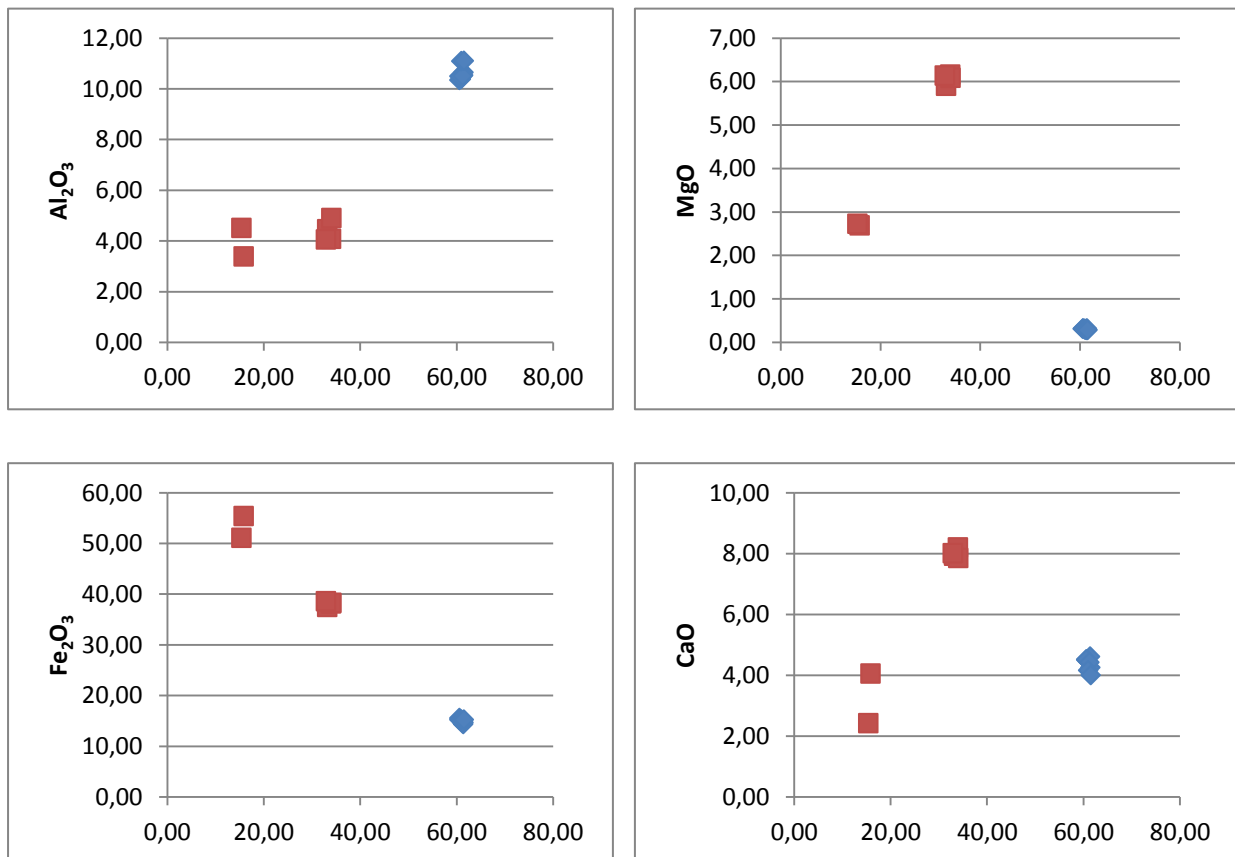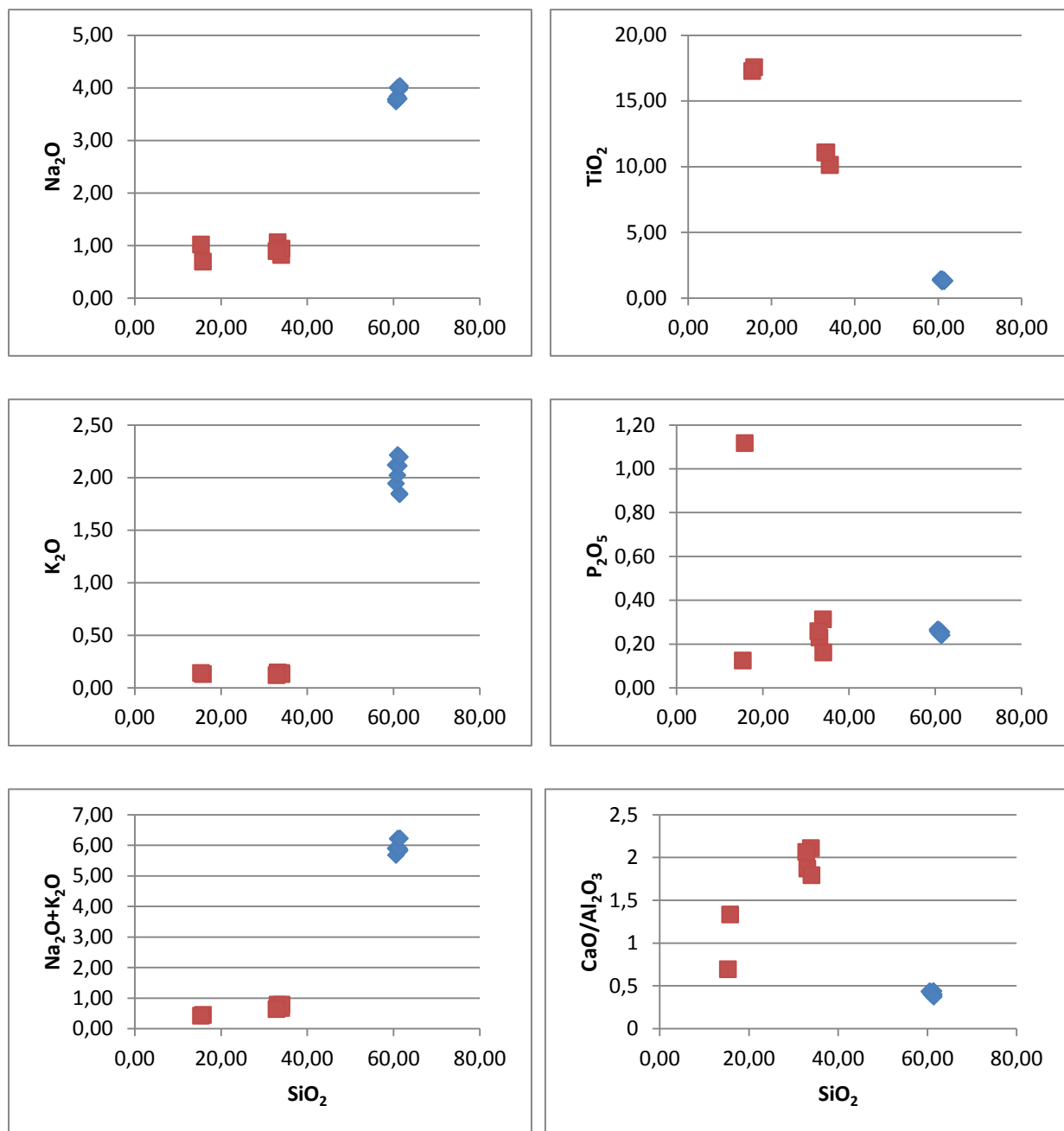
Figure 5-37: Harker diagrams display the variations in some major oxides vs. SiO$_2$ for the analysed samples (in wt. %), where the samples from the SH are blue and the samples from the iron-rich phase are red.

5.4 Fluid Inclusions

The optical properties of the FI were previously described in chapter 5.2.4. The microthermometry measurements were performed on 7 samples in total (table 4.1). Only fluid inclusions considered to be primary FI were measured. The fluid inclusions measured were located in quartz, in the last crystallizing granophyre masses. For a list of all

temperature measurements refer to appendix D. Depending on the amount of measureable FI, between 27-71 measurements were performed on each sample.

Based on visual interpretation, only one type of FI was identified at room temperature, although there were some variations in vapour bubble volume. They mostly had the same visual properties during heating and cooling, and an example of this can be seen in figure 5-38. Most of the FI had similar hydro-halite formations and homogenization temperatures, but the only visible ice melting phase was measured in FI in the UZc' (sample SK08-105) (except for 1-2 measurements in the LZc' and the UZb'). Few FI had sluggish melting of hydro-halites, which resulted in the melting temperature being considerable above 0°C.

Based on the melting temperature of ice the FI were in the H_2O-NaCl system, as previously described by Larsen (Larsen et al., 1992), and contained minor amounts of CH_4.
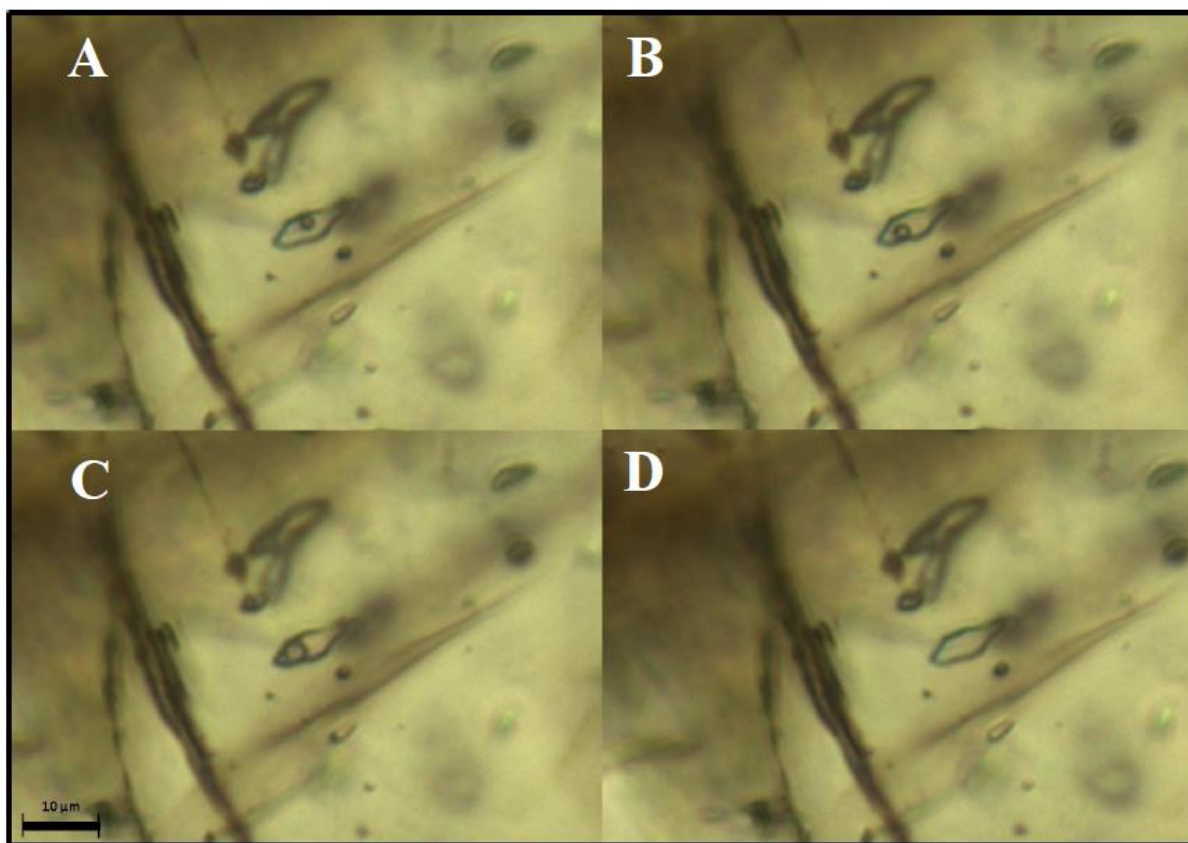
Figure 5-38: Example of fluid inclusion during measurements. A is during freezing, B is at room temperature, C is during heating, and D is after homogenization.

By assuming that the volatiles in the UBS all have the same salinity, which can be calculated from the melting temperature of ice, it was equivalent to 24.87 mass% NaCl during the

crystallization of the granophyric melt. That means that the FI in the UBS were more saline than the FI in the LS, or about a difference of 2-7 mass% NaCl (Larsen et al., 1992).

If the salinity was calculated based on hydro-halite melting for each and every layer in the LS, the average salinity was 26.14 mass% NaCl, which was even higher than calculated from the ice melting temperature. There was a 3-9.5 mass% NaCl difference from what has been previously observed in the LS (Larsen et al., 1992).

Both salinity results have been plotted in figure 5-39. There, it was evident that both salinities were close to the salinity of the peritectic point in the H₂O-NaCl binary phase diagram, which was in accordance if the hydro-halite melting of the FI occurred just a few degrees away from the peritectic point.
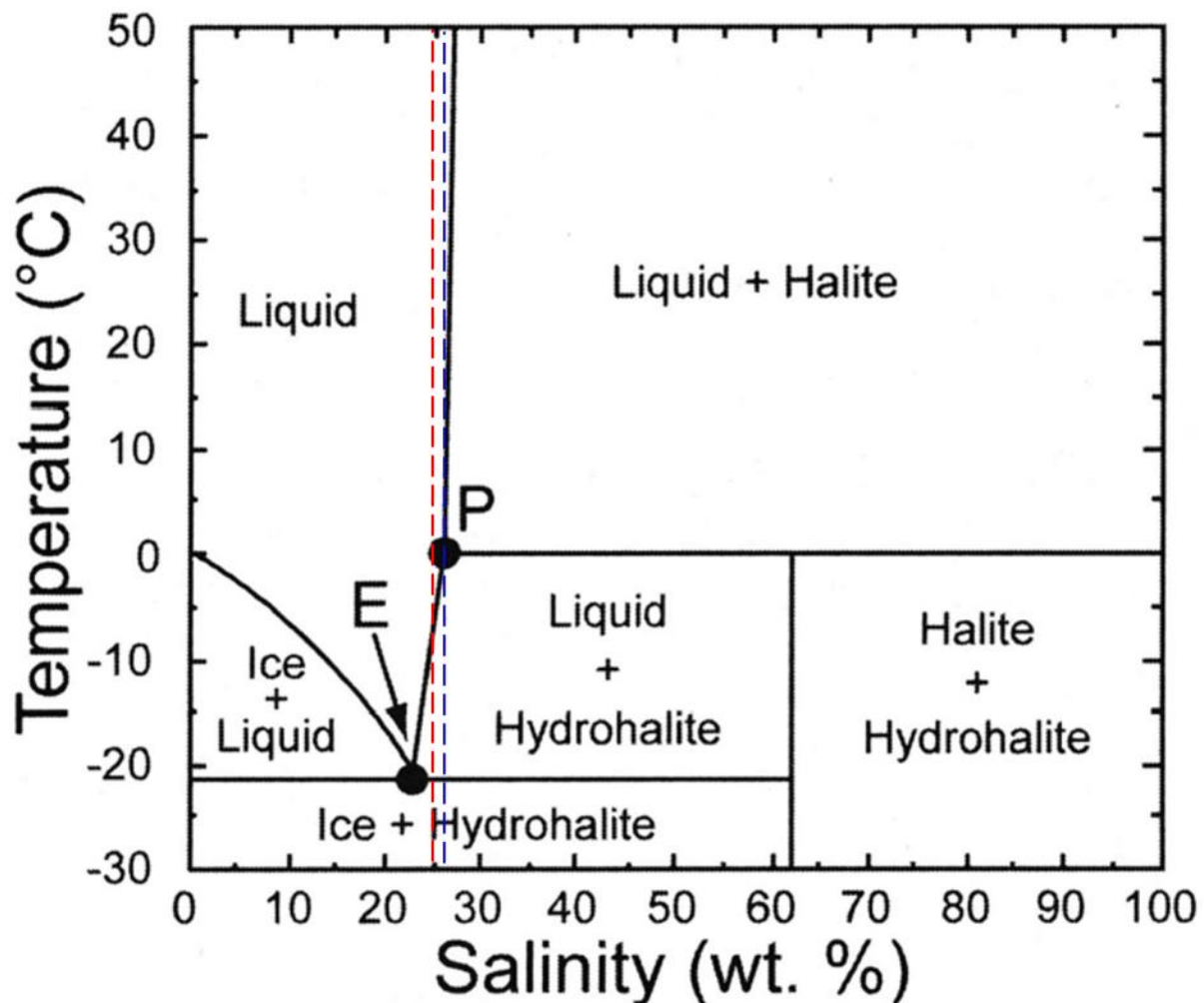
Figure 5-39: Phase relations in the H2O-NaCl system along with the calculated salinity of the FI.
Source: (Samson et al., 2003).

The results from the salinity calculations can be seen in table 5.1. The gradual increase in fluid density was observed in the LS but not in the UBS.

Table 5.1: The salinity in each layer in the UBS. Tmice are the results from the melting temperature of ice. TmHydrate are the result from the hydro-halite melting.

Layer	Salinity from Tm_{ice} in mass%	Salinity from $Tm_{Hydrate}$ in mass%
LZb'	-	26.14
LZc'	23.68	26.20
MZ'	-	26.24
UZa'	-	26.15
UZb'	22.69	26.14
UZc'	25.01	26.09
SH	-	26.05

Homogenization of the FI happened in the liquid phase for the majority of the fluid inclusions, although few had homogenized in the gas phase. The homogenization temperature was the lowest possible formation temperature for the FI. The homogenization temperature for the FI can be seen in table 5.2. As seen there the lowest homogenization temperature was at 178.8°C while the highest was at 305°C, which was quite a big temperature gap. Even bigger temperature gap was found within each layer, but the temperature appeared to correlate to the size of the vapour bubble, as FI with bigger vapour bubble generally homogenized at a higher temperature than FI with smaller vapour bubble. In total 8 FI did not homogenize before 400°C, and these normally had vapour bubble volume above average. The FI that did not become homogeneous before 400°C were not included in the following results as the exact homogeneous temperature was not known.

Table 5.2: The median homogenization temperature at each layer in the UBS.

Layer	Homogenization temperature (°C)
LZb'	246.95
LZc'	226.55
MZ'	178.8
UZa'	305
UZb'	232.1
UZc'	255.3
SH	258.5

The isochores for both salinities were steep, but had a similar slope to the isochores in the H_2O-NaCl system at 25 wt.% NaCl (Bodnar and Vityk, 1994). Figure 5-40 shows the isochores calculated from the melting point of ice, while figure 5-41 shows the isochores calculated from the melting point of hydro-halites.
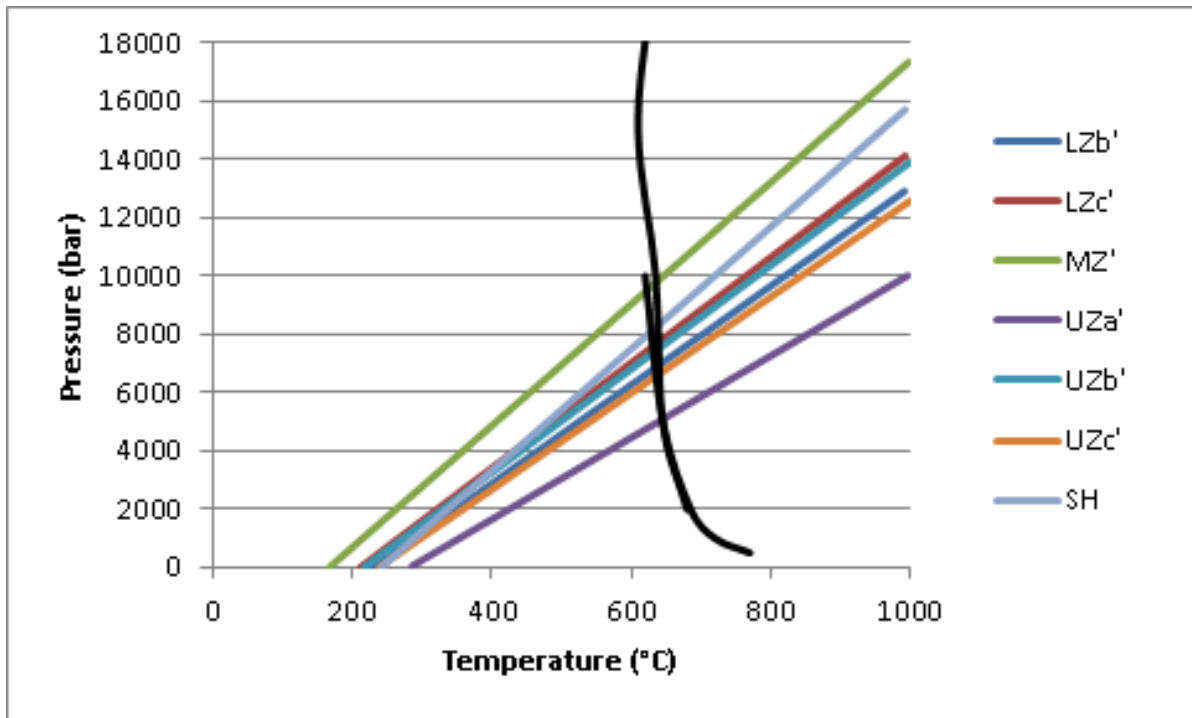
Figure 5-40: Isochores for the FI in the UBS calculated from the melting temperature of ice. The granitic minimum melt field is shown for quartz-albite-orthoclase system at H$_2$O saturation conditions and with 0-5 mol% CH$_4$. The granitic minimum melt lines are based on solidus and liquidus experiments.
Source: Granitic minimum melt from (Johannes and Holtz, 1996).
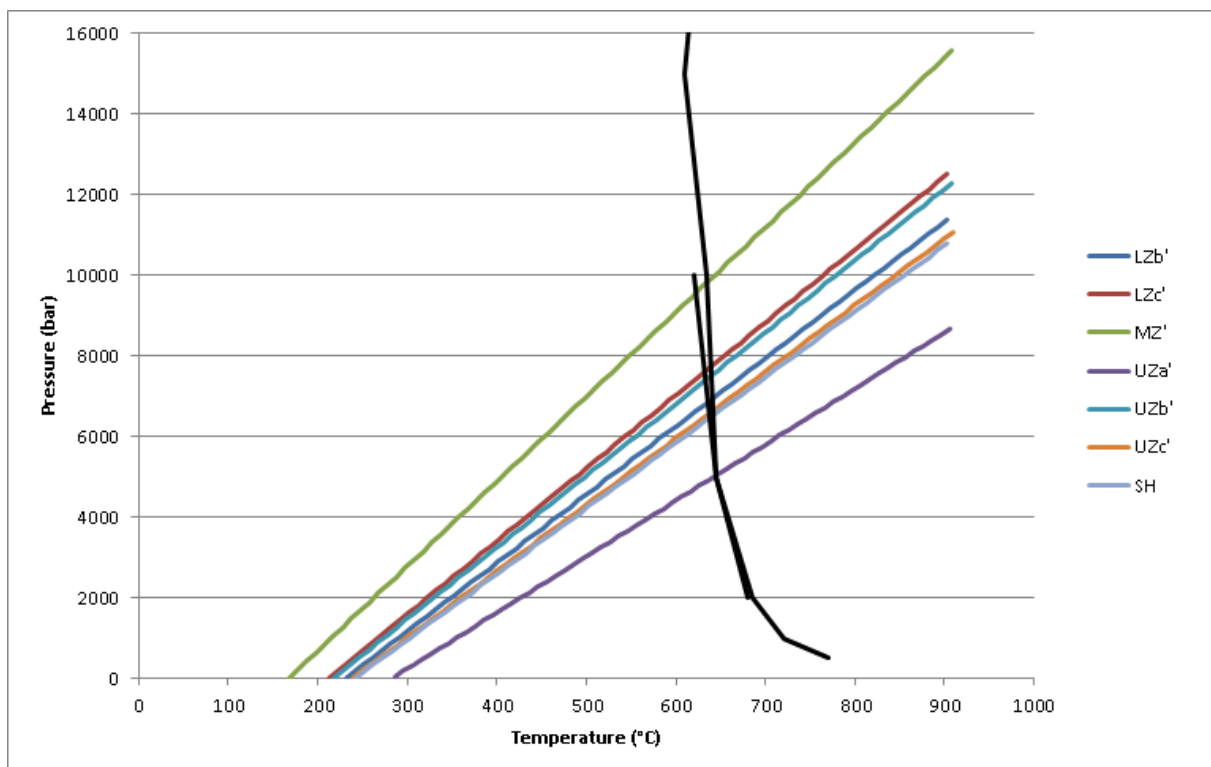
Figure 5-41: Isochores for the FI in the UBS calculated from the melting of hydro-halite. The granitic minimum melt field is shown for quartz-albite-orthoclase system at H$_2$O saturation conditions and with 0-5 mol% CH$_4$. The granitic minimum melt lines are based on solidus and liquidus experiments.
Source: Granitic minimum melt from (Johannes and Holtz, 1996).

The crystallization of granophyre masses was estimated to have occurred between 655 and 770°C with thermodynamic consideration of mineral composition (Larsen et al., 1992), whereas the minimum crystallization temperature was estimated to be 770°C by using the mineral thermometric of pegmatites (Hirschmann et al., 1997). If the isochores in figure 5-40 and 5-41 were compared to these temperatures the pressure during the formation of these FI would be above 5 kbars, which is the equivalent of >16,5 km depth in the earth with a pressure gradient of 1 kbar/3.3 km. This is an unrealistically high pressure.

Following are the results and the normal curve for each layer.

LZb' (SK08-200)

Table 5.3: The parameters and statistics for the FI from LZb'.

LZb' (SK08-200)	Min. value	Max. value	Average	Median	Std. dev.
$Tm_{initial}$	-48.3	-41.6	-45.35	-45.15	1.98
$Tm_{Hydrate}$	-4.9	1.7	-1.97	-1.8	1.36
$Tm_{Homogenization}$	111	369.8	248.48	246.95	73.15
Vol.% vapour	5	40	20.57	20	9.11
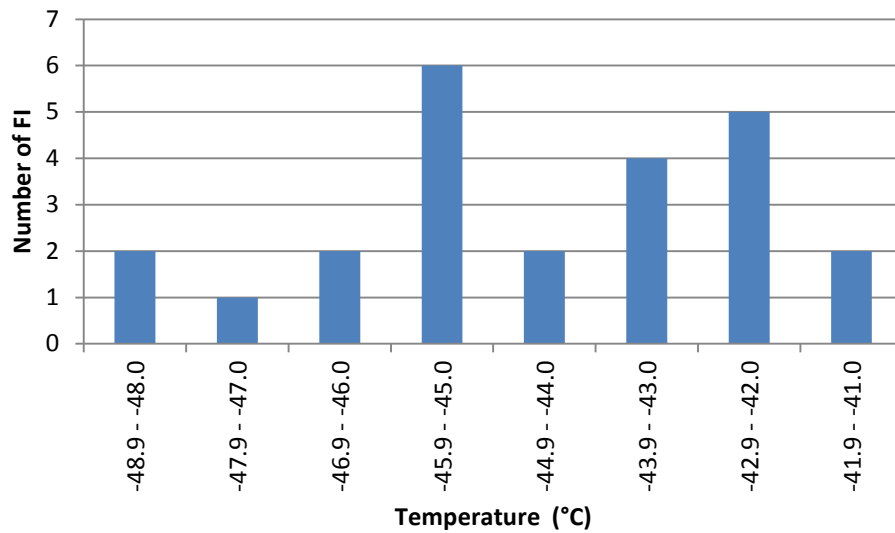
Figure 5-42: The normal curve for Tminitial in the LZb'.
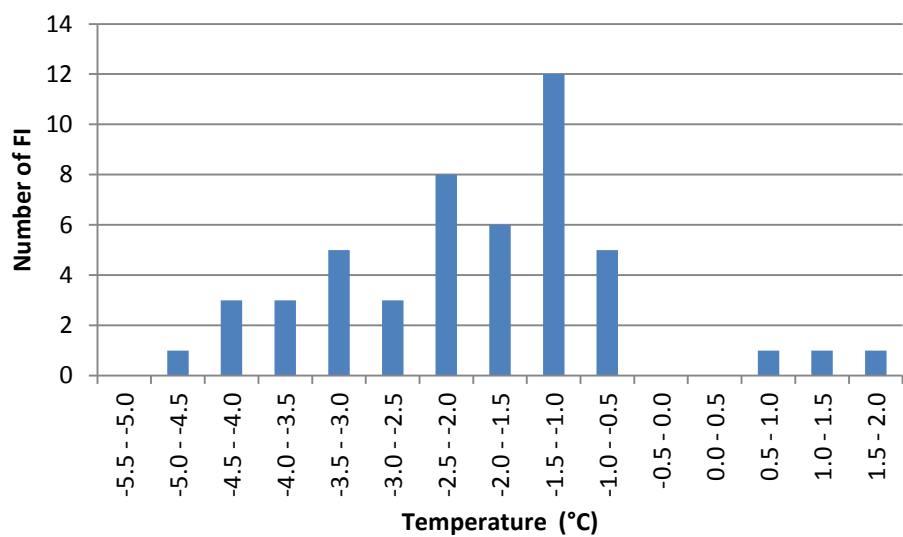
Figure 5-43: The normal curve for TmHydrate in the LZb'.
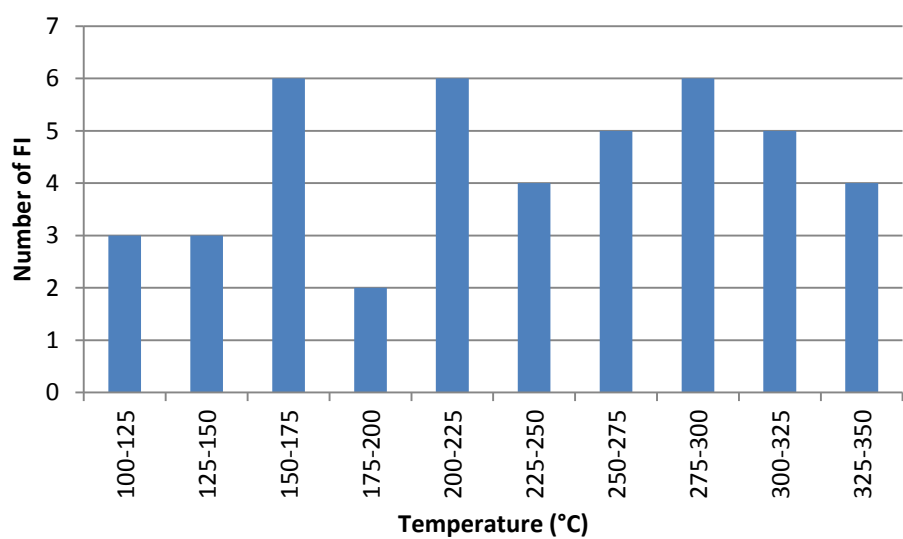
Figure 5-44: The normal curve for Th-total in the LZb'.
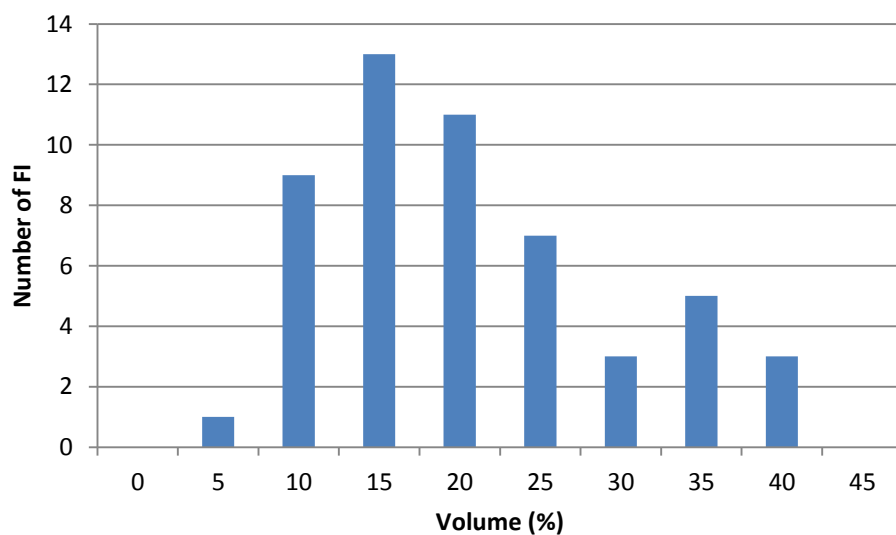
Figure 5-45: The normal curve for vapour volume % in the LZb'.

LZc' (SK08-197)

Table 5.4: The parameters and statistics for the FI from LZc'.

LZc' (SK08-197)	Min. value	Max. value	Average	Median	Std. dev.
$Tm_{initial}$	-46.7	-41	-44.23	-45	2.92
Tm_{ice}	-22	-22	-22	-22	0
$Tm_{Hydrate}$	-4.5	13.4	-0.44	-0.7	2.84
$Tm_{Homogenization}$	129.6	387.7	236.95	226.55	75.54
Vol.% vapour	10	45	18.17	15	7.82
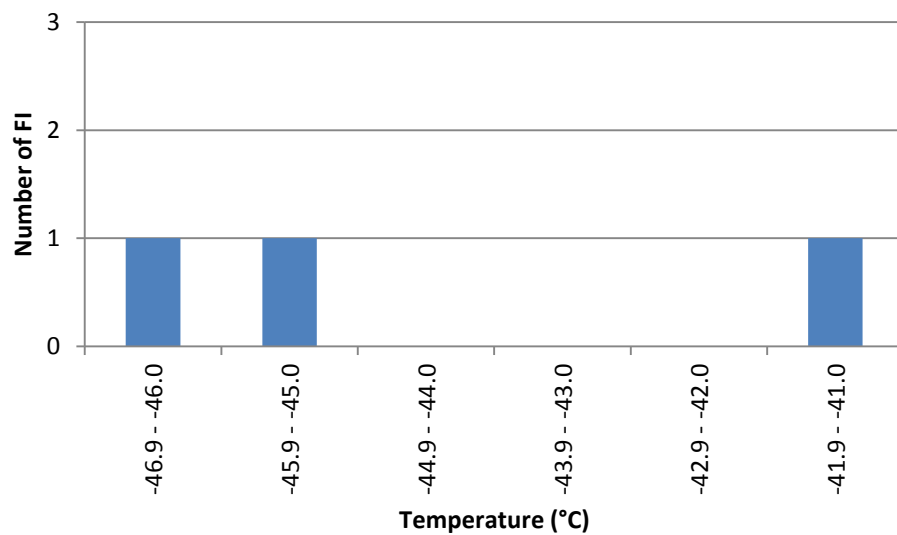
Figure 5-46: The normal curve for Tminitial in the LZc'.
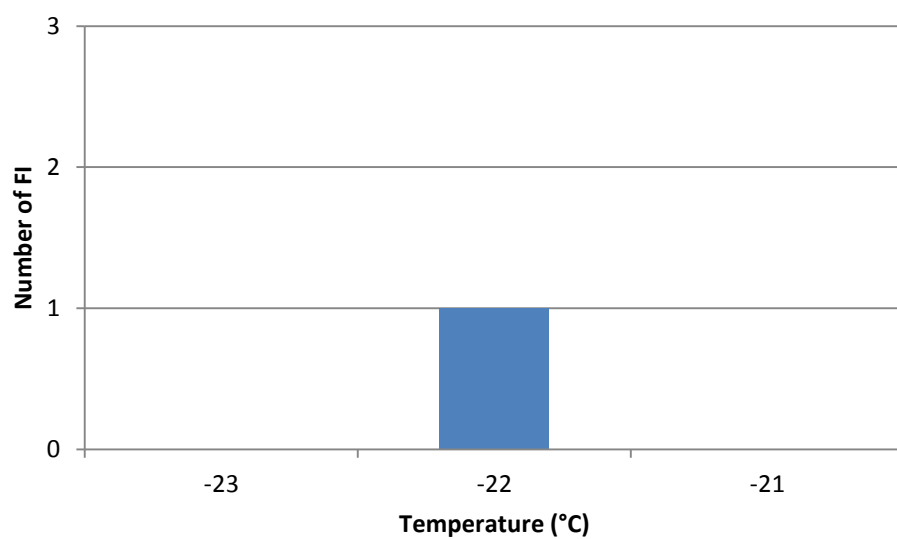
Figure 5-47: The normal curve for Tmice in the LZc'.
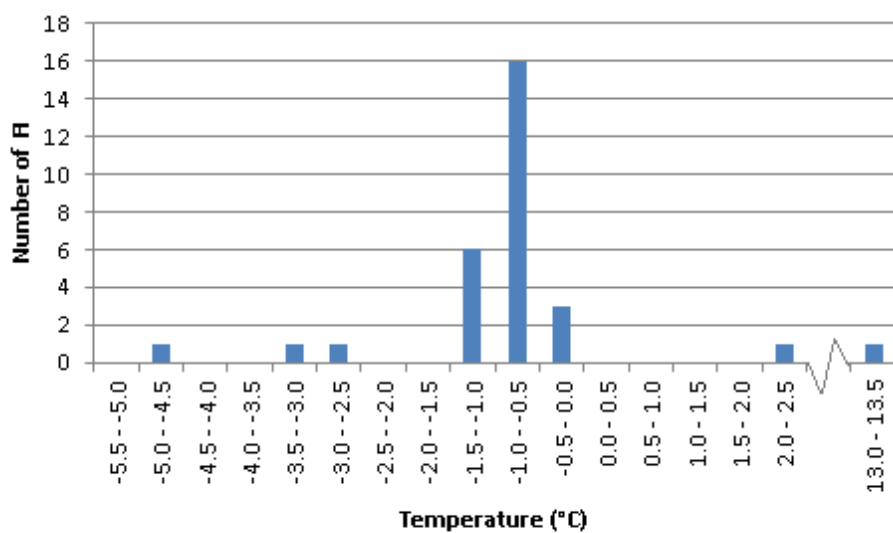
Figure 5-48: The normal curve for TmHydrate in the LZc'.
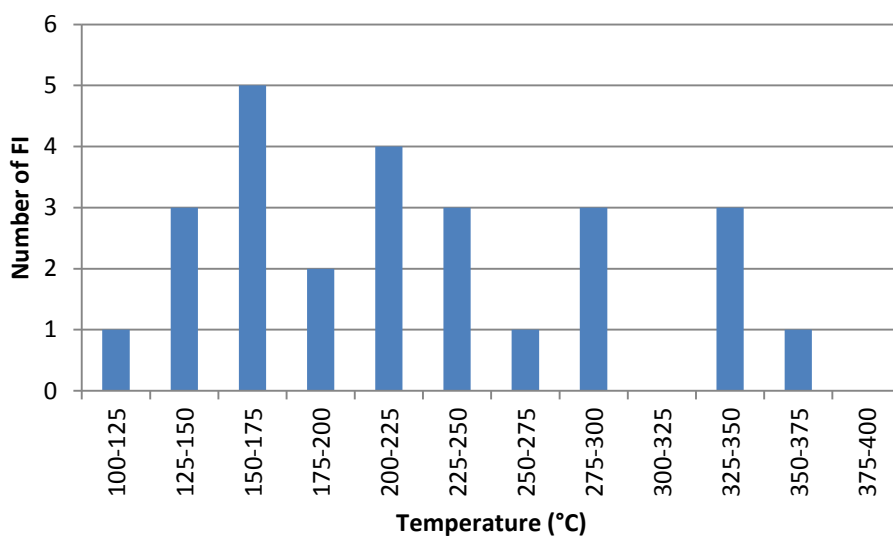
Figure 5-49: The normal curve for Th-total in the LZc'.
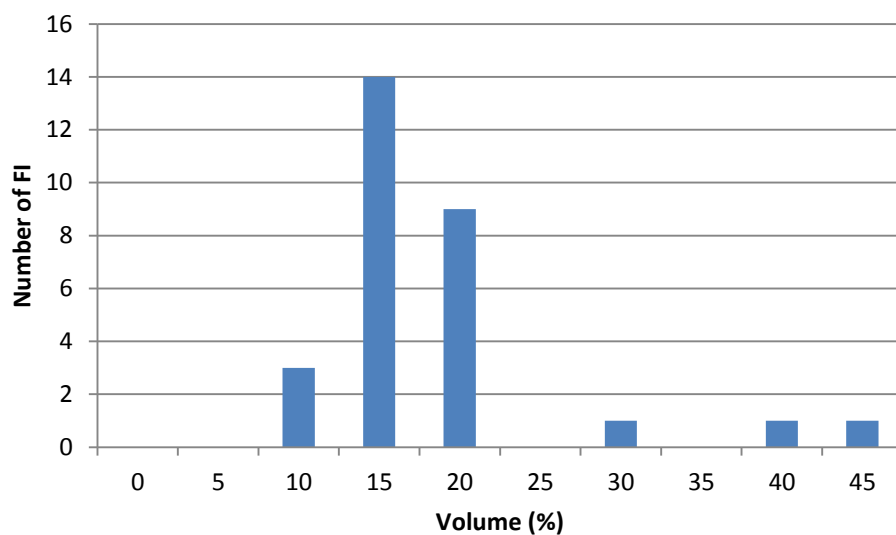
Figure 5-50: The normal curve for vapour volume % in the LZc'.

MZ' (SK08-162)

Table 5.5: The parameters and statistics for the FI from MZ'.

MZ' (SK08-162)	Min. value	Max. value	Average	Median	Std. dev.
$Tm_{initial}$	-49	-37	-43.4	-44	4.62
$Tm_{Hydrate}$	-3.7	3.8	-0.92	-0.3	1.78
$Tm_{Homogenization}$	120.8	383.9	218.34	178.8	81.42
Vol.% vapour	5	35	17.97	15	6.82
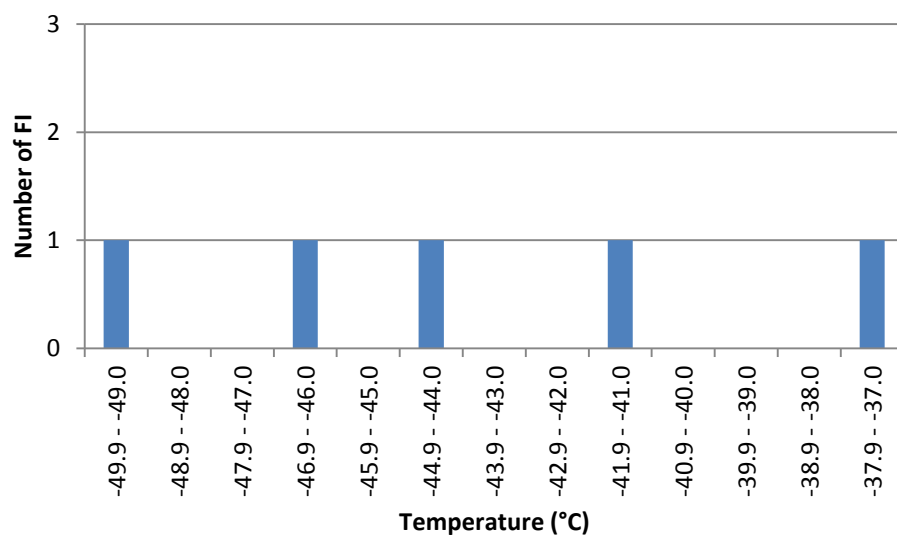
Figure 5-51: The normal curve for Tminitial in the MZ'.
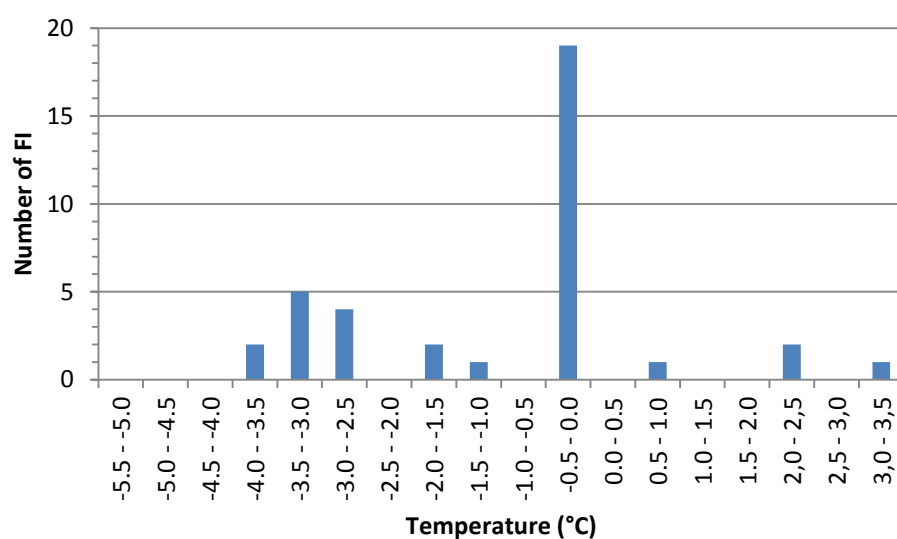
Figure 5-52: The normal curve for TmHydrate in the MZ'.
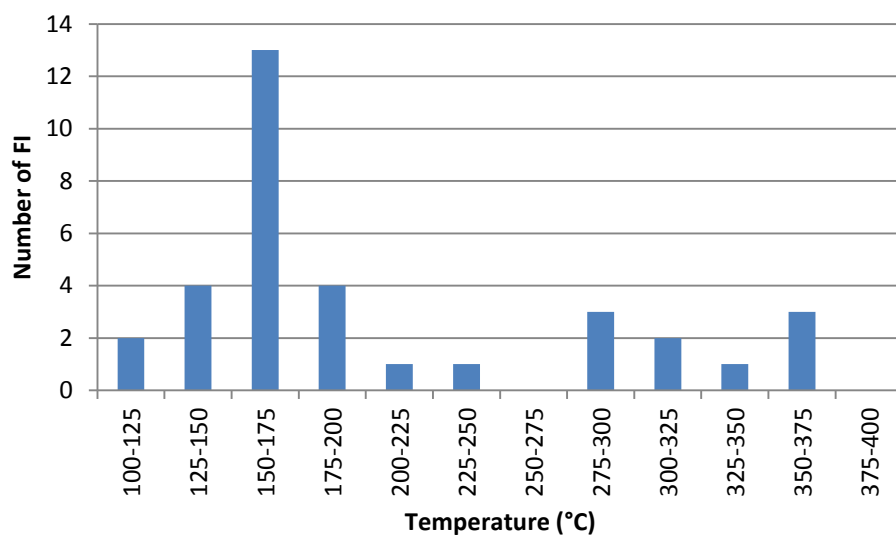
Figure 5-53: The normal curve for Th-total in the MZ'.
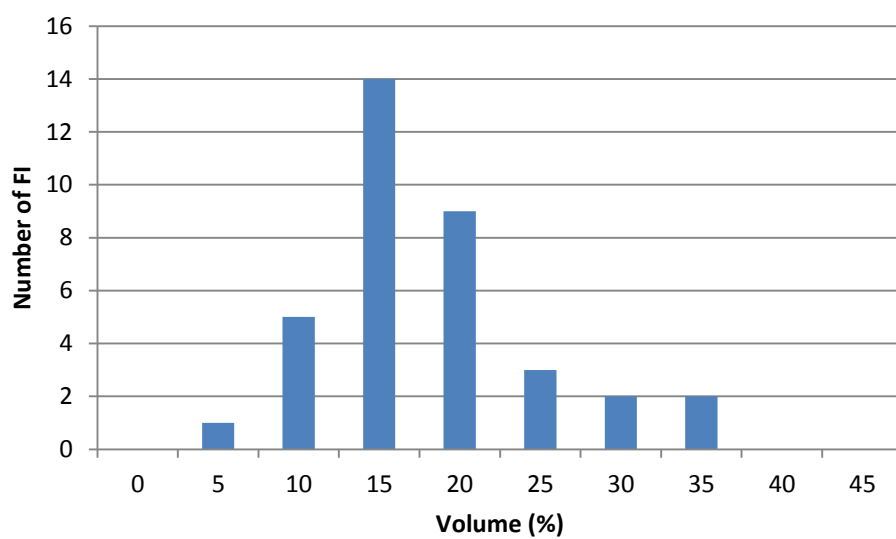
Figure 5-54: The normal curve for vapour volume % in the MZ'.

UZa' (SK08-158)

Table 5.6: The parameters and statistics for the FI from UZa'.

UZa' (SK08-158)	Min. value	Max. value	Average	Median	Std. dev.
$Tm_{initial}$	-44	-42	-43	-43	0.82
$Tm_{Hydrate}$	-4,8	-0.2	-1.27	-0.95	1,17
$Tm_{Homogenization}$	162.7	378.6	294.22	305	61.26
Vol.% vapour	10	80	24.06	20	13.04
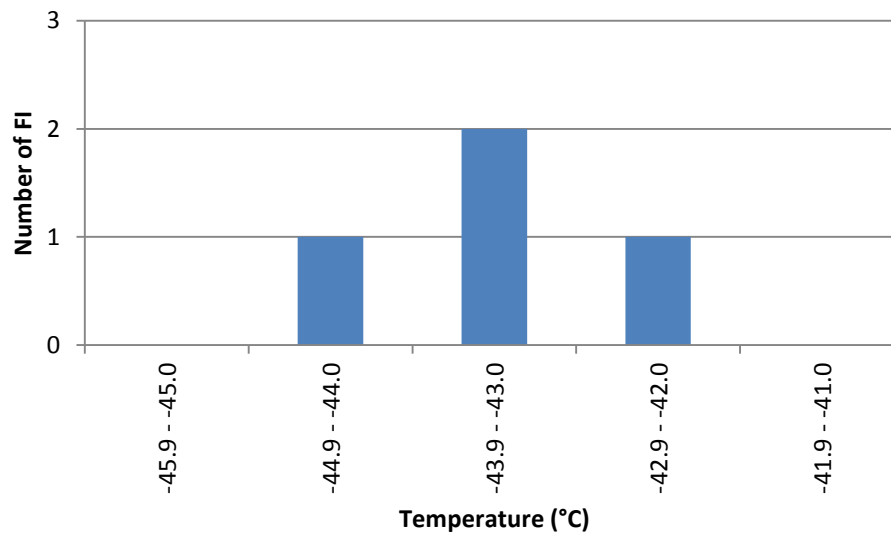
Figure 5-55: The normal curve for Tminitial in the UZa'.
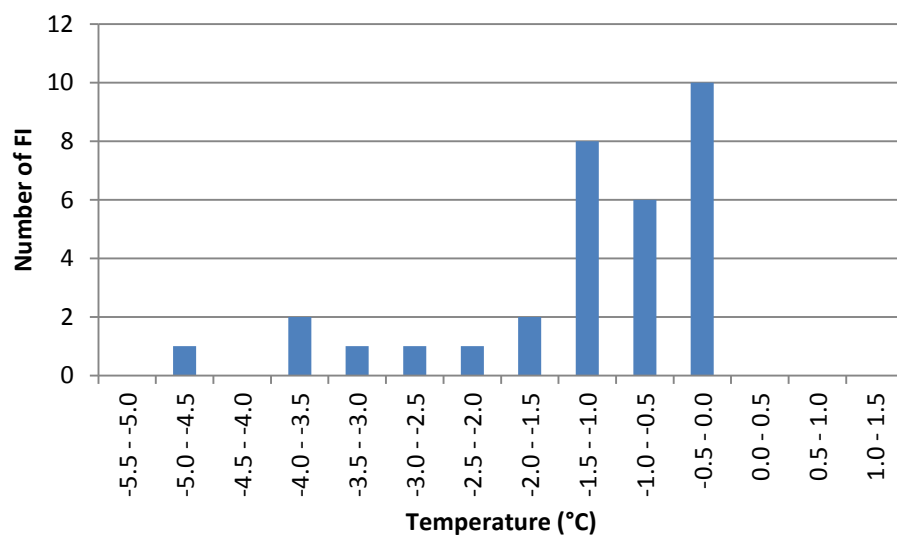
Figure 5-56: The normal curve for TmHydrate in the UZa'.
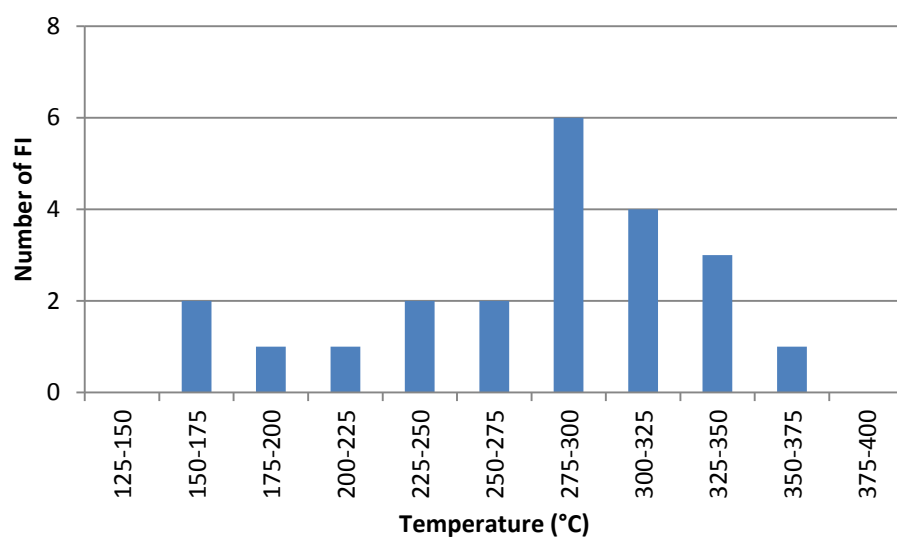
Figure 5-57: The normal curve for Th-total in the UZa'.
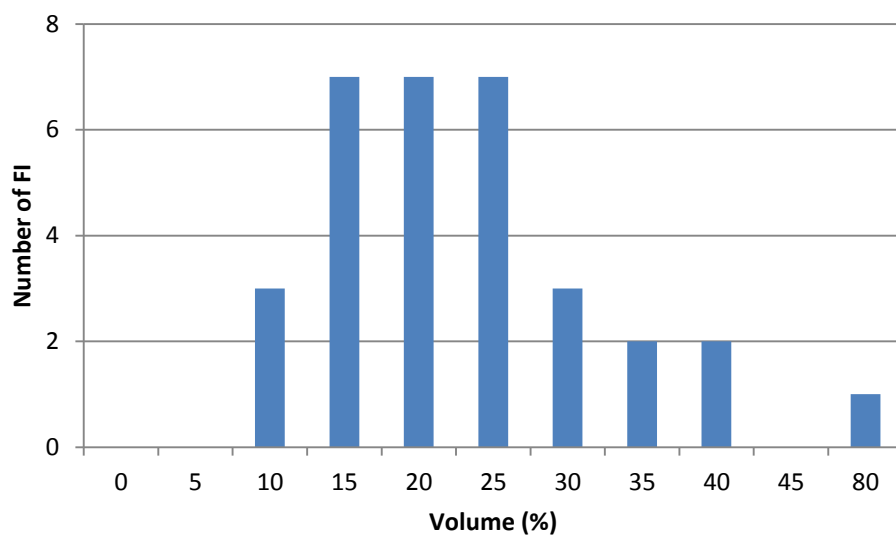
Figure 5-58: The normal curve for vapour volume % in the UZa'.

UZb' (SK08-156)

Table 5.7: The parameters and statistics for the FI from UZb'.

UZb' (SK08-156)	Min. value	Max. value	Average	Median	Std. dev.
$Tm_{initial}$	-48	-43	-45.8	-47	2.17
Tm_{ice}	-23	-18	-20.5	-20.5	3.54
$Tm_{Hydrate}$	-4.8	19.1	-0.90	-1.4	3.89
$Tm_{Homogenization}$	155.4	378.8	246.33	232.1	56.49
Vol.% vapour	10	40	19.55	20	6.66
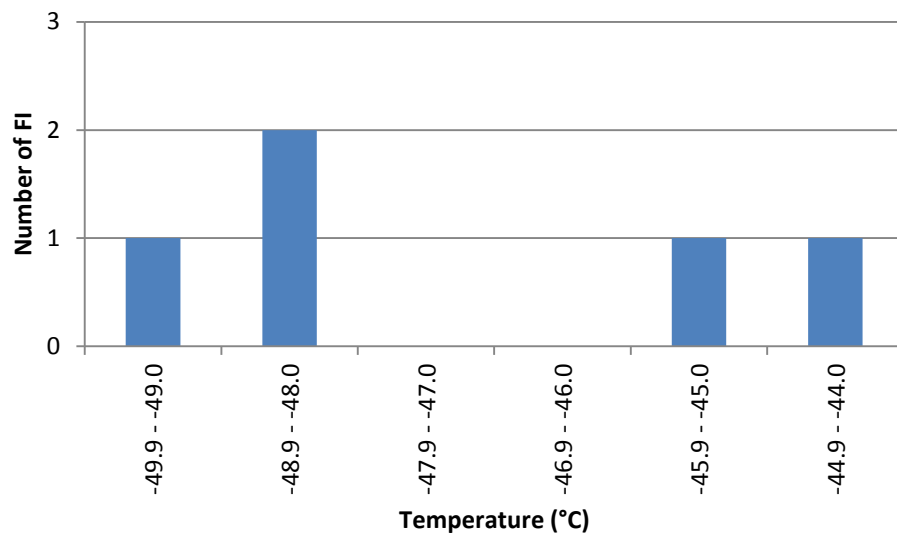
Figure 5-59: The normal curve for Tminitial in the UZb'.
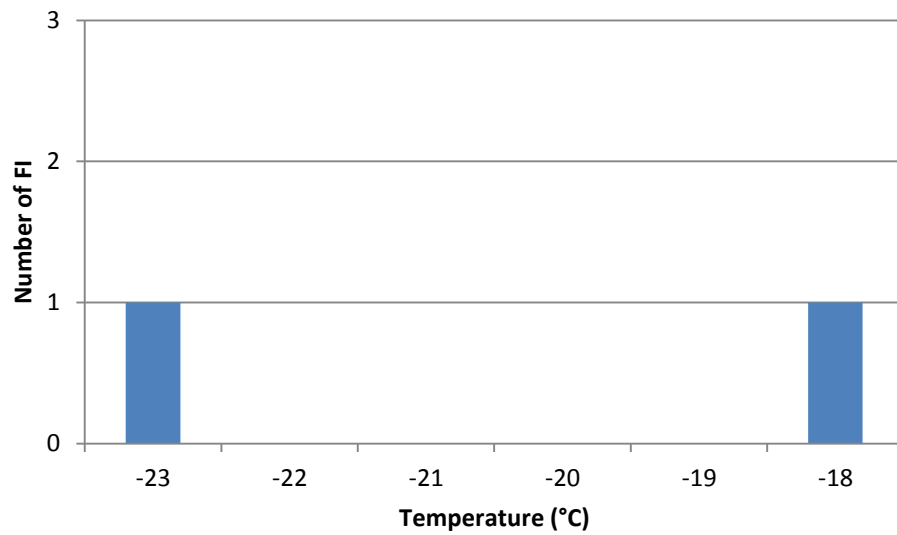
Figure 5-60: The normal curve for Tmice in the UZb'.
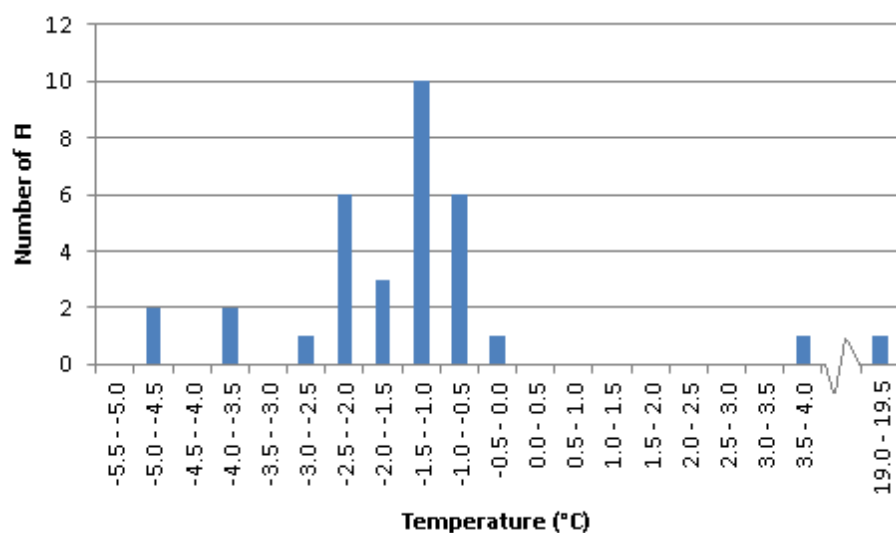
Figure 5-61: The normal curve for TmHydrate in the UZb'.
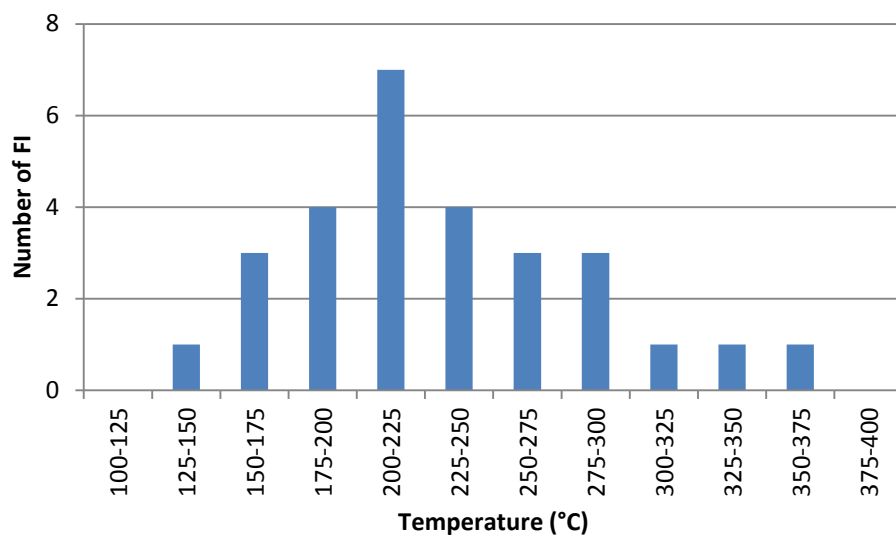
Figure 5-62: The normal curve for Th-total in the UZb'.
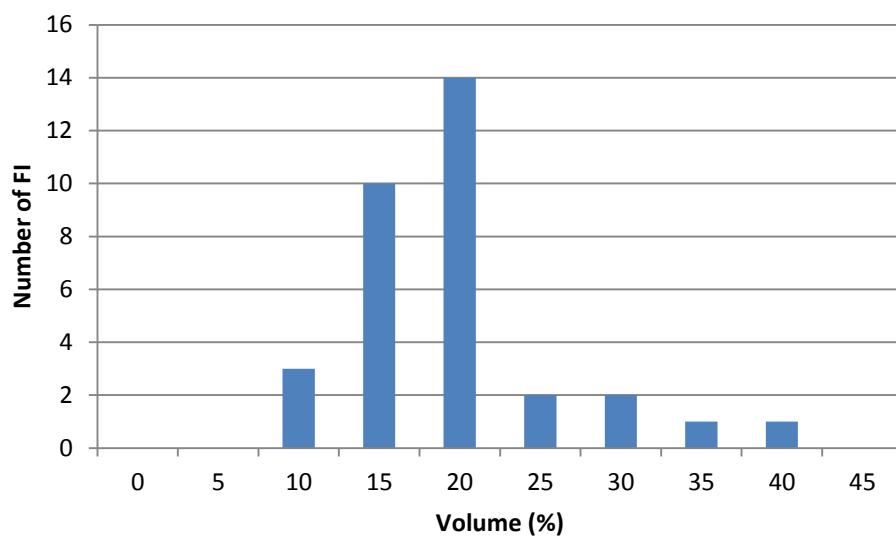
Figure 5-63: The normal curve for vapour volume % in the UZb'.

UZc' (SK08-105)

Table 5.8: The parameters and statistics for the FI from UZc'.

UZc' (SK08-105)	Min. value	Max. value	Average	Median	Std. dev.
$Tm_{initial}$	-44.7	-26	-37.16	-41.4	8.10
Tm_{ice}	-26.7	-23.6	-24.65	-24.2	1.20
$Tm_{Hydrate}$	-9.3	0.2	-2.63	-1.3	2.98
$Tm_{Homogenization}$	160.3	354.2	246.65	255.3	41.59
Vol.% vapour	5	45	18.89	15	8.24
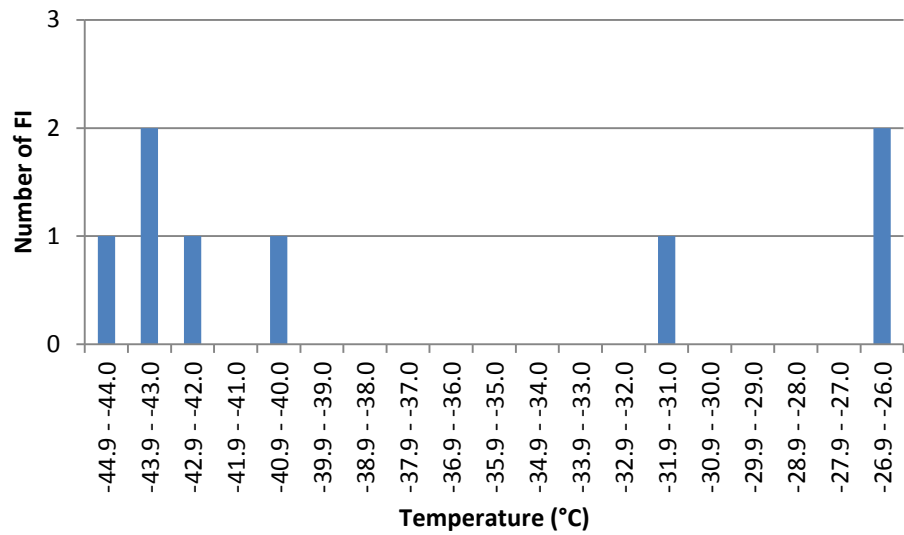
Figure 5-64: The normal curve for Tminitial in the UZc'.
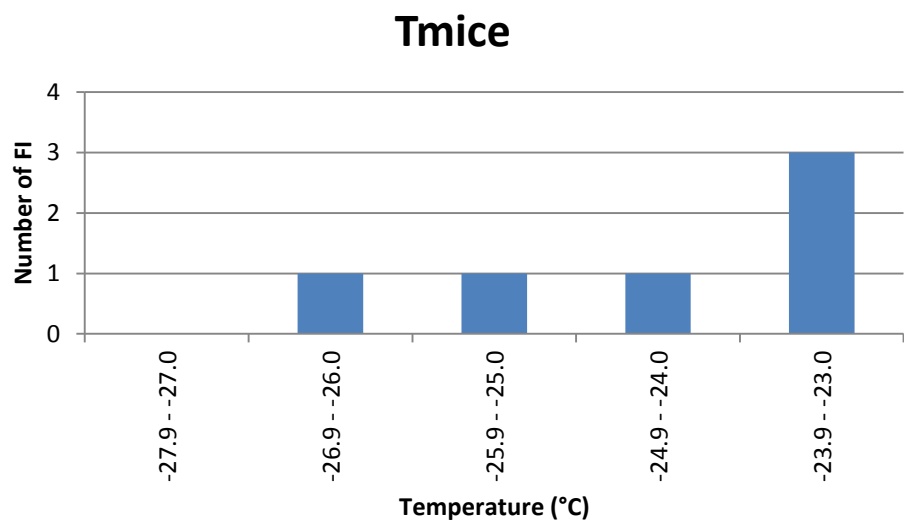
Tmice

Figure 5-65: The normal curve for Tmice in the UZc'.
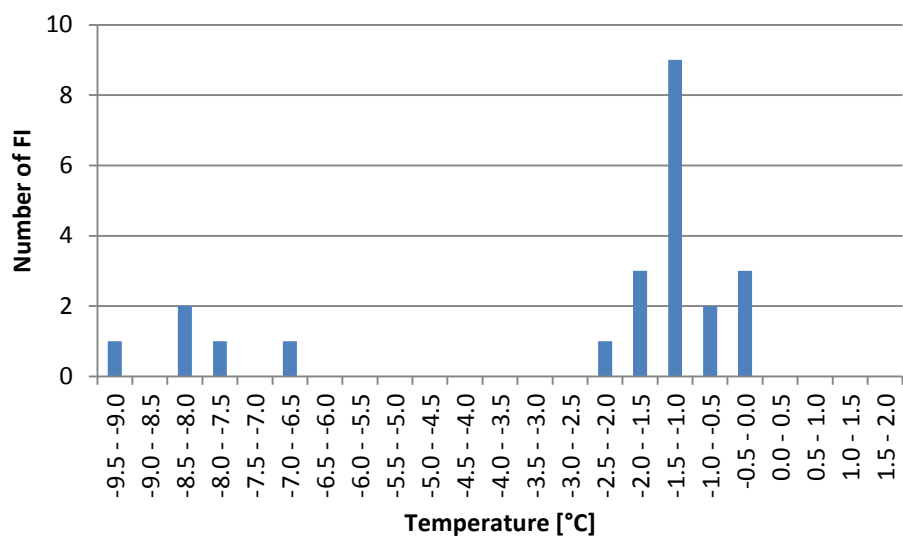
Figure 5-66: The normal curve for TmHydrate in the UZc'.
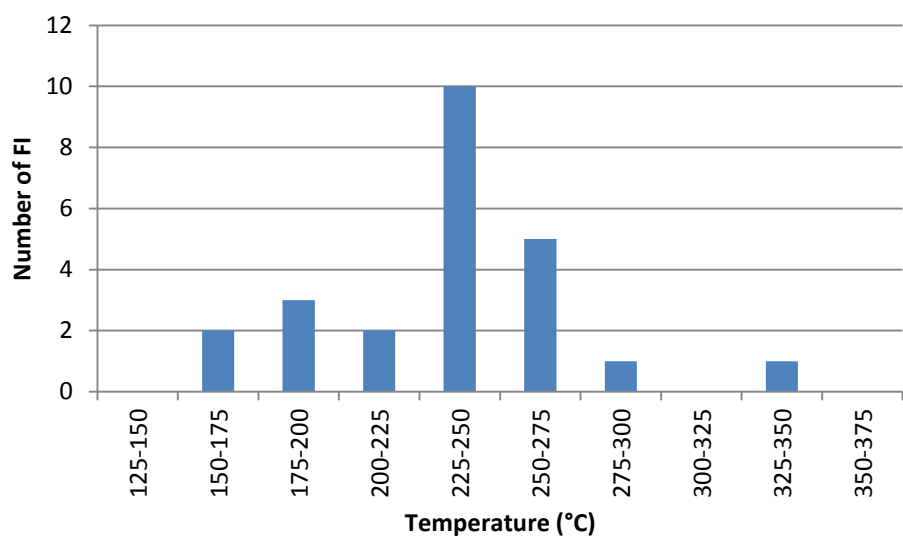
Figure 5-67: The normal curve for Th-total in the UZc'.
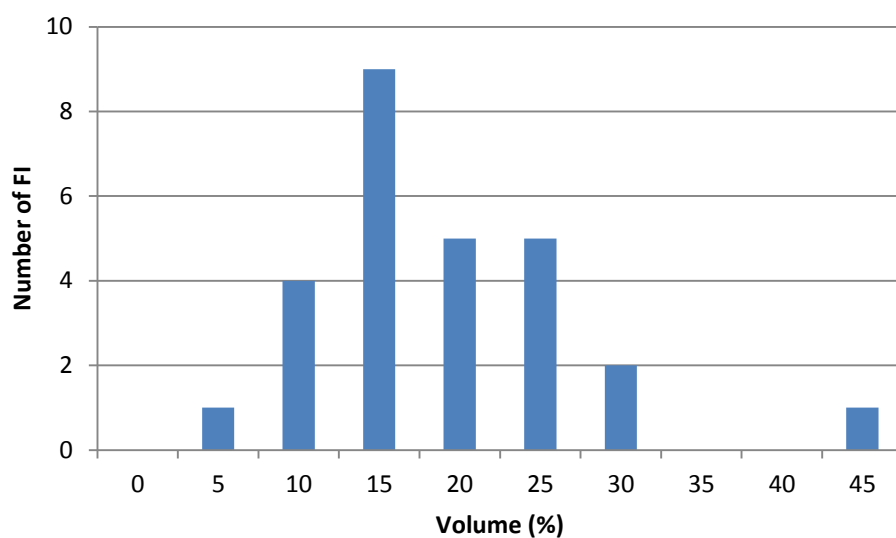
Figure 5-68: The normal curve for vapour volume % in the UZc'.

SH' (SK08-110)

Table 5.9: The parameters and statistics for the FI from SH.

SH (SK08-110)	Min. value	Max. value	Average	Median	Std. dev.
$Tm_{initial}$	-52.2	26.5	-42.30	-46.4	8.01
$Tm_{Hydrate}$	-4.7	-0.2	-1.49	-1.6	0.81
$Tm_{Homogenization}$	166.5	356.9	258.83	258.5	29.70
Vol.% vapour	5	40	17.86	20	6.40
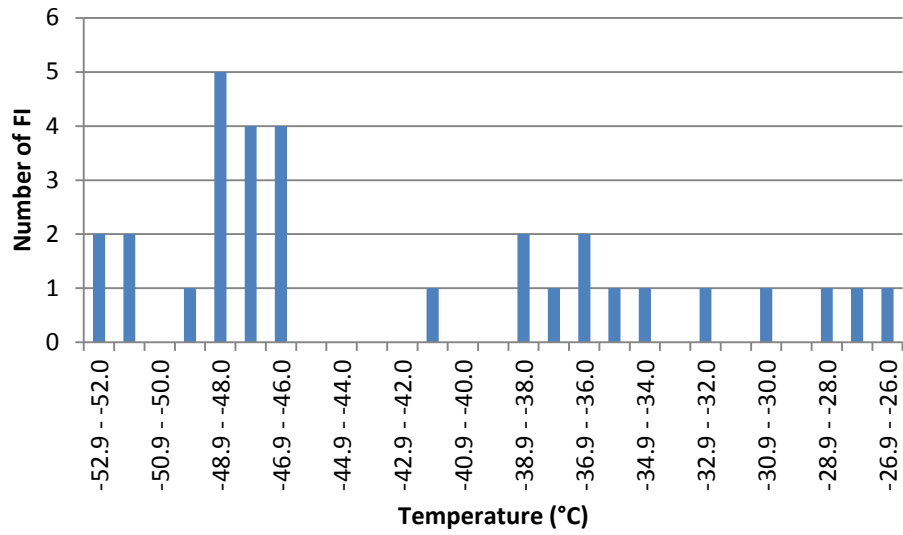
Figure 5-69: The normal curve for Tminitial in the SH.
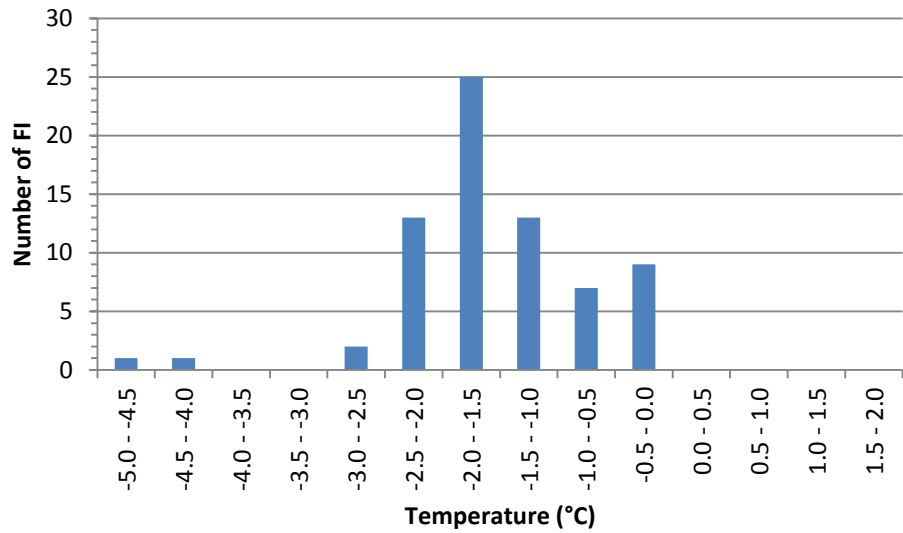
Figure 5-70:The normal curve for TmHydrate in the SH.
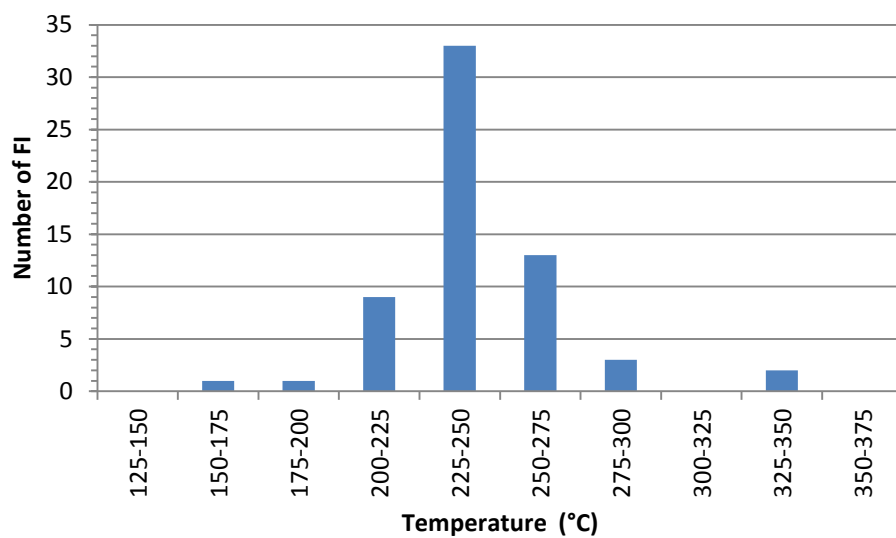
Figure 5-71: The normal curve for Th-total in the SH.
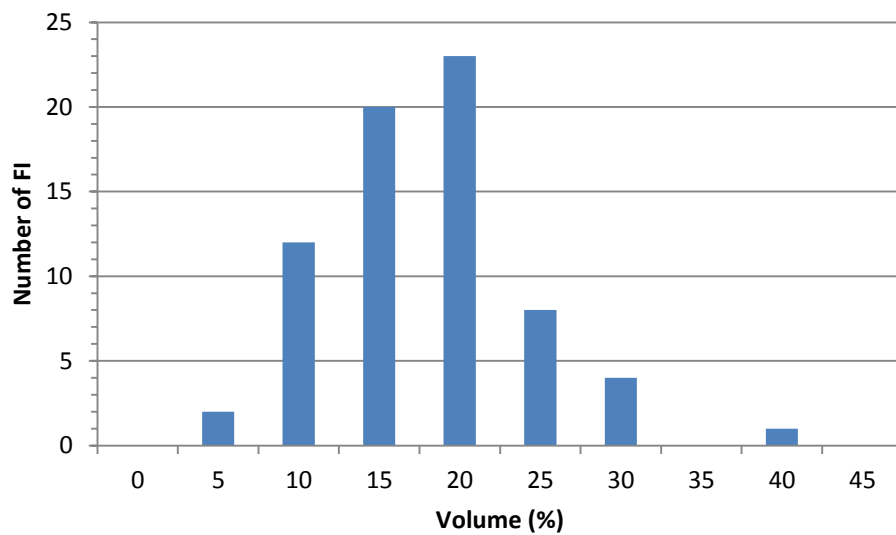
Figure 5-72: The normal curve for vapour volume % in the SH.

6 Discussion

6.1 Fieldwork

6.1.1 Austurhorn

The magma enclaves at Austurhorn seem to have formed due to incomplete magma mixing, when the intrusion was only partially crystallized mush. The mush was felsic and much colder than the mafic and felsic melts that intruded the mush. Due to the heat difference the intrusive mafic melts quenched and formed pillow-like structures with a chilled margin, and also caused angular fragmentation and partial resorption of some of the pillows. The same phenomena are not present in the felsic enclaves, which had rounder edges, as the heat difference was probably not as severe between them and the mush, and thus did not lead to as prominent separation between the enclaves and the mush it intruded into. This corresponds with previous research in the area, which had indicated that the rock structures to be the result of incomplete magma mixing (de Jesus Padilla, 2011); this happened in a dynamic magma chamber that was repeatedly recharged and tapped during a constant fractionated of the magma in the chamber (Thorarinsson and Tegner, 2009).

6.1.2 Vestrahorn

De Jesus Padilla (2011) describes Vestrahorn to have formed by magma mixing, although this notion is not from field observations. Moreover Roobol (1974) considered the granophyres to have an intrusive nature. The rock structures observed in the field are however estimated to be similar to the rock structures described by Larsen and Brooks (1994) from the Skaergaard intrusion because of the relationship between layered gabbro, gabbro pegmatites and melano-granophyres.

Order of gabbro formation

The coarse-grained gabbro was found underlying and intruding into the dominating partially-layered gabbro. Therefore, the coarse-grained gabbro is considered to have formed after the layered gabbro. However, the fact that the coarse-grained gabbro intrudes into the normal gabbro, the irregular contact between the rock types, and there is no visible quenching between these two rock types, supports the concept that the emplacement of the coarse-grained gabbro occurred while the normal gabbro was still at least partially molten and that there was not a significant temperature difference between them. As the normal gabbro was

still partially molten, the system must have contained some heat before the coarse-grained gabbro intruded into the system, having a longer time to crystallize and becoming even more coarser grained. The coarser grain size might also indicate that this gabbro is more evolved, with a lower crystallization temperature, which again resulted in it having a longer time to crystallize.

Pegmatites

Roobol (1974) found the various granophyre sheets at Vestrahorn to have invaded into the gabbroic magma, which consisted of a rigid, interlocking framework of crystals. The description of these granophyre structures corresponds with the field observations made, described as pegmatite columns, veins and batches.

Larsen and Brooks (1994) concluded that the pegmatite structures in the Skaergaard intrusion to have formed from intercumulus liquid derived from the parental melts of the intrusion. They are late-magmatic products, forming at the last stages of crystallization of the layered gabbro. Additionally late magmatic fluids in granophyre were similar to those found in pegmatite and anorthosite structures. Due to density differences between the melt and the already crystallised cumulates, the pegmatite melts were able to rise upward in a diapiric flow and/or through syn-magmatic weakness zones and fractures.

The structures at Vestrahorn are not considered to have an intrusive nature like Roobol (1974) described, but instead correlate with the field description from Larsen and Brooks (1994) where they assumed to have formed from intercumulus melt. The magma that formed the host rock is thought to have contained enough crystals to form a rigid, interlocking framework that was incapable of flowing. It has been assumed that the late-stage melt at Vestrahorn must have been volatile-rich, which would have resulted in a density contrast between the melt and the interlocking crystals (Cargill et al., 1928, Guðmundsson, 2009). The volatile-rich melt would be less dense, correlating with Larsen and Brooks's (1994) observations in the Skaergaard intrusion where the pegmatite structures formed due to buoyant force of the less dense melt. Furthermore, the pegmatite structures at Vestrahorn have well-defined boundaries towards the host rock, with a diapiric shape, which indicates that they rose up due to being less dense than the cumulus minerals with a diapiric flow. Afterwards both the host rock and the pegmatite structures were cross-cut by later intrusions.

The pegmatite structures at Vestrahorn have coarse-grained, mafic margins, which grade into a felsic centre. Larsen and Brooks (1994) identified three separate zonation in the pegmatites from the margins inwards with the margins composed of plagioclase laths, the gabbroic zone dominated by plagioclase, pyroxene, olivine and iron-titanium oxides and the granophyric zone in the centre composed of quartz, orthoclase and plagioclase. These zones correlate with the zonation seen at Vestrahorn, although the marginal zone composed of plagioclase was not identified, possibly either due to how thin it is or that it does not exist with the pegmatites at Vestrahorn.

The pegmatite structures at both Skaergaard and Vestrahorn also contain the same main mineral composition, that is feldspars, pyroxene and iron-titanium oxides (Larsen et al., 1992, Roobol, 1974), although there are some variations in the mineral composition of the pegmatites at Skaergaard based on their location (Larsen et al., 1992).

The pegmatite structures have a different geometry in Skaergaard, which is related to their location. Although there existed different geometric shapes in the pegmatite structures at Vestrahorn, there was no correlation between their locations and geometry. The variety of pegmatite structures is assumed to be related to the amount of interstitial melt that was able to separate from the cumulates and collect while rising upwards. If only a small amount of pegmatitic melt separates it forms isolated pegmatite batches, while more material forms pegmatite columns. If huge amounts separate they form larger pegmatite bodies. As the pegmatite bodies generally seem to intrude horizontally, it is assumed that they are either denser than the pegmatite batches and columns because the melt was poorly separated from the cumulates and had a neutral buoyancy, or the pegmatite melt was running into an obstacle while rising upwards.

The vein structure at location 4 is considered to have the same origin as the other pegmatite structures. However instead of rising up through a mostly crystalline material like the pegmatite structures, it followed structural weaknesses in the layered gabbro. As the host rock was colder than the host rock of the pegmatites, the vein did not have the time to form the same zonation as is typical of the pegmatites, that is coarse-grained margins and a felsic centre.

Although the one XRD analysis that was completed did not reveal ferrobustamite it is not possible to exclude that the pegmatite bodies do contain ferrobustamite, as only a small

sample was analysed. The thin section did not contain granophyre masses, but the quartz formed masses similar to the underdeveloped granophyre masses found in the LZc' of the Skaergaard intrusion, and the masses have been found to vary between samples in the Skaergaard intrusion.

The discontinuous anorthosite structures described by Larsen and Brooks (1994) resemble the vein structures found in the mine (location 5), which they assumed had risen upward due to buoyant forces like the pegmatite structures, as they formed by aqueous volatiles that escaped from melano-granophyre. At Vestrahorn these structures did not form the same zonation as the pegmatite structures, probably because of their chemical composition, as they were simply lacking the mafic elements to form these mafic minerals, which supports the observations at Skaergaard where the mafic minerals would crystallise first. No chemical analysis was however performed on these structures at Vestrahorn to confirm this. Conversely the amount of sulphide surrounding these structures was unexpected, especially as the same sulphide enrichment was not found in relation to the pegmatite structures. This might be the result of the magma that formed these structures to be more evolved and having concentrated sulphides.

The formation of the rock structures observed at Vestrahorn are thought to have formed with the migration of the intercumulus melt to an area where it collected and grew, before being arrested and crystallised, creating the structures that can be seen today. Therefore, although chemical analyses were not performed, it is assumed, based on visual observations, that these structures have similar properties and formed in the same way as the pegmatite structures in the Skaergaard intrusion.

6.2   Petrography study, the UBS of the Skaergaard intrusion

Most of the samples analysed were from the Kilen profile, and the samples that were analysed cover the stratigraphy of the UBS, from the SH up to the LZb'. Additionally one sample from the Hammer Pas profile was analysed and four samples from the Brødretoppen profile. No clear visible difference was found between the profiles in neither the mineral assemblage, nor the alteration.

The samples used for geochemical analyses were also analysed petrographically. They contained the same minerals as the rest of the Skaergaard intrusion, however in different

concentrations. The iron-rich phase was mostly composed of igneous lamination of iron-titanium oxides, along with plagioclase and augite. Meanwhile the samples from the SH were mostly composed of plagioclase and granophyre masses, in addition to being highly altered.

All the samples had sustained considerable alteration by hydrothermal fluids, which resulted in complications during the identification of some minerals. Naslund (1984) had already reported that the UBS to contains more altered rocks than the LS, so this was expected. This alteration however indicates that there might have been a hydrothermal circulation system that strongly influenced the mineral assemblage after crystallization. These alteration minerals included a mineral, identified as ilvaite, which had been previously only mentioned by Naslund et al. (1983) in the Skaergaard intrusion, but which is not commonly mentioned in relation to the intrusion.

The crystallization sequence is mostly similar to previous research by Salmonsen and Tegner (2013), with the same cumulus phases observed. These are olivine and plagioclase that first crystallise together, followed by augite, iron-titanium oxides, sulphides, apatite, and ferrobustamite. Plagioclase was found throughout the layered gabbro, commonly constituting 50-60% model of the samples, but it varied between 40-75%. Olivine was not always found as a cumulus phase in the LZ', as it is generally not very abundant, and is highly altered where it occurs. Naslund (1984) identified less than 5% pigeonite, which was not found during this study.

Granophyre masses

The granophyre masses were found interstitially between cumulus phases in the UBS, which implies that the granophyric masses crystallized from the last melt in each layer. This implies that the fluid in the FI coexisted with the intercumulus magma, which enables the evaluation of the system's properties during the crystallization of the last melt in each layer. Additionally the amount of granophyre in each layer could influence the distribution of elements and volatiles, as the last melt to crystallize can have higher concentrations of volatiles and incompatible elements than the original melt. Therefore the minimum and maximum volume of granophyre was estimated for each layer in the UBS and listed in table 6.1, however as there was no sample from the LZa', no estimate was calculated.

The volume of the UBS is approximately 35.21-41.52 km^3 (Nielsen, 2004), from which the estimated volume of granophyre masses in the UBS is about 0.793-2.286 km^3. This volume

would probably be slightly higher if data for the volume of granophyre masses in the LZa' was available.

Table 6.1: An estimate of the minimum and maximum volumes of granophyre for each layer of the UBS.

Layer	Minimum volume in km^3	Maximum volume in km^3
LZa'	-	-
LZb'	0.084	0.497
LZc'	0	0.030
MZ'	0.048	0.280
UZa'	0.104	0.409
UZb'	0.281	0.663
UZc'	0.276	0.407
Total volume in the UBS	0.793	2.286

6.3   Geochemical analyses

There was an obvious chemical difference between samples from the SH and the iron-rich gabbroic pegmatite, which was visible in both main and trace elements. The iron-rich phase samples were rich in Fe_2O_3, TiO_2 and MgO, while the SH was rich in SiO_2, Al_2O_3 and alkalis. In addition there was also a noticeable difference between the two iron-rich samples, as the sample that was collected in 2009 was richer in iron and titanium. The concentration of SiO_2 in the samples from the SH indicates that they have a granitic or granodioritic composition.

As the SH consists of the last melt to crystallize, and granophyre is generally the last melt to crystallize, the SH should contain a significant amount of granophyric masses. The samples from the SH have a typical chemical composition for granophyre masses (Best, 2013) indicating that this is the first identified major accumulation of granophyre masses in the SH.

The Skaergaard evolution trend typically plots with a progressively higher Fe content than the tholeiitic trend in an AFM diagram. The samples from the SH plot on the typical Skaergaard evolution trend, while the samples from the iron-rich phase were too alkali-poor to plot on it, and instead corresponds with previous research by Veksler (2009) who focused on rocks from the LS.

The immiscibility of a silica-rich and iron-rich silicate liquids in the Skaergaard intrusion has been demonstrated (Holness et al., 2011, Jakobsen et al., 2005), but only in melt inclusions and microstructures. One of the liquids was granophyric and the other should have been mafic, although this has not been documented so far (Larsen and Brooks, 1994). The samples analysed in this study make up a considerably larger volume than in previous research.

The samples from the SH plot within the immiscible field, as the intermediate silica-rich samples by (McBirney and Nakamura, 1974), but they are not chemically identical. However all the iron-rich samples plot outside of the immiscibly field, with two of the iron-rich samples being substantially more iron-rich. It is possible that the melt in the system simply did not contain enough SiO_2 to be able to plot on the separate ends of the immiscibility plot, as both samples are poor in SiO_2 compared to the typical chemical composition during silica-liquid immiscibility (Philpotts, 1982). Moreover all the iron-rich samples contain more titanium than previous studies (e.g. (Dixon and Rutherford, 1979, Jakobsen et al., 2005, McBirney and Nakamura, 1974, Philpotts, 1982)).

In an immiscible silicate liquid pair the iron-rich phase should contain greater amounts of P_2O_5, TiO_2, MgO, MnO, Zr and rare earth elements (REE), while the silicate-rich phase have higher concentrations of K_2O, Na_2O, Al_2O_3 and Rb (Best, 2013, Jakobsen et al., 2011). This is not in total agreement with the geochemical results, although the samples do plot comparably in a Harker diagram for FeO and SiO_2 as the immiscible silicate liquid did in the study by Jakobsen et al. (2005). Additionally the iron-rich sample phase plots at the iron-rich end of the immiscible liquid field, while the samples from the SH plot inside of the immiscibility field. This suggests that the iron-rich phase is essentially an immiscible phase, which separated from the melt and crystallized. It is uncertain whether the samples from the SH also formed due to liquid immiscibility as they plot within the immiscibility field and do not completely follow the chemical distribution generally assumed to form during silicate liquid immiscibility. However the samples from the SH contain higher concentration of Al_2O_3 than the iron-rich phase, and generally amount of Al_2O_3 should decrease during evolution of melt, but during silicate-liquid immiscibility the Al_2O_3 is concentrated in the silicate liquid, which indicates that this might be the result of a silicate-liquid immiscibility.Silicate liquid immiscibility would have had great effects on the magma, as it would have redistributed

both the major and trace elements. Immiscibility would also result in the sinking of the denser phase and the rise of the less dense phase.

Moreover the chemical composition contrast between the two immiscible silicate melts usually increases with decreasing temperature (Jakobsen et al., 2011), not identifiable here, but could explain the geochemical difference between the two separate group of iron-rich samples.

Elements that are typically included strongly in mafic minerals (e.g. Co, Ni, Sc, Cu, Sr) are more common in the iron-rich phase than in the SH samples, except for Sr, which was more common in the SH samples as expected. In addition highly water-soluble elements (e.g. Rb and Ba) partition strongly into the SH samples, which correlates with increasing H_2O during magma crystallisation, and the SH being the end product of the differentiation of the Skaergaard parental melt.

The Zr content in the samples was quite high in the samples from the SH. This is in agreement with previous research by Brooks (Brooks, 1969), where the Zr increase with the differentiation of the melt, and reached a value of 1300 ppm in the SH, which is a bit lower than this study's highest value. This is due to Zr being immobile and an incompatible element and so ends up in the final, most evolved melt.

Phosphorus was also incompatible until apatite formed as a primocryst, however contrary to the main layered series, apatite began to form quite early in the UBS as demonstrated by the presence of primocryst apatite throughout the UBS.

6.4 Fluid Inclusions

The fluid inclusions in each zone homogenized over a wider temperature range than the one found by previous research in the LS (Larsen et al., 1992), where the narrowest temperature range is ±24°C for all FI from the same rock type (Larsen et al., 1992). The wide temperature range for homogenization surveyed here substantially influences the isochores, as the EoS is heavily dependent on the density, i.e. the homogenisation temperature of the FI. Three possible reasons for this wide temperature range are considered:

1. Inaccurate measurements, either due to instrument or human error
2. The fluid inclusions were not all primary fluid inclusions
3. The fluid inclusions re-equilibrated after formation

Inaccurate measurements could explain some of the deviations between the measured temperature and the real homogenisation temperature. However the instruments used allow for the very slow heating of the sample and are closely monitored. In addition, standards were used to correct for possible deviations caused by the instruments. As the instruments are automatic they also reduce the possibility of a human error during heating, and allow for a gradual and constant heat or cooling rate. Nevertheless the ability to notice the phase changes at the correct temperature is influenced by the researcher. By heating the sample gradually it is possible to minimise that error, therefore this is not a likely explanation for a temperature difference of over ±80°C for each zone.

It was tried to the utmost to only measure primary fluid inclusions based on textural evidence and avoid structures that might facilitate the formation of secondary fluid inclusions. The fluid inclusions that were measured were, based on visual observations, concluded to have been primary. However, the wide temperature gap indicates that these FI did not form during one specific event, yet they are all found in granophyre masses that are petrographically identical. In addition they all have very similar salinities, which indicate that they formed from one homogenous fluid that existed at a similar time throughout the system. Hence these FI likely formed at the same time during the same general event.

Constant fluid density and composition are the main requirements for using FI as an indicator for system conditions during entrapment. Quartz generally conserves FI relatively well as it is quite resistance to changes by external sources, and is therefore generally the preferred host mineral when it comes to microthermometry. But even though quartz is resistant to changes, both the quartz and the FI can be affected by external events, which may influence their properties. Re-equilibration of FI can result in volume changes, or components being added or removed from the inclusions (Samson et al., 2003).

The FI used here are all found in granophyre masses that crystallized at comparable conditions, and should consequently have a narrow range of homogenisation temperature, only influenced by changes in the pressure. Therefore this wide difference in homogenisation temperatures might suggest that the FI have been subjected to post entrapment modification as a result of full or partial re-equilibration. If that is correct, the FI with the highest homogenisation temperature should have the most original fluid properties from the crystallization of the granophyric masses, while the FI with the lowest

homogenisation temperature would have had the most intensive re-equilibration. Conversely the volume of FI can also be affected by re-equilibration, which would be noticeable in changes to the vapour bubble volume, as long as nothing was added or removed from the FI during re-equilibration. If both the homogenisation temperature and the volume of the vapour bubble were influenced by alteration and re-equilibration, trends between these two factors should become apparent, thus the homogenisation temperature versus the estimated volume of the vapour bubble is shown in figure 6-1. To note is that the volume of the vapour bubble was based on visual estimate and can contain some error (estimated ±5 %). All of the figures demonstrate a trend between homogenisation temperature and volume of the vapour bubble.

MZ'

UZa'

UZb'
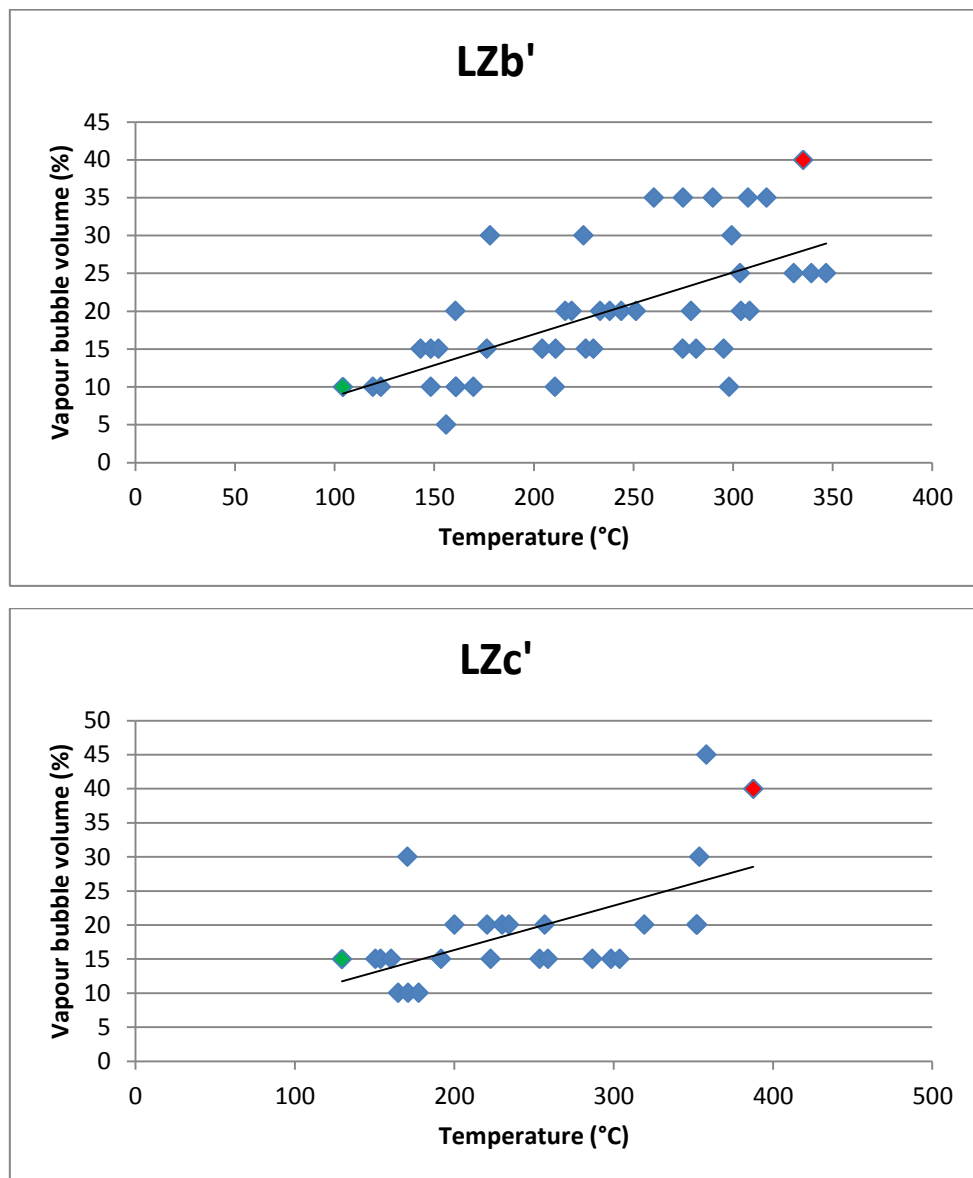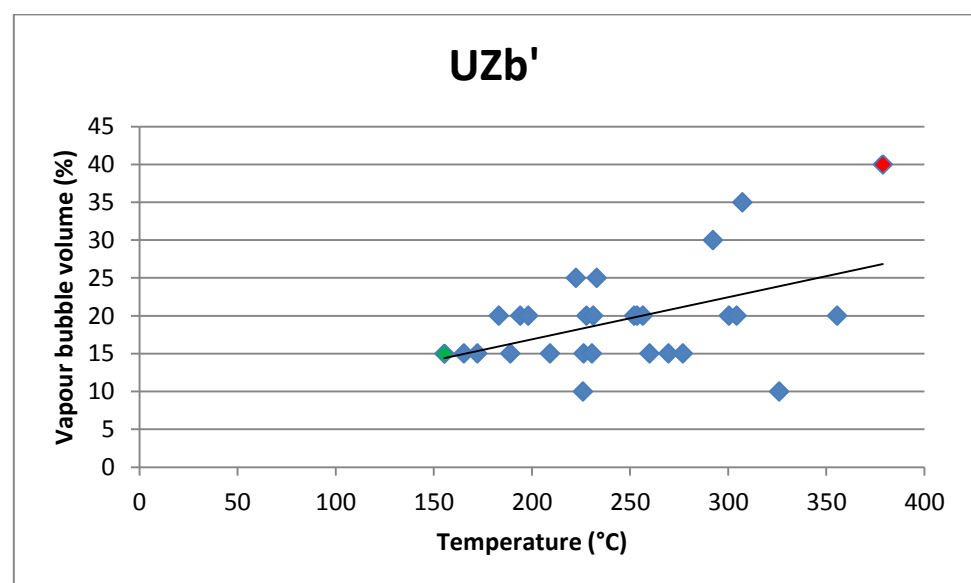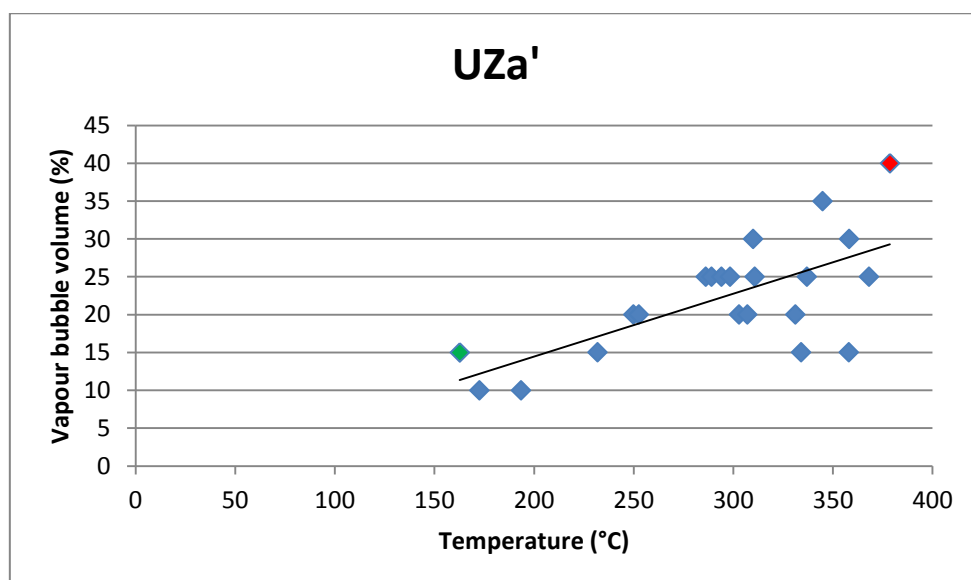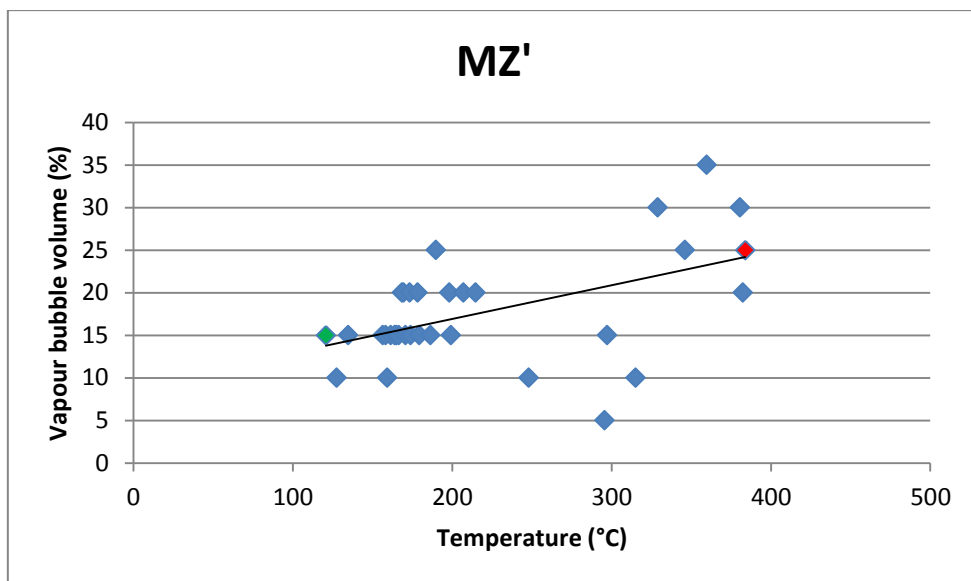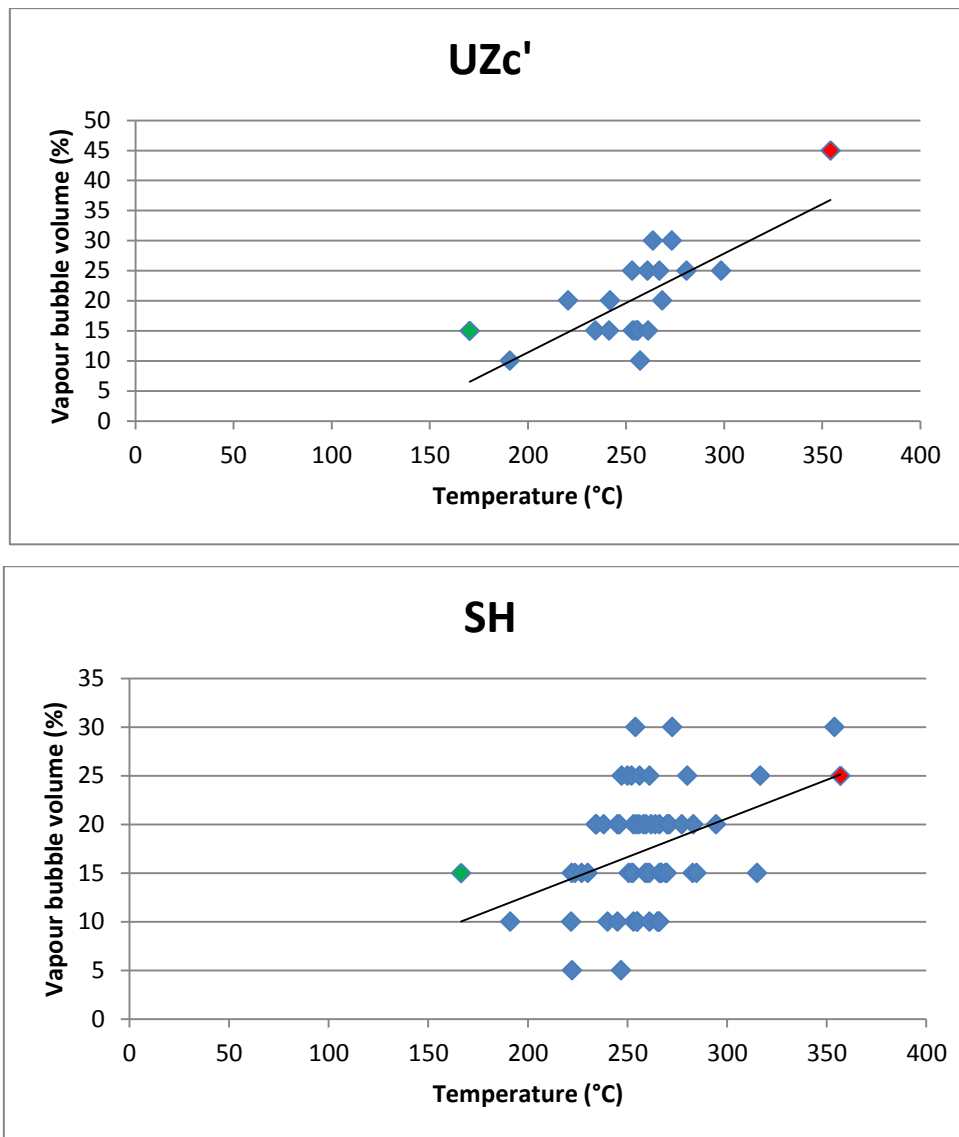
Figure 6-1: Homogenisation temperature versus the estimated vapour bubble volume for the zones analysed. There was some positive correlation between homogenisation temperature and vapour bubble volume. The points marked with red are the most preserved and are used to calculate the isochores shown in figure 6-2. The green points have undergone the most re-equilibration and are shown in figure 6-5.

The FI marked with red in figure 6-1 are considered to be the FI witch has been subjected to the least amount of re-equilibrium as they generally have the highest homogenisation temperature and a considerably larger vapour bubble. On the other end are the FI with the lowest homogenisation temperature and smaller vapour bubble marked with green. These FI are used to calculate new isochores, which are shown in figures 6-2 and 6-4.
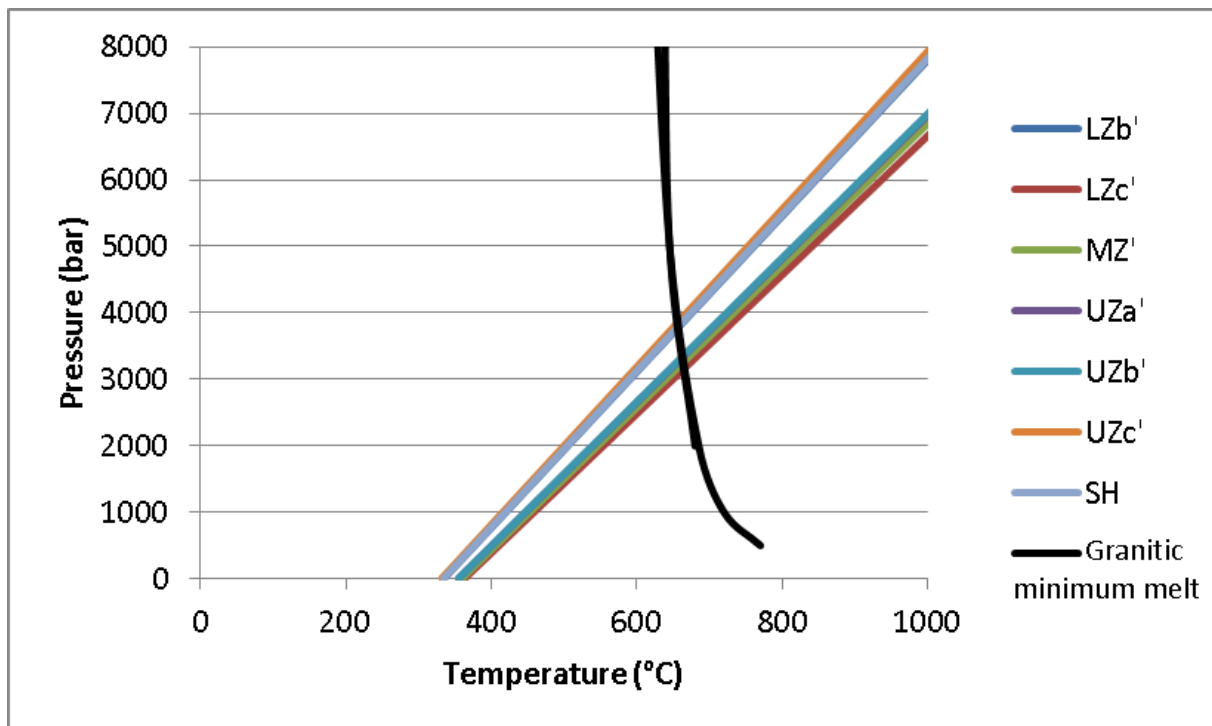
Figure 6-2: Isochores for each layer, plotted from the FI in each layer with the highest homogenisation temperature, and voluminous vapour bubble. The granitic minimum melt field is shown for quartz-albite-orthoclase system at H_2O saturation conditions and with 0-5 mol% CH_4. The granitic minimum melt lines are based on solidus and liquidus experiments. A close up of where the granitic melt intersects the isochores can be seen in figure 6-3.
Source: Granitic minimum melt from (Johannes and Holtz, 1996).

A better distinction between the isochores where they intersect the granitic minimum melt field can be seen in figure 6-4. The top and bottom layers plot closely together (LZb', UZc' and SH) at a higher pressure than the layers in the centre of the UBS, (MZ', UZa', UZb' and UZc').

The order of isochores (MZ', UZa', UZb' and UZc') correlate with the sequence of isochores and pressures found in previous research of the LS (Larsen and Tegner, 2006), where the pressure increased during crystallization of the LS. As the UBS sequence crystallized from the roof, the pressure grows from the roof downwards, opposite to the LS where the pressure grew from the floor upwards. However the FI in the UBS formed at a higher pressure than the FI in the same layers in the LS (3,15-3,34 kbar compared to about 2,8 kbar), and additionally the FI in the LS existed over a wider pressure range than the FI in the UBS. However Larsen and Tegner (2006) did not include results from the UZ, which would have formed at a higher pressure.

Other possible causes for the differences between the pressures in the UBS and the LS can be from differences between the two researches, either due to error from analytical

instruments, human error, chemical differences during the crystallisation of the intrusion, or that all FI in the UBS possibly had experienced some re-equilibration, thereby the FI used in figure 6-2 have experienced the least re-equilibration and store the most original properties.

However the pressures for the LZb', UZc' and SH, 3760-3860 bar, do not correlate with prior studies of the LS (Larsen and Tegner, 2006). This probably caused by these layers having been affected by more alteration and re-equilibration than the layers in the centre of the UBS, leaving no FI with its original properties. Previous research found a wide pressure gap in the SH, of about ±1.3 kbar, which did not exist in the LS (Larsen et al., 1992) and is in accordance with these results.

Earlier research has a significantly higher homogenisation temperature (Larsen and Tegner, 2006) than this study, as can be seen in figure 6-3. The samples used are from separate sampling profiles and have been subjected to different level of alteration, in this research they are from Kilen, while the samples used by Larsen and Tegner (2006) are from Basistoppen. The latter area has lower $\delta^{18}O$ values than Kilen (Taylor and Forester, 1979), indicating that it has been subjected to more alteration by the meteoric-hydrothermal system. The hydrothermal circulation system is fault- and fracture-controlled. The NE part of the intrusion, which is closer to where Kilen is located, contains a high abundance of fault and fractures, in addition to be shallow dipping, with the gneiss boundaries underlying the intrusion. Additionally the Kilen profile is closer to the margins of the intrusion which might have facilitated intense hydrothermal alteration.
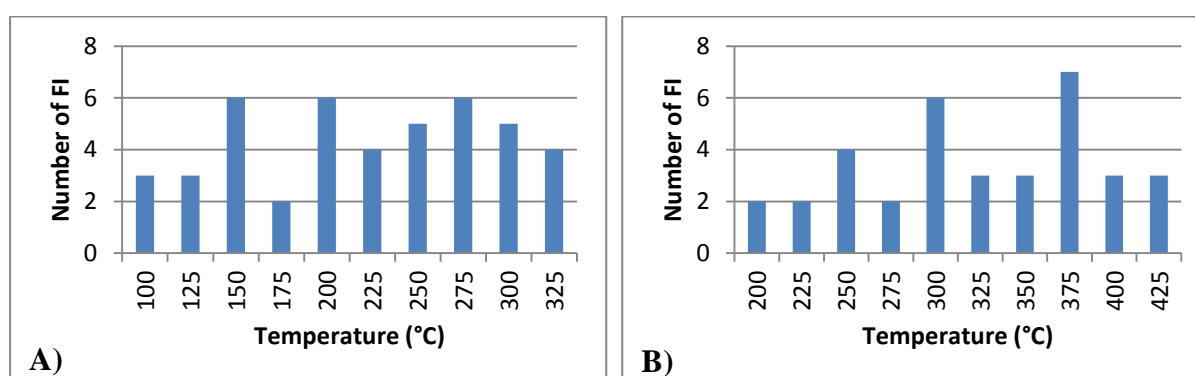
Figure 6-3: The homogenisation temperature in SH. A) The results from this research. B) The results from Larsen and Tegner (2006).

Furthermore Larsen and Tegner (2006) performed Raman spectroscopy, and found that the SH was the only sample that contained CH_4 below the detection limit of the machine. As the

salinities in all zones are similar this denotes that there has been some minor disturbance of the chemical composition of the FI, which did not influence the salinities.

Previous work (Bindeman et al., 2008, Taylor and Forester, 1979, Wotzlaw et al., 2012) has shown that the Skaergaard intrusion drove its own hydrothermal circulating system. The $\delta^{18}O$ values in plagioclase demonstrate that the hydrothermal system heavily influenced UBS as water could easily percolate downwards through the basalt into the roof section, but the hydrothermal system did not seriously impact the LS. The hydrothermal system probably collapsed inwards as the intrusion crystallized, overprinting the $\delta^{18}O$ values of the rock assemblage at subsolidus conditions. In addition the Basistoppen Sill later intruded into the Skaergaard intrusion where it perhaps partially re-melted the SH, increasing the thermal energy around the SH, thus causing increased alteration (Wotzlaw et al., 2012) and re-equilibration of the FI. The alteration by the hydrothermal circulation system resulted in inconsistent thermometric behaviour of the FI.
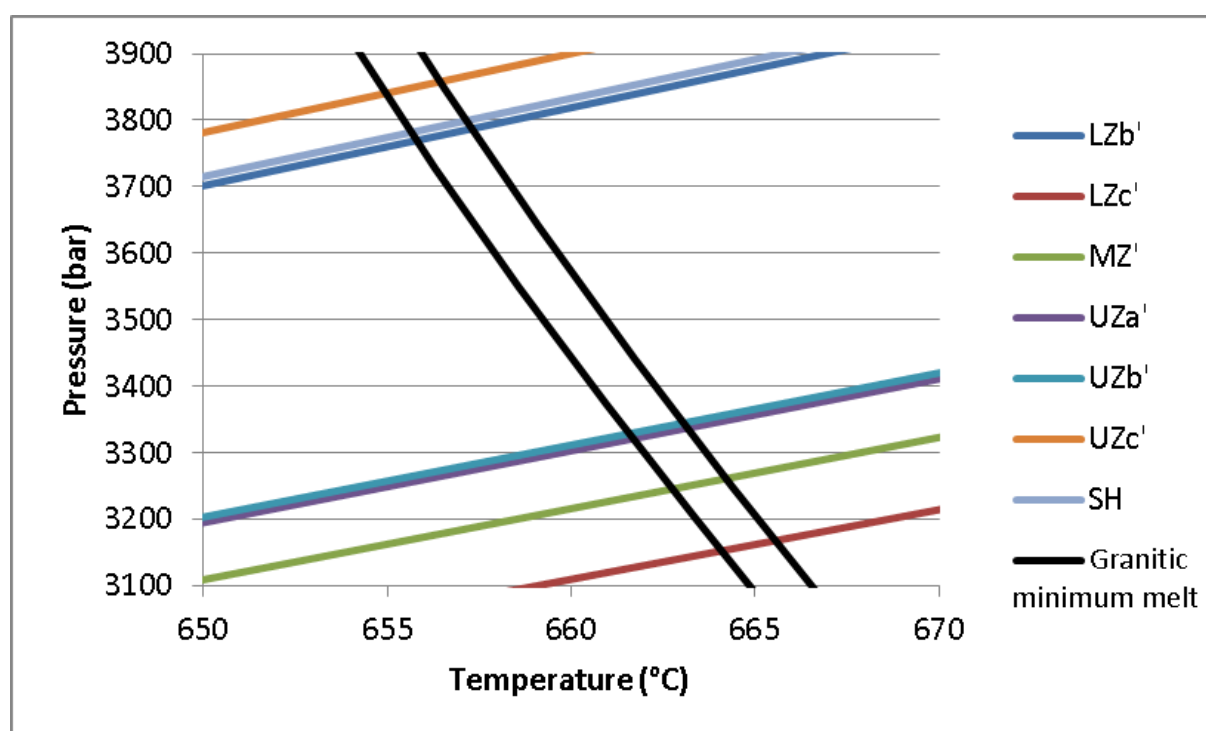
Figure 6-4: Closer view of the isochores from figure 6-2. The granitic minimum melt field is shown for quartz-albite-orthoclase system at H2O saturation conditions and with 0-5 mol% CH4. The granitic minimum melt lines are based on solidus and liquidus experiments.
Source: Granitic minimum melt from (Johannes and Holtz, 1996).

The isochores in figure 6-5 were calculated from one fluid inclusion from each zone. The FI with the lowest homogenisation temperature and small vapour bubble was used in each case. The FI were found to have similar salinities to the FI used to calculate the isochores in

figure 6-2, so the alteration and re-equilibrium by the hydrothermal circulation system had not influenced the chemical composition of the FI. The isochores illustrate the pressure to have been 9-13 kbar at the granitic minimum melt, which is considerably higher pressure than calculated in figure 6-2 where the highest homogenisation temperature was used.

However if the FI re-equilibrated due to hydrothermal circulation, they would have done so at a lower temperature. Previous research has estimated that to have happened at around 400-500°C (Taylor and Forester, 1979) or 400-600°C (Wotzlaw et al., 2012) (figure 6-6). Figures 6-5 and 6-6 have an ambiguous stratigraphic correlation, where the layers at the top of the intrusion plot with the highest pressure, and the bottom of the UBS plots with the lowest pressure. The fact that the isochores do not plot in reverse order, as the isochores in figure 6-2, implies that the pressure was related to the collapsing hydrothermal circulation system, which started outside of the intrusion, and then worked its way toward the centre of the intrusion.

The isochores do not plot completely in the same order as their stratigraphic height. This is probably the result of the FI in the system not reaching equilibrium during the hydrothermal circulation of fluids through the intrusion.
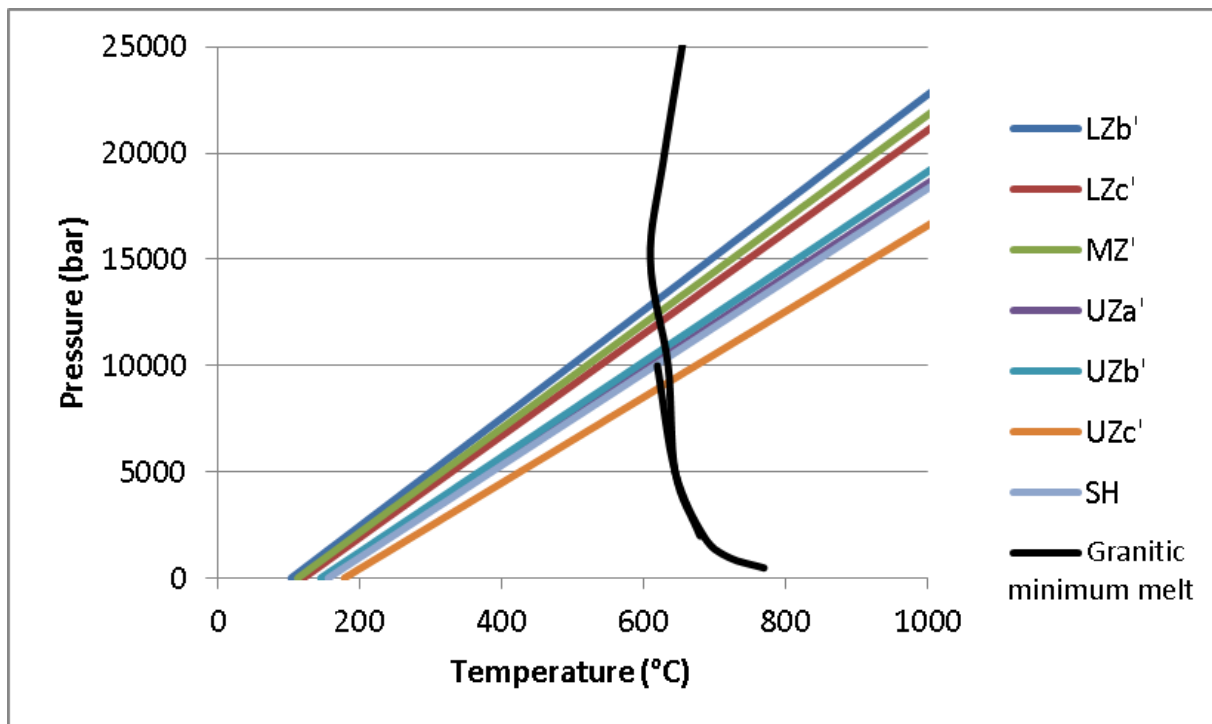
Figure 6-5: Isochores for each layer, plotted from one FI in each layer with a combination of low homogenisation temperature, and small vapour bubble. The granitic minimum melt field is shown for quartz-albite-orthoclase system at H2O saturation conditions and with 0-5 mol% CH$_4$. The granitic minimum melt lines are based on solidus and liquidus experiments.
Source: Granitic minimum melt from (Johannes and Holtz, 1996).

The FI used to calculate the isochores in figure 6-5 could have formed at considerably lower pressure if they re-equilibrated at a lower temperature, than if they would have formed at the granitic minimum melt line, or 4.5-12.5 kbar. They however still formed at a substantially higher pressure than earlier studies have shown.
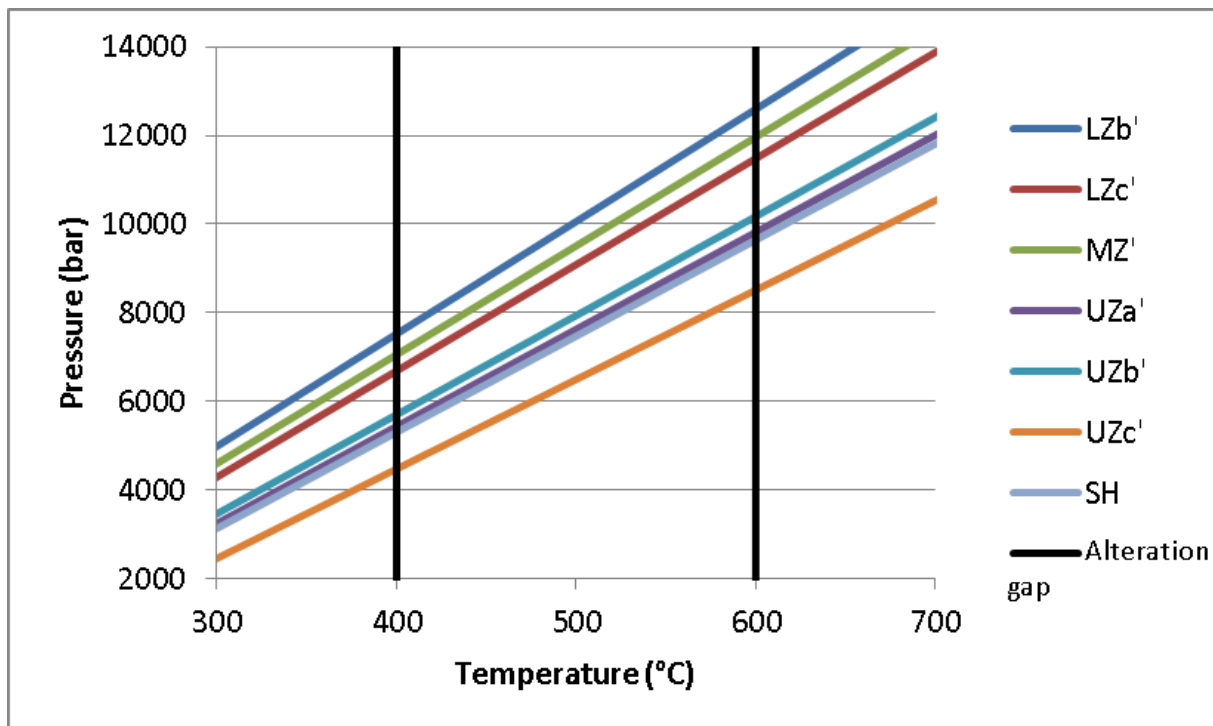
Figure 6-6: Closer view of the isochores from figure 6-4 and the alteration gap from previous research. The isochores plot at 4,5-12,5 kbar. Without further study it is not possible to constrain accurate pressures for the isochores. The granitic minimum melt fiel is shown for quartz-albite-orthoclase system at H_2O saturation conditions and with 0-5 mol% CH_4. The granitic minimum melt lines are based on solidus and liquidus experiments.
Source: Granitic minimum melt from (Johannes and Holtz, 1996).

It is questionable whether the FI show the pressure of the system during alteration, which would have been post crystallisation of the Skaergaard intrusion. During a continuous flood basalt eruption the pressure should have increased in the intrusion, which would result in a higher pressure during alteration than during crystallisation of the intrusion. Yet at 400°C, which is the lowest identified influx temperature of H_2O, the pressure is 4.4-7.6 kbar for the intrusion and thus considerably higher than realistic pressure in an extensional continental rift during flood basalt volcanism.

This is however based on lithostatic pressure. An extensional regime is a favourable setting for the development of faults and fractures, which facilitated permeability and fluid circulation of meteoric water from the surface. This would in turn mean that the pressure in the system would be hydrostatic, not lithostatic. The hydrostatic pressure is caused by a column of water above the intrusion, in the flood basalt, which based on earlier research has been estimated to be approximately 5-10 km thick, resulting in 490-980 bar pressure (figure 6-7). This might indicate that the hydrothermal circulation system caused the re-equilibration of FI at a temperature down to 110-230°C, although the hydrothermal circulation system might have existed at an even lower temperature.

As the meteoric water had travelled down through the overlaying flood basalt, which is chemically similar to the Skaergaard intrusion, it reacted with it and attained chemical equilibrium. Therefore there is not a noticeable chemical alteration in the Skaergaard intrusion, although it caused changes in the $\delta^{18}O$ and δD isotopes (Taylor and Forester, 1979).
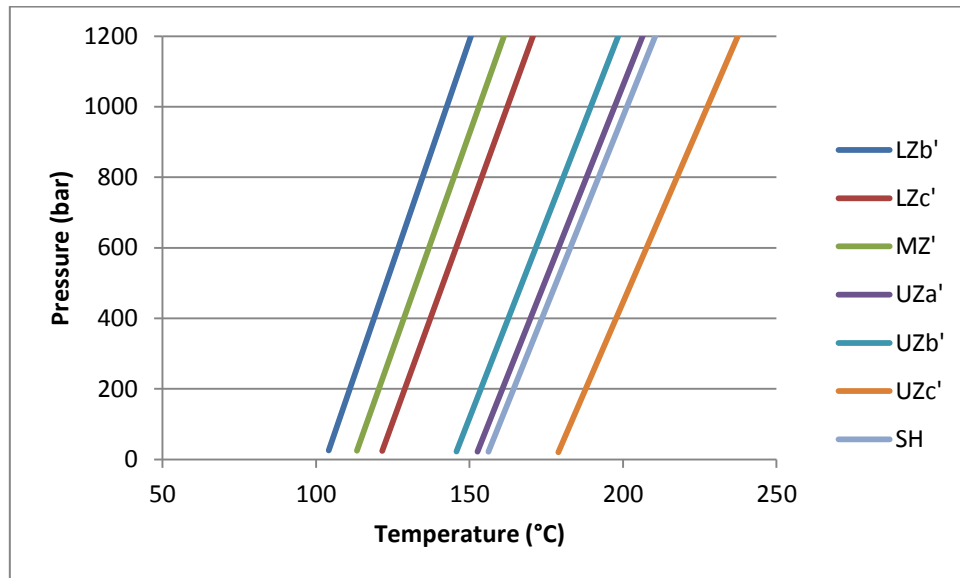
Figure 6-7: Hydrostatic pressure would result in a considerably lower pressure than lithostatic pressure. The hydrostatic pressure would have been dominant during hydrothermal circulation of fluids.

When the FI were viewed in microscope there was generally a trend for the FI in the same areas to have similar homogenisation temperatures, but this was not ubiquitous. No connection was found between how close the FI were to the margins of the FI, and the homogenisation temperature. In some areas small cracks close to the FI might have made FI in the crystal more susceptible to re-equilibration by volatiles, but there was no general explanation for the different homogenisation temperature in the crystals.

Larsen and Tegner (2006) found a steady decrease from the LZa up to the SH in the size of the vapour bubble within the FI, which was not noticed here. Instead the vapour bubbles had relatively stable volume size throughout the UBS.

The content of the FI is not considered to have been influenced as the FI that seem to have sustained various re-equilibration have similar salinities, which are comparable with previous study by Larsen et al. (1992). Larsen et al. (1992) found the salinity of the FI to be lower than what is found here, but partial leakage of water from the FI would have increased

the salinity, but decreased the pressure estimate of the FI. Therefore partial leakage of water from the FI is not considered likely.

If the volume of the FI was influenced and reduced by the alteration caused by the hydrothermal circulation system, without it influencing the content of the FI, it would have resulted in increased pressure. It is however considered to have affected each quartz grain differently, which might be influenced by permeability in the intrusion and the surrounding host rock.

7   Conclusions

The pegmatite structures at Vestrahorn are considered to have formed by the same process as the pegmatite structures in the Skaergaard intrusion, that is as late-magmatic structures during the late stages of crystallisation. Both the pegmatite structures and the granophyre masses were associated with an aqueous solution of the same chemical composition in the Skaergaard intrusion, which probably also applies to the structures at Vestrahorn. The pegmatite structure formed when the intercumulus melt separated from the already crystallized cumulates, and due to density difference rose upwards before crystallizing. The melt either rose with diapiric flow, or through structurally weaknesses or fractures.

Significant sections of the Skaergaard intrusion have already crystallized from iron- and silica-rich immiscible melts. Therefore it was reasonable that the samples geochemically analysed in this study might have been cumulates, or the most extreme end members, of the phases that formed as a result of immiscibility in the melt. The iron-rich phase probably formed as one end member of a silica liquid immiscibility, while the samples from the SH were granophyre accumulates, with not as clear immiscibility relations.

The petrography study correlates with previous research of the UBS, with the same order of cumulate minerals. Granophyre masses crystallized from intercumulus liquid, which was the last fraction of melt to crystallize in each layer. The alteration minerals found also supports earlier research, in addition to ilvaite, which is not commonly mentioned in petrography studies on the Skaergaard intrusion. The alteration minerals indicate that the intrusion sustained substantial hydrothermal alteration by meteoric-hydrothermal fluid, post-crystallization of the intrusion during subsolidus cooling; this caused alteration of the mineral assemblage and re-equilibration of fluid inclusions.

The fluid inclusions did not all sustain the same level of re-equilibration, but they all seem to contain about the original salinity concentrations. The FI with the highest homogenisation temperature and the biggest vapour bubble volume are probably the most preserved, and correlate with previous research from the LS, which suggests increasing pressure during crystallization due to the progressive burial by flood basalt. The hydrothermal-meteoric circulation system however may have caused considerable re-equilibrium on some of the FI. These FI instead correlate to their stratigraphy location in the intrusion, which is possibly the

result of a hydrostatic pressure dominating the system instead of lithostatic pressure post-crystallization.

7.1   Recommendations for future research

As with many research projects, time was a limiting factor. In order to obtain a better understanding of the overall meteoric-hydrothermal circulation system that dominated the volatile system post-crystallization of the intrusion, an in-depth overview over the FI in the UBS would be of great interest. This would e.g. include a larger dataset with a higher sampling density throughout the series, to identify differences between profiles in the Skaergaard intrusion, and to make sure that FI that have sustained the least amount of re-equilibration and the most intensive re-equilibration are documented during measurements.

A detailed study of the types and distribution of alteration minerals could be used to establish whether mineral alteration is consistent throughout the UBS and whether it correlates with the re-equilibration of FI. This could also serve as an indicator for possible chemical variations due to hydrothermal alteration in the intrusion. As ilvaite has only been mentioned in one previous study (Naslund et al., 1983), future research should consider this during petrography studies, as its location in the intrusion is not well documented.

Methods could include further analyses of mineral alteration and locations in the intrusion, along with an SEM-CL analysis of the FI. The latter would help assess whether the quartz has recrystallized, re-equilibrated or suffered other changes due to alteration, and to identify how much alteration each FI had sustained. Additionally the distance from margins and cracks in the quartz grains to the FI could be measured, to evaluate whether these factors influence the amount of re-equilibration of the FI.

Hydrothermal solutions can contribute to the dissolution and redistribution of elements, and therefore the influences of the meteoric-hydrothermal system might be of an importance for the distribution of elements in the Skaergaard intrusion.

8 References

ANDERSEN, J. C., RASMUSSEN, H., NIELSEN, T. F. & RONSBO, J. G. 1998. The Triple Group and the Platinova gold and palladium reefs in the Skaergaard Intrusion; stratigraphic and petrographic relations. *Economic Geology,* 93**,** 488-509.

ARCHER, D. G. 1992. Thermodynamic Properties of the NaCl+ H2O System. II. Thermodynamic Properties of NaCl (aq), NaCl· 2H2 (cr), and Phase Equilibria. *Journal of Physical and Chemical Reference Data,* 21**,** 793-829.

BAKKER, R. 2009. Package FLUIDS. Part 3: correlations between equations of state, thermodynamics and fluid inclusions. *Geofluids,* 9**,** 63-74.

BAKKER, R. & DIAMOND, L. 2000. Determination of the composition and molar volume of H 2 O-CO 2 fluid inclusions by microthermometry. *Geochimica et Cosmochimica Acta,* 64**,** 1753-1764.

BAKKER, R. J. 2003. Package< i> FLUIDS</i> 1. Computer programs for analysis of fluid inclusion data and for modelling bulk fluid properties. *Chemical Geology,* 194**,** 3-23.

BAKKER, R. J. 2012. Package FLUIDS. Part 4: thermodynamic modelling and purely empirical equations for H2O-NaCl-KCl solutions. *Mineralogy and Petrology,* 105**,** 1-29.

BAKKER, R. J. & BROWN, P. E. 2003. Computer modelling in fluid inclusion research. *Fluid inclusions: Analysis and interpretation,* 32**,** 175.

BAKKER, R. J. & JANSEN, J. B. H. 1994. A mechanism for preferential H2O leakage from fluid inclusions in quartz, based on TEM observations. *Contributions to Mineralogy and Petrology,* 116**,** 7-20.

BALDASSARO, P. & BODNAR, R. 2000. Low temperature phase relations in the system H2O–NaCl–FeCl2: application to fluid inclusion studies. *Geol Soc Am Abstr Program A-4 (2): A-4*.

BEST, M. G. 2013. *Igneous and metamorphic petrology*, John Wiley & Sons.

BINDEMAN, I., BROOKS, C., MCBIRNEY, A. & TAYLOR, H. 2008. The Low-δ18OδO18 Late-Stage Ferrodiorite Magmas in the Skaergaard Intrusion: Result of Liquid Immiscibility, Thermal Metamorphism, or Meteoric Water Incorporation into Magma? *The Journal of Geology,* 116**,** 571-586.

BJARNASON, I. T. 2008. An Iceland hotspot saga. *Jökull,* 58**,** 3-16.

BLAKE, D. 1966. The net-veined complex of the Austurhorn intrusion, southeastern Iceland. *The Journal of Geology***,** 891-907.

BODNAR, R. 1993. Revised equation and table for determining the freezing point depression of H< sub> 2</sub> O-NaCl solutions. *Geochimica et Cosmochimica Acta,* 57**,** 683-684.

BODNAR, R., BINNS, P. & HALL, D. 1989. Synthetic fluid inclusions-VI. Quantitative evaluation of the decrepitation behaviour of fluid inclusions in quartz at one atmosphere confining pressure. *Journal of Metamorphic Geology,* 7**,** 229-242.

BODNAR, R. & VITYK, M. O. 1994. Interpretation of microthermometric data for H2O-NaCl fluid inclusions. *Fluid inclusions in minerals: methods and applications***,** 117-130.

BORISENKO, A. 1977. Study of the salt composition of solutions in gas-liquid inclusions in minerals by the cryometric method. *Soviet Geology and Geophysics,* 18**,** 11-18.

BOUDREAU, A., MATHEZ, E. & MCCALLUM, I. 1986. Halogen geochemistry of the Stillwater and Bushveld Complexes: evidence for transport of the platinum-group elements by Cl-rich fluids. *Journal of Petrology,* 27**,** 967-986.

BOUDREAU, A. E. The Stillwater and Bushveld magmas were wet. 9th International Platinum Symposium, Abstract with program, 2002. 21-25.

BROOKS, C. K. 1969. On the distribution of zirconium and hafnium in the Skaergaard intrusion, East Greenland. *Geochimica et Cosmochimica Acta,* 33**,** 357-374.

BROOKS, K. 1989. Major gold find in Greenland. *Terra Nova,* 1**,** 591-593.

BROOKS, K. 2005. The Skaergaard intrusion: from icon to precious metal deposit. *Geology Today,* 21**,** 218-221.

BROWN, G. & PECKETT, A. 1977. Fluorapatites from the Skaergaard intrusion, east Greenland. *Mineralogical Magazine,* 41**,** 227-232.

BURKE, E. A. 2001. Raman microspectrometry of fluid inclusions. *Lithos,* 55**,** 139-158.

CAMPBELL, I. H. 2005. Large igneous provinces and the mantle plume hypothesis. *Elements,* 1**,** 265-269.

CARGILL, H. K., HAWKES, L. & LEDEBOER, J. A. 1928. The major intrusions of south-eastern Iceland. *Quarterly Journal of the Geological Society,* 84**,** 505-535.

DE JESUS PADILLA, A. 2011. *Volcano-pluton connections in silicic magmatic systems: insights from southeast Iceland and southern Nevada.* Vanderbilt University.

DEER, W. & WAGER, L. 1938. Two new pyroxenes included in the system clinoenstatite, clinoferrosilite, diopside and hedenbergite. *Min. Mag,* 25**,** 15-22.

DIXON, S. & RUTHERFORD, M. 1979. Plagiogranites as late-stage immiscible liquids in ophiolite and mid-ocean ridge suites: an experimental study. *Earth and Planetary Science Letters,* 45**,** 45-60.

DUAN, Z., MØLLER, N. & WEARE, J. H. 1995. Equation of state for the NaCl $\cdot$ H_2O $\cdot$ CO_2 system: prediction of phase equilibria and volumetric properties. *Geochimica et Cosmochimica Acta,* 59**,** 2869-2882.

DUBESSY, J., BOIRON, M.-C., MOISSETTE, A., MONNIN, C. & SRETENSKAYA, N. 1992. Determinations of water, hydrates and pH in fluid inclusions by micro-Raman spectrometry. *European journal of mineralogy,* 4**,** 885-894.

DUBOIS, M. & MARIGNAC, C. 1997. The H_2O-NaCl-$MgCl_2$ ternary phase diagram with special application to fluid inclusion studies. *Economic Geology,* 92**,** 114-119.

EGGLER, D. 1974. Volatiles in ultrabasic and derivative rock systems. Carnegie Inst. Wash. *Year Book,* 73**,** 215-224.

EINARSSON, P. & SAEMUNDSSON, K. 1987. *Earthquake Epicenters 1982-1985 and Volcanic Systems in Iceland: Upptok Jardskjalfta 1982-1985 Og Eldstodvakerfi a Islandi*, Menningarsjodur.

FURMAN, T., MEYER, P. S. & FREY, F. 1992. Evolution of Icelandic central volcanoes: evidence from the Austurhorn intrusion, southeastern Iceland. *Bulletin of volcanology,* 55**,** 45-62.

GALE, N., MOORBATH, S., SIMONS, J. & WALKER, G. 1966. KAr ages of acid intrusive rocks from Iceland. *Earth and Planetary Science Letters,* 1**,** 284-288.

GUÐMUNDSSON, A. T., ÞORMÓÐSDÓTTIR, S. & VALSSON, Ó. 2003. *Íslenskar eldstöðvar*, Vaka-Helgafell.

GUÐMUNDSSON, S. 2009. *Ummyndun í gabbróinnskotum á Suðausturlandi.* BS, Háskóli Íslands.

HALL, D. L., STERNER, S. M. & BODNAR, R. J. 1988. Freezing point depression of NaCl-KCl-H 2 O solutions. *Economic Geology,* 83**,** 197-202.

HAMILTON, D., BURNHAM, C. W. & OSBORN, E. 1964. The solubility of water and effects of oxygen fugacity and water content on crystallization in mafic magmas. *Journal of Petrology,* 5**,** 21-39.

HANAN, B. B. & SCHILLING, J.-G. 1997. The dynamic evolution of the Iceland mantle plume: the lead isotope perspective. *Earth and Planetary Science Letters,* 151**,** 43-60.

HIRSCHMANN, M. M., RENNE, P. R. & MCBIRNEY, A. R. 1997. 40Ar39Ar dating of the Skaergaard intrusion. *Earth and Planetary Science Letters,* 146**,** 645-658.

HOLNESS, M. B., STRIPP, G., HUMPHREYS, M., VEKSLER, I. V., NIELSEN, T. F. & TEGNER, C. 2011. Silicate liquid immiscibility within the crystal mush: late-stage magmatic microstructures in the Skaergaard intrusion, East Greenland. *Journal of Petrology,* 52**,** 175-222.

IMPERIAL-COLLEGE. 2007. *Imperial College Rock Library* [Online]. Available: https://wwwf.imperial.ac.uk/earthscienceandengineering/rocklibrary/viewglossrecord.php?gID=00000000077 [Accessed 30. Mars 2015].

IRVINE, T. & BARAGAR, W. 1971. A guide to the chemical classification of the common volcanic rocks. *Canadian journal of earth sciences,* 8**,** 523-548.

JAKOBSEN, J. K., VEKSLER, I., TEGNER, C. & BROOKS, C. K. 2005. Immiscible iron-and silica-rich melts in basalt petrogenesis documented in the Skaergaard intrusion. *Geology,* 33**,** 885-888.

JAKOBSEN, J. K., VEKSLER, I. V., TEGNER, C. & BROOKS, C. K. 2011. Crystallization of the Skaergaard intrusion from an emulsion of immiscible iron-and silica-rich liquids: evidence from melt inclusions in plagioclase. *Journal of Petrology***,** egq083.

JOHANNES, W. & HOLTZ, F. 1996. *Petrogenesis and experimental petrology of granitic rocks*, Springer Berlin.

KLAUSEN, M. 2006. Geometry and mode of emplacement of dike swarms around the Birnudalstindur igneous centre, SE Iceland. *Journal of volcanology and geothermal research,* 151**,** 340-356.

KNIGHT, C. & BODNAR, R. 1989. Synthetic fluid inclusions: IX. Critical PVTX properties of NaCl-H 2 O solutions. *Geochimica et Cosmochimica Acta,* 53**,** 3-8.

LARSEN, R. B. & BROOKS, C. K. 1994. Origin and evolution of gabbroic pegmatites in the Skaergaard intrusion, East Greenland. *Journal of Petrology,* 35**,** 1651-1679.

LARSEN, R. B., BROOKS, C. K. & BIRD, D. K. 1992. Methane-bearing, aqueous, saline solutions in the Skaergaard intrusion, east Greenland. *Contributions to Mineralogy and Petrology,* 112**,** 428-437.

LARSEN, R. B. & TEGNER, C. 2006. Pressure conditions for the solidification of the Skaergaard intrusion: eruption of East Greenland flood basalts in less than 300,000 years. *Lithos,* 92**,** 181-197.

LI, C. & RIPLEY, E. M. 2005. Empirical equations to predict the sulfur content of mafic magmas at sulfide saturation and applications to magmatic sulfide deposits. *Mineralium Deposita,* 40**,** 218-230.

LINKE, W. 1958. Solubilities, Inorganic and Metal Organic Compounds.

LUNDEGÂRDH, P. 1945. Distribution of vanadium, chromium, cobalt and nickel in eruptive rocks. *Nature, Lond,* 155**,** 753.

MARSHALL, D. J. & MARIANO, A. N. 1988. *Cathodoluminescence of geological materials*, Taylor & Francis.

MATHEZ, E. 1995. Magmatic metasomatism and formation of the Merensky Reef, Bushveld Complex. *Contributions to Mineralogy and Petrology,* 119**,** 277-286.

MAVROGENES, J. A. & O'NEILL, H. S. C. 1999. The relative effects of pressure, temperature and oxygen fugacity on the solubility of sulfide in mafic magmas. *Geochimica et Cosmochimica Acta,* 63**,** 1173-1180.

MCBIRNEY, A. R. & NAKAMURA, Y. 1974. Immiscibility in late-stage magmas of the Skaergaard intrusion. *Carnegie Institution of Washington Yearbook,* 73**,** 348-352.

MCBIRNEY, A. R. & SONNENTHAL, E. L. 1990. Metasomatic replacement in the Skaergaard Intrusion, East Greenland: preliminary observations. *Chemical geology,* 88**,** 245-260.

MOORBATH, S., SIGURDSSON, H. & GOODWIN, R. 1968. KAr ages of the oldest exposed rocks in Iceland. *Earth and Planetary Science Letters,* 4**,** 197-205.

MORGAN, W. J. 1972. Deep mantle convection plumes and plate motions. *AAPG Bulletin,* 56**,** 203-213.

MYSEN, B. O. 1977. The solubility of H2O and CO2 under predicted magma genesis conditions and some petrological and geophysical implications. *Reviews of Geophysics,* 15**,** 351-361.

NALDRETT, A. J. 2004. *Magmatic sulfide deposits: geology, geochemistry and exploration*, Springer Science & Business Media.

NASLUND, H. 1984. Petrology of the Upper Border Series of the Skaergaard intrusion. *Journal of Petrology,* 25**,** 185-212.

NASLUND, H., HUGHES, J. & BIRNIE, R. 1983. Ilvaite, an alteration product replacing olivine in the Skaergaard intrusion. *American Mineralogist,* 68**,** 1004-1008.

NIELSEN, T. & SCHØNWANDT, H. 1990. Gold and platinum group metal mineralisation in the Skaergaard intrusion, southern east Greenland. *Grùnlands Geologiske Undersùgelse Rapport,* 148.

NIELSEN, T. F. 2004. The shape and volume of the Skaergaard intrusion, Greenland: implications for mass balance and bulk composition. *Journal of Petrology,* 45**,** 507-530.

NWE, Y. Y. 1976. Electron-probe studies of the earlier pyroxenes and olivines from the Skaergaard intrusion, East Greenland. *Contributions to Mineralogy and Petrology,* 55**,** 105-126.

O'REILLY, S. Y., GRIFFIN, W. & SEGELSTAD, T. 1990. The nature and role of fluids in the upper mantle: evidence in xenoliths from Victoria, Australia. *Stable Isotopes and Fluids in Mineralization, Special Publication,* 13**,** 315-323.

OAKES, C. S., BODNAR, R. J. & SIMONSON, J. M. 1990. The system NaCl・ CaCl 2 ・ H 2 O: I. The ice liquidus at 1 atm total pressure. *Geochimica et Cosmochimica Acta,* 54**,** 603-610.

PHILPOTTS, A. 1982. Compositions of immiscible liquids in volcanic rocks. *Contributions to Mineralogy and Petrology,* 80**,** 201-218.

PICOT, P. & JOHAN, Z. 1982. *Atlas of ore minerals*, BRGM.

PLATINARESOURCES. 2015. *Skaergaard* [Online]. Available: http://www.platinaresources.com.au/projects/skaergaard/ [Accessed 10. January 2015].

ROBB, L. 2009. *Introduction to ore-forming processes*, John Wiley & Sons.

ROEDDER, E. 2002. Fluid Inclusions. *Encyclopedia of Physical Sciences and Technology,* Third Edition**,** 71-77.

ROEDDER, E. & RIBBE, P. 1984. *Fluid inclusions*, Mineralogical Society of America Washington, DC.

ROOBOL, M. 1972. Size-graded, igneous layering in an Icelandic intrusion. *Geological Magazine,* 109**,** 393-404.

ROOBOL, M. 1974. The geology of the Vesturhorn intrusion, SE Iceland. *Geological Magazine,* 111**,** 273-286.

ROSASCO, G. J. & ROEDDER, E. 1979. Application of a new Raman microprobe spectrometer to nondestructive analysis of sulfate and other ions in individual phases in fluid inclusions in minerals. *Geochimica et Cosmochimica Acta,* 43**,** 1907-1915.

SALMONSEN, L. P. & TEGNER, C. 2013. Crystallization sequence of the Upper Border Series of the Skaergaard Intrusion: revised subdivision and implications for chamber-scale magma homogeneity. *Contributions to Mineralogy and Petrology,* 165**,** 1155-1171.

SAMSON, I., ANDERSON, A. & MARSHALL, D. D. 2003. *Fluid inclusions: analysis and interpretation*, Mineralogical Association of Canada.

SIGURDSSON, H. 1969. Nýjar aldursákvarðanir á íslenzku bergi. *Náttúrufræðingurinn,* 38**,** 187-193.

SONNENTHAL, E. L. 1992. Geochemistry of dendritic anorthosites and associated pegmatites in the Skaergaard Intrusion, East Greenland: evidence for metasomatism by a chlorine-rich fluid. *Journal of Volcanology and Geothermal Research,* 52**,** 209-230.

STEPHEN, H. & STEPHEN, T. 1963. *Solubilities of inorganic and organic compounds*, Pergamon Press Oxford.

STERNER, S. M., HALL, D. L. & BODNAR, R. J. 1988. Synthetic fluid inclusions. V. Solubility relations in the system NaCl-KCl-H 2 O under vapor-saturated conditions. *Geochimica et Cosmochimica Acta,* 52**,** 989-1005.

SUN, S.-S. & MCDONOUGH, W. 1989. Chemical and isotopic systematics of oceanic basalts: implications for mantle composition and processes. *Geological Society, London, Special Publications,* 42**,** 313-345.

TAYLOR, H. P. & FORESTER, R. W. 1979. An oxygen and hydrogen isotope study of the Skaergaard intrusion and its country rocks: a description of a 55 my old fossil hydrothermal system. *Journal of Petrology,* 20**,** 355-419.

THORARINSSON, S. B. & TEGNER, C. 2009. Magma chamber processes in central volcanic systems of Iceland: constraints from layered gabbro of the Austurhorn intrusive complex. *Contributions to Mineralogy and Petrology,* 158**,** 223-244.

THY, P., LESHER, C. E. & TEGNER, C. 2009. The Skaergaard liquid line of descent revisited. *Contributions to Mineralogy and Petrology,* 157**,** 735-747.

VAN DEN KERKHOF, A. M. & HEIN, U. F. 2001. Fluid inclusion petrography. *Lithos,* 55**,** 27-47.

VINK, G. E. 1984. A hotspot model for Iceland and the Vøring Plateau. *Journal of Geophysical Research: Solid Earth (1978–2012),* 89**,** 9949-9959.

VOZNYAK, D. & KALYUZHNIY, V. 1976. Utilization of decrepitated inclusions for reconstruction of PT conditions of mineral formation [on example of pegmatitic quartz from Volyn]. *Mineral Sb,* 30**,** 31-40.

WAGER, L. & BROWN, G. 1953. Layered intrusions. *Medd. dansk geol. Foren,* 12**,** 335-349.

WAGER, L. R. 1932. Preliminary Account of the Geology and Geomorphology of the Angmagssalik District and the Coast Northwards to Kangerdlugsuak Fjord. *Geografisk Tidsskrift,* 35.

WAGER, L. R. & BROWN, G. M. 1967. Layered igneous rocks.

WAGER, L. R., DEER, W. A. & EXPEDITION, B. E. G. 1939. *Geological investigations in East Greenland, pt. 3, The petrology of the Skaergaard intrusion, Kangerdlugssuaq, East Greenland*, CA Reitzel.

WAGER, L. R., DEER, W. A., WAGER, H. G. & GORDON, M. 1937. The Kangerdlugssuak Region of East Greenland. *The Geographical Journal,* 90**,** 393-421.

WAGER, L. R. & MITCHELL, R. L. 1951. The distribution of trace elements during strong fractionation of basic magma—a further study of the Skaergaard intrusion, East Greenland. *Geochimica et Cosmochimica Acta,* 1**,** 129-208.

WAGER, L. R., VINCENT, E. A. & SMALES, A. A. 1957. Sulphides in the Skaergaard intrusion, east Greenland. *Economic Geology,* 52**,** 855-903.

WALKER, G. P. 1964. Geological investigations in eastern Iceland. *Bulletin of Volcanology,* 27**,** 351-363.

WENDLANDT, R. F. 1982. Sulfide saturation of basalt and andesite melts at high pressures and temperatures. *American Mineralogist,* 67**,** 877-885.

WHITE, R. & MCKENZIE, D. 1989. Magmatism at rift zones: the generation of volcanic continental margins and flood basalts. *Journal of Geophysical Research: Solid Earth (1978–2012),* 94**,** 7685-7729.

WINTER, J. D. 2010. *Principles of igneous and metamorphic petrology*, Prentice Hall New York.

WOTZLAW, J.-F., BINDEMAN, I. N., SCHALTEGGER, U., BROOKS, C. K. & NASLUND, H. R. 2012. High-resolution insights into episodes of crystallization, hydrothermal alteration and remelting in the Skaergaard intrusive complex. *Earth and Planetary Science Letters,* 355**,** 199-212.

YODER, H. & TILLEY, C. Natural tholeiite basalt-water system. Vortragsreferat; Annual Meetings Geol. Soc. Amer., 1956.

ZHANG, Y.-G. & FRANTZ, J. D. 1987. Determination of the homogenization temperatures and densities of supercritical fluids in the system NaClKClCaCl 2 H 2 O using synthetic fluid inclusions. *Chemical Geology,* 64**,** 335-350.

Appendix A – Samples from Vestrahorn

Samples collected at Vestrahorn, along with their location and rock type. The coordinates are in hddd°mm.mmm´ format.

Sample number	Latitude	Longitude	Description and location
MT14-01	**N 64°14.380´**	**W014°58.958´**	Felsic dyke
MT14-02	**N 64°14.352´**	**W014°58.834´**	Felsic dyke
MT14-03	**N 64°14.319´**	**W014°58.889´**	Melano-granophyric, location 1
MT14-04	**N 64°14.319´**	**W014°58.889´**	Pegmatite, location 1
MT14-05	**N 64°14.319´**	**W014°58.889´**	Pegmatite, location 1
MT14-06	**N 64°14.317´**	**W014°58.863´**	Coarse gabbro
MT14-07	**N 64°14.319´**	**W014°58.458´**	Fine grained centre of pegmatite, location 2
MT14-08	**N 64°14.319´**	**W014°58.458´**	Fine gabbro, location 2
MT14-09	**N 64°14.362´**	**W014°58.365´**	Felsic dyke
MT14-10	**N 64°14.366´**	**W014°58.360´**	Coarse gabbro, location 4
MT14-11	**N 64°14.366´**	**W014°58.334´**	Melano-granophyric, pegmatite, fine gabbro
MT14-12	**N 64°14.380´**	**W014°58.197´**	Melano-granophyric dyke, location 5
MT14-13	**N 64°14.380´**	**W014°58.197´**	Melano-granophyric center and pegmatitic margins, location 5
MT14-14	**N 64°15.303´**	**W014°59.379´**	Melano-granophyric dyke, location 6
MT14-15	**N 64°15.303´**	**W014°59.379´**	Coarse gabbro, location 6
MT14-16	**N 64°14.380´**	**W014°58.197´**	Melano-granophyric center and pegmatitic margins, location 5
MT14-17	**N 64°14.315´**	**W014°58.588´**	Fine gabbro
MT14-18	**N 64°14.306´**	**W014°58.605´**	Pegmatite
MT14-19	**N 64°14.301´**	**W014°58.632´**	Fine gabbro
MT14-20	**N 64°14.317´**	**W014°58.683´**	Fine gabbro
MT14-21	**N 64°14.298´**	**W014°58.767´**	Removed and not used
MT14-22	**N 64°14.305´**	**W014°58.845´**	Coarse gabbro
MT14-23	**N 64°14.304´**	**W014°58.890´**	Coarse gabbro

Appendix B – Petrography study

Short overview of each sample that was studied.

Sample name	Location	Layer	Main minerals	Texture	Grain size	Comments
SK08-1	UBS, Brødretoppen	LZb'	Plag, augite, qtz, apatite, oxides.	Poikilitic texture, ophitic texture, spinifex texture.	<7 mm	Skeletal to dendritic oxide growth.
SK08-2	UBS, Brødretoppen	LZb'	Plag, augite, qtz, apatite, oxides.	Poikilitic texture, ophitic texture, spinifex texture.	<13 mm	Skeletal to dendritic oxide growth.
SK08-12	UBS, Brødretoppen	LZb'	Plag, augite, qtz, apatite, oxides, sulphide.	Poikilitic texture, ophitic texture, granophyre texture.	>10 mm	Skeletal to dendritic oxide growth.
SK08-58	UBS, Brødretoppen	LZb'	Plag, augite, qtz, apatite, oxides, sulphide.	Poikilitic texture, ophitic texture, granophyre texture.	<7 mm	Skeletal to dendritic oxide growth.
SK08-104	UBS, Kilen	UZc'	Plag, qtz, olivine, oxides.	Granophyre texture.	<4 mm	>90% are plag and qtz (or altered plag). The oxides form small aggregates.
SK08-105	UBS, Kilen	UZc'	Plag, augite, qtz, olivine, apatite, oxides, sulphide	Poikilitic texture, granophyre texture.	<4 mm	Highly altered. Skeletal to dendritic oxide growth.

SK08-106	UBS, Kilen	UZc'	Plag, augite, qtz, olivine, apatite, oxides, sulphide	Poikilitic texture, granophyre texture.	<4 mm	Highly altered. Skeletal to dendritic oxide growth.
SK08-110	UBS, Kilen	SH	Plag, augite, qtz, olivine, oxides, sulphide	Poikilitic texture, granophyre texture.	<4 mm	>80% are plag and qtz (or altered plag). Highly altered. Skeletal to dendritic oxide growth.
SK08-142	UBS, Hammer Pas	UZa'	Plag, augite, qtz, olivine, apatite, oxides, sulphide	Poikilitic texture, ophitic texture, granophyre texture.	<6 mm	Skeletal to dendritic oxide growth.
SK08-148	UBS, Kilen	UZb'	Plag, qtz, olivine, apatite, oxides, sulphide.	Granophyre texture.	<7 mm	Mostly composed of granophyre masses.
SK08-150	UBS, Kilen	UZb'	Plag, augite, qtz, olivine, apatite, calcite, chlorite, oxides, sulphide.	Poikilitic texture, granophyre texture.	<6 mm	Highly altered. Skeletal to dendritic oxide growth.
SK08-154	UBS, Kilen	UZb'	Plag, augite, qtz, olivine, apatite, calcite, oxides, sulphide.	Poikilitic texture, granophyre texture.	<6 mm	Highly altered. Skeletal to dendritic oxide growth.
SK08-155	UBS, Kilen	UZb'	Plag, augite, qtz,	Poikilitic texture,	<7 mm	Highly altered. Skeletal to

			olivine, apatite, oxides, sulphide.	granophyre texture.		dendritic oxide growth.
SK08-156	UBS, Kilen	UZb'	Plag, augite, qtz, olivine, apatite, oxides, sulphide.	Poikilitic texture, granophyre texture.	<3 mm	Highly altered. Skeletal to dendritic oxide growth. Ilvaite.
SK08-158	UBS, Kilen	UZa'	Plag, augite, qtz, olivine, apatite, chlorite, oxides, sulphide.	Poikilitic texture, ophitic texture, granophyre texture.	<5 mm	Skeletal to dendritic oxide growth.
SK08-159	UBS, Kilen	MZ'	Plag, augite, qtz, olivine, apatite, oxides.	Poikilitic texture, ophitic texture, granophyre texture.	<7,5 mm	Skeletal to dendritic oxide growth.
SK08-162	UBS, Kilen	MZ'	Plag, augite, qtz, apatite, oxides, sulphide.	Poikilitic texture, ophitic texture, granophyre texture.	<5 mm	Skeletal to dendritic oxide growth.
SK08-164	UBS, Kilen	UZb'	Plag, augite, qtz, olivine, apatite, oxides.	Poikilitic texture, granophyre texture.	<9 mm	Highly altered. Skeletal to dendritic oxide growth. Ilvaite.
SK08-165	UBS, Kilen	UZb'	Plag, augite, qtz, olivine, apatite, oxides, sulphide.	Poikilitic texture, ophitic texture, granophyre texture.	<10 mm	Highly altered. Skeletal to dendritic oxide growth. Contains abnormally much

						of sulphides. Ilvaite.
SK08-197	UBS, Kilen	LZc'	Plag, augite, qtz, olivine, apatite, oxides.	Poikilitic texture, ophitic texture, granophyre texture.	<6 mm	The granophyre texture is underdeveloped. Skeletal to dendritic oxide growth.
SK08-198	UBS, Kilen	LZc'	Plag, augite, qtz, olivine, apatite, oxides, sulphide.	Poikilitic texture, ophitic texture, granophyre texture.	<8 mm	The granophyre texture is underdeveloped. Skeletal to dendritic oxide growth.
SK08-199	UBS, Kilen	LZb'	Plag, augite, qtz, apatite, oxides, sulphide.	Poikilitic texture, ophitic texture, granophyre texture.	<12 mm	Skeletal to dendritic oxide growth.
SK08-200	UBS, Kilen	LZb'	Plag, augite, qtz, oxides, sulphide.	Poikilitic texture, ophitic texture, granophyre texture.	<7 mm	Skeletal to dendritic oxide growth.
SK08-201	UBS, Kilen	LZb'	Plag, augite, qtz, apatite, oxides, sulphide.	Poikilitic texture, ophitic texture, granophyre texture.	<7 mm	Skeletal to dendritic oxide growth.
SK11-50	UBS	SH	Plag, augite, qtz, olivine, oxides, sulphide.	Poikilitic texture, granophyre texture, spinifex texture.	<4 mm	Highly altered. Oxide needles, >80% plag and qtz. Ilvaite.
SK11-51	UBS	SH	Plag, augite, qtz, olivine, oxides,	Poikilitic texture, granophyre texture,	<3,5 mm	Highly altered. Oxide needles, >80% plag and qtz.

				sulphide.	spinifex texture.		Ilvaite.
SK11-52	UBS	SH	Plag, augite, qtz, olivine, oxides, sulphide.	Poikilitic texture, spinifex texture.	<7 mm	Highly altered. Oxide needles, >80% plag and qtz. Ilvaite.
SK11-55	UBS	SH	Plag, augite, qtz, olivine, oxides, sulphide.	Poikilitic texture, spinifex texture.	<6,5 mm	Highly altered. Oxide needles, >80% plag and qtz. Ilvaite.
458291	UBS	Iron rich phase	Plag, augite, qtz, olivine, oxides, sulphide.	Poikilitic texture, cumulative oxides.	>40 cm	70-90% skeletal to dendritic oxide growth.
SK-5A	LS	Iron rich phase	Plag, augite, qtz, olivine, oxides, sulphide.	Poikilitic texture, cumulative oxides.	<11 mm	Skeletal to dendritic oxide growth.
SK-5B	LS	Iron rich phase	Plag, augite, qtz, olivine, oxides, sulphide.	Poikilitic texture, cumulative oxides.	<10 mm	Skeletal to dendritic oxide growth.

Appendix C – Geochemical analysis

XRF analysis for major elements in wt. %.

	SK11-50-A	SK11-50-B	SK11-51-A	SK11-51-B	SK11-52-A	SK11-52-B	SK11-55-A	SK11-55-B	SK-5-A	SK-5-B	SK-5-C	SK-5-D	458291-A	458291-B
SiO_2	61.39	61.46	60.89	60.58	60.55	61.22	60.99	61.50	33.95	34.04	33.14	32.91	15.85	15.35
TiO_2	1.33	1.27	1.25	1.35	1.41	1.32	1.41	1.31	10.11	10.13	11.07	11.07	17.55	17.27
Al_2O_3	10.54	10.65	10.38	10.34	10.50	10.51	11.09	11.1	4.08	4.9	4.46	4.06	3.39	4.51
Fe_2O_3	14.35	14.67	15.10	15.56	15.21	14.60	15.27	14.36	38.18	38.28	37.47	38.63	55.37	51.11
MnO	0.29	0.28	0.23	0.23	0.23	0.21	0.26	0.24	0.40	0.39	0.39	0.40	0.43	0.37
MgO	0.32	0.30	0.31	0.32	0.31	0.28	0.29	0.28	6.16	6.09	5.90	6.14	2.69	2.73
CaO	4.61	4.26	4.45	4.51	4.52	4.42	4.16	4.00	8.20	7.85	7.93	8.01	4.05	2.42
Na_2O	3.97	4.01	3.83	3.74	3.78	3.79	4.00	4.03	0.82	0.94	1.06	0.89	0.69	1.02
K_2O	1.85	1.84	2.02	1.94	2.12	2.11	2.21	2.20	0.14	0.13	0.15	0.12	0.13	0.14
P_2O_5	0.24	0.25	0.26	0.26	0.27	0.26	0.25	0.24	0.31	0.16	0.23	0.26	1.12	0.12
Sum	98.88	98.99	98.72	98.83	98.90	98.71	99.93	99.26	102.35	102.91	101.80	102.49	101.27	95.04
LOI	0.14	0.22	0.23	0.34	0.15	0.26	0.37	0.36	-1.70	-1.76	-1.69	-1.70	-3.26	-3.61

XRF analysis for trace elements in ppm.

	SK11-50-A	SK11-50-B	SK11-51-A	SK11-51-B	SK11-52-A	SK11-52-B	SK11-55-A	SK11-55-B	SK-5-A	SK-5-B	SK-5-C	SK-5-D	458291-A	458291-B
Sc	15	12	15	18	13	17	14	16	69	66	68	71	43	47
V	5	4	3	2	5	5	4	5	839	864	830	855	1819	2471
Cr													13	20
Co	1		1	3				2	110	111	112	113	142	169
Ni	30	27	27	27	25	27	29	26	102	100	101	109	212	236
Cu	169	159	119	124	168	151	170	163	1411	1303	997	1017	3054	1116
Zn	252	254	258	258	237	196	242	232	271	277	271	276	487	511
Ga	41	42	41	40	41	40	39	39	33	32	32	32	51	55
As	7	7	8	12	5	7	6	6	8	5	7	9	20	24
Rb	42	43	51	53	54	53	50	50	19	17	18	18	23	24
Sr	262	260	253	257	231	223	215	217	83	92	95	83	65	65
Y	143	138	141	140	128	117	131	131	34	28	27	30	44	21
Zr	1032	950	1191	1364	688	905	962	952	137	125	136	128	191	158
Nb	69	66	65	68	59	58	66	62	15	14	17	15	29	21
Mo									1	2	2	1	4	2
Sn	1			2	3	4		1						
Sb				1		1		2						
Cs	10	5	6	11	2	6	6	8	5	12	20	14	25	30
Ba	459	444	467	474	431	433	459	473						
La	74	71	81	81	69	71	77	71	21	18	18	13	11	4
Ce	167	169	184	181	173	156	167	172	28	20	29	27	67	28
Pb	5	3	4	5	6	5	6	6						
Th	5	5	6	7	7	6	6	7	2	1	3	2	1	1
U	2	2	1	1	2	2	1	2	4	1	3	3	5	6

Appendix D – Microthermometry results

Table D.1: Results from LZb' (SK08-200).

Tmi	TmHydrate	Vol.%	Th-total	Th phase
-45.2	-1.4	35	328	Liquid
-47.3	-1.6	40		Liquid
-41.6	-1.4	15		Vapor
	-1.4	10	171.5	Liquid
-44.4		25	369.8	Liquid
		10	317.9	Liquid
-47	-0.7	15	314.9	Liquid
	-0.7	40	357.5	Liquid
-46.5		35	277.6	Liquid
-43.4	-3.2	15	300.2	Liquid
	-3.2	20	297.4	Liquid
-42.1	0.6	25	>400	Liquid
-45.1	-0.7	25	361.9	Liquid
	-1.1	25		Liquid
	-0.7	25		Liquid
-47.7	-2.6	20		Liquid
	-2.4	20	267.9	Liquid
	-1.7	5	166.3	Liquid
	-0.9	10	158	Liquid
	1.1	10	127.1	Liquid
	-1.9	10	131.3	Liquid
	1.7	15	152.6	Liquid
-44.7	-1.6	10	111	Liquid
-44.7	-4.4	15	162.1	Liquid
	-4.2	20	171.3	Liquid
-46.3	-2	20	253.8	Liquid
-43.4	-2	15	292.9	Liquid
	-2.1	15	225	Liquid
	-1.8	10	224.5	Liquid
	-2.4	15	188.1	Liquid
	-2.1	10	180.9	Liquid
	-2.1	10	171.6	Liquid
	-2.1	15	158	Liquid
-44.5	-1.2	15	245.1	Liquid
	-1.2	25	323.6	Liquid
-46.2	-1.2	20	248.8	Liquid
	-3	35	337.9	Liquid
	-1.7	30	239.8	Liquid
	-1.4	20	324.2	Liquid

	-1.4	20	233.5	Liquid
-41.8	-3.9	20	328.8	Liquid
-44	-3.9	25	352.4	Liquid
-44.9	-1.3	30	189.8	Liquid
-47.5	-2.9	15		Liquid
	-4.2	40	>400	Liquid
-46.6	-3.9	30	319.2	Liquid
	-4.9	15	241	Liquid
	-3.1	20	260	Liquid
-48.3	-1.4	35	293.2	Liquid
-47.2	-3.4	35	309	Liquid
-48	-1	15	217.8	Liquid
	-2.7	20	230.1	Liquid

Table D.2: Results from LZc' (SK08-197).

Tmi	Tmice	TmHydrate	Vol.%	Th-total	Th-phase
		-0.7	15	153.7	Liquid
		2.4	15	129.6	Liquid
		-0.6	15	150.5	Liquid
		-1.2	20	220.7	Liquid
		-0.4	20		
		-0.5	15	258.8	Liquid
		-0.5	15	286.7	Liquid
-46.7		-0.6	20	319.3	Liquid
		-0.5	30	170.6	Liquid
	-22	13.4	10	154.2	Liquid
		-0.3	45	358.2	Liquid
		-1	20	352.5	Liquid
		-0.7	15	191.8	Liquid
		-4.5	15	303.8	Liquid
-45		-1.4	15	298.4	Liquid
		-1.4	15	160.4	Liquid
		-0.6	10	164.9	Liquid
		-1.4	10	171.1	Liquid
-41		-0.8	20	230.2	Liquid
		-0.8	20	256.8	Liquid
		-0.4	15	253.7	Liquid
		-0.6	15	222.9	Liquid
		-0.8	10	177.7	Liquid
		-0.7	20	234.3	Liquid
		-0.6	20	200.2	Liquid
		-0.6	15		

		-0.5	15		
		-1	15		
		-3.2	40	387.7	Liquid
		-0.7	20	>400	Liquid
		-0.5	30	353.8	Liquid
		-2.6	20	352.1	Liquid
		-0.7	10	>400	Liquid

Table D.3: Results from MZ' (SK08-162).

Tmi	TmHydrate	Vol.%	Th-total	Th phase
-46	-0.2	20	173.2	Liquid
	-0.2	20	169.4	Liquid
-41	-0.2	20	207.1	Liquid
	2.4	15	120.8	Liquid
	0	15	163.9	Liquid
	-1.2	15	134.8	Liquid
-37	-0.3	35		
	0	15	170.6	Liquid
	-0.3	10	315	Vapor
	-0.3	10	159.3	Liquid
	-0.2	15	161.5	Liquid
	-0.2	15	158.2	Liquid
	3.8	15	156.4	Liquid
	-0.2	25	383.9	Liquid
	-1.5	20		Vapor
	0.9	5	295.5	Liquid
	-1.8	15	297.1	Liquid
-44	-0.2	25	345.9	Liquid
	2.2	10	247.9	Liquid
-49	-0.1	20	198.1	Liquid
	-0.3	30	329	Liquid
	-0.3	20	382.3	Liquid
	-0.3	20	214.6	Liquid
	-0.3	35	359.6	Liquid
	-0.3	30	380.5	Liquid
	-2.9	10		
	-2.9	20	168.4	Liquid
	-2.9	15	186.4	Liquid
	-3.1	15	173.9	Liquid
	-3.1	15	179.3	Liquid
	-3.3	15	164.9	Liquid
	-3.3	15	199.2	Liquid

	-3.7	20	178.3	Liquid
	-3.7	25	189.7	Liquid
	-3.2	15	166.4	Liquid
	-2.9	15	164.9	Vapor
	-0.1	10	127.5	Liquid

Table D.4: Results from UZa' (SK08-158).

Tmi	TmHydrate	Vol.%	Th-total	Th phase
-43	-0.6	25	368.2	Liquid
	-0.6	20	307.1	Liquid
	-0.6	20		
-42	-0.6	30	310.1	Liquid
	-0.3	15	358.1	Liquid
	-0.3	15		Liquid
-43	-0.8	25	298.5	Liquid
	-1.3	10	193.5	Liquid
	-2.4	25	294.2	Liquid
	-1.6	25	289.2	Liquid
	-1.4	20		
	-1.4	25	310.8	Liquid
	-1.2	30		Vapor
	-1.4	30	358.2	Liquid
	-1.7	35		
-44	-1.2	25	286.3	Liquid
	-1.4	15	232	Liquid
	-3.1	25	337	Liquid
	-3.7	40	378.6	Liquid
	-1.1	10	172.6	Vapor
	-0.6	15	162.7	Liquid
	-2.7	20	252.7	Liquid
	-3.5	20	302.9	Liquid
	-4.8	20	331.2	Liquid
	-0.3	15	334.2	Liquid
	-0.3	35	344.9	Liquid
	-0.3	15		Vapor
	-0.2	40		Vapor
	-0.2	10		Vapor
	-0.3	15		Vapor
	-0.3	20	249.9	Liquid
	-0.3	80	>400	Liquid

Table D.5: Results from UZb' (SK08-156).

Tmi	Tmice	TmHydrate	Vol.%	Th-total	Th phase
		-1.3	20		Liquid
		-1.4	20	253.6	Liquid
		-1.4	15	189.1	Liquid
		-0.9	15	165.4	Liquid
		4	10		Liquid
		-2.1	40	378.8	Liquid
-48		-2.2	30	>400	Liquid
	-23	-0.1	15	155.4	Liquid
		-2	15	230.6	Liquid
		-2	25	222.4	Liquid
		-2.4	10	226	Liquid
		-2	15	260	Liquid
		-4.5	20	304.3	Liquid
		-1.3	20	227.8	Liquid
		-1.7	35	307.2	Liquid
-44		-1.4	15	269.6	Liquid
		-2.6	20	252.2	Liquid
-47		-0.5	15	172.3	Liquid
		19.1	10	326	Liquid
		-0.5	15	276.9	Liquid
		-1	20	194	Liquid
		-3.9	15	226.3	Liquid
		-1.1	20	355.5	Liquid
		-0.7	20		Liquid
		-0.7	20	>400	Liquid
		-1.4	20	300.4	Liquid
		-0.7	30	292.2	Liquid
-47		-1	20	256.5	Liquid
	-18	-4.8	15	209.3	Liquid
		-3.7	20	183.1	Liquid
		-1	20	198.1	Liquid
-43		-1	20	231.2	Liquid
		-1.6	25	233	Liquid

Table D.6: Results from UZc' (SK08-105).

Tmi	Tmice	TmHydrate	Vol.%	Th-total	Th phase
	-26.7		5	208.2	Liquid
		-6.9	20	>230	Liquid
			10	193.3	Liquid

-44.7	-24.5	-7.6	20	220.5	Liquid
-40.8	-23.9		15	170.3	Liquid
		-0.3	25	280.8	Liquid
-26	-25.4	-8.3	15	253.5	Liquid
-31	-23.8	-9.3	20	268.4	Liquid
	-23.6	-8.1	15	254.7	Liquid
			10	160.3	Liquid
		-1.5	20		Liquid
		-2.4	30	273.4	Liquid
-26		-0.7	45	354.2	Liquid
		-0.7	25	298.4	Liquid
		-0.2	15	261.3	Liquid
-42		0.2	15	255.9	Liquid
		-1.3	10	190.8	Liquid
		-1.3	30	263.8	Liquid
		-1.3	20	241.9	Liquid
		-1.3	10	257.2	Liquid
-43		-1.3	25	267	Liquid
		-1.3	15	255.9	Liquid
		-1.3	25	260.9	Liquid
-43.8		-1.6	15	234.4	Liquid
		-1.3	15		Liquid
		-1.3	25	253.2	Liquid
		-1.5	15	241.4	Liquid

Table D.7: Results from SH (SK08-110).

Tmi	TmHydrate	Vol.%	Th-total	Th phase
-28.7	-0.2	20	270	Liquid
	-0.2	25	280	Liquid
	-0.2	15	315	Liquid
	-0.6	15		
	-0.6	20		
	-0.6			
	-1	20	258	Liquid
	-1	15	267	Liquid
	-1	25	261	Liquid
	-1	15	267	Liquid
	-1	20		
-32.3	-2.1	10	240	Liquid
	-2.1	10	244.9	Liquid
	-2.1	10		
-30.2	-2.1	15	260	Liquid

	-2.1	10	253	Liquid
	-0.4	15	230	Liquid
	-0.4	25	256	Liquid
	-0.4	20		
	-0.4	25	250	Liquid
-35	-1.5	20	266	Liquid
	-1.5	10	266	Liquid
	-1.6	10	261	Liquid
	-1.6	20	270	Liquid
	-1.6	10	265	Liquid
	-1.6	15	266	Liquid
-26.5	-1.2	20	253	Liquid
-27	-0.4	10	265.5	Liquid
	-0.4	10	221.6	Liquid
	-1.2	15	252	Liquid
-37	-1.7	25	247	Liquid
-36	-1.7	25	252	Liquid
-38	-1.7	20	261.8	Liquid
	-1.7	10	254.7	Liquid
-36	-1.5	30	272.4	Liquid
-34	-1.6	20	264	Liquid
	-1.6	15	269	Liquid
	-1.9	10	255	Liquid
-52.2	-1.6	5	222.2	Liquid
-46.4	-1.4	5	246.7	Liquid
	-1.3	15	259	Liquid
	-1.6	20	245	Liquid
-49.5	-2.2	15	250.6	Liquid
	-2.2	15	227	Liquid
-47.6	-1.6	20	259.3	Liquid
	-2.1	20	283	Liquid
	-1.1	25	316.7	Liquid
-38	-2	20	254.5	Liquid
-47.2	-1.6	30	254	Liquid
-41.3	-1.6	30	353.9	Liquid
	-1.2	15	222	Liquid
-48	-0.8	25	356.9	Liquid
-47.3	-0.7	40	>400	Liquid
-47	-2.1	20	238	Liquid
	-1.8	20	234	Liquid
	-0.8	20		
-46	-2.7	20	234.4	Liquid
	-2.2	15	223.6	Liquid
-51	-4.7	20	277.2	Liquid
	-4.4	15	252.7	Liquid

-48.7	-1.7	20	255.9	Liquid
-48.1	-1.6	15	269.7	Liquid
-46.6	-1.7	15	261	Liquid
-51.6	-1.3	10	191.2	Liquid
	-1.4	20	246	Liquid
	-1.7	15	166.5	Liquid
	-2.6	30		
-46	-0.9	15	282.8	Liquid
-48	-2	20	294.4	Liquid
-48	-2.2	15	284.6	Liquid
-52.2	-1.7	20	271	Liquid